RICE UNIVERSITY

ANISOTROPIC HARDENING OF AN INITIALLY ISOTROPIC POROUS LIMESTONE

by

CESARE CAFFERATA CELLE

A THESIS SUBMITTED
IN PARTIAL FULFILLMENT OF THE
REQUIREMENTS FOR THE DEGREE OF

MASTER OF SCIENCE

Thesis Director's Signature

J B Cleathan Jr.

Houston, Texas

MAY 1975

ABSTRACT

ANISOTROPIC HARDENING OF
AN INITIALLY ISOTROPIC POROUS LIMESTONE

by Cesare Cafferata Celle

The lack of a good description of the behavior of a compacting material that exhibits yield-strength dependence upon hydrostatic pressure, prompted the present study to determine experimentally a yield envelope that would predict the material behavior more accurately.

True triaxial tests were performed on Cordova Limestone in order to find detailed information about the stress-strain behavior of this material. From the results of these tests a yield surface was obtained and the experimental data showed normality to be a very good approximation for the actual plastic strains produced by the initial yielding of the material studied.

Subsequent yield surfaces were obtained experimentally and it was found that the yield surface displaces in the stress space as hardening takes place.

Different tests were performed in order to obtain the shape of the low hydrostatic stress region of the yield envelope. Induced anisotropy due to hardening led to a

closing of this yield envelope and a kinematic hardening rule completed the description of the limestone's plastic behavior.

The consistency between the predicted and observed stress-strain behavior indicates that the proposed yield envelope model and a kinematic hardening rule correspond to a proper description of the behavior of this limestone.

TABLE OF CONTENTS

NOMENCLATURE

I,II,III	First three invariants of the stress tensor
J_2	Second invariant of the deviatoric stress
p_c	Confining pressure
z,x,y = 1,2,3	Material axes
$\sigma_1,\sigma_2,\sigma_3$ =	
$\sigma_z,\sigma_x,\sigma_y$	Principal stresses
ϵ^p_{ij}	Plastic strain tensor
$\dot{\epsilon}^p_{ij}$	Plastic strain rate tensor
ϕ	Angle of internal friction for Coulomb type yield condition
c	Positive constant, cohesive strength of Coulomb material
$\Delta\sigma_z,\Delta\sigma_1$	Differential axial stress ($\sigma_z - p_c$)
$\Delta\sigma_{x,y},\Delta\sigma_{2,3}$	Differential radial stress
κ	Work-hardening parameter
k	Yield stress in pure shear of a metal, positive constant

ACKNOWLEDGEMENTS

The author wishes to express his gratitude to Dr. John B. Cheatham for his advice and support during the research for and the writing of this thesis.

The suggestions and assistance of David L. Garrett and Tom S. Marshall in performing experiments are also greatly appreciated.

I. INTRODUCTION

This work is an attempt to explain the plastic behavior of a general type of material that compacts or shows a volume decrease as it undergoes permanent deformation, and exhibit yield strength dependence upon hydrostatic pressure.

As it has been remarked by Shield and Ziegler (15), in order to describe the mechanical behavior of a work-hardening material, three ingredients are needed. The first two are the initial yield condition and a flow rule to be associated with the initial and subsequent loading surfaces. The third ingredient is still in an uncertain state of development and is a subject still open to suggestion, namely the determination of a hardening law, i.e. the manner of constructing the subsequent loading surfaces. Here it is often convenient to regard the problem of specification as divided into two parts : (a) the determination of the shape of the loading surface, and (b) its functional dependence on parameters that measure the degree of hardening taking place.

Induced anisotropy due to hardening is to be considered as a particular case.

This thesis attempts to obtain an experimental solution for a yield envelope for Cordova limestone and its hardening behavior. Several types of true-triaxial tests will be performed for this purpose and the material to be considered

is Cordova limestone.

The second chapter is a brief review of plasticity theory and related work ; in the third chapter, the equipment and experimental procedures are described. Finally, in chapter four, the experimental results are analyzed. Our first step is to obtain an initial yield envelope for our compacting material. Then several exploratory tests are performed to analyze the behavior of this initial yield surface as hardening takes place. Normality of the strain-rate vector to the loading surface is computed and analyzed at corners due to intersection of two surfaces.

A study of induced anisotropy due to hardening taking place is undertaken and utilized to obtain the graphical solution for our model.

Subsequent yield surfaces are obtained through different loading paths, and a model for a yield envelope is obtained that satisfies the hardening behavior of our material.

Finally, it is found that this model follows a kinematic hardening rule and this concept was tested through different hardening paths.

The improved graphical solution for a yield envelope model and its hardening rule for a Cordova limestone should be of use to others studying compacting materials.

II. LITERATURE SURVEY

Theoretical Background

This section will contain a brief review of basic plasticity theory as well as a thorough review of workhardening theories and yield conditions generally associated with soil and rock mechanics. Time and thermal effects in plasticity will not be discussed in the review as they are neglected or assumed negligible in the analysis of the rock studies.

In this discussion, as well as in the remainder of this work, it will be convenient to refer the state of stress of a point in the body to a point in stress space. The stress point should ideally be in a nine-dimensional space ; however, it is often more convenient and instructive to use sub-spaces when possible.

The concept of a yield function or loading function is used to specify the elastic or plastic character of the material behavior.

The yield function

$$f = f\ (\sigma_{ij},\ \epsilon^{p}_{ij},\ \kappa)$$

may be expressed as a function of the stresses σ_{ij}, plastic strains ϵ^{p}_{ij}, and the stress or strain histories, where here κ is a workhardening parameter defining the stress or strain histories. The value of f is restricted such that $f \leq 0$.

When $f < 0$ the material behaves elastically, and when $f = 0$ the material may or may not behave plastically. Now since

$$\dot{f} = \frac{\partial f}{\partial \sigma_{ij}} \dot{\sigma}_{ij} + \frac{\partial f}{\partial \epsilon^{p}_{ij}} \dot{\epsilon}^{p}_{ij} + \frac{\partial f}{\partial \kappa} \dot{\kappa}$$

the following conditions may prevail when $f = 0$, and when

$$\dot{f} = \frac{\partial f}{\partial \sigma_{ij}} \dot{\sigma}_{ij} < 0$$

the material is going from a plastic to an elastic state (unloading)

$$\frac{\partial f}{\partial \sigma_{ij}} \dot{\sigma}_{ij} = 0$$

the loading path is tangent to the surface defined by $f = 0$ and no plastic strains occur (neutral loading)

$$\frac{\partial f}{\partial \sigma_{ij}} \dot{\sigma}_{ij} > 0$$

the material goes from one plastic state to another accompanied by plastic strains (loading).

When the state of stress is such that $f = 0$, the surface described by $f = 0$ in stress space is termed the yield surface. The yield surface for a virgin material is called the initial yield surface, and the manner in which the surface changes shape or translates is called the hardening rule. The yield surfaces must be at least piecewise continuous.

Other restrictions are imposed upon f by the fundamental postulate of plasticity, referred to as Drucker's postulate.

Drucker (1) stated that when a stable, workhardening body, in equilibrium with a given set of loads has another set of self-equilibrating external loads slowly applied and removed, positive work must be done by the external loads during application of the loads and non-negative work must be done during the loading cycle. This statement is often paraphrased to say that no useful net energy above any elastic cycle may be extracted from a stable, workhardening body and a system of stresses. It may be written as :

$$W_e = \int_{t_1}^{t_2} (\sigma_{ij} - \sigma_{ij}^*)\ \dot{\epsilon}_{ij}^p\ dt \geq 0$$

where W_e is the work done by the external loads, σ_{ij} are the stresses caused by the external load, σ_{ij}^* are the equilibrium stresses and $\dot{\epsilon}_{ij}^p$ are the plastic strain rates associated with the deformation. Consequently a Taylor's series expansion of W_e about $t = t_1$ gives :

$$(\sigma_{ij} - \sigma_{ij}^*)\ \dot{\epsilon}_{ij}^p \geq 0$$

and if $\sigma_{ij} = \sigma_{ij}^*$, the second term of the expansion also implies that :

$$\dot{\sigma}_{ij}\ \dot{\epsilon}_{ij}^p \geq 0$$

Now assuming f = 0 for plastic flow and the state of stress

is such that $f = 0$, the above implies that :

(1) the surface $f = 0$ must be convex ;

(2) $\dot{\epsilon}_{ij}$ is parallel to the normal of the smooth segment of the surface.

If the surface is piecewise continuous and the loading point is at a corner of the yield surface, the direction of $\dot{\epsilon}^p_{ij}$ lies between the normals of the adjacent regular portions of the surface (see figure II - 1a,b). J.L. Sanders (6) stated that at a corner developed by the intersection of two yield surfaces, the strain rate $\dot{\epsilon}^p_{ij}$ is the vector sum of the contribution from both loading surfaces (see figure II - 1c).

The fact that $\dot{\epsilon}^p_{ij}$ is parallel to the normal of the yield surface formalizes the generally used concept of the plastic potential where the plastic strain rates are proportioned to the gradient of the yield function.

Since the gradient of f defines the normal of the surface $f = 0$,

$$\dot{\epsilon}^p_{ij} = \lambda \frac{\partial f}{\partial \sigma_{ij}}$$

where λ is an arbitrary positive constant. Thus by Drucker's postulate the yield function dictates the plastic strains of the material, and a consistent theory requires the plastic strain rates to be derivable from the yield condition. In the presence of finite deformation, Naghdi and Trapp (14) proved normality of the strain-rate vector to the loading surface in stress space for a special class of elastic-plastic

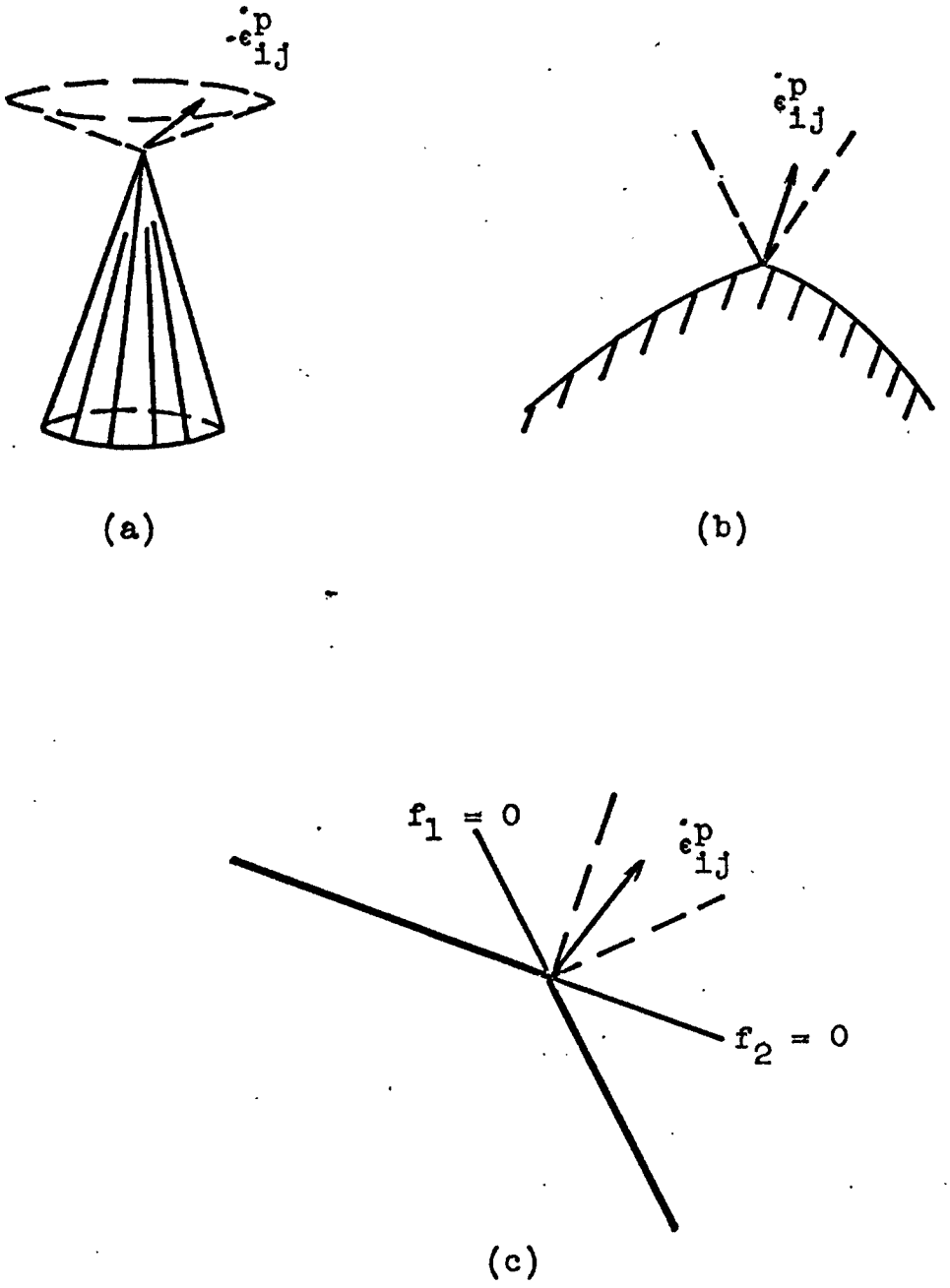

Figure II - 1 Strain rates vectors at a corner

materials and for rigid-plastic materials.

In spite of the results of Drucker's postulate, some workers attempt to evoke plasticity theory using yield function with non associated flow rules (De Jung (2), Barden, and Khayatt (3)). This is indicative that either the material behavior cannot be described using plasticity theory or that the yield functions are improperly chosen.

Often corners in yield functions are proposed in order to allow a consistent yield function and strain rate field that matches a material's observed behavior (Jenike and Shield (4)).

The plastic strain rates are defined kinematically by

$$\dot{\epsilon}_{ij} = \tfrac{1}{2} \left(\frac{\partial v_i}{\partial x_j} + \frac{\partial v_i}{\partial x_i} \right)$$

where

x_i are the spatial or Eulerian coordinates of the body

$v_i = v_i (x_j, t)$ are the velocities in terms of the Eulerian coordinates.

Thus the plastic strain rates are independent of the reference state, and normality (or the plastic potential) holds regardless of the magnitude of the strains. Since the plastic strain rates are defined in terms of spatial variables,

$$\int_{t_o}^{t} \dot{\epsilon}^{p}_{ij} \, dt$$

is physically meaningless in terms of total plastic strain

at a material point. It might be possible to interpret the integral as a material time integral (analogue of material time derivative) that follows a particle through its motion : and thus the result could be interpreted as a total plastic strain. However, the actual mathematical process of evaluating that integral would be a complex or perhaps an impossible task. See Malvern (5).

If we assume infinitisemal strains, the elastic and plastic parts of a deformation can be superimposed such that :

$$\epsilon_{ij} = \epsilon^{e}_{ij} + \epsilon^{p}_{ij}$$

where

$$\epsilon_{ij} = \tfrac{1}{2} \frac{\partial u_i}{\partial x_j} + \frac{\partial u_j}{\partial x_i}$$

u_i are components of a displacement,

x_i are components of the spatial or material coordinates,

ϵ^{e}_{ij} are components of the elastic strains,

ϵ^{p}_{ij} are components of the plastic strains.

Assuming linear elasticity holds, then :

$$\epsilon^{e}_{ij} = C^{-1}_{ijkl}\, \sigma_{kl}$$

where

C^{-1}_{ijkl} are components of the inverse elastic cons-

tants for a generalized Hooke's law.

Then the plastic strain becomes :

$$\epsilon^{p}_{ij} = \tfrac{1}{2} \left(\frac{\partial u_i}{\partial x_j} + \frac{\partial u_j}{\partial x_i}\right) - C^{-1}_{ijkl}\, \sigma_{kl}$$

Note that this definition holds only for infinitesimal strains in a linear elastic/plastic material ; but that the plastic strain rates derived from the yield functions are exact regardless of the amount of deformation.

The most commonly used yield functions for metals are the von Mises or maximum distortional energy and the Tresca or maximum shear stress yield functions. They can be expressed in terms of principal stresses as follows :

von Mises

$$f = \frac{1}{6} (\sigma_1 - \sigma_2)^2 + (\sigma_1 - \sigma_3)^2 + (\sigma_2 - \sigma_3)^2 - k^2$$

Tresca

$$f = \sigma_{max} - \sigma_{min} - 2k$$

where k is the yield stress in pure shear. The appropriate yield surface for a von Mises function is a cylinder in the principal stress space with the hydrostatic line ($\sigma_1 = \sigma_2 = \sigma_3$) as its axis and with radius k^2 (see figure II - 2). The Tresca yield condition describes a regular hexagonal prism with the hydrostatic line as its axis (see figure II - 3,4).

If k is a constant, then the yield conditions above describe a perfectly plastic material. That is a material

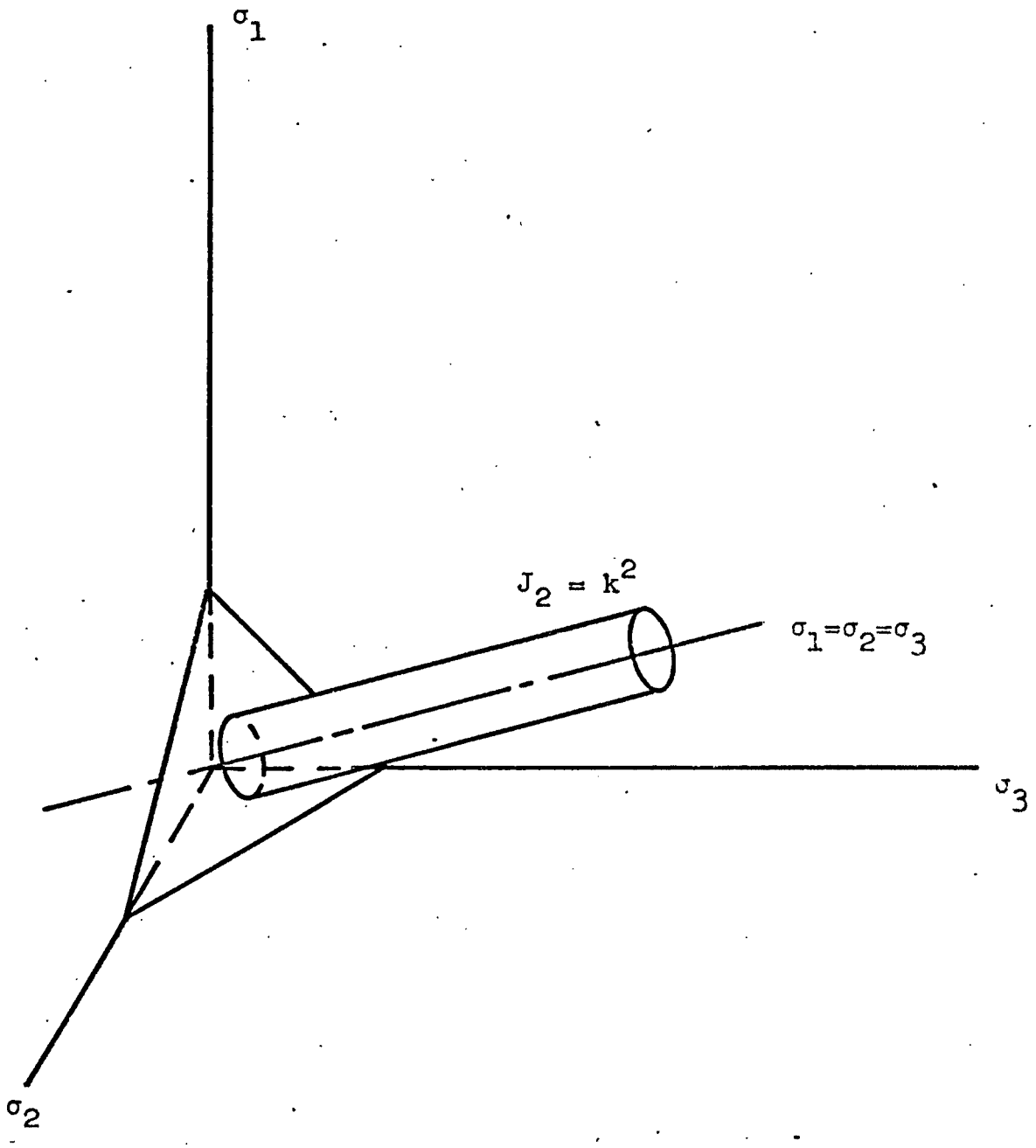

Figure II - 2 Yield surface for von Mises yield condition plotted in principal stress space

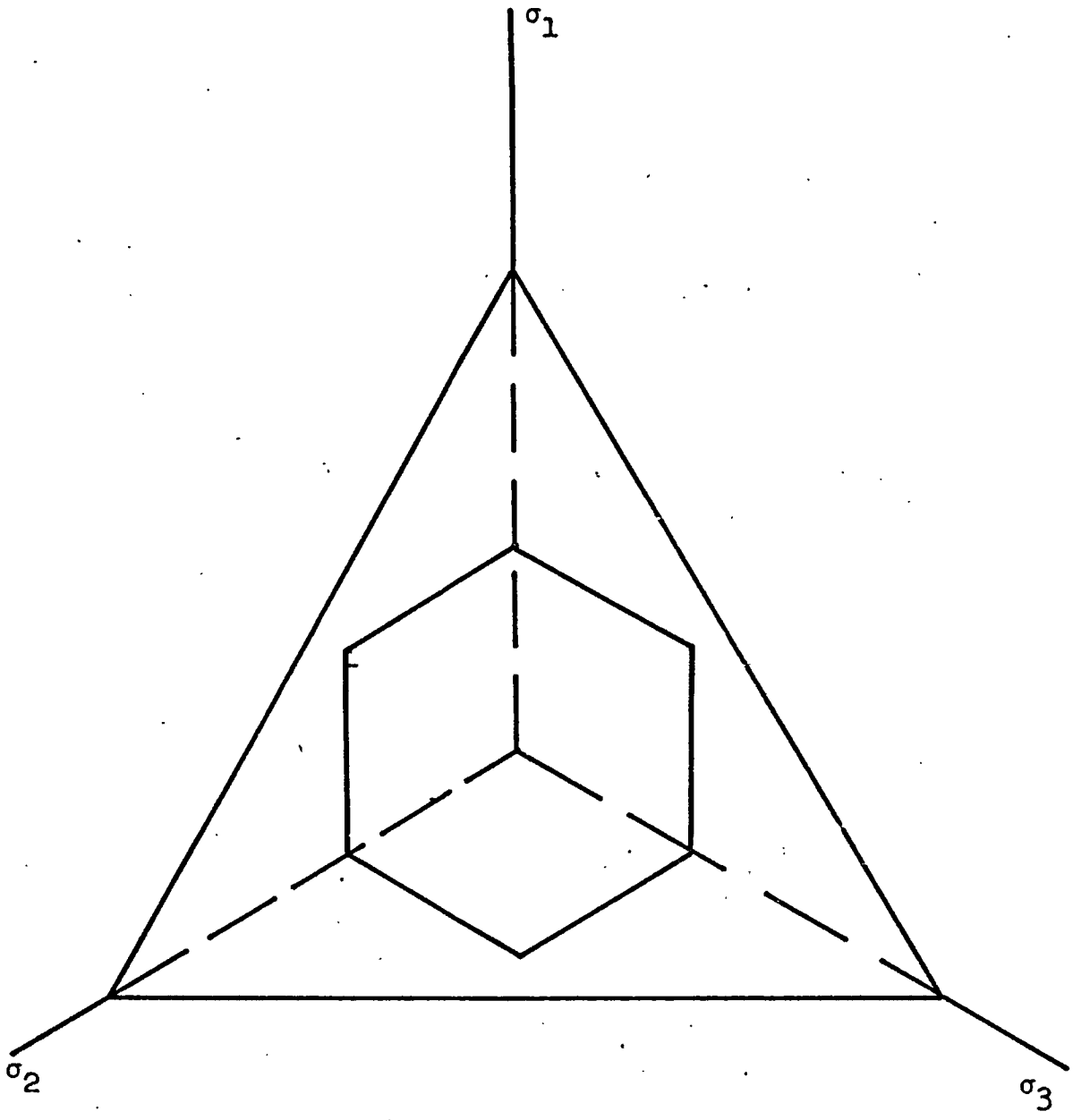

Figure II - 3 The Tresca yield surface is represented in the form of a regular hexagonal prism constituted by six planes perpendicular to the plane π.

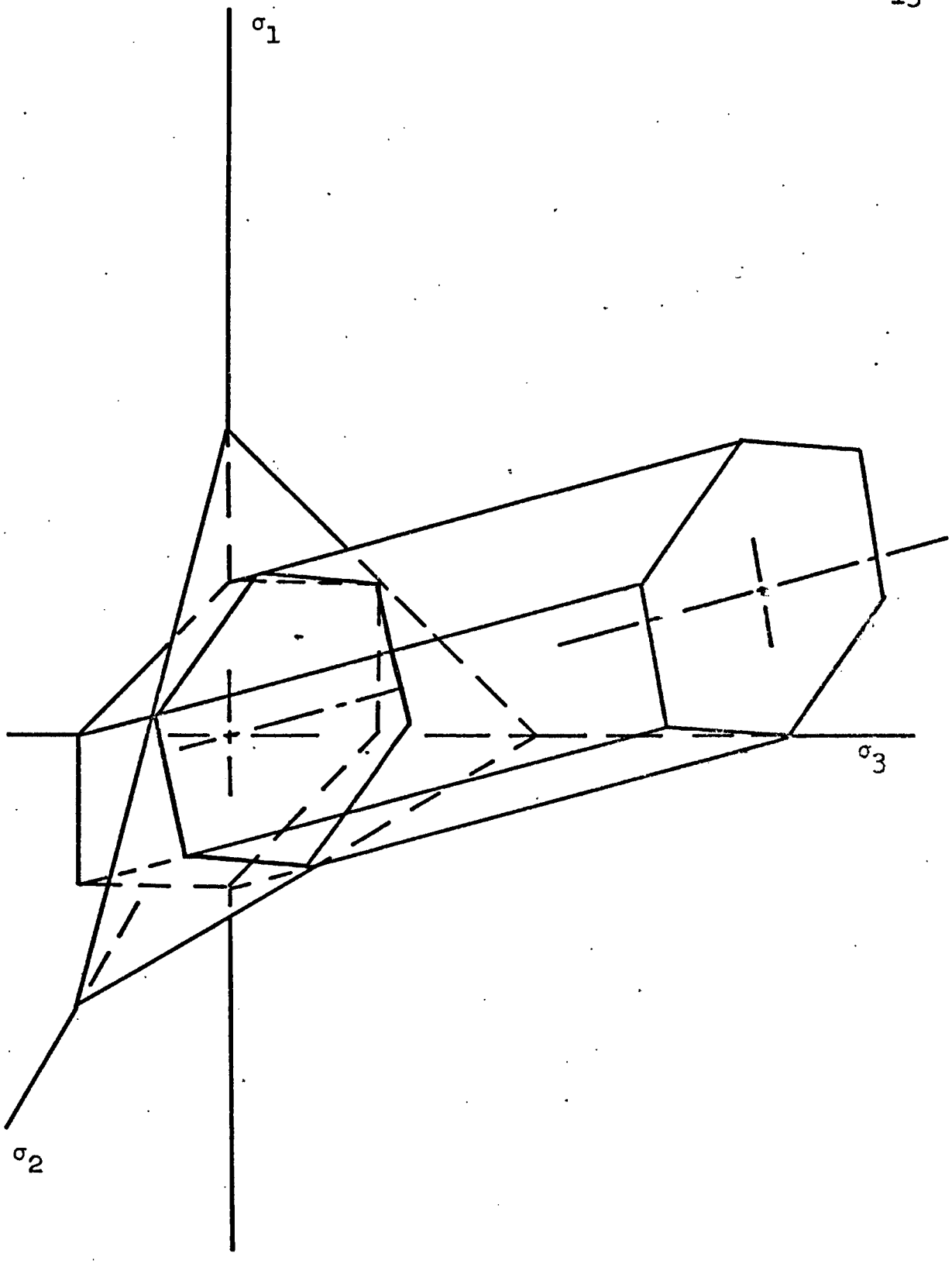

Figure II - 4 Yield surface for Tresca yield condition plotted in principal stress space

that is independent of the stress and strain histories.

Improved description of material behavior results if the yield function is expressed in a more general form :

$$f = f\ (\sigma_{ij},\ \epsilon^{p}_{ij},\ \kappa)$$

where κ can be a workhardening parameter. The ability to assign the functional dependence on ϵ^{p}_{ij} and κ allows the yield surface to change shape and/or translate in the stress space ; the manner in which the yield surface is transformed is called a hardening rule. For a virgin material there is no strain history and the initial yield surface is defined by a yield function of the form :

$$f = f\ (\sigma_{ij})$$

For an isotropic material this can be reduced even further. An isotropic material is a material such that any arbitrary rotation about any axis has no effect on the yield function. For such a material the yield function may be written as :

$$f = f\ (I,\ II,\ III)$$

where I, II and III are the first three invariants of the stress tensor,

$$I = \sigma_1 + \sigma_2 + \sigma_3$$

$$II = \sigma_1\sigma_2 + \sigma_2\sigma_3 + \sigma_1\sigma_3$$

and $$III = \sigma_1\sigma_2\sigma_3$$

In practice the third invariant is neglected and the yield condition is written as :

$$f = f\ (I,\ II)$$

or more commonly, as :

$$f = f\ (J_2,\ I)$$

where J_2 is the second invariant of the deviatoric stress tensor.

$$J_2 = \frac{1}{6}\left((\sigma_1 - \sigma_2)^2 + (\sigma_2 - \sigma_3)^2 + (\sigma_3 - \sigma_1)^2\right)$$

written in this form von Mises yield condition becomes :

$$f = J_2 - k^2$$

and the first invariant, or the hydrostatic stress, is neglected. This non dependence on hydrostatic stress is a unique property of metals.

Several more general yield conditions are :
the extended von Mises

$$f = J_2 - \alpha I - k$$

the extended Tresca

$$f = \sigma_{max} - \sigma_{min} - \alpha I - k$$

and the Mohr Coulomb

$$f = \sigma_{max} - \sigma_{min} - \alpha\ (\sigma_{max} + \sigma_{min}) - k$$

In these yield conditions, as in the rest of this

thesis, compressive stresses are considered positive. The extended von Mises yield condition forms a cone in principal stress space with the hydrostatic line as its axis (figure II - 5a). The extended Tresca and Mohr Coulomb yield functions describe a regular hexagonal pyramid with the hydrostatic line as its axis (figure II - 5b). All three yield conditions predict a linear increase in strength with increasing hydrostatic pressure, and with slightly different α's and k's they all reduce to the well known Coulomb yield condition for plane strain.

$$\left(\left(\frac{\sigma_x - \sigma_y}{2} \right)^2 + \tau_{xy}^2 \right)^{\frac{1}{2}} - \frac{\sigma_x + \sigma_y}{2} \sin \phi - c \cos \phi = 0$$

where c = cohesive strength, and

ϕ = angle of internal friction (figure II - 5c)

Application of Normality to any of the three Coulomb type yield conditions above, by using the yield condition as a plastic potential function, predicts a volume increase during any plastic deformation. As an example to illustrate this we will use the extended von Mises yield condition.

The volumetric strain is defined as the sum of the three principal strains

$$\dot{\epsilon}^p = \dot{\epsilon}_1^p + \dot{\epsilon}_2^p + \dot{\epsilon}_3^p$$

Using the yield function

$$f = J_2^{\frac{1}{2}} - \alpha I - k$$

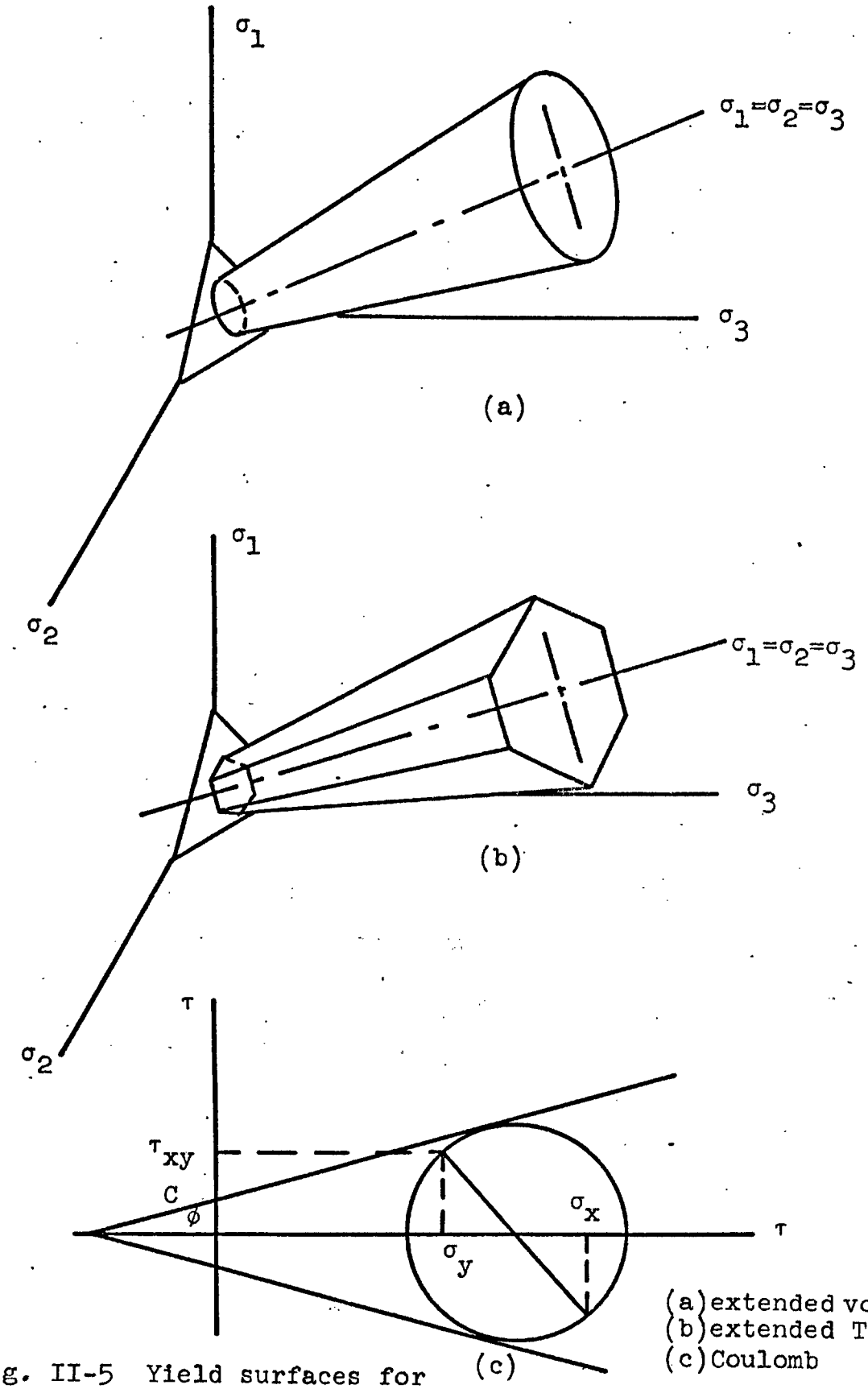

Fig. II-5 Yield surfaces for

as a plastic potential gives

$$\dot{\epsilon}_i^p = \lambda \frac{\partial f}{\partial \sigma_i} = \lambda \left\{ \frac{\partial f}{\partial J_2^{\frac{1}{2}}} \frac{\partial J_2^{\frac{1}{2}}}{\partial \sigma_i} + \frac{\partial f}{\partial I} \frac{\partial I}{\partial \sigma_i} \right\}$$

Now

$$\frac{\partial J_2^{\frac{1}{2}}}{\partial \sigma_1} = 6 \frac{1}{J_2^{\frac{1}{2}}} \left((\sigma_1 - \sigma_2) + (\sigma_1 - \sigma_3) \right)$$

and

$$\dot{\epsilon}_1^p = \lambda \left\{ \frac{6}{J_2^{\frac{1}{2}}} \left((\sigma_1 - \sigma_2) + (\sigma_1 - \sigma_3) \right) - \alpha \right\}$$

Cyclic permutation of 1, 2 and 3 yield

$$\dot{\epsilon}_2^p = \lambda \left\{ \frac{6}{J_2^{\frac{1}{2}}} \left((\sigma_2 - \sigma_1) + (\sigma_2 - \sigma_3) \right) - \alpha \right\}$$

and

$$\dot{\epsilon}_3^p = \lambda \left\{ \frac{6}{J_2^{\frac{1}{2}}} \left((\sigma_3 - \sigma_1) + (\sigma_3 - \sigma_2) \right) - \alpha \right\}$$

Thus

$$\dot{\epsilon}^p = - 3\lambda\alpha$$

which in a system of positive compressive stresses predicts a plastic volumetric increase.

Jenike and Shield (4) and Drucker (7) have discussed the inherent instability of a material that expands while deforming. Such a volumetric increase has been observed by several experimentors (7) (see experiments on this thesis) but is not common in rocks and soils. It would appear then

that a Coulomb type yield function cannot adequately describe the behavior of many rocks and soils. This inconsistency has led many authors to terminate a generalized Coulomb type yield condition with an end cap. Such an end cap would allow Drucker's postulate to predict a volume decrease or compaction during plastic deformation.

Although the addition of an end cap allows a volume decrease and thus increases the accuracy of predictions, the yield conditions are still limited to isotropic materials. That is to say materials with no directional dependence. Work-Hardening may be considered as a particular case of induced anisotropy on formerly isotropic (or slightly anisotropic) materials. Several yield conditions have been proposed for this kind of anisotropy (8) and for natural anisotropy. These will be discussed in the next section.

As previously mentioned, the manner in which the yield surface is transformed is called a hardening rule. Figures II - 6a,f illustrate five generally used hardening rules applied to the Tresca Yield Condition (9) (13).

The most widely used approach to hardening assumes a uniform expansion of the initial yield surface and is termed isotropic hardening (figure II - 6b) since it implies that no anisotropy is introduced during plastic flow. The subsequent yield surfaces may be written as :

$$f = f^{*} (J_2, J_3) - k = 0$$

where k depends on the plastic strain history. Isotropic

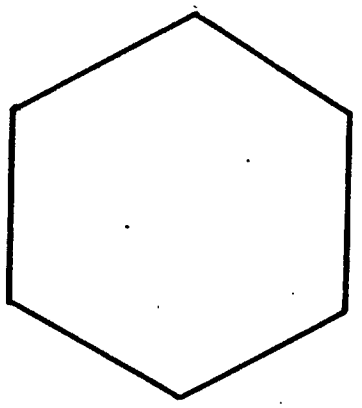

(a) Initial yield condition Tresca

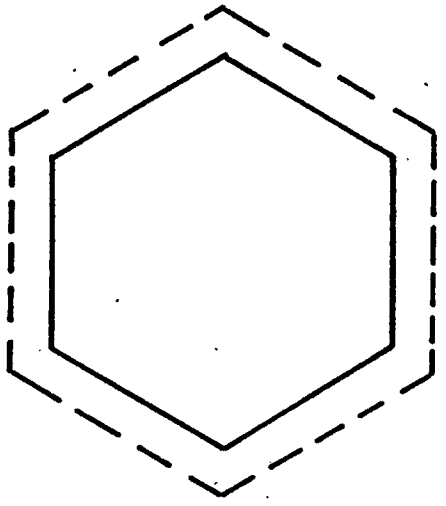

(b) isotropic hardening

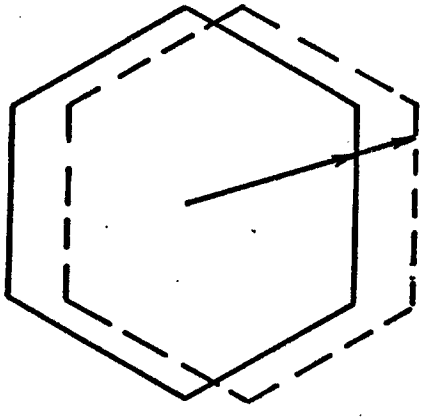

(c) Kinematic hardening Prager (10)

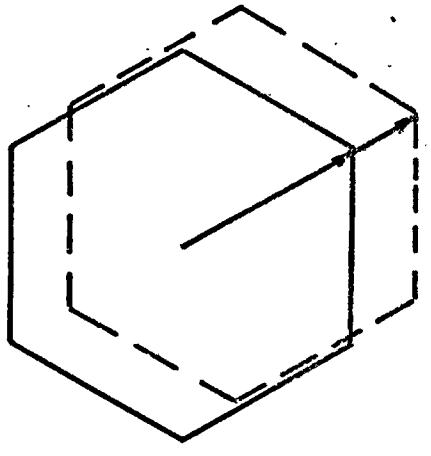

(d) Kinematic hardening Ziegler's modification (11)

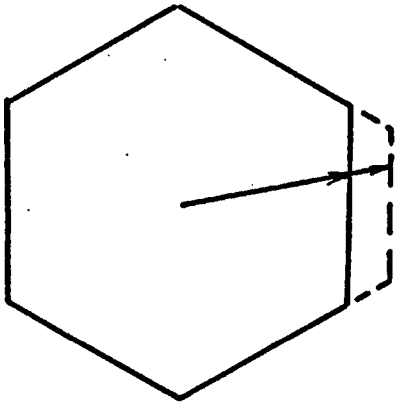

(e) Independently acting plane loading surfaces

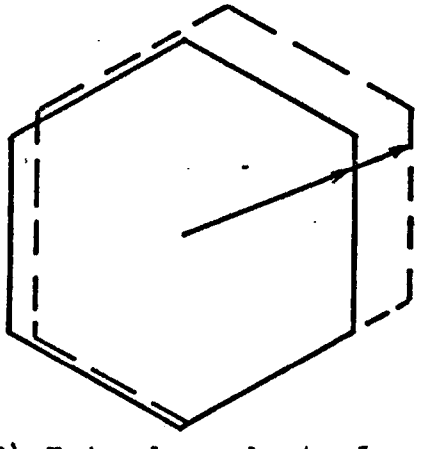

(f) Interdependent plane loading surfaces (Naghdi (12))

Figure II - 6

hardening, though widely used in analysis, has little experimental support because it does not explain the Bauschinger effect.

Prager (10) has proposed a kinematic hardening rule as a proper generalization of the Bauschinger effect observed in uniaxial tension and compression tests. In this case the yield surface is specified to translate as a rigid body in stress space without rotation. To explain this rule, Prager used a mechanical model. With reference to figure II - 7a, a rigid frame in the shape of the yield surface is used to describe the loading surface in stress space. The state of stress before yield occurs is represented by the position of a pin free to move within the frame and originally at the origin. As the pin contacts the side of the frame, yielding occurs; with further loading the pin engages the frame (which is assumed to be constrained against rotation), causing it to translate. The frame is assumed smooth so that only motion normal to the surface is possible. At corners, if the motion of the pin engages both sides (i.e. if the direction of $\dot{\sigma}_{ij}$ falls within the fan of normals), the frame translates in the direction of the motion of the pin. If the pin disengages and moves away from the frame, the frame stays put, and the change represents an unloading. It is obvious that none of the flow rules deduced from Drucker's hypothesis is violated. Depending on the materials to be described by the model (i.e. rigid/perfectly plastic, rigid/work-hardening, elastic/perfectly plastic) the state

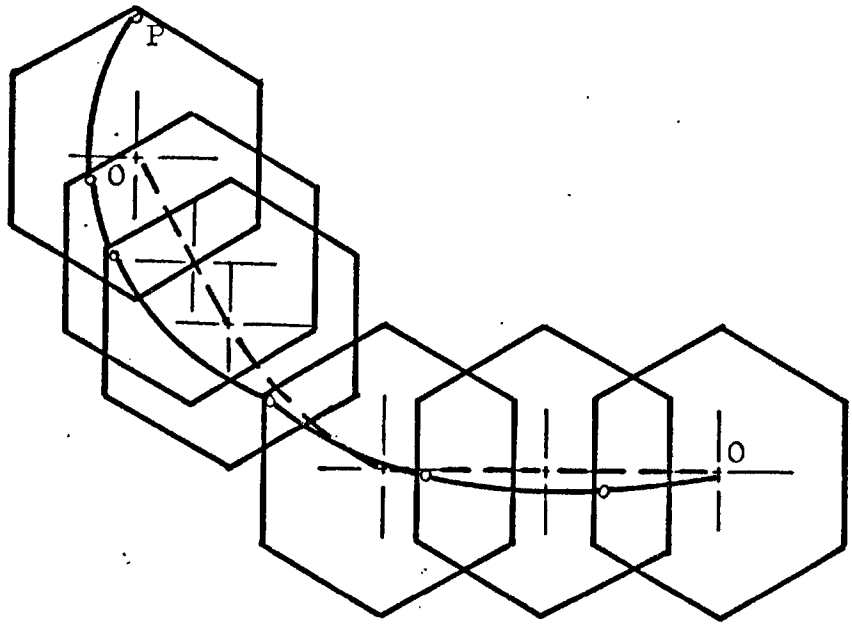

(a) Prager's kinematic model

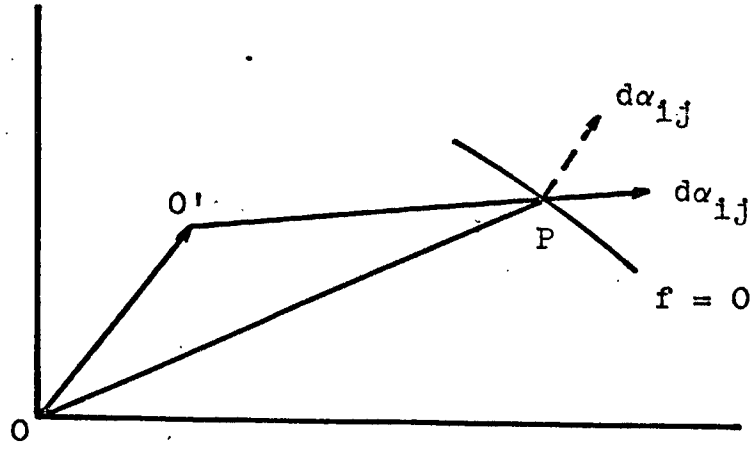

(b) Comparison of the direction of translation $d\alpha_{ij}$ of the yield surface for Prager's hardening rule (shown dotted) and Ziegler's modification (shown solid)

In the modified version, the motion is along the direction O'P instead of along the normal to f = 0 at P

Figure II - 7

of stress and the state of strain are represented in the model in different ways. For example, for a rigid work-hardening material the displacement of the center of the frame relative to O is proportional to the total strain and the state of stress is represented by the position of the pin also relative to O.

The model described above is termed kinematic, since both stress and strain are represented by displacements.

For this hardening rule, after a certain amount of plastic flow, the yield function is given by

$$F\ (\sigma_{ij} - \alpha_{ij}) = k^2$$

where the tensor α_{ij} represents the total translation, and it can be function of either the stress or strain histories. Because α_{ij} is not necessarily the isotropic tensor δ_{ij}, where δ_{ij} is the kronecker delta, the material becomes anisotropic as a result of the hardening process. After Shield and Ziegler (15) the α_{ij} may be specified by the rule :

$$\dot{\alpha}_{ij} = C\ \dot{\varepsilon}^{p}_{ij}$$

where C is a positive constant for linear work-hardening. Since from normality :

$$\dot{\varepsilon}^{p}_{ij} = \frac{\partial f}{\partial \sigma_{ij}}$$

and from the condition that during the plastic flow $\dot{f} = 0$

$$\dot{f} = \frac{\partial f}{\partial \sigma_{ij}} \dot{\sigma}_{ij} + \frac{\partial f}{\partial \alpha_{ij}} \dot{\alpha}_{ij}$$

and since

$$\frac{\partial f}{\partial \sigma_{ij}} = \frac{\partial f}{\partial \alpha_{ij}}$$

it follows that :

$$\lambda = \frac{1}{C} \frac{\frac{\partial f}{\partial \sigma_{ij}} \dot{\sigma}_{ij}}{(\frac{\partial f}{\partial \sigma_{kl}})(\frac{\partial f}{\partial \sigma_{kl}})}$$

thus the α_{ij} can be found to within an arbitrary constant from the loading function, and the hardening rule is specified, if the $\dot{\alpha}_{ij}$ are assumed equal to zero for no plastic strain.

Shield and Ziegler (15) have shown that the translation of the yield surface normal to the loading point of the yield surface is not always the case when some sub-spaces are chosen to represent the yield surface. Ziegler (11) has proposed a modification of Prager's rule in order to provide a consistent translation of the yield surface for any sub-space representations. Ziegler proposed that the translation tensor be defined by :

$$\dot{\alpha}_{ij} = \dot{u} (\sigma_{ij} - \alpha_{ij})$$

By the same process as above,

$$\dot{u} = \left(\frac{\partial f}{\partial \sigma_{ij}}\right) \dot{\sigma}_{ij} \,/\, (\sigma_{kl} - \alpha_{kl}) \frac{\partial f}{\partial \sigma_{kl}}$$

$\dot{u}$ is some positive quantity that forces the translation tensor increment α_{ij} to be directed along the line from the instantaneous center of the yield surface to the loading point ; and the time derivative is used so that the units will be consistent. Thus the yield surface translates along the direction of the stress vector directed from the instantaneous origin of the translating yield surface (figure II - 7b). Ziegler has shown this to be invariant under reduction of space dimensions.

There is, however, an objection to this modification : strict kinematic hardening can be shown to imply some measure of uniqueness of the solution to certain boundery value problems concerning work-hardening solids, and this uniqueness is lost for modified kinematic hardening (16).

Figures II - 6e and f show two other hardening rules ; in figure II - 6e, the plastic deformation causes a linear segment to move. In figure II - 6f, the plane loading surfaces changes with plastic loading in some interdependent manner.

More complicated hardening rules have been proposed from time to time. For example, Hodge (17) has extended the kinematic hardening to include an expansion of the yield surface simultaneously with its translation. For an account of these theories the reader is referred to references (16) and (13).

Review of Related Work

This thesis will attempt to obtain a graphical solution for a yield envelope for Cordova limestone and its hardening behavior. As we know, Cordova limestone is a compacting material. Several theories have been presented involving end caps on a generalized Coulomb type of yield condition in order to describe compacting materials. Most of these theories included a work-hardening theory that allows the end cap to grow as the material compacts.

One of the first references to an end cap is given by Drucker, Gibson and Henkel (18). They proposed a hemispherical end cap to an extended von Mises yield condition in order to explain the compaction of wet clays.

Cheatham (19), in an experimental study, definitely showed evidence of compaction in the plastic flow of a porous limestone. An end cap would be necessary to predict such behavior.

Miller (20), in a similar experimental study, recorded similar results. He proposed an end cap to a Coulomb type of yield condition. The initial yield surface predicted by Miller theory would be two regular hexagonal pyramids with the hydrostatic line as their axis. These pyramids have opposite slopes and intersect so that they form a closed surface. He proposed a work-hardening theory to predict the behavior of a compacting material. The end cap was allowed to grow as plastic work was done on the material but it was always limited by the Coulomb yield condition.

M. Smith (21) proposed a yield condition to cover porous anisotropic materials. His experimental study is further limited to transversely isotropic materials due to the fact that transversely isotropic (layered) rocks are very common in nature. He also applied his yield condition to Cordova limestone as this rock presents bedding planes and a small initial anisotropy. His general yield condition reduces to simpler yield conditions in order to describe simpler materials.

F. Stassi D'Alia (8) proposed four different theories for anisotropic yield conditions which he applied to materials initially isotropic that became anisotropic due to work-hardening. Each theory corresponded to one kind of introduced anisotropy.

In our work we will attempt to obtain a model that will apply to any kind of anisotropic hardening.

III. EXPERIMENTAL APPARATUS

Design of Apparatus

The basic difference between the apparatus used in this work and other tri-axial test machines is the fact that this apparatus uses mechanical pressure to provide the three principal stresses.

The stresses are applied by five hydraulic rams and one load cell arranged to form an orthogonal system. The lateral stresses are applied by two sets of two hydraulic rams each. The vertical stress is applied by a hydraulic ram opposed by a load cell. Each set of rams is actuated by a separate hydraulic pump. Therefore, each of the three principal stresses can be varied independently of the others. However, valves are arranged so that all five rams can be operated by one pump. The apparatus is designed to accept two different sample sizes. For relatively weak materials, each ram is capped by a one inch square head and a one inch cubical sample is used. For stronger materials, the lateral rams are capped by one-half inch by one inch heads and the vertical ram is capped with a one quarter inch square head. The heads are mounted to the rams with curved surfaces. This is to allow the heads to adjust to the sample if the sides of the sample are not exactly parallel. The heads are held in

place with rubber sleeves. The rams used were Blackhawk twelve ton rams with a maximum working pressure of 8639 psi. The lateral rams were actuated by Enerpac pumps. The vertical ram was actuated by a Ruska volumetric pump. The twelve-ton rams give a maximum stress of 24,000 psi in all three directions for the one inch samples. For the half inch samples, lateral stresses of 48,000 psi and a vertical stress of 96,000 psi are possible. One advantage of this apparatus is the possibility of achieving very high stress states without the problems and dangers caused by the high hydraulic pressures. The outer case of the rams are threaded so that they screw directly into the main body of the apparatus. The load cell mounts to the top of the apparatus. It consists of two parts. There is an outer container which is threaded to screw directly into the top of the body of the apparatus. Then there is an inner cylinder with a narrow section with strain gages mounted to it. The gages are wired to form a wheatstone bridge circuit and the circuit is calibrated to provide a signal that determines sample stress. The load cell was originally calibrated with a Rheile test machine and was checked periodically against hydraulic pressure by inserting a steel sample into the apparatus.

A cross-sectional view of one of the hydraulic rams is shown in Figure III - 1. As can be seen from the figure, the back plate moves with the head of the ram. Therefore it is possible to measure the deformation of the sample by measuring the displacement of this plate. This is done with

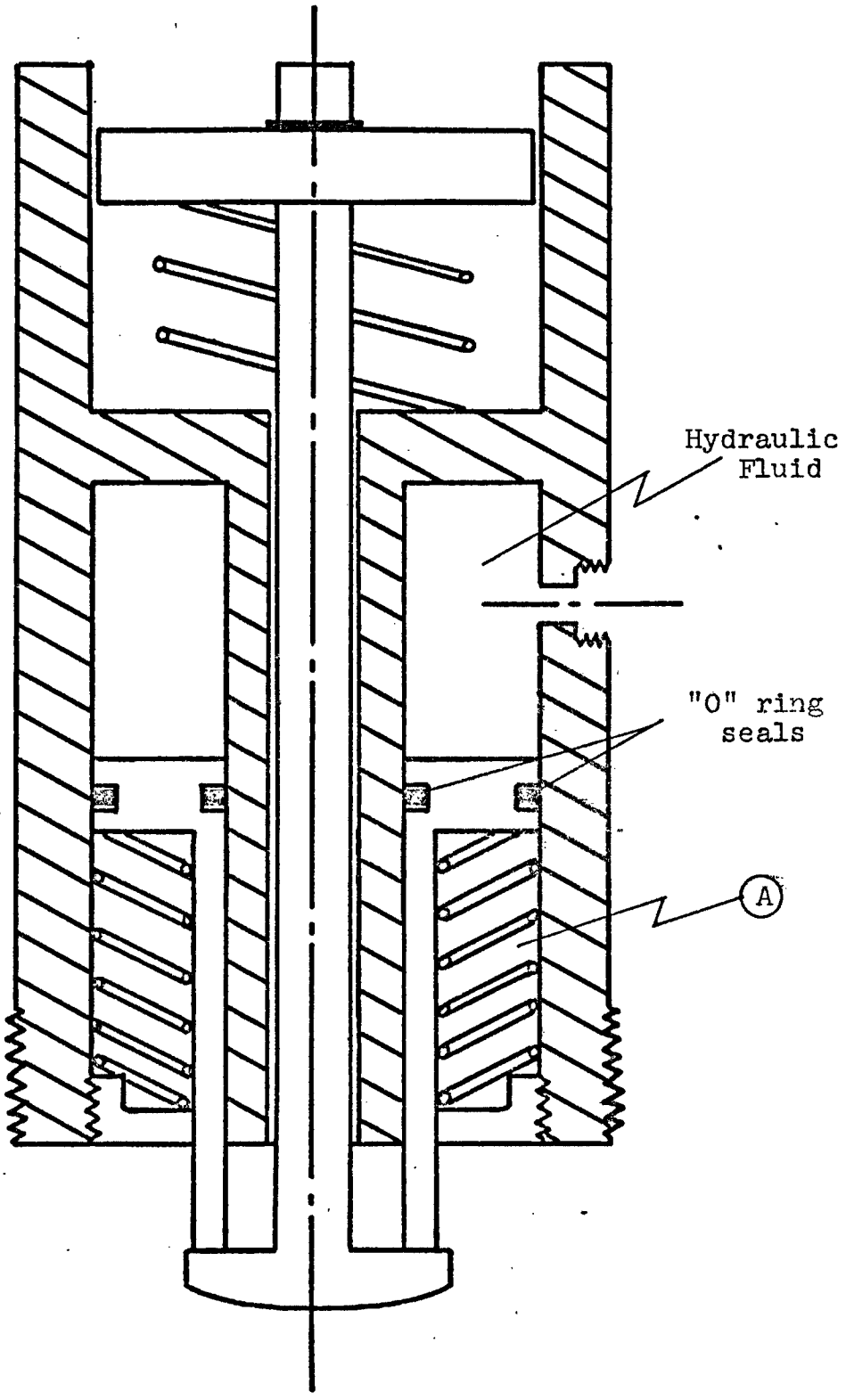

Fig. III - 1 Cross sectional view of hydraulic ram used in experimental apparatus.

simple displacement transducers made from aluminium cantilever beams. The displacement transducers were calibrated with dial indicators. As described above, there is a stress measuring device on the vertical axis and strain measuring devices on all three axes. Therefore, if the other two stresses are set at values below the plastic yield limit and then held constant during the test, all three principal stresses are known at the yield point and the strains in the principal directions are known throughout the test. The four measuring devices are connected to a Honeywell Visicorder. This gives four traces with respect to time which can be translated into stress-strain curves. The stress and strain measuring devices on the vertical axis are also connected to an X-Y Recorder in order to obtain stress-strain curves for the vertical axis directly.

To avoid friction between the ram heads and the samples, these samples were placed in a rubber membrane of a common commercial variety. The membrane was then coated with silicon grease, and the sample was placed in the apparatus.

In order to avoid possible interference between the rams as the sample is compressed, the samples were prepared slightly larger than the rams, so the displacement transducers were calibrated assuming a sample 1/16" larger in all dimensions than the nominal sample size (i.e. a nominal 1" x 1" x 1" cubical sample would be 1 1/16" x 1 1/16" x 1 1/16"). Figure III - 2 shows a diagram of the equipment which was used ; Figure IV - 2b shows a perspective view of experimental apparatus.

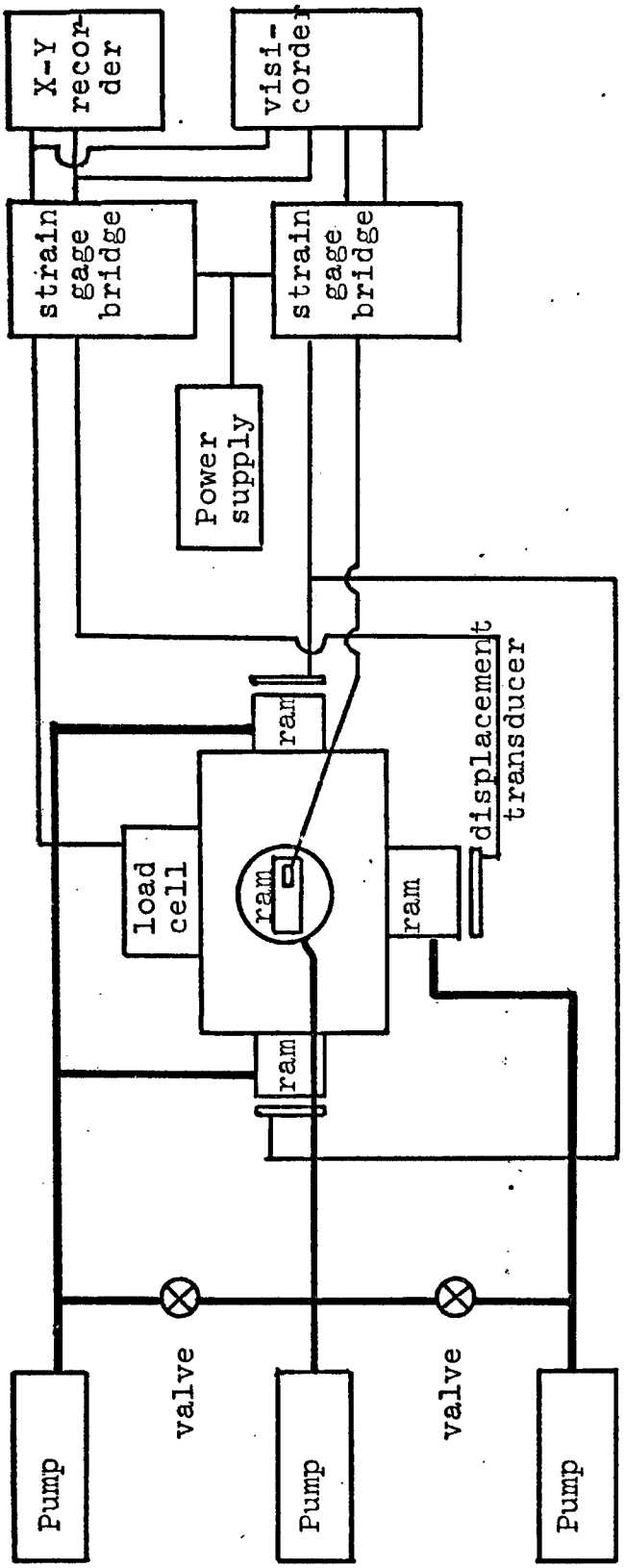

Figure III - 2 Equipment Diagram

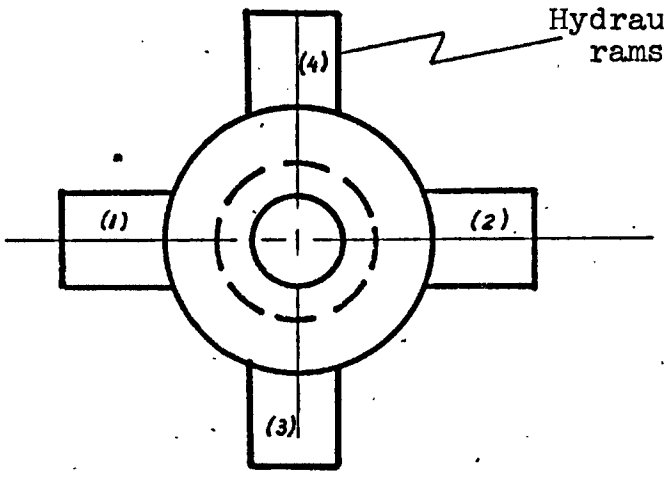

(a) Top view

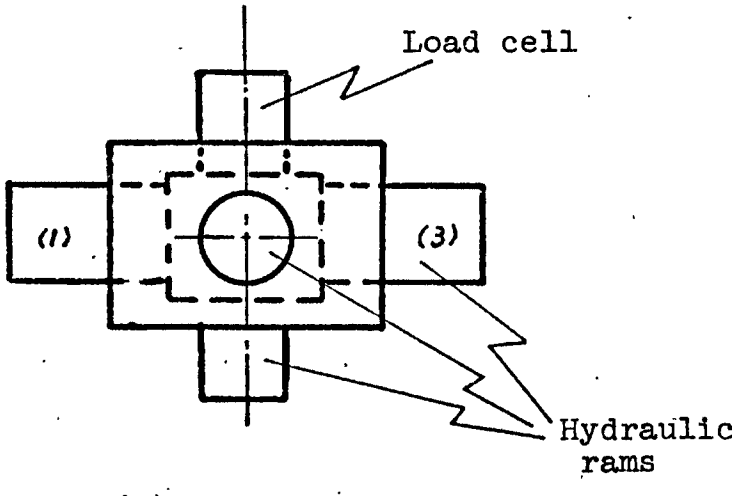

(b) Front view

Figure III-2b Perspective view of Experimental Apparatus

Experimental Procedure

Five types of experiments can be performed with this equipment. The types are identified by the stress state at failure and by the path followed in principal stress space to reach the failure surface.

The first type of test will be referred to as a conventional compression test. This is the type of experiment normally performed with an apparatus that uses a fluid confining pressure to provide two of the principal stresses. The test begins by raising the three principal stresses together until a preselected hydrostatic stress is reached. The stress on one axis is then increased to failure while the other two principal stresses are held constant. The resulting stress state at failure is :

$$\sigma_1 > \sigma_2 = \sigma_3$$

The next type of experiment is a hydrostatic stress test. In this test all three principal stresses are raised together until the sample yields. With a perfectly isotropic sample it would only be necessary to measure the strain on one axis in order to determine the yield point, however, with an anisotropic material it is necessary to measure the strain on all three principal axes since the weakest axis will yield first and this will be the yield stress for the sample. The stress state at failure will be :

$$\sigma_1 = \sigma_2 = \sigma_3$$

The third type of test is an intermediate stress test. In this test all three principal stresses are raised together to the preselected value of the minimum stress. The stress on one axis is then held constant at this value while the stress on the other two axes is increased to the preselected value of the intermediate stress. The stress on a second axis is held constant at this value and the stress on the third axis is increased until the plastic yield limit is reached. The stress state at yielding is :

$$\sigma_1 > \sigma_2 > \sigma_3$$

The fourth type of test is a conventional extension test. All three principal stresses are raised together to a relatively high hydrostatic stress and then two stresses are held constant while the third stress is lowered. The yield stress state is :

$$\sigma_1 = \sigma_2 > \sigma_3$$

The last type of test is an extension test. The final stress state at yield for this test is the same as a conventional extension test but the loading path is different. In this test all three principal stresses are raised together to a relatively low hydrostatic stress. The stress on one axis is then held constant at this value while the stress on the other two axes is increased to plastic failure.

If the plastic yield limit is truly path independent, then the last two test types discussed above should yield identical results.

Initial Yield Point

In order to determine the initial yield point of the material being studied, it is necessary to define it.

With some metals, such as steel, the yield point is very sharply defined and there is no trouble detecting it. However, this is not often the case when dealing with rocks and soils. Some metals, such as aluminium and copper, do not have a clear yield point and a 0.2 % strain effect is defined as the yield point. This method has not proved effective for rocks since many rocks exhibit some non-linear elastic behavior before yielding. The method most used in this work is to approximate the stress strain curve for the material as an elastic-linear-hardening material as seen in figure III - 5a. In some cases this is not possible. For compacting materials when yielding very near, or at the hydrostatic yield point, there is no linear portion of the curve. Since it is noticed that the yield point as selected above usually occurs very near the stress of 1 % offset, the stress at 1 % offset is selected as the yield point for these tests. This is seen in figure III - 5b. Other materials after briefly yielding begin to fracture completely and lose strength. In these cases the maximum stress is chosen as the failure point. This condition cannot be classified as a yield point since the behavior of the material is brittle rather than plastic.

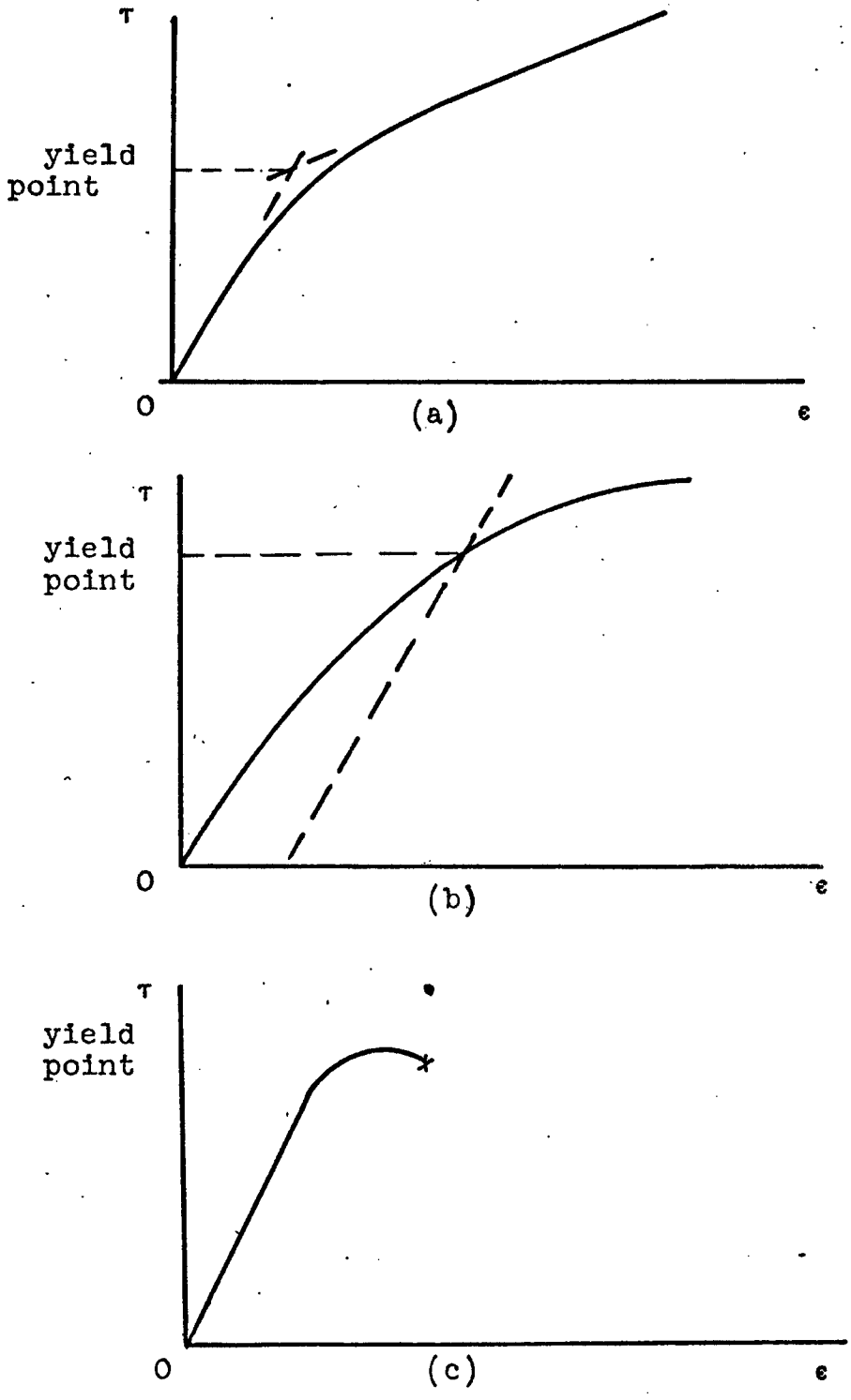

Figure III-5 Definition of yield points for experimental results

Sample Orientations and Specifications

Cordova Cream limestone is a weak porous limestone commonly known as Austin Chalk.

Previous experimental work (20) done with Cordova limestone had confirmed the existence of bedding planes which cause the rock to be transversely isotropic, this means that two of the axes of the material are the same. In the rest of this thesis, the axes will be referred to as the x, y and z axes or 2, 3 and 1 axes respectively, with the x and y (2 and 3) axes being interchangeable so that the material is rotationally symmetric about the z axis. (see figure III - 3).

This anisotropy in the undeformed state is evidenced by a difference in the stresses in the two independent directions at yield.

This initial difference in yield point is less than 20 %.

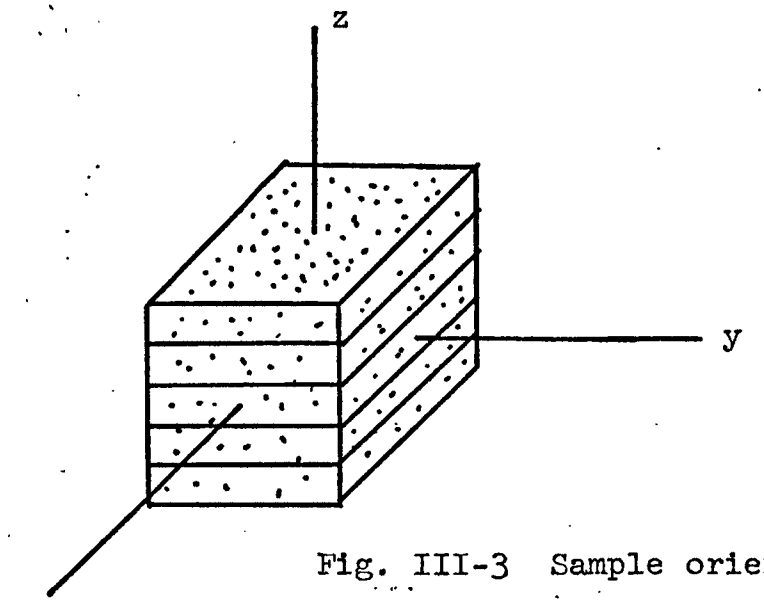

Fig. III-3 Sample orientation

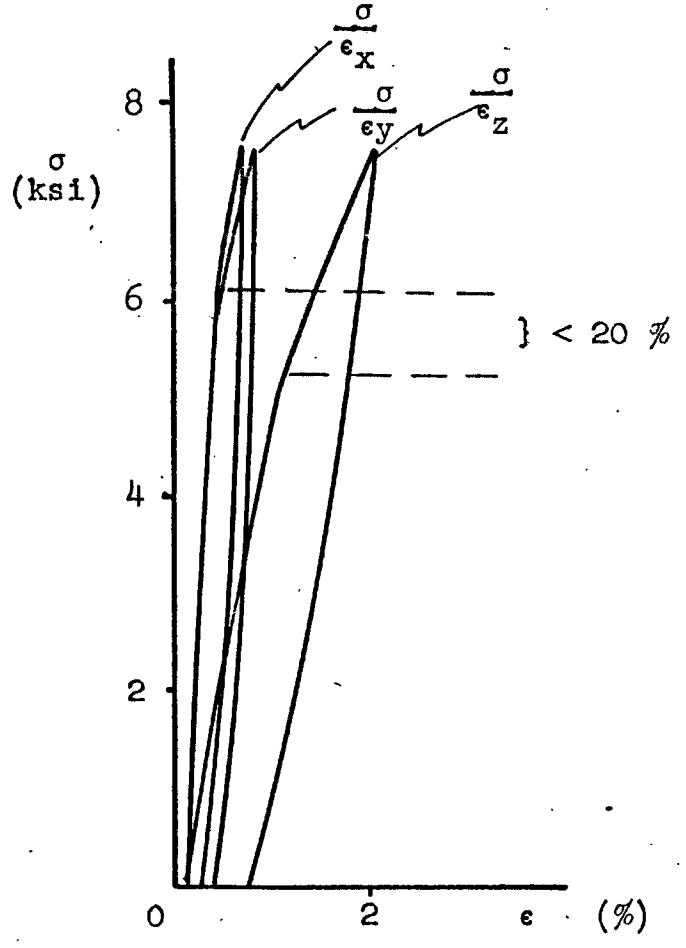

Fig. III-4 Hydrostatic stress test on Cordova limestone

Initial Yield Surface

The experiments to be performed for obtaining the initial and subsequent yield surfaces give results that are applicable to only one portion of the yield surface of the material tested. That part of the yield surface is the part cut by a plane containing the lines $\sigma_1 = \sigma_2$, and the σ_1 axis ; therefore the best stress space representation for the test results is two dimensional cartesian space with axes σ_1 and $\sqrt{2}\sigma_2$.

The yield surface is experimentally determined by "probing tests" which consist of tests on a single sample at different confining pressures. The procedure for these "probing tests" can be described as :

1. One sample is loaded at a high confining pressure until yield is reached and then it is unloaded ;
2. The confining pressure is lowered a set amount ;
3. The sample is loaded until yield is reached at the new confining pressure and then it is unloaded ;
4. The confining pressure is lowered another set amount ;
5. The sample is loaded again until yield is reached at the new confining pressure and then it is unloaded...

This procedure can be continued until the desired number of yield stress values are obtained. As long as the strain hardening is very small on each step, we can assume that every yield point lies on the same yield surface. In order to correct a possible error on obtaining the data, the

same kind of test are performed on another sample but starting with an initial low confining pressure which will be increased a set amount on each step. The points obtained from this second experiment will also be plotted and our final yield envelope will be an inner surface

Extension tests are used to perform the "probing tests" in order to complete the yield envelope with the surface that falls below the hydrostatic axis ($\sigma_1 = \sigma_2 = \sigma_3$).

Subsequent Yield Surfaces

A subsequent yield surface can be experimentally determined (assuming axial compression tests only) by :

1. Loading the material to a set differential axial stress (σ_{Z_4}) at a particular confining pressure (p_c), C where $\sigma_Z = (\sigma_Z - p_c)$, and then unloading the sample ;
2. Changing the confining pressure ;
3. Loading the sample until yield is reached at the new confining pressure.

The value of the differential axial stress σz before unloading the sample at the first confining pressure gives one point on a subsequent yield surface caused by a loading path described in (1) above and shown in figure III - 6a. Another point on the subsequent yield surface is given by

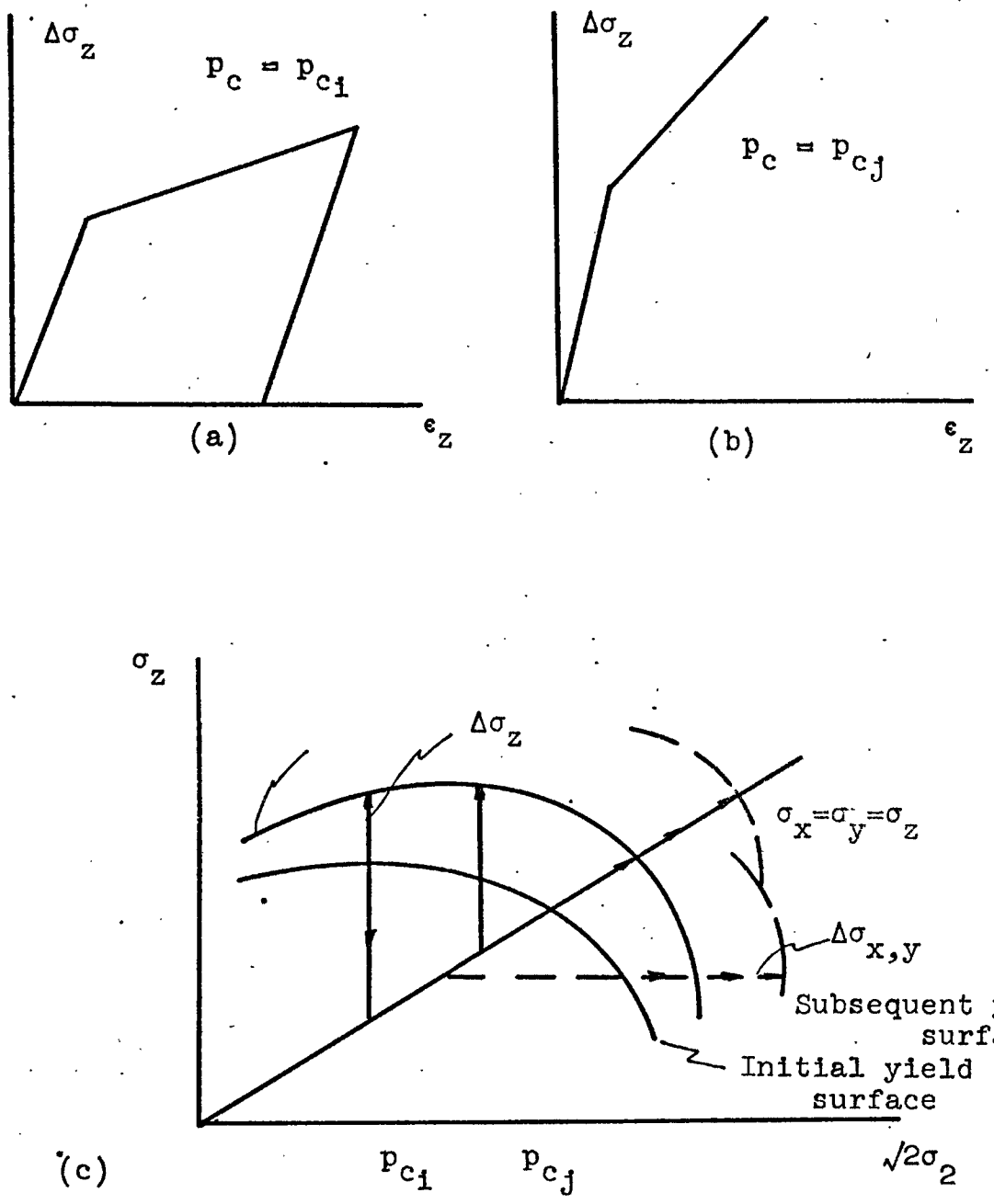

Figure III - 6 (a) Differential Axial Stress versus axial strain at some particular confining pressure (loading and unloading).
(b) Differential axial stress versus axial strain at some other confining pressure (loading).
(c) Changes in the yield surface due straining the material at p_{c_i} as detected by axial compression test at some other confining pressure.

the yield point of the stress-strain curve at the other confining pressure (assuming no yield during change in confining pressure) show in figure III - 6b. The representation in stress space of this procedure is seen in figure III - 6c.

Probing tests are performed to obtain more yield stress values on the same subsequent yield surface.

In order to be able to obtain a hardening rule to complete the description of the material behavior, two more types of tests will be performed to obtain subsequent yield surfaces :

A - 1. Load the material to hydrostatic stress value above the yield stress ($\sigma_x = \sigma_y = \sigma_z$) (figure III - 6c) ;

2. Perform probing tests to obtain more yield stress values on the same subsequent yield surface.

B - 1. Load the material to a set differential radial stress (σ_x) at a particular confining pressure (p_c), and then unload the sample (figure III - 6c) ;

2. Perform probing tests to obtain more yield stress values in the same subsequent yield surface.

Experimental Accuracy

There are several sources of errors in this experimental apparatus. These are all very small compared to the inhomogeneity present in most rocks. One possible source

of error is the strain created on the hydraulic rams, but since the ram is of large cross sectional area and constructed of steel, this strain is much smaller than the measured values for the sample, and it is treated as negligible. Other negligible errors could also be created by the springs in the hydraulic rams and by the loading caused by the displacement transducers. In figure III - 1, we can see that section A could create a pressure chamber when filled with hydraulic fluid due to leakage through the O-rings, a situation that did not happen during our tests.

It was observed that there was no delay in response of the X-Y recorder and Visicorder upon loading with the pump. A friction test was made and consisted of loading a steel sample and making readings in a digital voltmeter from the load cell output every 400 psi. The pressure was controlled with a pressure gage on the hydraulic line. Nine readings were made during loading and unloading and the test was performed three times. In figure III - 7, we can see a chart of pressure vs. voltage. To compute if the friction was significant, the following procedure was followed : (least squares fit)

$$z_i = \frac{1}{3} \sum_i (V^u - V^l)_i$$

where

$$i = 1, 2, 3$$

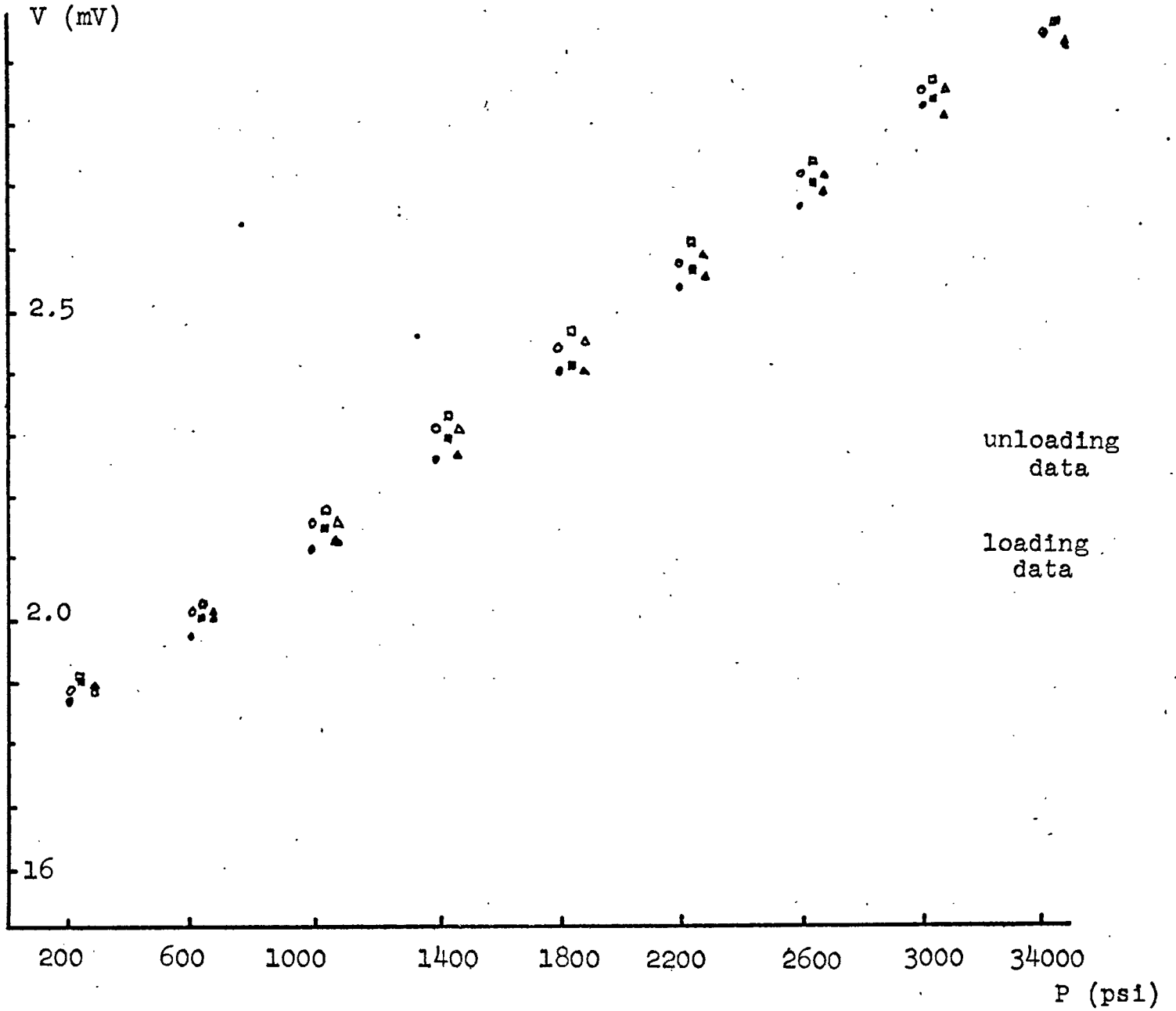

Figure III - 7 Friction test chart

V^u = voltage unloading

V^l = voltage loading

$$u_z = \frac{\Sigma z_i}{(9 - 1)} = - .033$$

$$s_z^2 = \frac{\Sigma (z_i - u_i)^2}{8}$$

$$s_z = .0135$$

comparing $/u_z/$ with $/s_z/$ we see that $/u_z/ < 2 /s_z/$, then friction is not significant.

To keep consistency between the different experiments, all the connections were carefully made and reviewed, and the voltage and current were constantly checked during the experiments. The load cell displayed some non-linearity during loading. However, the error was less than 5 % over the entire range of the apparatus. The displacement transducers were accurate to $\pm$ 3 % over a range of - 10 % strain to + 10 % strain.

Another source of error was the width of the trace of the visicorder used to record the measurements. The trace was .05" wide. In experiments involving large deflections on the visicorder (large strains or loads) this is a negligible error, but if the stresses or strains were low the width of the trace could be a measurable portion of the total measurement (5 % to 10 %). Probably the worst possible error produced by this would be $\pm$ 2 %. A method of getting more sharp-

ness of the tracing lights and consequently getting thinner traces, was to set the galvanometer's mirrors parallel to the panel before each experiment in order to avoid some light diffusion.

Another problem is the size of sample used which accuracy was of the order of $\pm$ 0.01" and this could cause small errors in the strain measurements because the displacement transducers were calibrated for 1 1/16" x 1 1/16" x 1 1/16" samples. The error involved is a maximum of 0.1 % and was treated as negligible. In the following description of the test A in figure III - 8, this effect can be seen, it corresponds to a stress-strain curve of the vertical axes for hydrostatic stress test and a conventional extension test. Before starting at O, the sample was cycled several times ; OA shows a perfectly linear elastic region and a clear yield point on this hydrostatic test ; ABC shows a perfect retracing on the unloading and reloading process and a sharp yield point ; the same can be observed on CDE ; EF corresponds to a vertical unloading while keeping σ_x and σ_y constant ; FG is vertical loading ; GH is vertical unloading ; HK is vertical loading and KL is vertical unloading.

To allow localized plastic deformation to reduce surface irregularities caused by sample preparation, the load was cycled several times in the elastic region before each experiment. This would also avoid certain inhomogeneity of the stress strain curves and get sharper yield points.

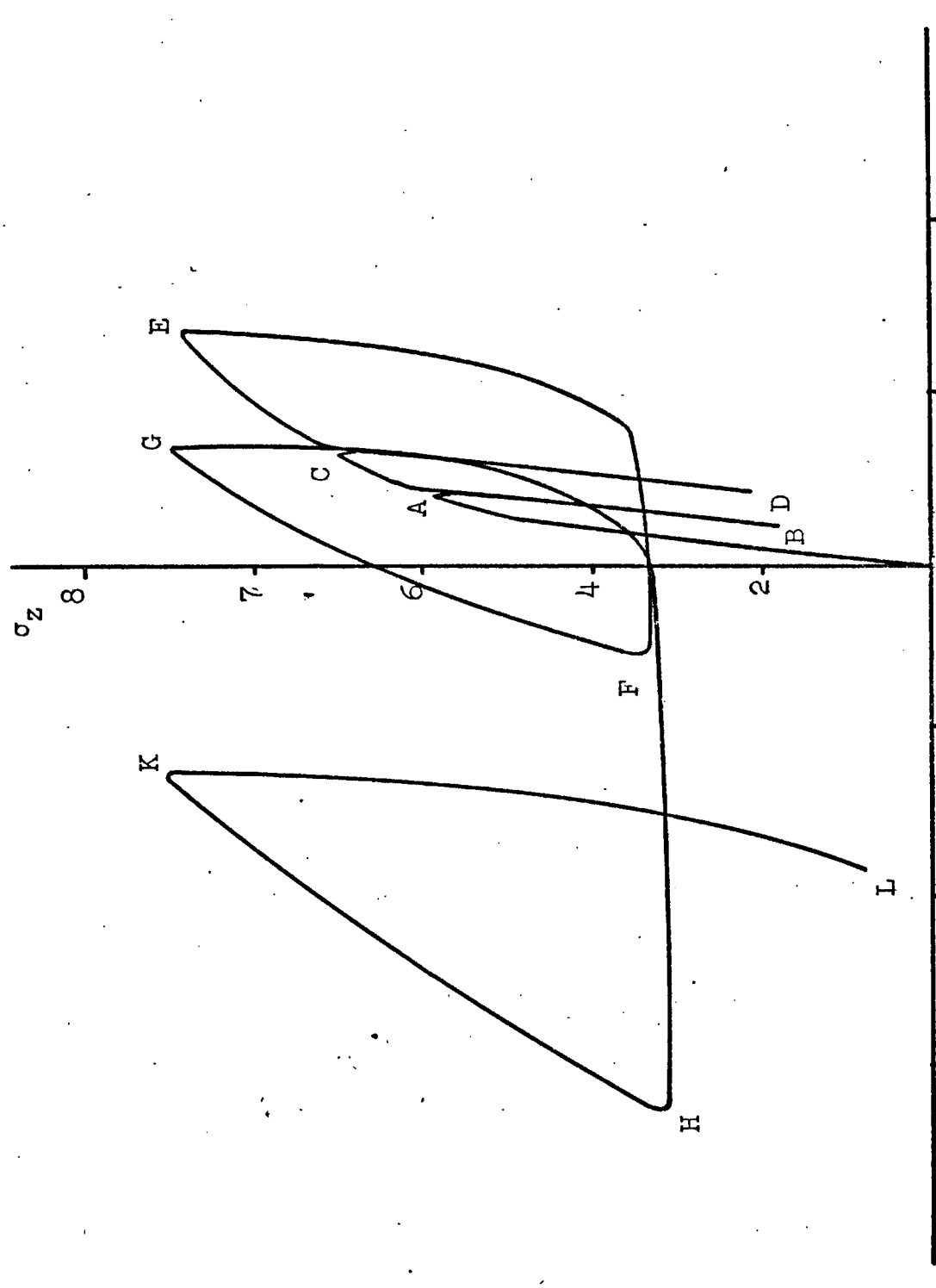

Fig. III-8 Effect of cycling on homogeneity of stress-strain curves - Test A

In the following test (B) (figure III - 9a) it can be seen that loops such as (H - K - L) on test (A) are due to friction on the lateral sides of the sample.

In test (B) the sample was loaded hydrostatically until reaching point (1) where σ_x and σ_y were kept constant at that value (7 500 psi) and the vertical axis was unloaded in a conventional extension test until reaching yield (2 000 psi). Then it was cycled several times loading and unloading the vertical axis. Assuming a friction factor of .02, the force that would offset the stress-strain curve from L - L and L' - L' would be about 600 psi. In figure III - 9b we can see that at points C and G the volumetric strain is about the same, which leads to the conclusion that the loop is completely elastic. In figure III - 9c we can see the elastic behavior of the other two axes.

In general the accuracy of all measurements was very good compared to the inhomogeneity of rocks which can be as great as 100 % (21, pp. 46).

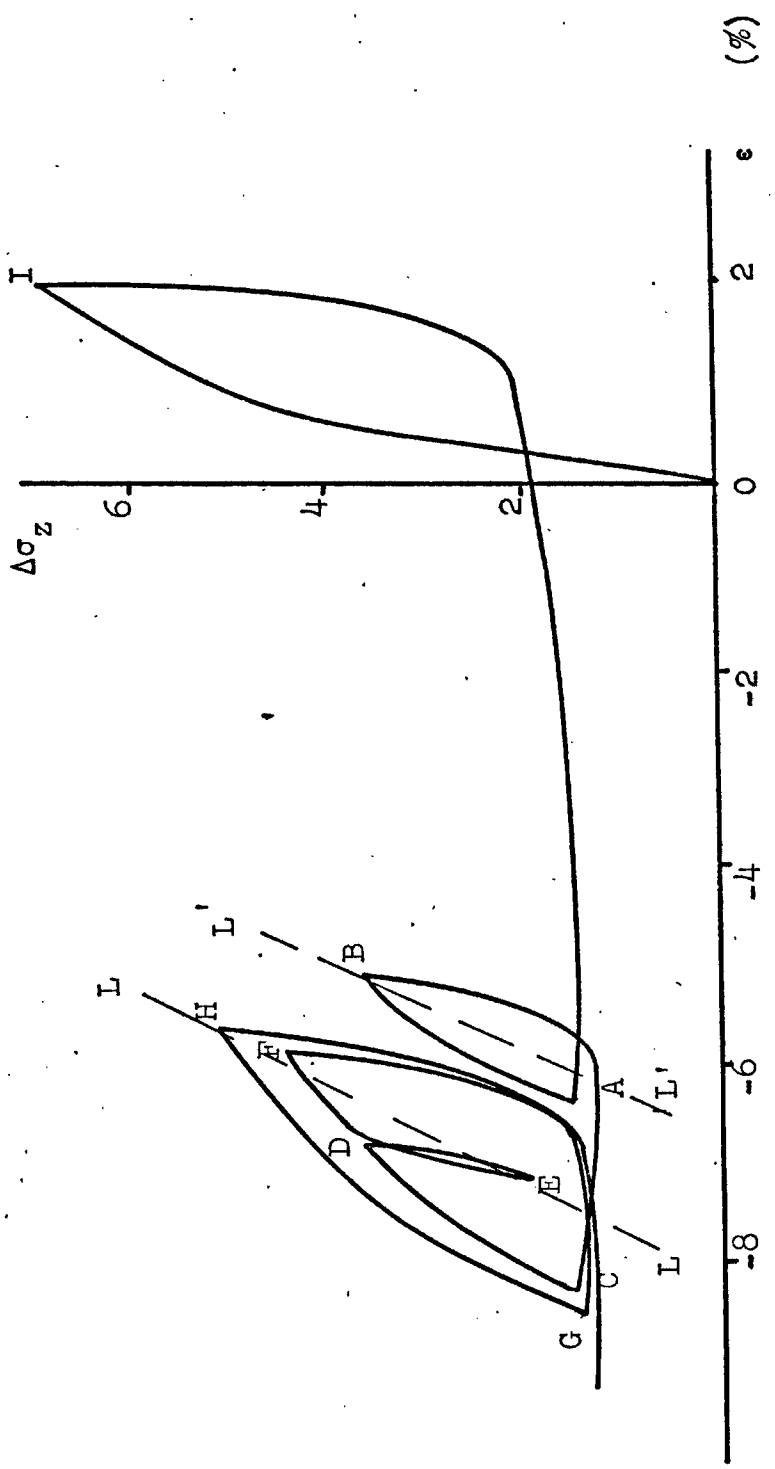

Figure III - 9 - a Test B

TEST B

Figure III - 9 a

O1 - hydrostatic loading

1A - vertical unloading (yield in extension)

AB - vertical loading

BC - vertical unloading

CD - vertical loading

DE - vertical unloading

EF - vertical loading

FG - vertical unloading

GH - vertical loading

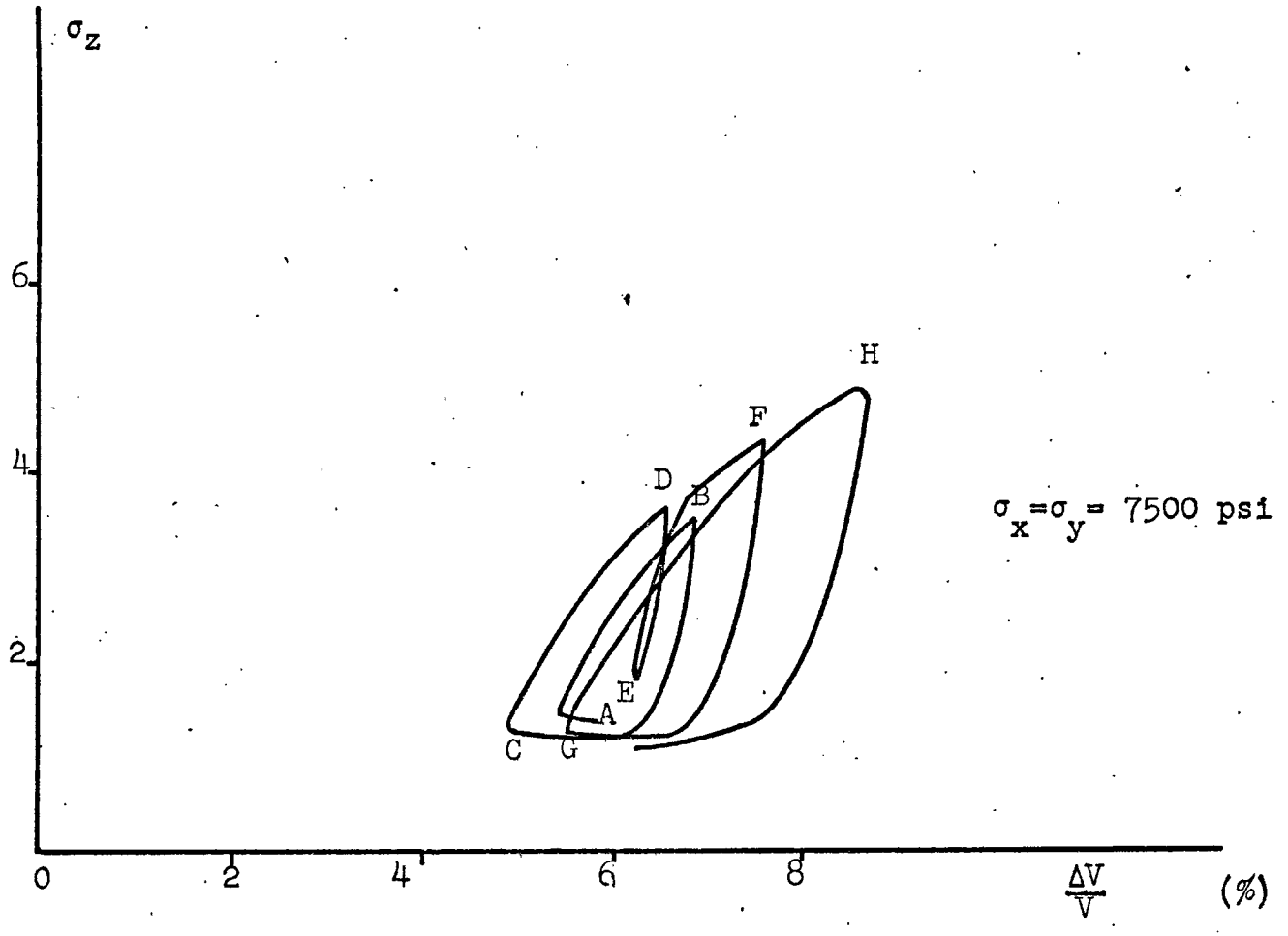

Figure III - 9 - b

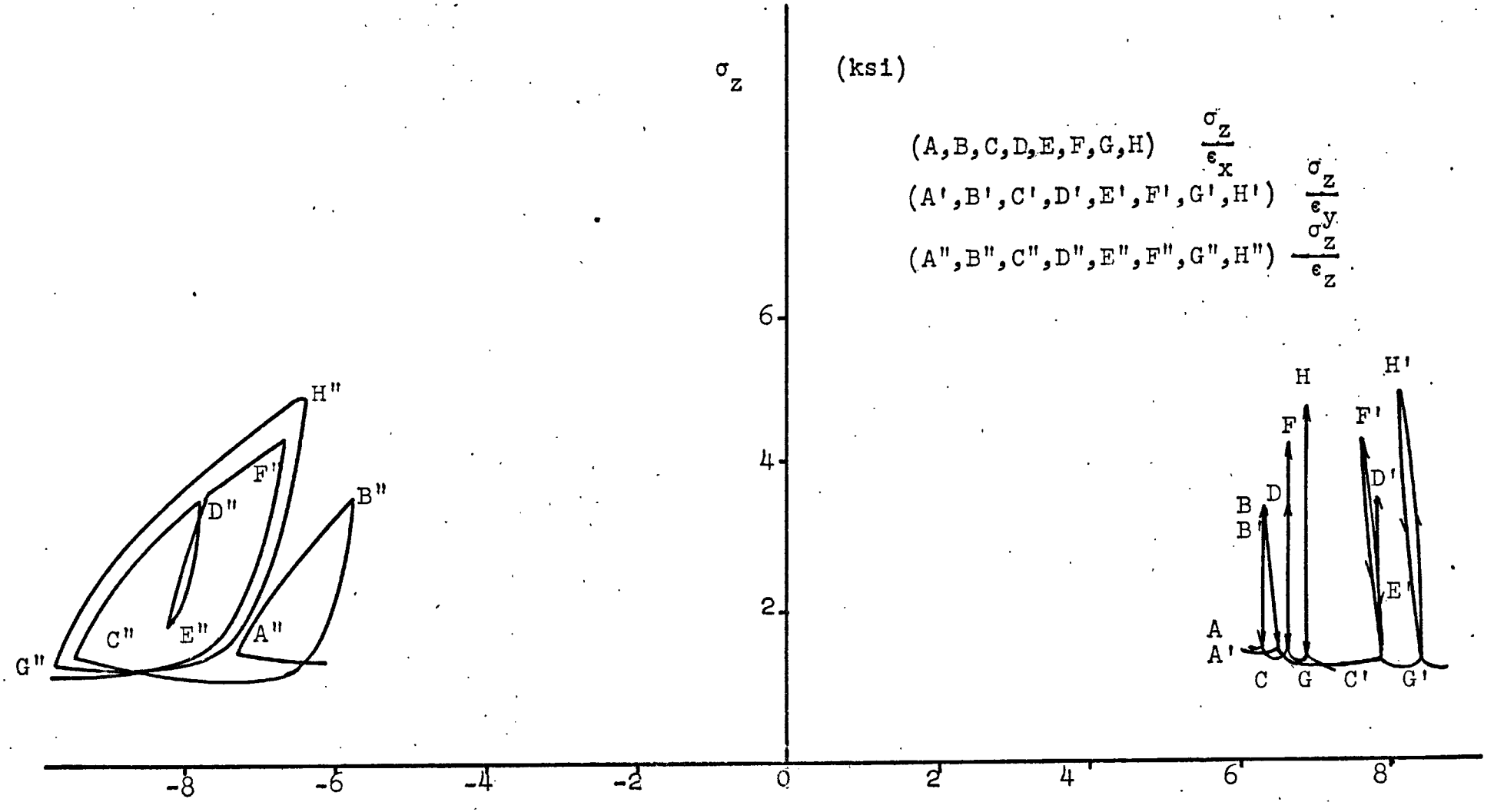

Figure III - 9 - c

IV. EXPERIMENTAL RESULTS

Initial Yield Surface

The Initial Yield Surface was obtained by performing four probing tests and a hydrostatic stress test.

In figure IV - 1a, stress strain curves for the vertical axis are shown. The sample was loaded hydrostatically to 1000 psi and a conventional compression test was performed, once yield was reached, it was unloaded to the confining pressure (curve 1). Then the confining pressure was raised to 2000 psi and another conventional compression test was performed at this p_c ; once yield was reached, the sample was unloaded to the last p_c (curve 2). Curves 3, 4, 5, 6, 7 in the figure correspond to conventional compression tests for the same sample performed at 3000, 4000, 5000, 5500, 6000 psi respectively. All the yield stress values obtained from this probing test are plotted in figure IV - 4.

Figure IV - 1b also shows stress-strain curves of conventional compression tests for one sample at different confining pressures, but in this case the first test was performed at a high p_c (5000) and this p_c was lowered before each test. The yield stress values obtained from this probing test are plotted in figure IV - 4.

Figure IV - 2a corresponds to stress-strain curves for

Sample VIII - 2

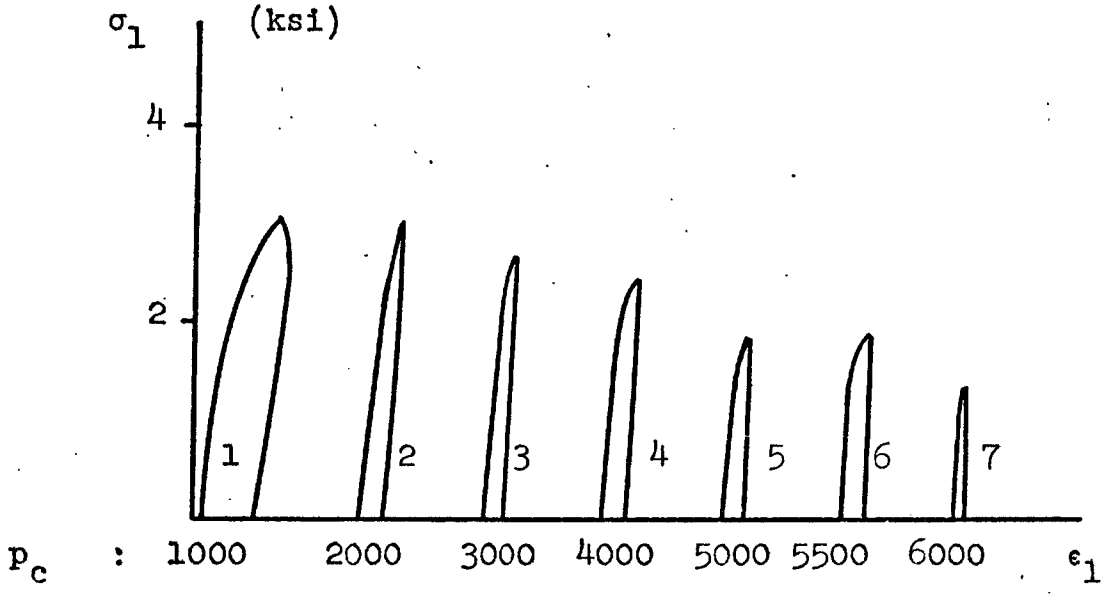

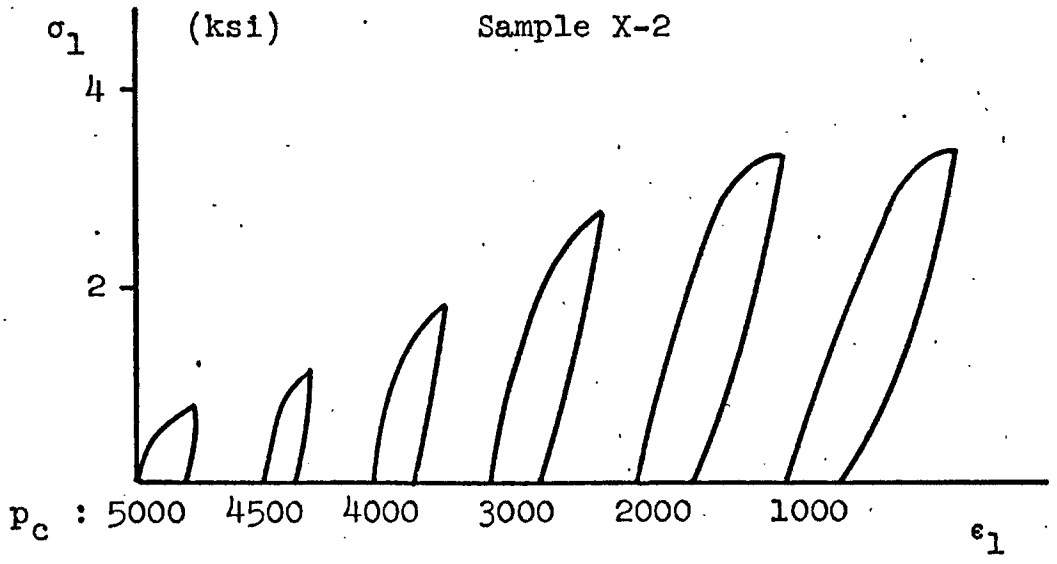

Figure IV - 1 Probing tests for initial yield surface

extension tests of one sample at different confining pressures. The initial confining pressure for this case was 2000 psi and it was increased before each extension test. The yield stress values obtained from this probing test are plotted in figure IV - 4.

Figure IV - 2b shows stress-strain curves for extension tests of one sample at different confining pressures. In this case, the initial confining pressure was 5000 psi and it was lowered before each test. The yield stress values obtained from this probing test are plotted in figure IV - 4.

Figure IV - 3 corresponds to a hydrostatic stress test that gives us a hydrostatic yield stress value of 5100 psi.

Figure IV - 4 shows all the yield stress values obtained from the previous tests. We can see that the dotted yield surface obtained from the tests IV - 1a and IV - 2a intersects the dotted yield surface obtained from the tests IV - 1b and IV - 2b. Our initial yield surface is the inner surface.

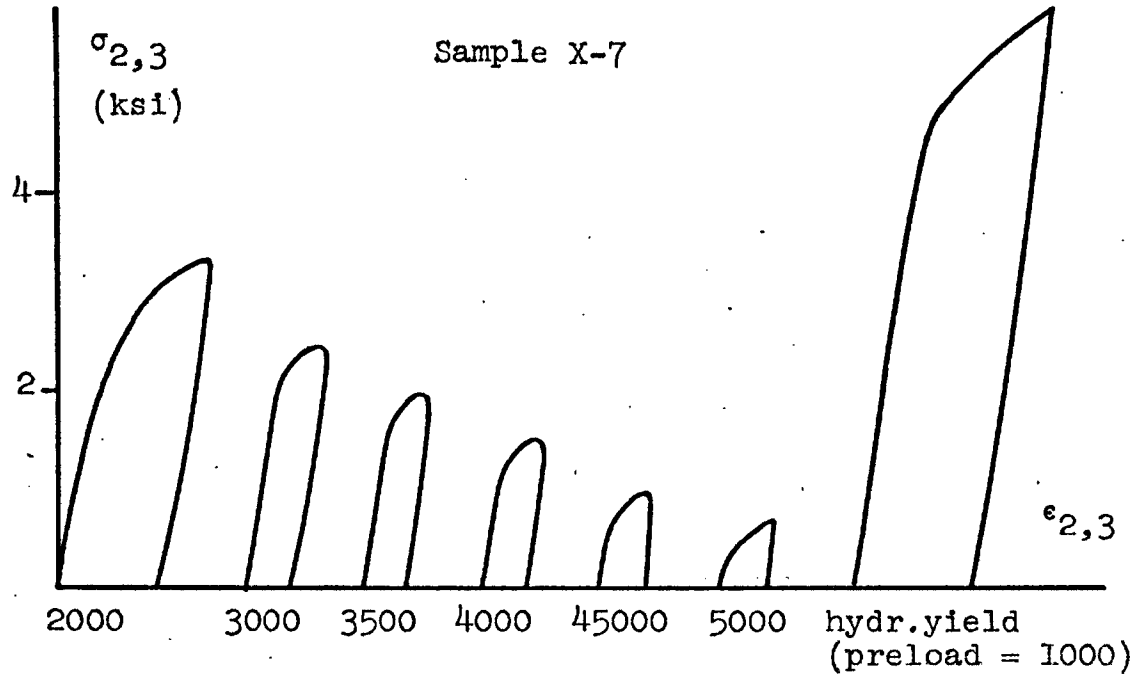

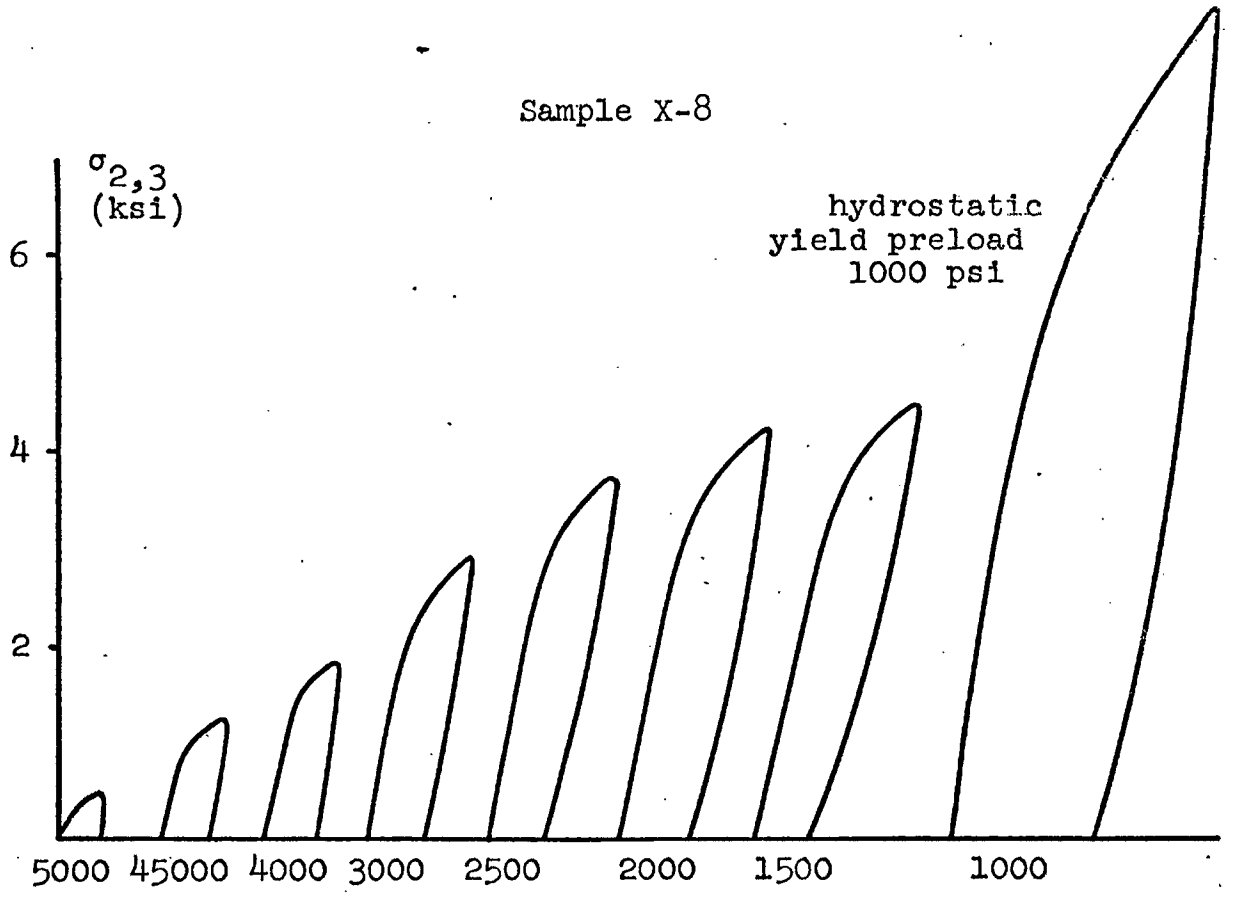

Figure IV - 2 Probing tests for initial yield surface

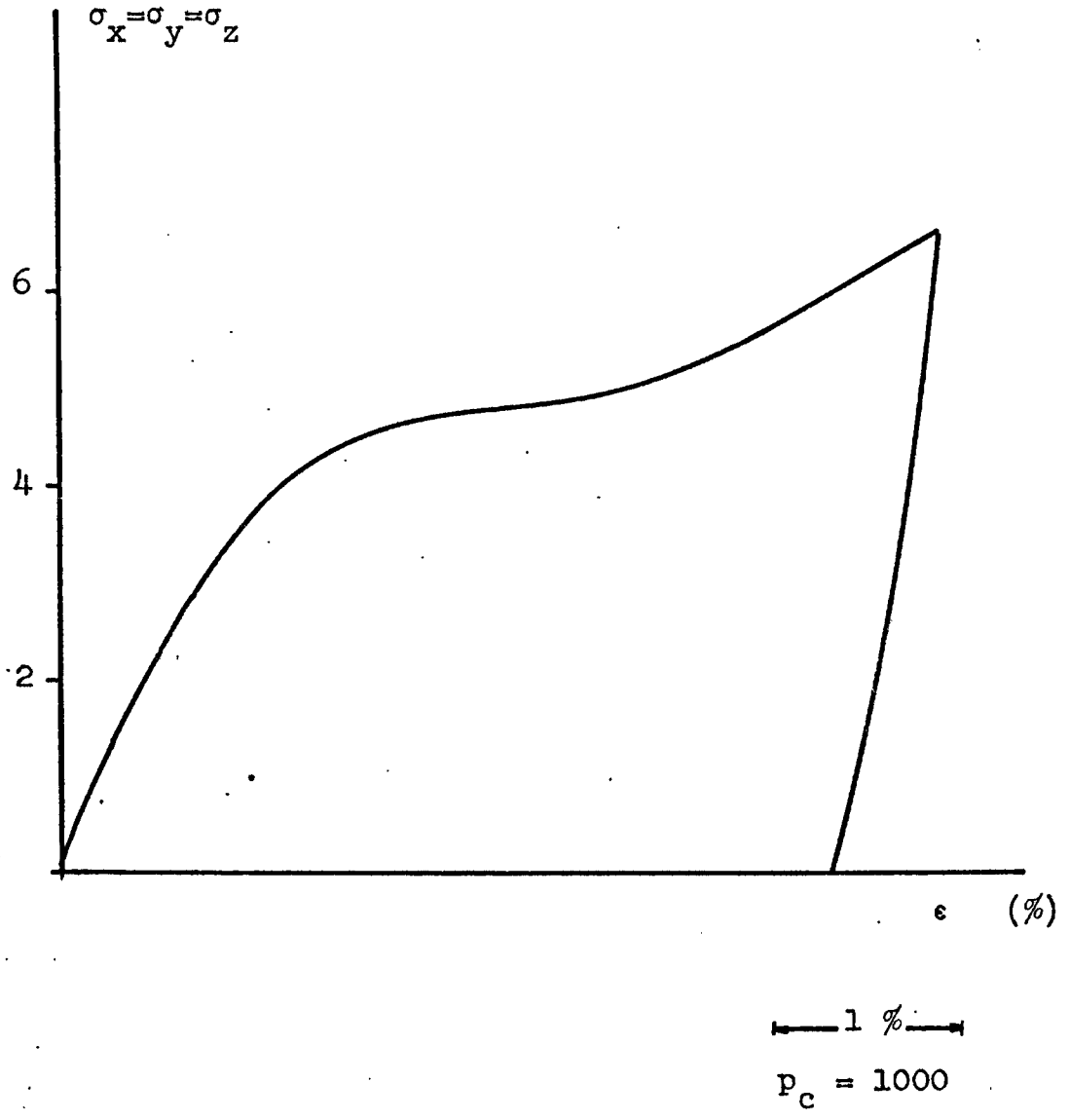

Figure IV - 3

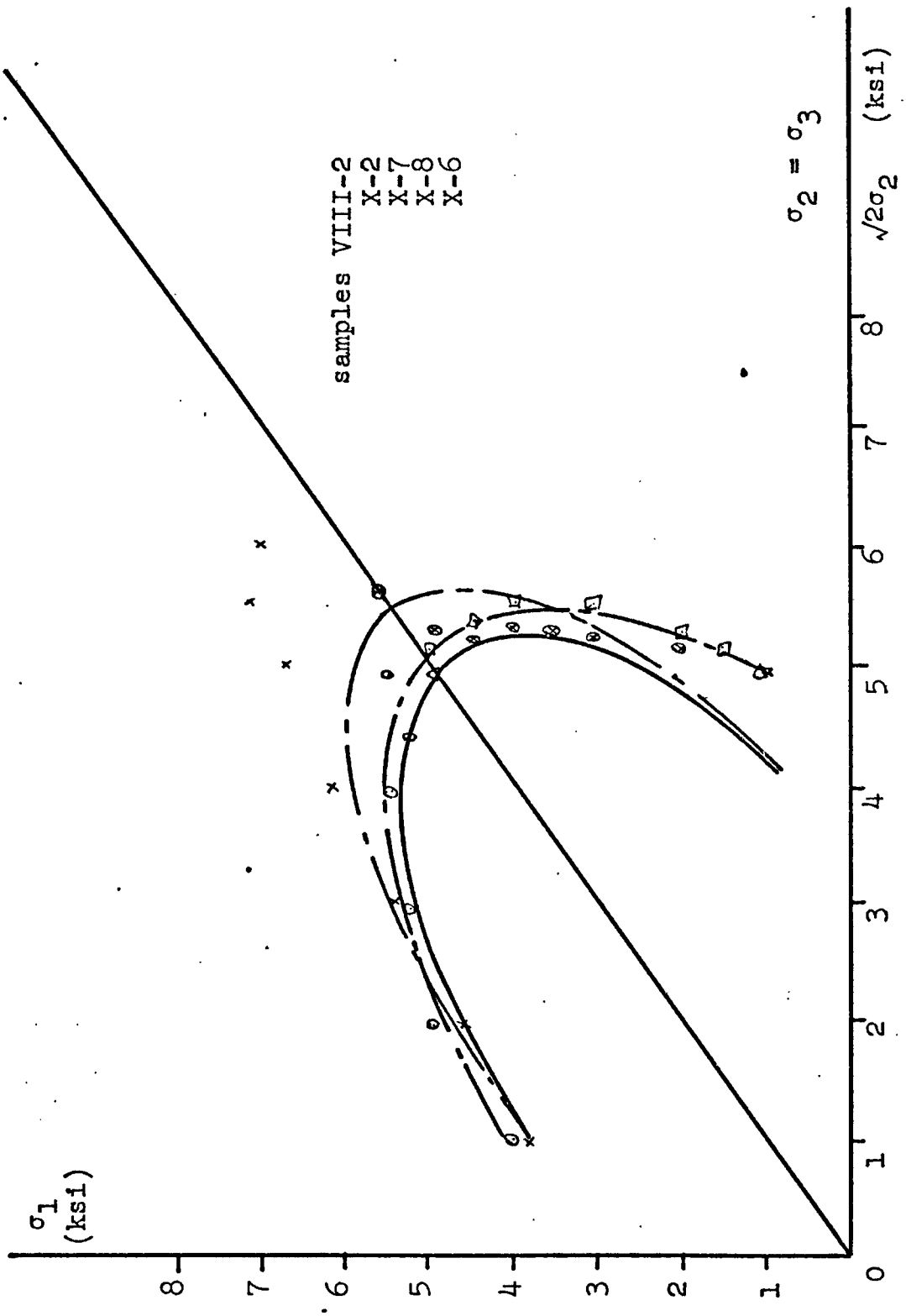
samples VIII-2
X-2
X-7
X-8
X-6
$\sigma_2 = \sigma_3$
σ_1 (ksi)
$\sqrt{2}\sigma_2$ (ksi)
0
1
2
3
4
5
6
7
8

Figure IV - 4

Normality

Three tests were performed to prove normality of the strain rate vector to the loading surface. The first of them is a conventional extension test which loading path is seen in figure IV - 5. In this test all three principal stresses are raised together above hydrostatic yield. At 7600 psi σ_2 and σ_3 are kept constant while the third stress, σ_1, is lowered falling in the elastic region of this subsequent yield surface until reaching it again and obtaining yielding in extension. The extension test was continued below yield.

In table 1 (Appendix A) the computed values of the strains for this test are shown. From this table, the values of the strain rate vector below yield in extension are computed and shown with dark lines (A, B, C, D) in figure IV - 5. We can see from this figure and from the initial yield surface previously obtained that the strain rate vectors obtained follow the normality principle. It can be seen that there is no significant change in the slope of these vectors through the extension tests, which means that the subsequent yield surfaces keep a constant slope along this shown path.

In this figure IV - 5, the letters A, B, C, D, E refer to table 1.

The second test is an extension test for which the loading path is seen in figure IV - 6. In this test the three principal stresses are raised to a low cinfining pressure (2300 psi). The stress on the vertical axis (σ_1)

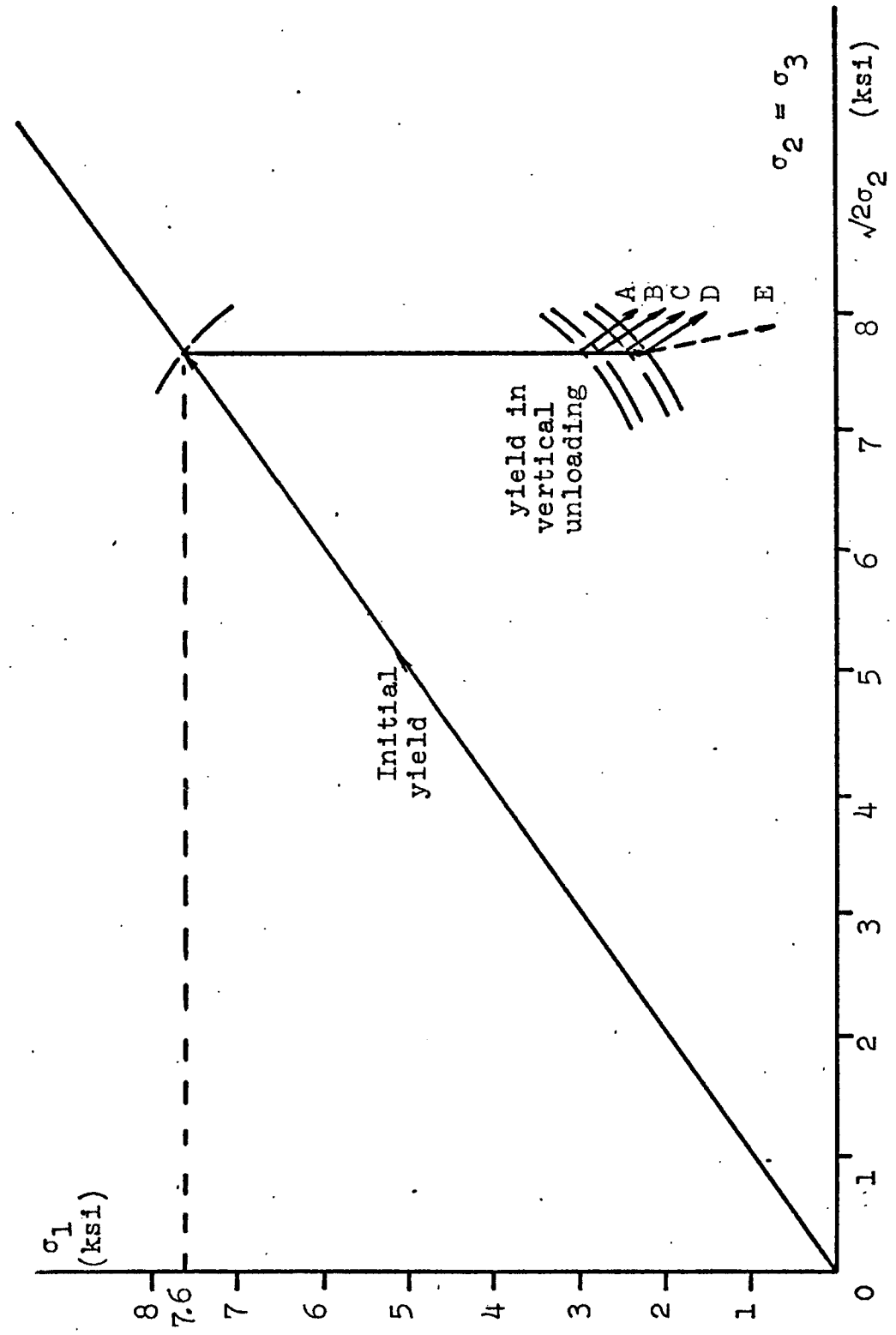

Figure IV - 5 Loading path for sample IV-a-1

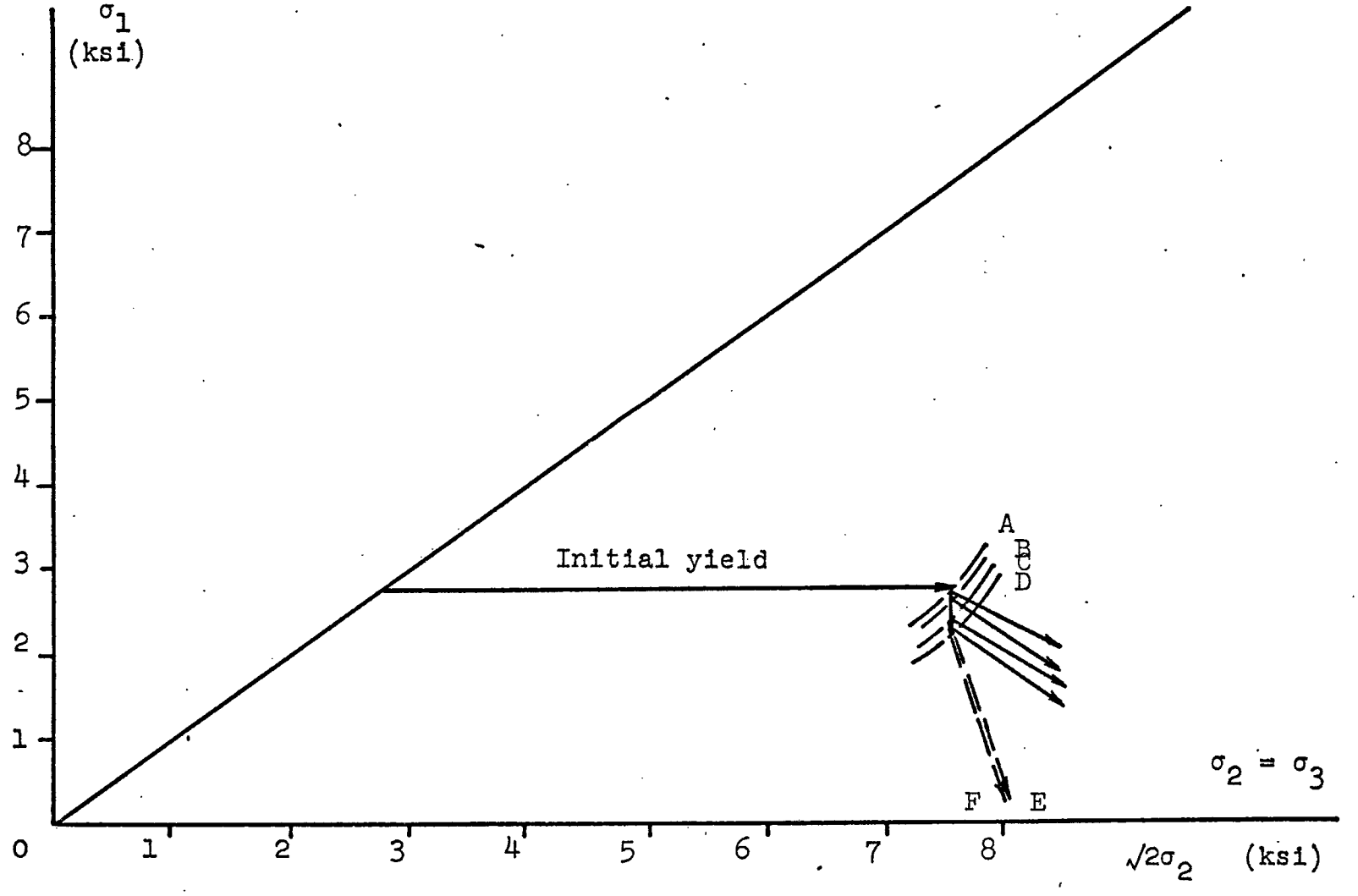

Figure IV - 6 Loading path for sample V-d

is then held constant at this value while the stress on the other two axes is increased until we reach a point close to the final stress state obtained in the first test (shown in figure IV - 5). At this point the stresses σ_2 and σ_3 are held constant and the vertical stress σ_1 is lowered.

In table 2 (Appendix A), the computed values of strains for this test are shown. From this table the values of the strain rate vector below yield in extension are computed and shown with dark lines (A, B, C, D) in figure IV - 5. We can also see in this test that the normality principle applies. Also it can be observed that the strain rate vector do not have a significant change in slope along the loading path, which leads us to conclude that the subsequent yield surfaces keep a constant slope along this shown path.

In figure IV - 6, the letters A, B, C, D, E, F are referred to table 2.

The third test is an extension test where the three stresses are raised together to a low confining pressure and then σ_2 and σ_3 are increased while σ_1 is kept constant ; this test is shown in figure IV - 7 ; in figure IV - 8, a stress-strain curve ($\Delta \sigma_2 = \Delta \sigma_3$) vs. ($\epsilon_2 = \epsilon_3$) for this extension test shows a yield stress of 4400 psi which correspond to $\sigma_2 - p_c$. At this yield point, the slope of the strain rate vector is shown in figure IV - 7, and again we see that this vector follows normality. In table III (Appendix A), the computed values for strains, in this test, are tabulated. More strain rate vectors are shwn in figure IV - 7 and it is

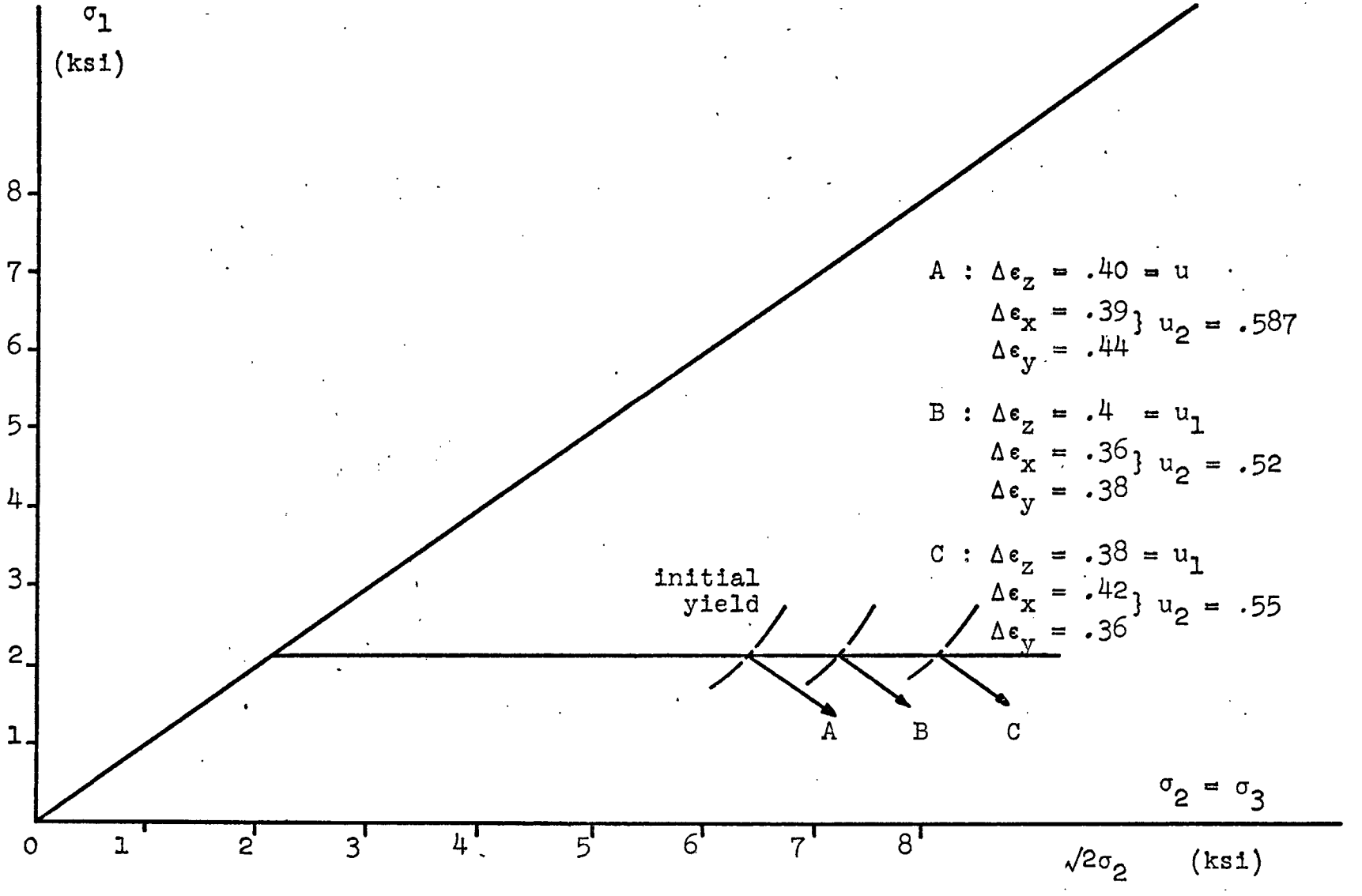

Figure IV - 7 Loading path for sample VI-a-1

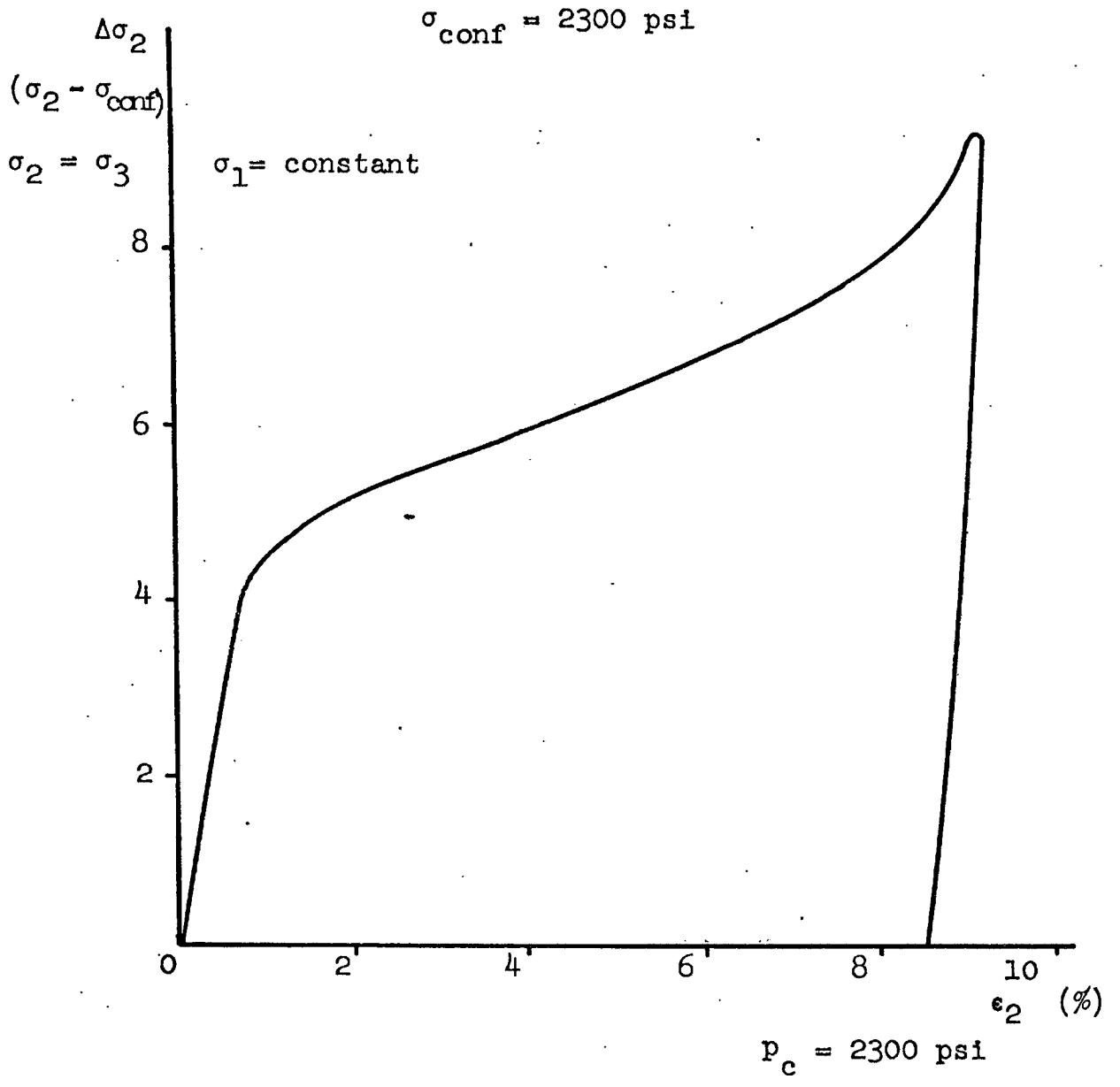

Figure IV - 8 Extension test for sample VI-a-1

clearly seen that, along this loading path, they keep a constant slope. The letters A, B, C are referred to table III. In these three tests the strain rate vectors were computed in the following fashion :

u_1 = unit vertical component of the strain rate vector ;

u_2 = unit horizontal component of the strain rate vector

where

$$u_1 = \Delta\ \epsilon_1 = \Delta\ \epsilon_z$$

$$u_2 = \sqrt{2}\ \left(\frac{\Delta\epsilon_x + \Delta\epsilon_y}{2}\right) = \sqrt{2}\ \left(\frac{\Delta\epsilon_2 + \Delta\epsilon_3}{2}\right)$$

once the values of u_1 and u_2 were obtained, the strain rate vector was plotted in the stress plane σ_1 vs. $\sqrt{2}\sigma_2$.

Failure Plane

The presence of a failure plane was detected through different experiments.

In figure IV - 9a, a stress-strain curve is shown for an extension test performed at 1000 psi confining pressure, the sample broke at $\Delta\ \sigma_2 = 4050$ psi. This value and the loading path are shown in figure IV - 12.

A second test was a conventional extension test in which the hydrostatic stress was raised to 4200 psi, and then σ_1 was lowered while keeping $\sigma_2 = \sigma_3 = 4150$ psi.

Rupture occured at σ_1 = 600 psi. A stress-strain curve for this test is shown in figure IV - 9b where OA is hydrostatic loading and AB corresponds to extension. The rupture value and this loading path are shown in figure IV - 12.

Figure IV - 5 corresponds to the loading path of the test performed on sample IV - 1a, in figure IV - 10 a stress-strain curve is shown for this same test where OA is hydrostatic loading, at A σ_2 and σ_3 are kept constant and σ_1 is lowered until yield is reached in extension ; after yield we see that plastic flow is occurring but the stresses remain constant ; this stress value and the loading path for this sample are plotted in figure IV - 12.

After removing the sample from the testing machine, we could observe that it was not broken but an incipient failure plane was clear. Incipient failure plane appears on a surface of a sample as a line along which (locally) large deformation is apparent.

Figure IV - 11 shows the stress-strain curve for the test performed on sample V - d which loading path was described in figure IV - 6. In this curve, OA corresponds to hydrostatic loading, at A, σ_1 is kept constant and $\sigma_2 = \sigma_3$ are raised till 7650 psi, at this point $\sigma_2 = \sigma_3$ are kept constant and σ_1 is lowered, we can see that yield occurs almost immediately and that during plastic flow the stress state remains constant. This constant value of stresses and the loading path are shown in figure IV - 12.

After removing the sample from the testing machine,

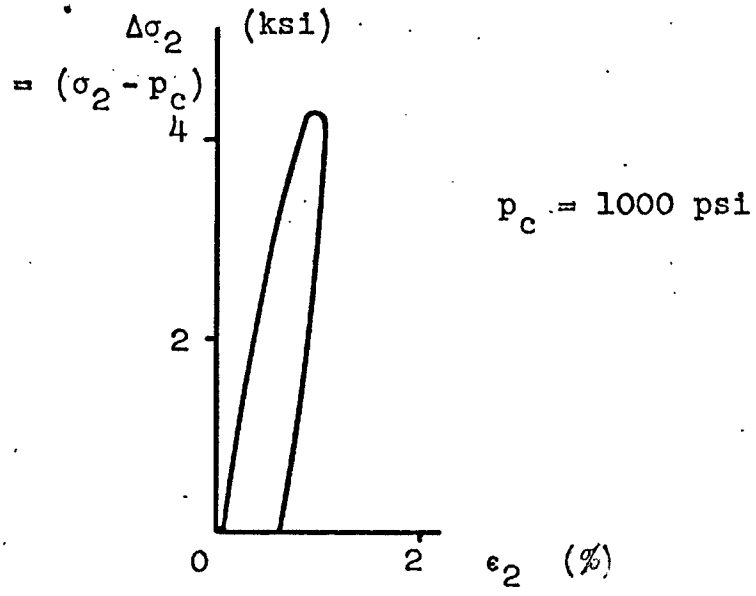

(a) extension test at p_c = 1000
sample VIII-4

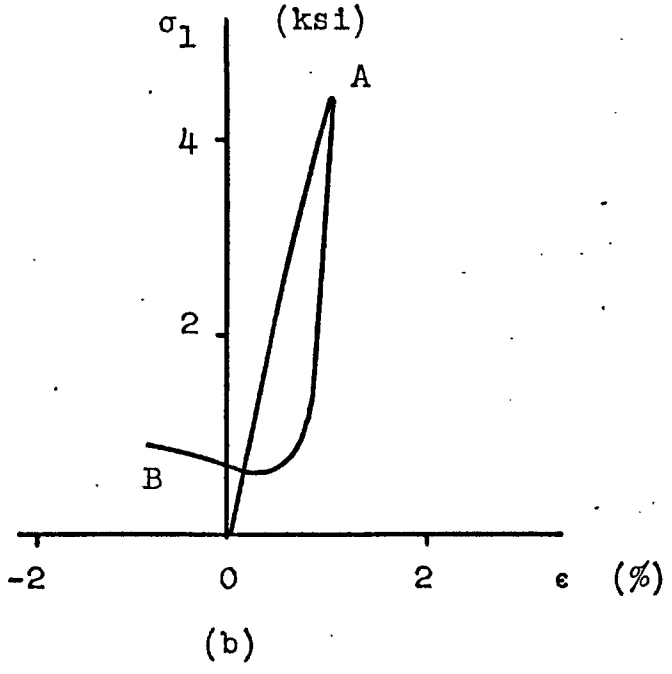

(b)
sample IV-b

Figure IV - 9

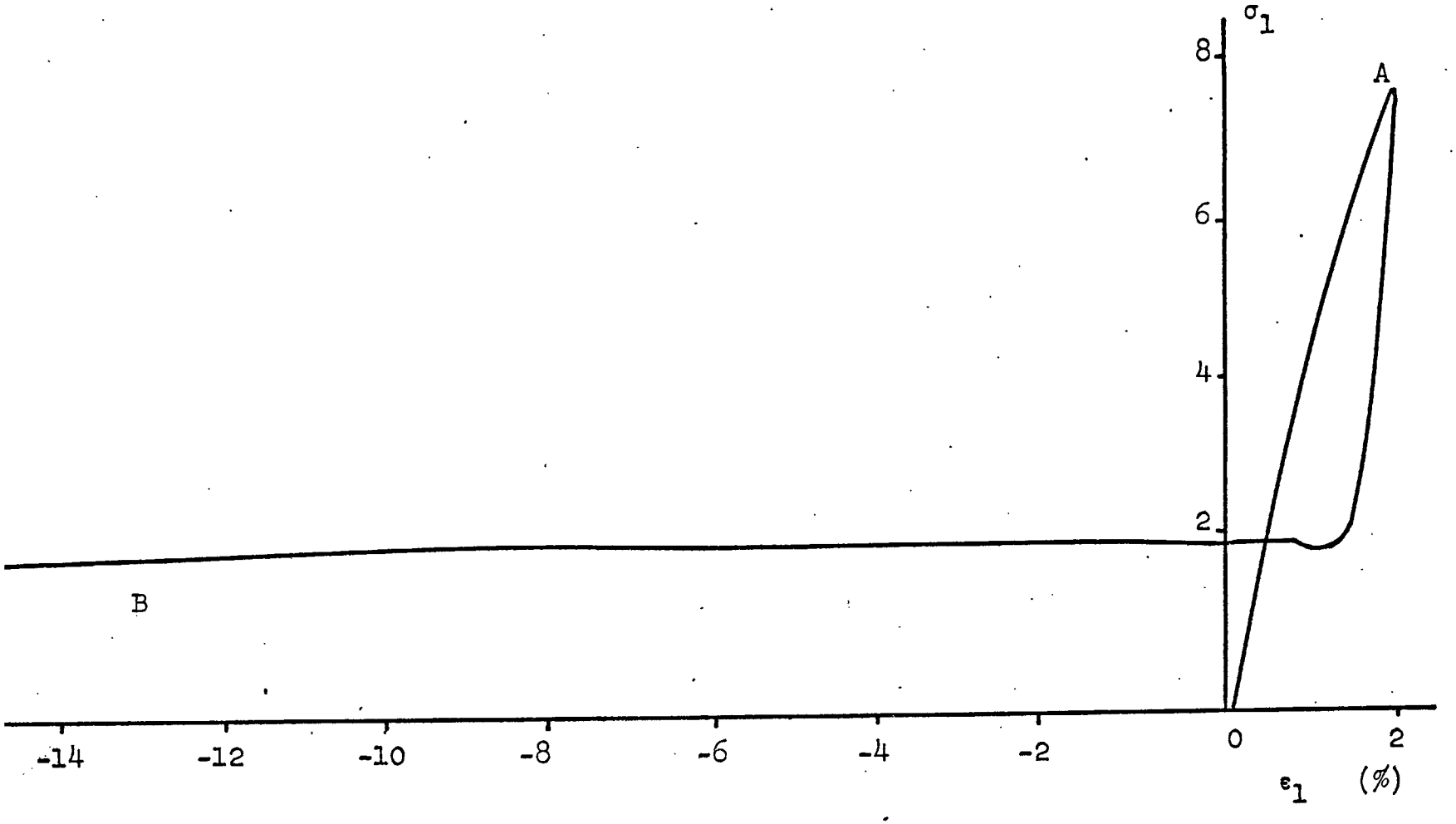

Figure IV - 10 Conventional extension test for sample IV-a-1

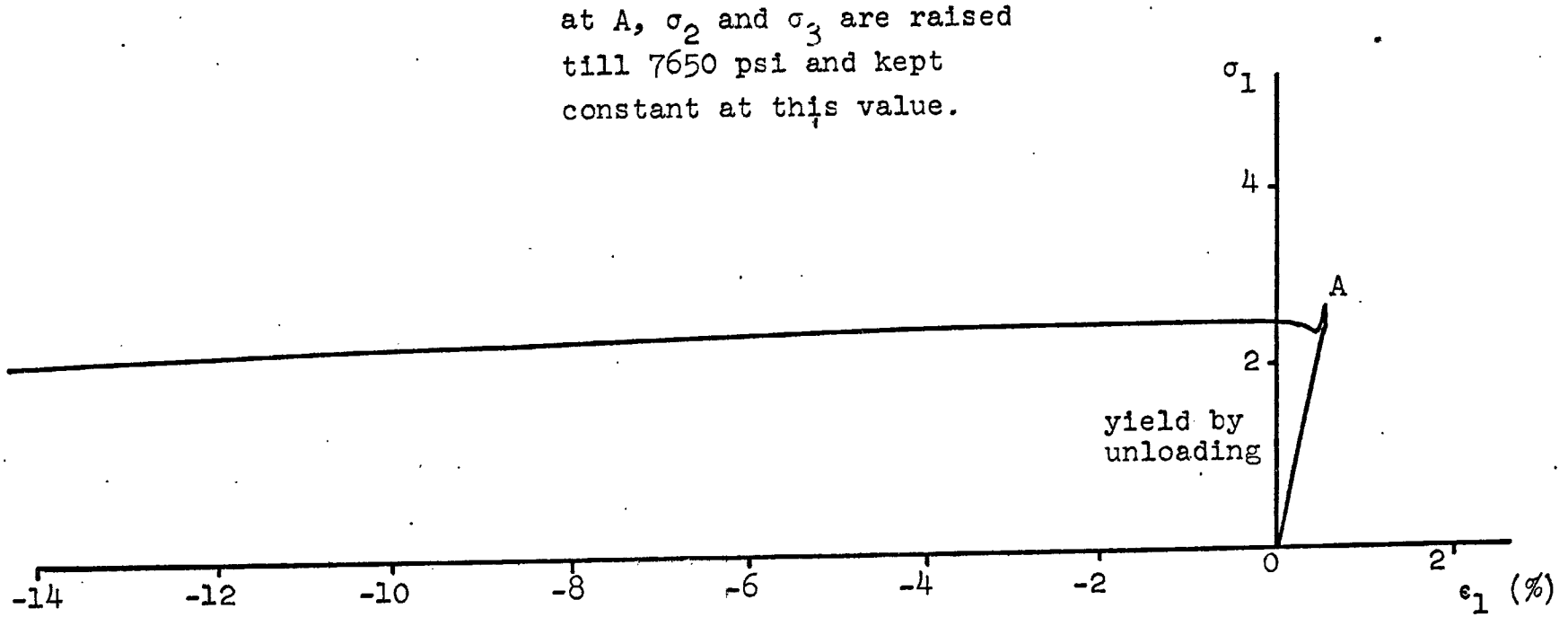

Figure IV - 11 Stress-strain curve of sample V-d

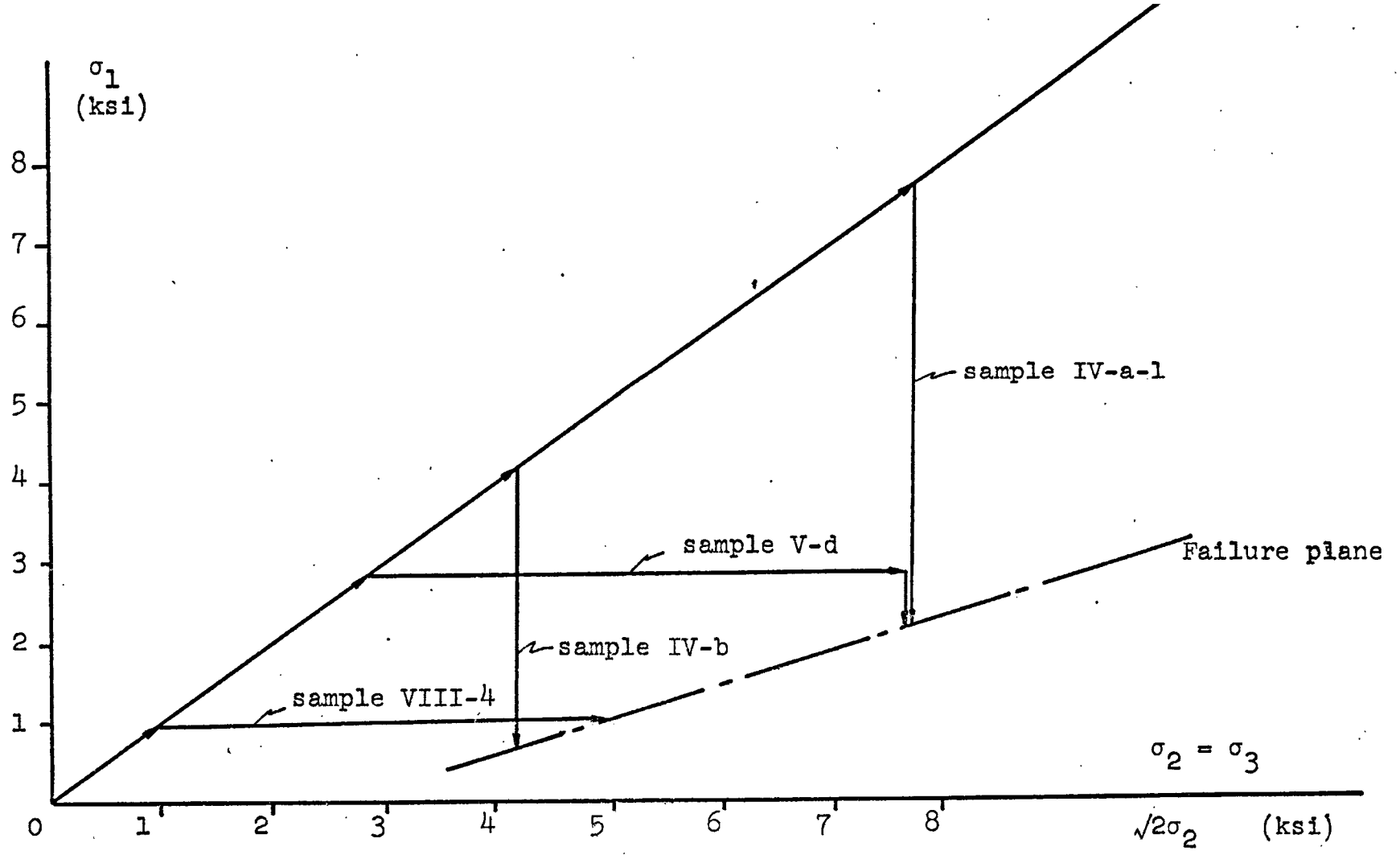

Figure IV - 12 Loading path and final state of stress of different samples

the sample was not broken and an incipient failure plane was observed.

Analyzing figure IV - 12 now, we can see that the four failure stresses plotted lay in a straight line which leads us to deduce that it corresponds to a failure plane.

Corners on Yield Surface

Three tests are analyzed here to study the strain rate vectors behavior under the presence of a corner (see Chapter II, pp

The first experiment to be analyzed is the one performed with sample IV -a1 which is shown in figures IV - 5 and IV - 10. From the two previous analyses, we can conclude that through a loading path corresponding to conventional extension test the yield surface approaches the failure plane without change in slope until it intersects the plane.

From table 1 the change in volumetric strain throughout the experiment is plotted in a stress volumetric strain curve in figure IV - 13. In this curve we can see that as the failure plane is approached, the volume of the sample decreases and once the two surfaces intersect the volume of the sample starts to increase. A strain-rate vector for this situation is plotted with dotted line in figure IV - 5 (vector E ; see values at (E) in table 1). This vector E is observed to be perpendicular to the failure plane obtained in the previous section.

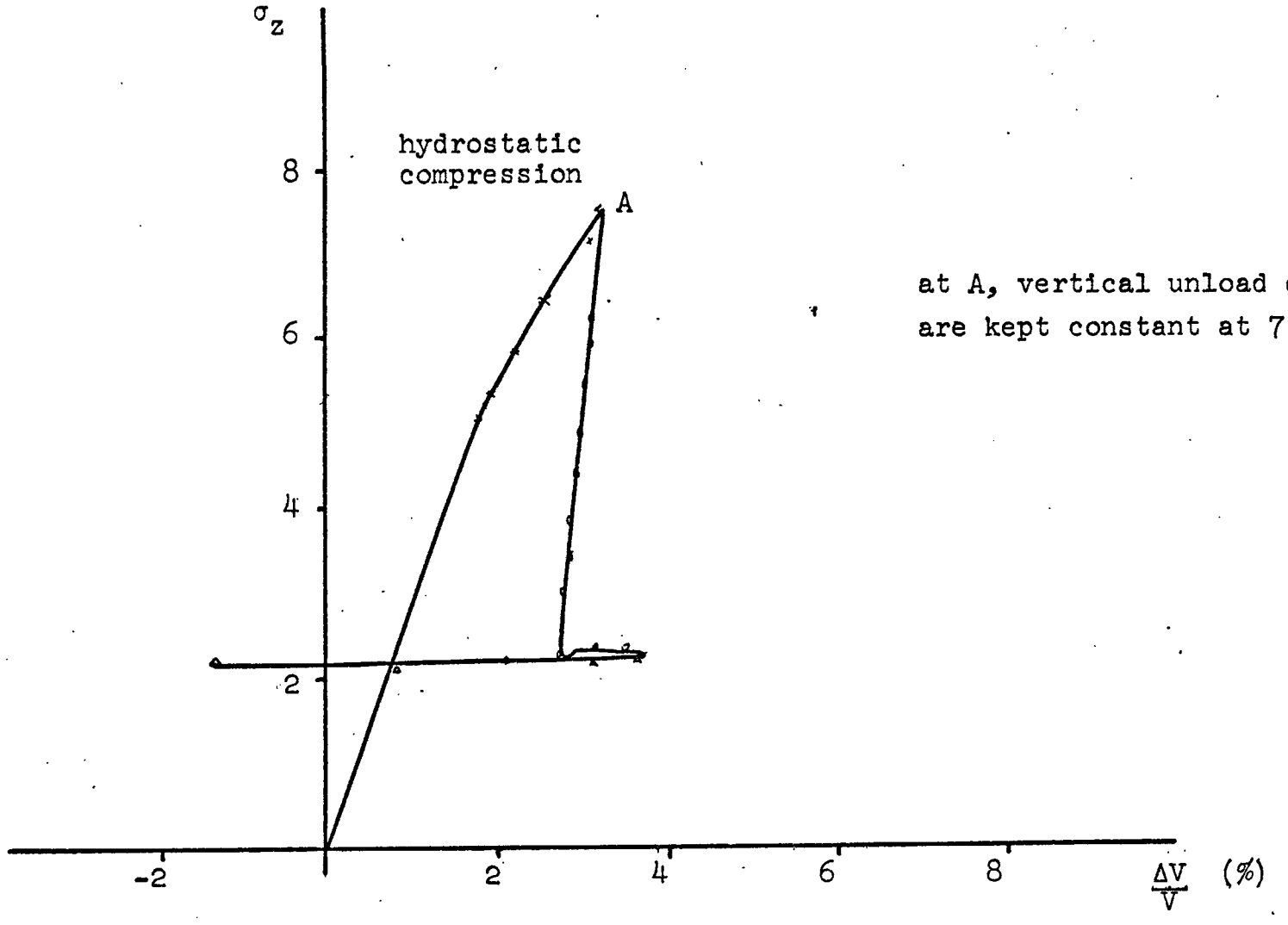

Figure IV - 13 Stress vs. volumetric strain for sample IV-a-1

The second test analyzed for this situation is the one performed with sample V - d which was presented previously in figures IV - 6 and IV - 11. From table 2 the change in volumetric strain is obtained and plotted in a stress volumetric strain curve in figure IV - 14. Samples V - d and IV - a1 were loaded by different paths but in the final stress state they lead to close points in the stress space, and we can see from figures IV - 14 and IV - 13 that the volumetric behavior is very similar through this two different paths. (For this purpose, figure IV - 13 is plotted with dotted lines on IV - 14).

Figure IV - 14 shows that as the yield surface and the failure plane intersect, the volume starts to increase. In figure IV - 6 two strain-rate vectors for this situation are plotted with dotted lines (vectors E and F ; see E and F in table 2) and they are perpendicular to the failure plane. From these experiments it can be seen that at a corner due to the intersection of the yield surface and the failure plane, the strain-rate vector rotates from a position perpendicular to the yield surface to a position perpendicular to the failure plane. It can also be seen that strain-rate vectors do not change in slope along the loading path.

Finally, an extension test was performed to analyze the behavior of the strain-rate vectors. A stress-strain curve is shown for this test in figure IV - 15 ($\Delta\sigma_2$ vs. ϵ_2), the confining pressure for this test is 2520 psi. Tabulated values of strains are in table 4 (Appendix A). In figure

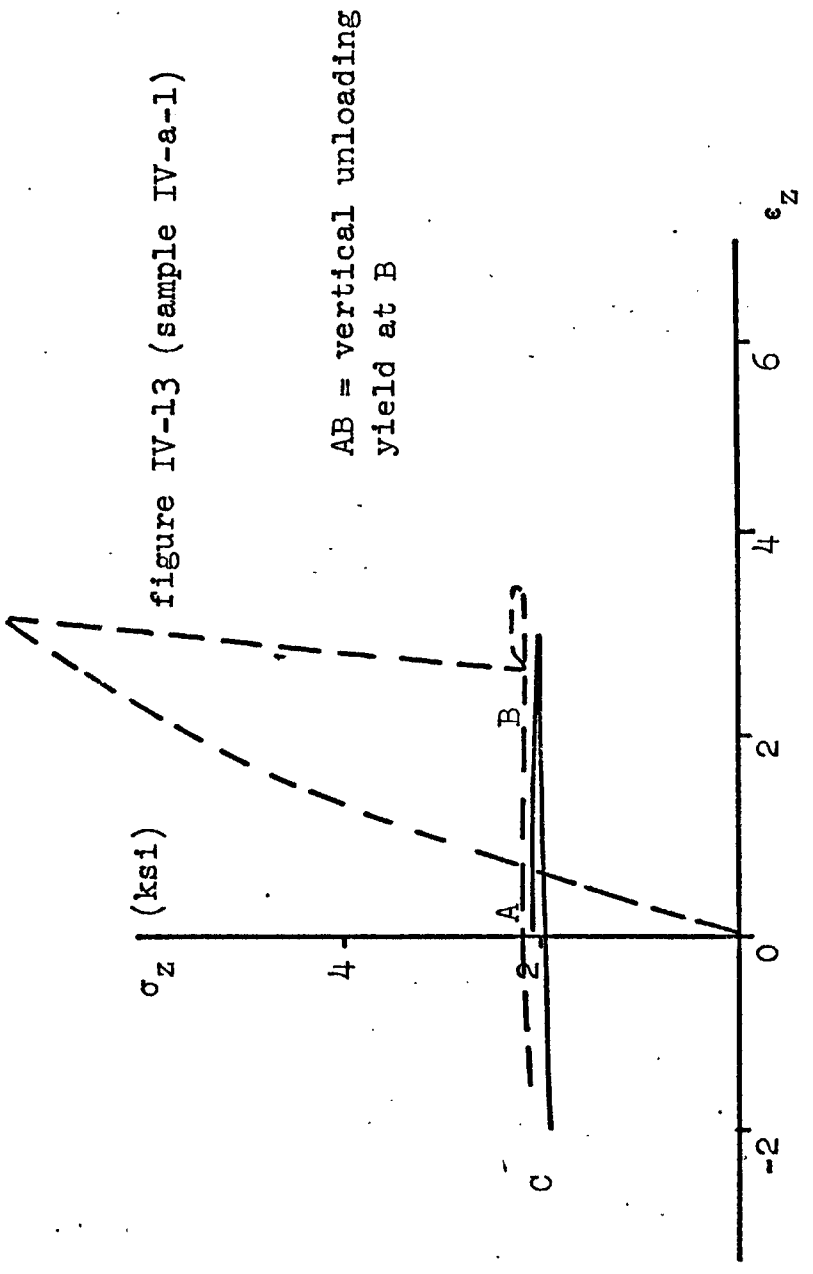

Figure IV - 14 Stress vs. volumetric strain for sample V-a

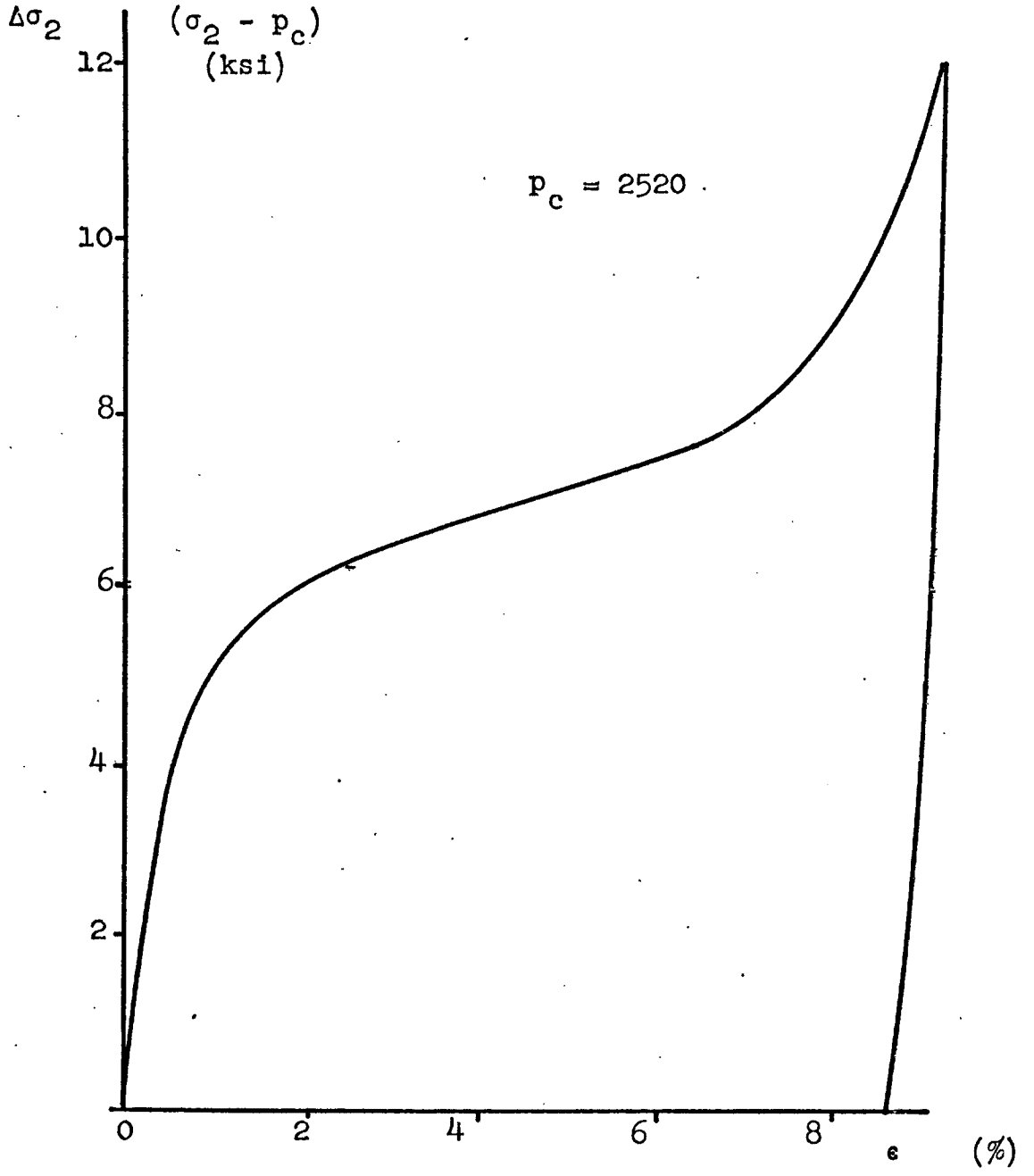

Figure IV - 15 Stress-strain curve for sample V-b (extension test)

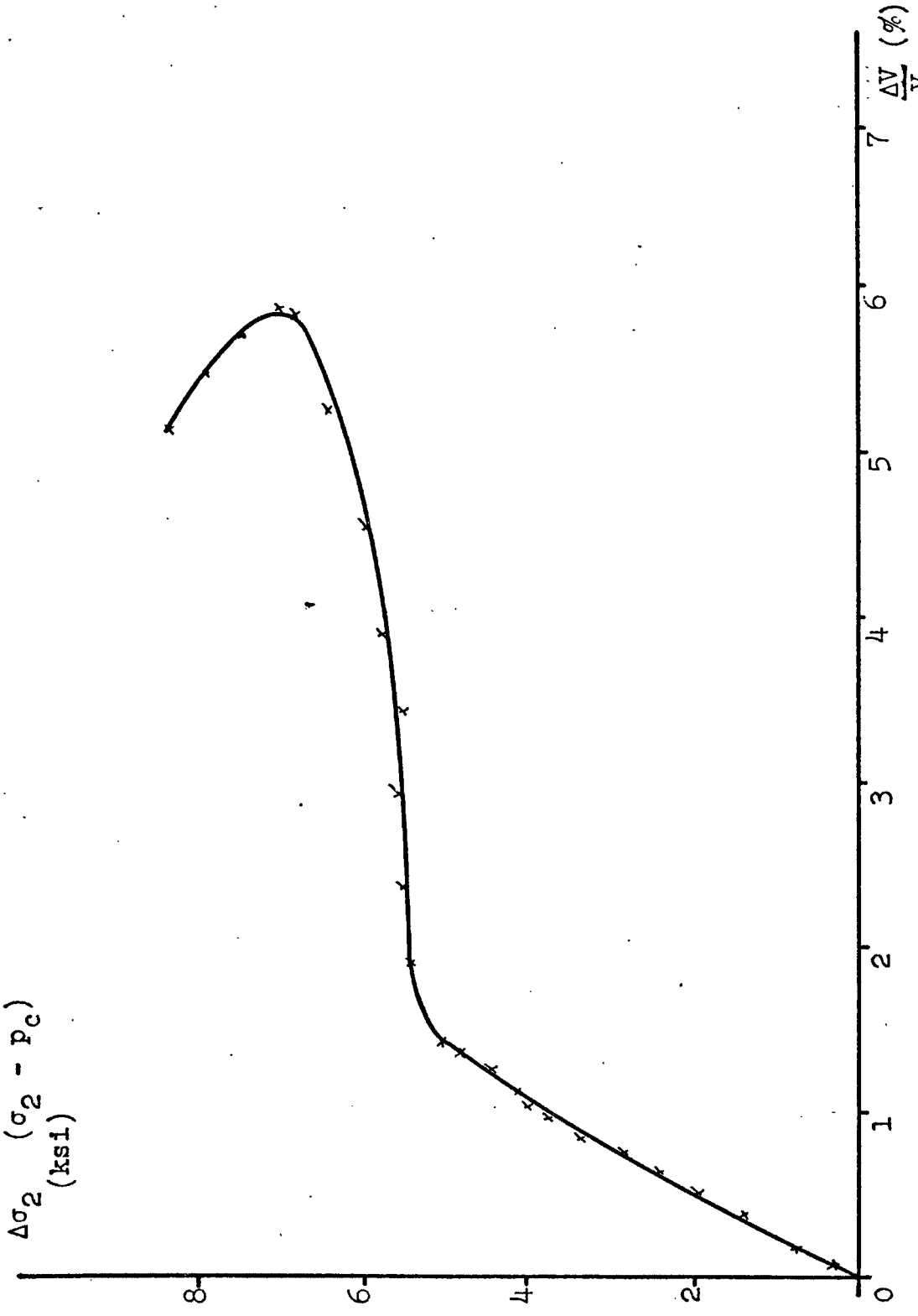

Figure IV - 16 Stress vs. volumetric strain for sample V-b

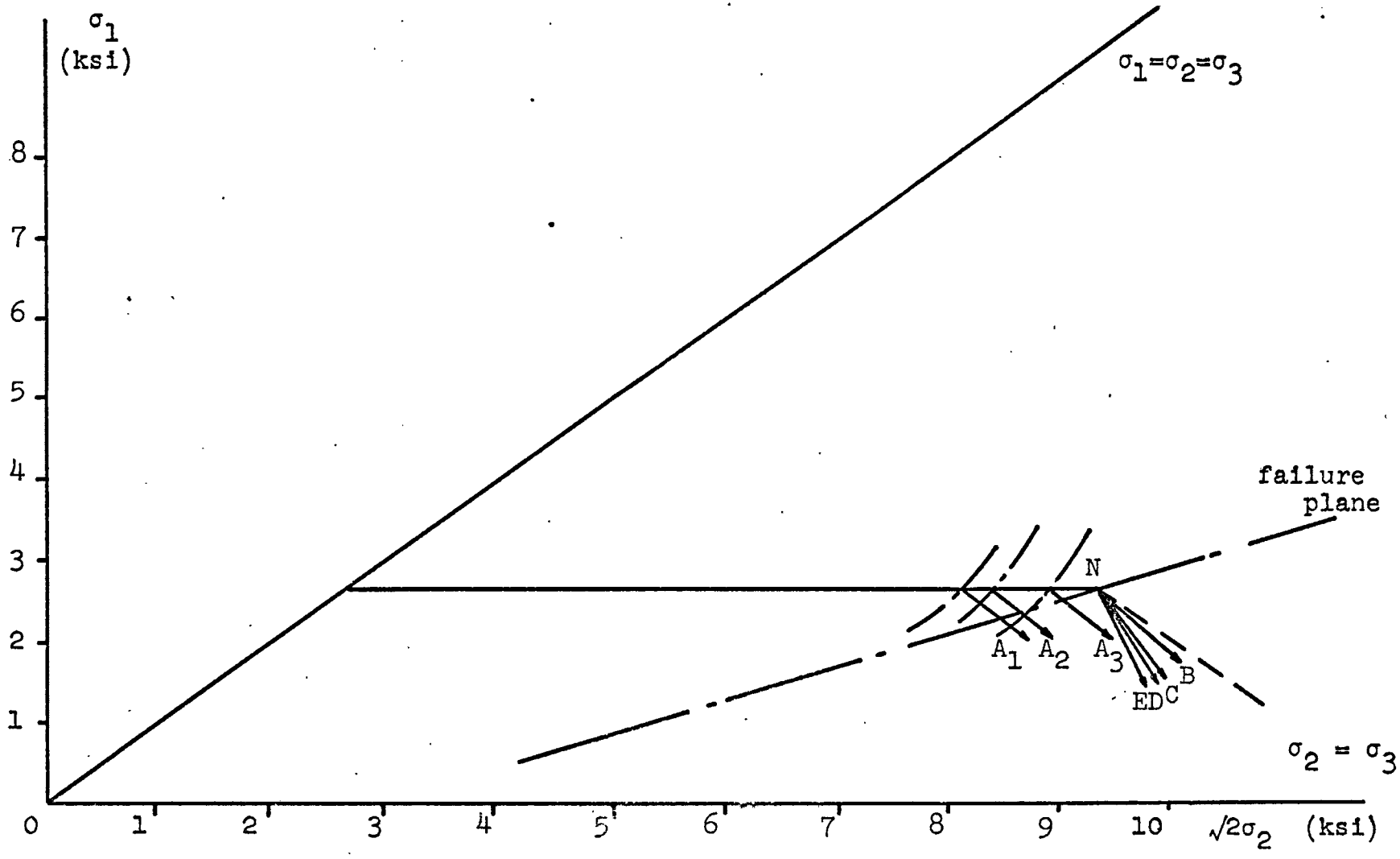

Figure IV - 17 Normality test for sample V-b

IV - 15 we see that the yield point is $\Delta\sigma_2 = 5500$ psi, this corresponds to point A_1 in table 4 and to the computed strain rate vector A in figure IV - 17. Figure IV - 16 shows the volumetric strain performance during this test and we can see that at 6800 psi the volume stops decreasing and starts increasing ; this point is plotted in figure IV - 17 (point N) and we can see that it coincides with the failure plane we had obtained previously. Also strain-rate vectors A_2 , A_3, B, C, D, E are computed from table 4 and we can see that A_1, A_2, A_3 stay parallel. When the loading path hits the failure plane, a corner is created and it is seen that the strain-rate vectors B, C, D, E rotate gradually to a final position perpendicular to the failure plane.

Induced Anisotropy

Before obtaining the subsequent yield surfaces, several tests were performed to determine if hardening developed along one axis could have any effect on the properties of the other axes. These tests were performed in order to prove that hardening a material along one path in the stress space would induce anisotropy in the sample ; these tests also would give an initial idea of the type of hardening that takes place when loading the yield surface.

All tests in this section are performed for a confining pressure = 3000 psi. Tests at $p_c = 2000$ psi (not presented in this section) were also performed and similar

results were obtained.

All tests performed along a single axis consisted of conventional compression tests.

Figure IV - 18 shows a characteristic stress-strain curve for conventional compression test at p_c = 3000 psi of the y axis.

Figure IV - 19 shows a characteristic stress-strain curve for conventional compression test at p_c = 3000 psi of the z axis. At A in this test, the sample was unloaded and rotated and then reloaded again till p_c = 3000 ; at this point a conventional compression test for the y axis was performed and we can see that the yield stress value for the y axis was lower than the expected value (from the characteristic curve in figure IV - 18) due to hardening along the z axis.

In figure IV - 20. OA shows a conventional compression test for the z axis which is compatible with the test in figure IV - 19 ; at point A, the sample was unloaded, rotated and reloaded to p_c = 3000 ; at this point a conventional compression test for the y axis was performed as shown by AB. This curve AB gives a lower yield point than the initial yield point obtained from the characteristic curve for the y axis (figure IV - 18).

At B the sample was unloaded, rotated and reloaded to p_c = 3000 ; at this point another conventional compression test on the z axis was made and it can be seen that the yield point obtained is lower than the expected one. At C

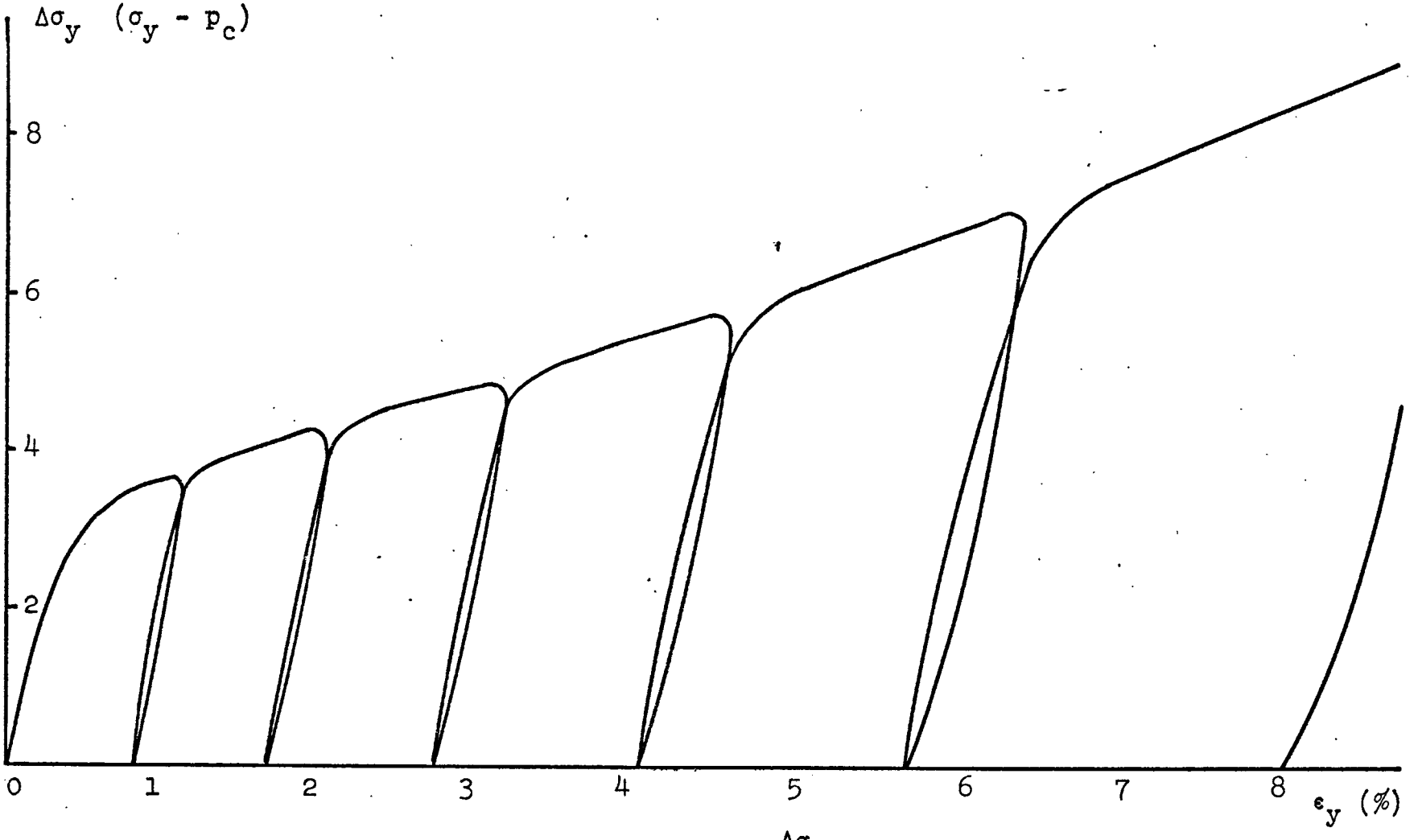

Figure IV - 18 Characteristic curve $\frac{\Delta\sigma_y}{\epsilon_y}$ for sample IX-17 $p_c = 3000$

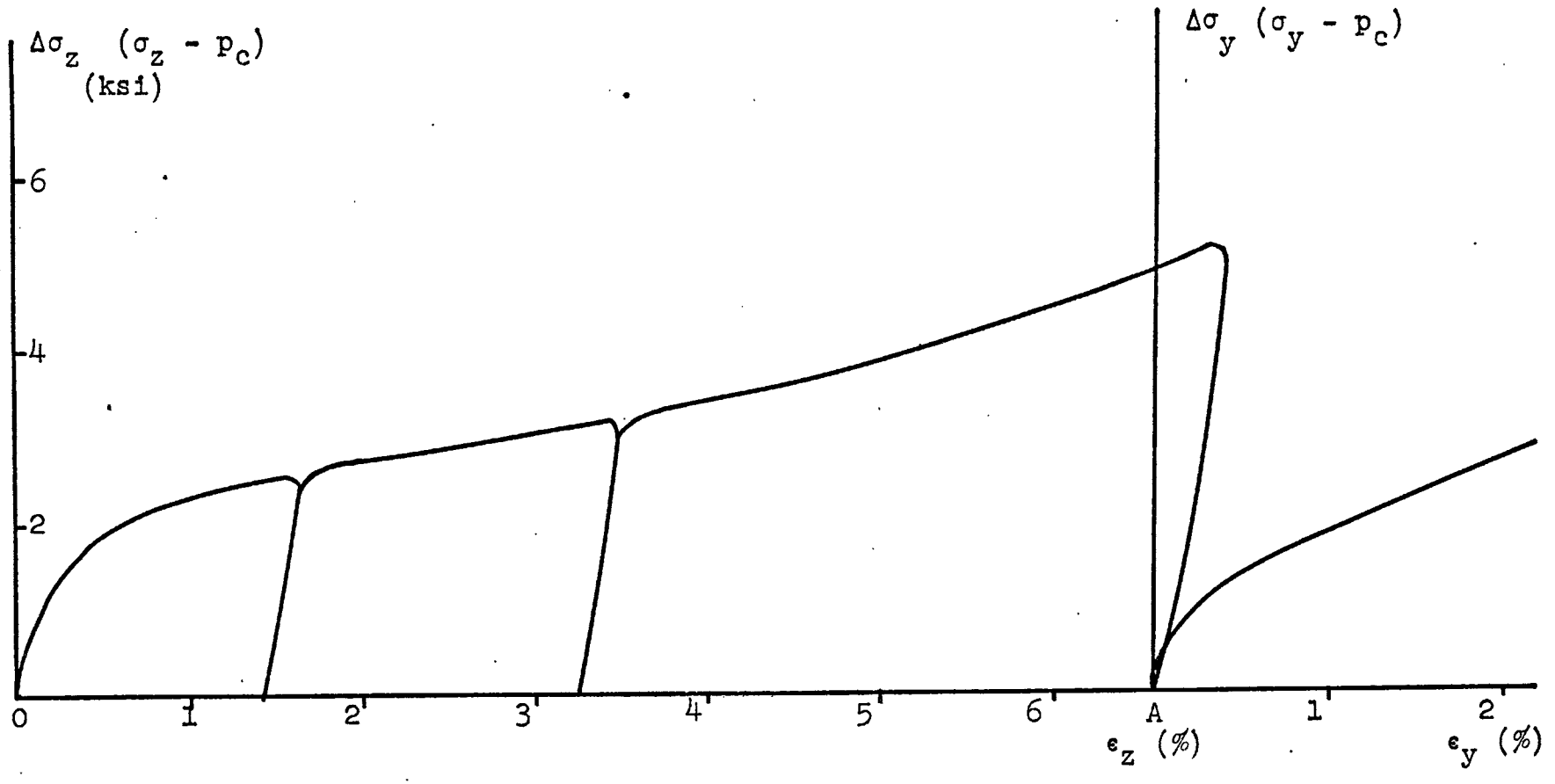

Figure IV - 19 Characteristic curve $\frac{\Delta\sigma_z}{\epsilon_z}$ for sample IX-7 p_c = 3000

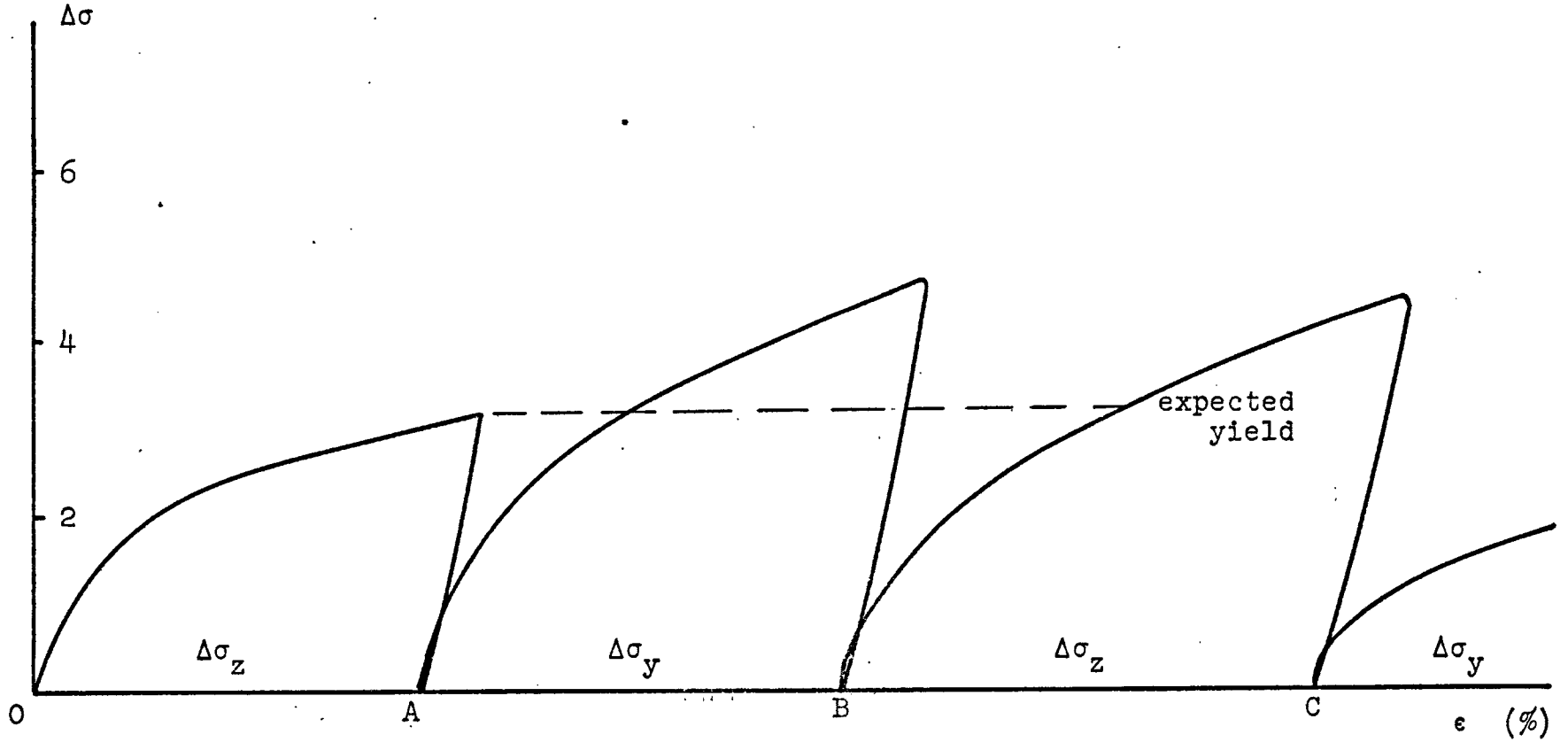

Figure IV - 20 Exploratory test for sample IX-13 p_c = 3000

the sample was again unloaded, rotated and reloaded to p_c = 3000 ; at this point another conventional compression test for the y axis was made and also in this case the yield point is lower than the expected value, we can see that we have almost immediate yield for this last case.

It was thought that this effect of lowering the yield point was caused by the unloading to atmospheric pressure and the rotation of the sample, so in the following experiments the samples will not be unloaded nor rotated.

In figure IV - 21, stress-strain curves for a conventional compression test along the z axis at p_c = 3000 is shown. At point A, the y axis was loaded up to $\Delta\sigma_y$ = 4500 psi (from figure IX - 17 we can see that this value is above the yield stress value for the y axis) and then unloaded to the confining pressure. The hardening on the y axis affected again the z axis in a similar fashion, the new yield point is higher than the previously obtained but is also lower than the expected one. As we can see, for this test the sample was not taken out during the test nor the confining pressure was lowered to atmospheric pressure.

In figure IV - 22, stress-strain curves are shown for conventional compression tests on the y axis. We tried to keep the values for the stresses in the y axis as well as in the z axis similar to the values in the previous test (figure IV - 21) ; in other words, these stress-strain curves for the y axis would describe the performance of the y axis on the previous test. At point A the z axis was loaded

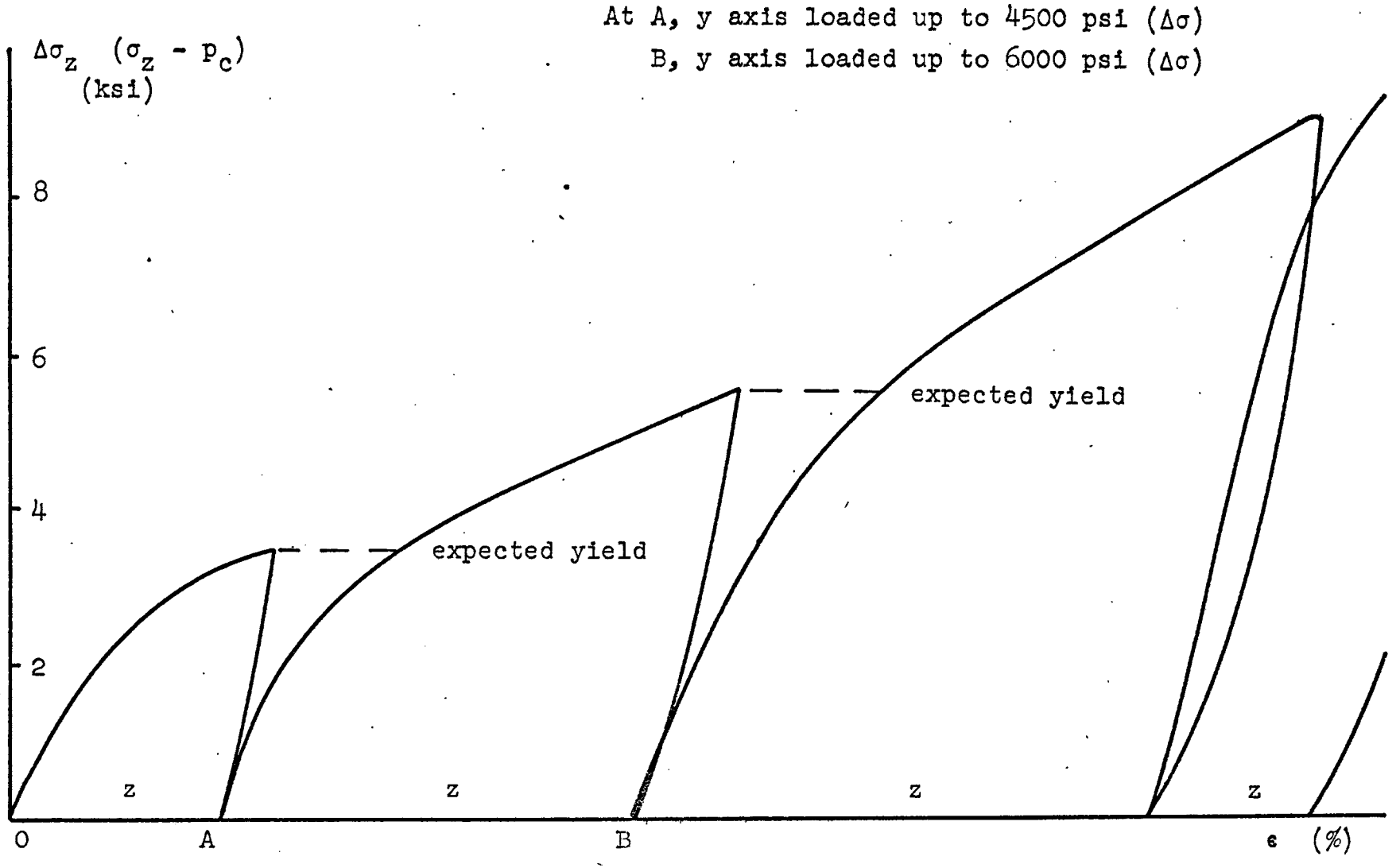

Figure IV - 21 Exploratory test for sample IX-14 p_c = 3000

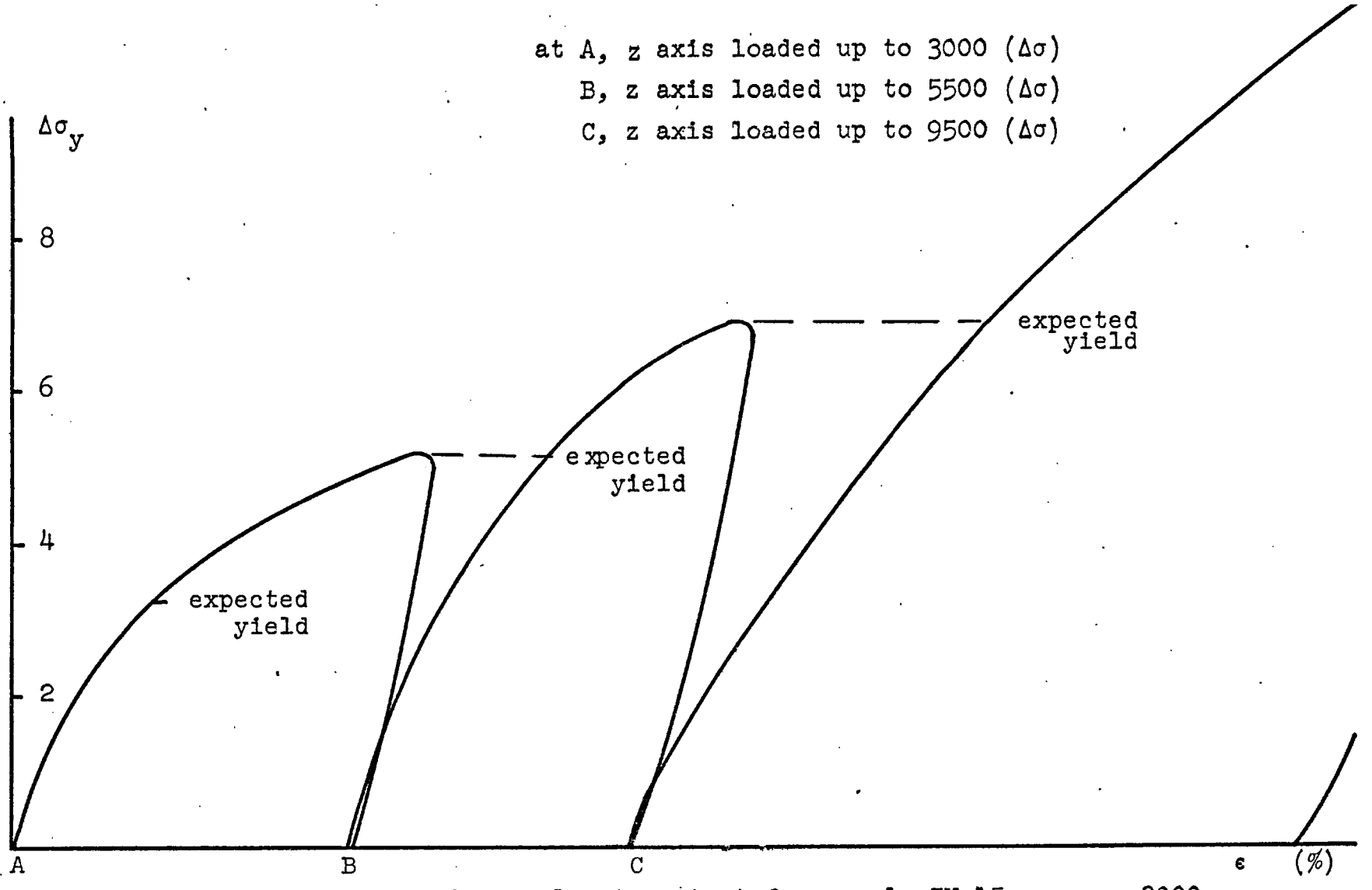

Figure IV - 22 Exploratory test for sample IX-15 p_c = 3000

to $\Delta\sigma_z$ = 3000 psi and unloaded ; then the conventional compression test was performed in the y axis and if we compare the curve obtained with the one in figure IV - 18, we can see that the yield point obtained is a little lower than the expected one. At point B the z axis was loaded to $\Delta\sigma_z$ = 5500 psi and unloaded to confining pressure ; then a new conventional compression test was made along the y axis and we can observe for the stress-strain curve that the new yield point is lower than the expected one but higher than the previous one. At point C the z axis was loaded to $\Delta\sigma_z$ = 9500 psi and unloaded to the confining pressure, then a conventional compression test was again performed along the y axis and now we can see that the new yield point, besides being lower than the expected one, is also lower than the initial value.

In figure IV - 23, stress-strain curves for the z axis are shown for conventional compression tests, the procedure was very similar to the previous test : at A the y axis was loaded to $\Delta\sigma_y$ = 4500 psi and unloaded, at B the y axis was loaded to $\Delta\sigma_y$ = 6000 psi and unloaded and at C the y axis was loaded to $\Delta\sigma_y$ = 9500 psi and unloaded. We can also see that the results are very similar ; we can conclude that upon small hardening on one axis, the other axis is not affected, but as the hardening increases in this axis, the other axis is affected. It can be seen that the hardening rate is also affected.

To observe the influence of the x over the y axis and

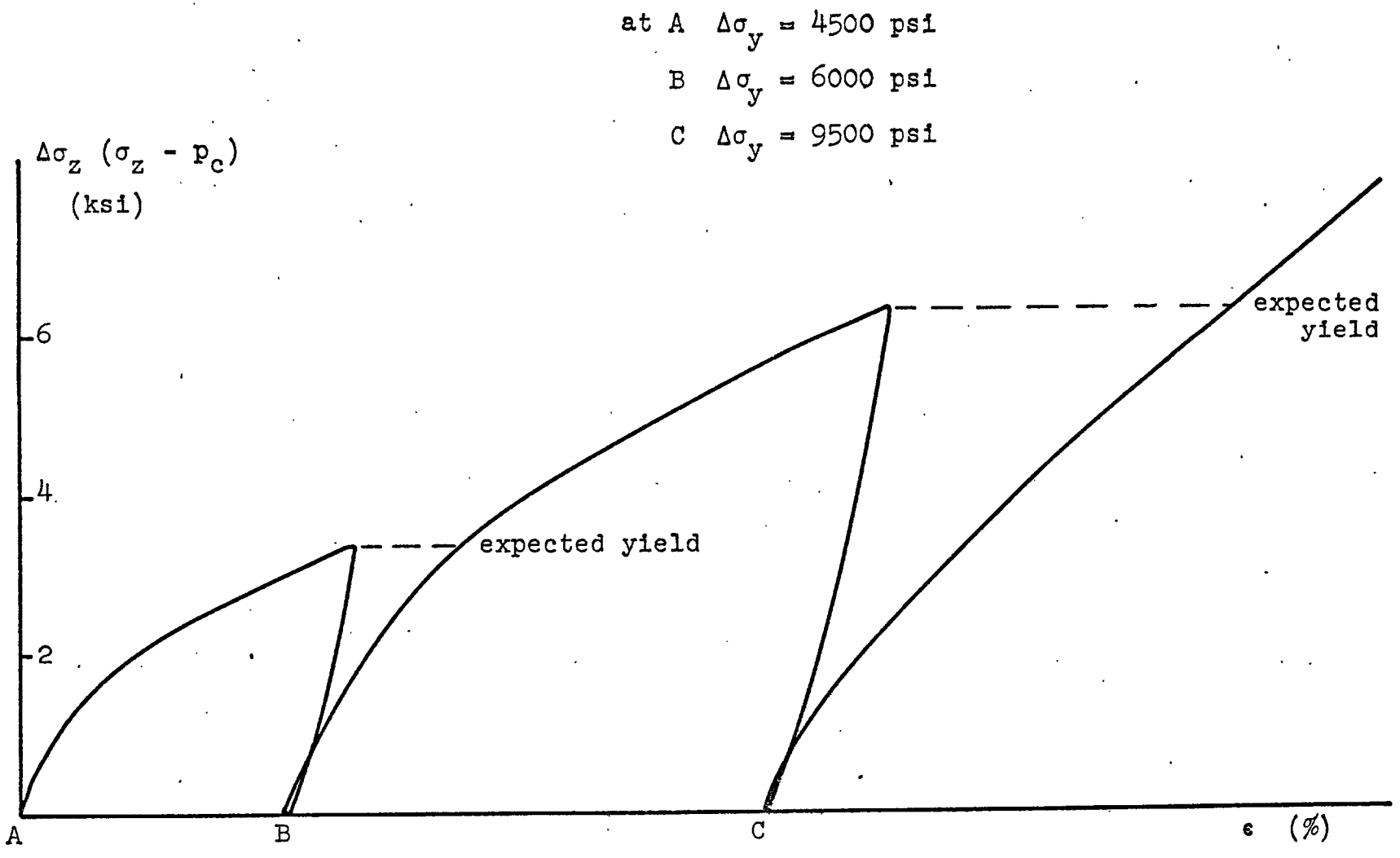

Figure IV - 23 Exploratory test for sample IX-20 p_c = 3000

vice-versa, figure IV - 24 shows conventional compression tests on the two axes. The sample was unloaded and turned around the axes of rotational symmetry after each test. From the stress-strain curves we can see that the results are very similar to the ones previously obtained.

Finally, the effect of hardening along the z axis over the x and y axes together (σ_z vs. $\sqrt{2}\sigma_x$ plane) was tested.

Figure IV - 25 shows a stress-strain characteristic curve for extension tests at $p_c = 3000$ psi where σ_z is kept at $p_c = 3000$ while σ_x and σ_y are raised together.

In figure IV - 26, we can see stress-strain curves where σ_x and σ_y are raised together in extension and unloaded. At A the z axis was loaded to $\Delta\sigma_z = 3000$ and unloaded then the x and y axes were loaded together on extension and unloaded. It can be seen that the expected yield point is almost unaffected but the hardening rate is affected. At B the z axis was loaded to $\Delta\sigma_z = 4000$ and then unloaded, then another extension test was performed, raising σ_x and σ_y together. It can be seen that the yield stress value obtained is lower than the expected value and again the hardening rate is affected.

Figure IV - 27 shows stress-strain curves for conventional compression tests along the z axis ; at A the x and y axes were loaded to $\Delta\sigma_{x,y} = 3000$ psi and unloaded. Then a new conventional compression test was performed along the z axis. It can be observed that the yield point obtained is lower than the expected value but higher than the initial

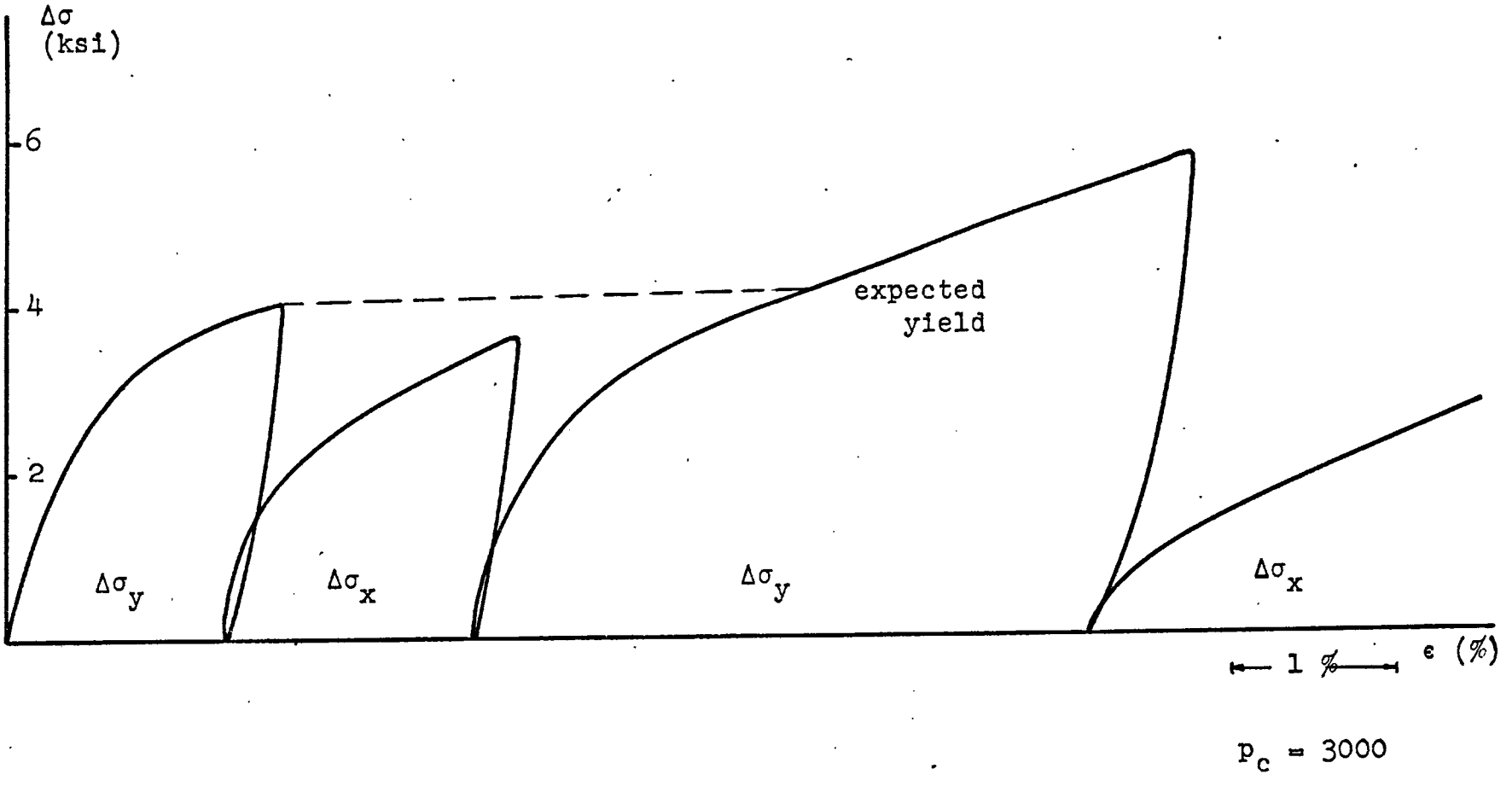

Figure IV - 24 Exploratory test for sample IX-21

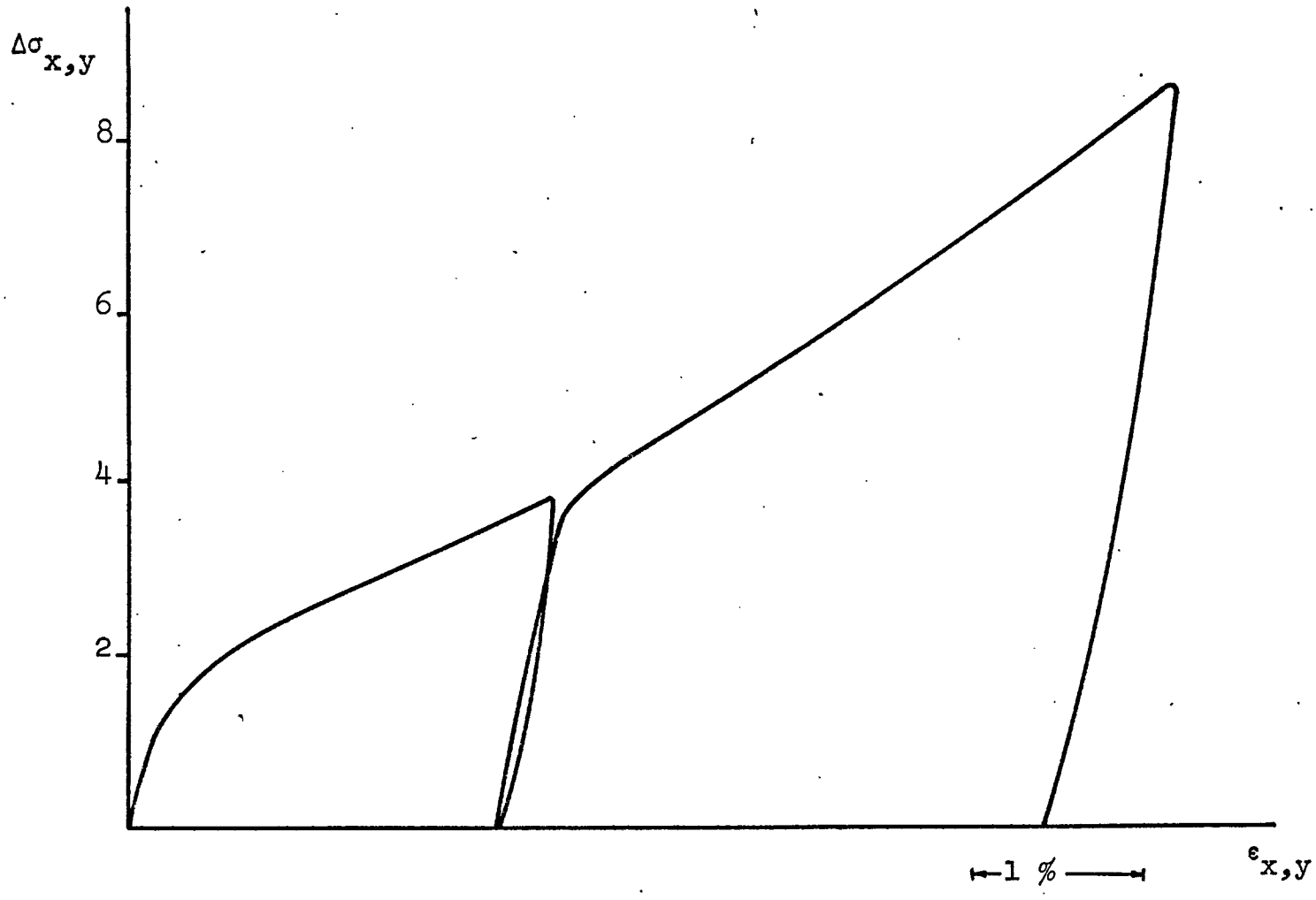

Figure IV - 25 Exploratory test for sample XI-2-a $p_c = 3000$

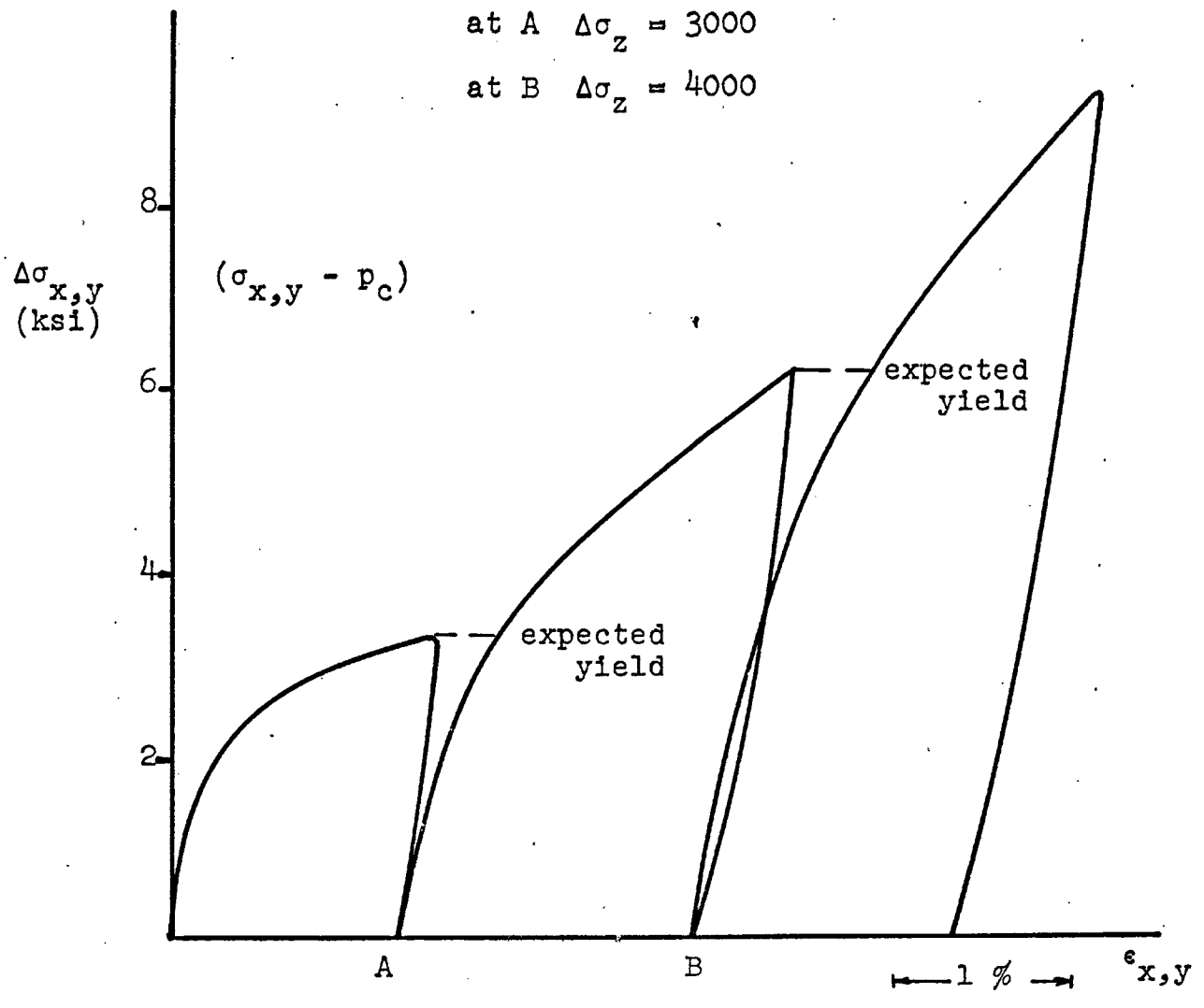

Figure IV - 26 Exploratory test for sample XI-1

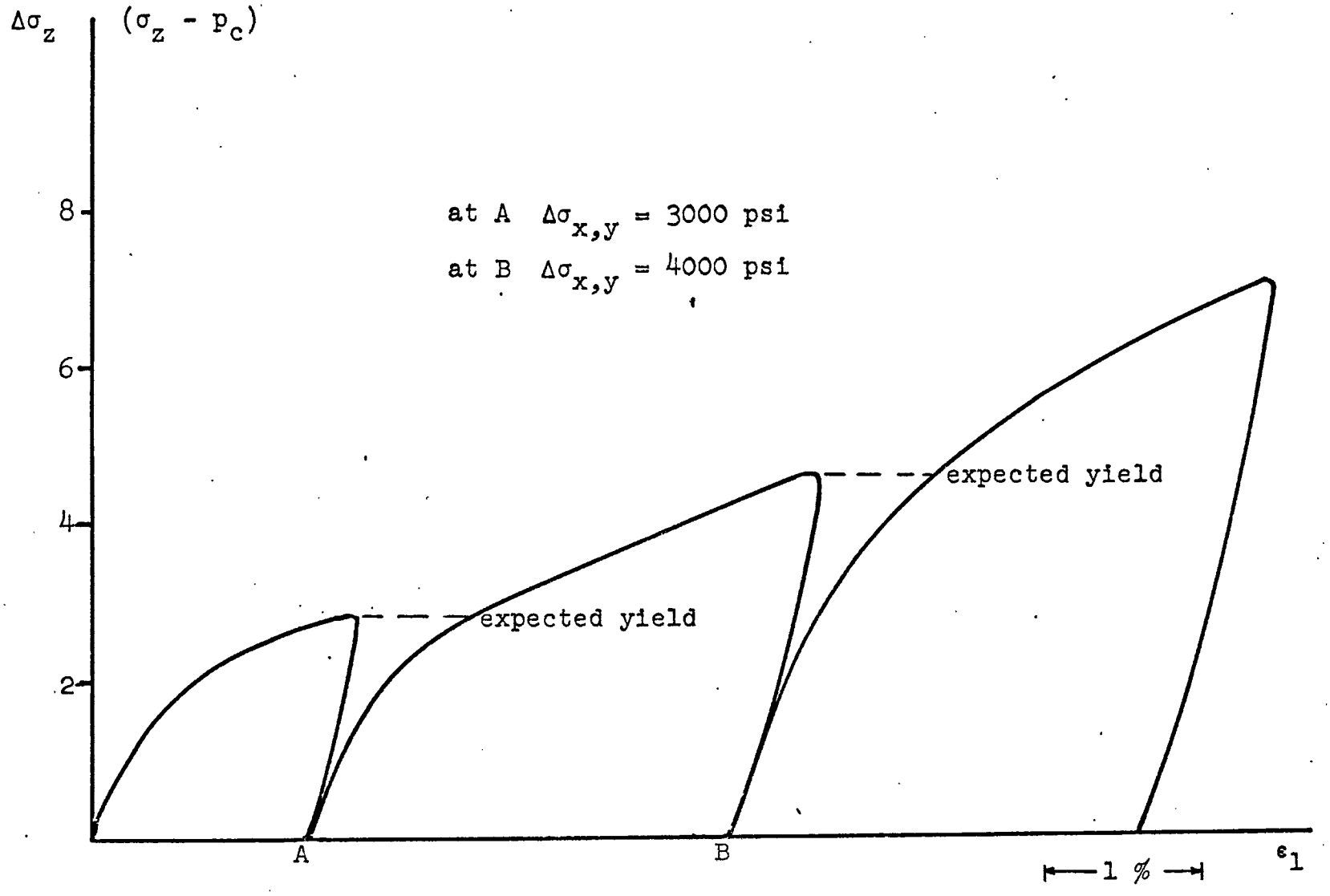

Figure IV - 27 Exploratory test for sample XI-3

one. At B, the x and y axes were loaded to $\Delta\sigma_{x,y}$ = 4000 psi and unloaded. Then a new conventional compression test was performed and the yield point obtained is lower than the expected one.

In the next section subsequent yield surfaces will be developed and the information obtained from all these sections and the next will be used to develop a model for a yield envelope.

Subsequent Yield Surfaces (Figures for this section are shown in Appendix D)

As described in Chapter III (figure III - 5), three different loading paths were used to obtain subsequent yield surfaces. For each loading path, three subsequent yield surfaces were obtained. The following procedure was performed to obtain the first set of subsequent yield surfaces :

(1) the material was loaded to a set differential axial stress ($\Delta\sigma_z$ = 3000 psi) at a confining pressure = 3000 psi and then it was unloaded ;

(2) Probing tests were performed to obtain more yield stress values in the same subsequent yield surface.

Changing $\Delta\sigma_z$ = 3000 psi to $\Delta\sigma_z$ = 4000 psi in step (1) above, a second subsequent yield surface was obtained. A third subsequent yield surface along this loading path was obtained by changing $\Delta\sigma_z$ = 3000 psi in step (1) above to $\Delta\sigma_z$ = 5000 psi.

Table V in Appendix A shows the computed yield stress

values from the probing tests for these first three subsequent yield surfaces.

Figures IV - 28 and IV - 29 show the probing tests for the first subsequent yield surface.

Figure IV - 30 shows the first subsequent yield surface plotted from the data obtained from the probing tests. It is shown in dark line.

In figures IV - 31 and IV - 32, the probing tests for the second subsequent yield surface can be seen. Figure IV - 33 shows this subsequent yield surface plotted. If we compare the plotted probing tests from the initial yield surface (figure IV - 4), the first subsequent yield surface ($\Delta\sigma_z = 3000$) (figure IV - 30) and this second subsequent yield surface ($\Delta\sigma_z = 4000$) (figure IV - 33), we can see that the distance between the intersection of the two surfaces that fall above the hydrostatic axis and the two surfaces that fall below it, is greater in the last test which is shown as AA' and BB' in figure IV - 33. It can be seen that this distance is not as large in figure IV - 30, and that in figure IV - 4 this distance does not exist. This means that the hardening path followed is inducing anisotropy (the difference between hydrostatic yield stress values for the vertical axis and the radial axis is becoming larger).

Figures IV - 34, IV - 35 and IV - 36 show the probing tests and the plotting for the third subsequent yield surface respectively.

Figure IV - 37 shows the superposition of the three

subsequent yield surfaces obtained using this first hardening path.

In figure IV - 34 the values for the confining pressures are :

Figure IV - 34a
1 = 1000
2 = 2000
3 = 3000
4 = 4000
5 = 5000
6 = 6000
7 = 7000
8 = 8000
9 = 9000
10 = 10000

Figure IV - 34b
1 = 7000
2 = 6000
3 = 5000
4 = 4000
5 = 3000
6 = 2000
7 = 1000

The first yield surface along the second path (as described in Chapter III, figure III - 5) was obtained by :

(1) Loading the material to a hydrostatic stress value above the yield stress ($\sigma_1 = \sigma_2 = \sigma_3 = 6000$)

(2) performing probing tests to obtain more yield stress values on the same subsequent yield surface.

By changing $\sigma_1 = \sigma_2 = \sigma_3 = 6000$ to $\sigma_1 = \sigma_2 = \sigma_3 = 7000$ in step (1) above, a second subsequent yield surface was obtained. A third subsequent yield surface along this hardening path was obtained by changing $\sigma_1 = \sigma_2 = \sigma_3 = 6000$ to $\sigma_1 = \sigma_2 = \sigma_3 = 8000$ in step (1) above.

Figures IV - 38, IV - 39 and IV - 40 show probing tests and plotting of first subsequent yield surface respectively.

Figures IV - 44, IV - 45 and IV - 46 show probing tests and plotting of third subsequent yield surface respectively.

Table 6 (Appendix A) shows computed yield stress values for all probing tests performed for this second set of subsequent yield surfaces. Figure IV - 47 shows the superposition of this three subsequent yield surfaces and the hardening path is shown.

It can be seen from figures IV - 40, IV - 43 and IV - 46 that this hardening path does not introduce anisotropy to the sample as it did in the previous hardening path.

Finally, a third set of subsequent yield surfaces was obtained. The first subsequent yield surface for this new hardening path was obtained by :

(1) loading the material to a set differential radial stress ($\Delta\sigma_2 = \Delta\sigma_3 = 3000$ psi) at a confining pressure = 3000 psi and then unloading it ;

(2) Performing probing tests to obtain more yield stress va-

lues in the same subsequent yield surface.

Changing $\Delta\sigma_2 = \Delta\sigma_3 = 3000$ psi to $\Delta\sigma_2 = \Delta\sigma_3 = 4000$ psi in step (1) above, a second subsequent yield surface was obtained.

Changing $\Delta\sigma_2 = \Delta\sigma_3 = 3000$ psi to $\Delta\sigma_2 = \Delta\sigma_3 = 5000$ psi in step (1) above, a third subsequent yield surface was obtained.

Figures IV - 48, IV - 49 and IV - 50 show probing tests and plotting of first subsequent yield surface respectively.

Figures IV - 51, IV - 52 and IV - 53 show probing tests and plotting of second subsequent yield surface respectively.

Figures IV - 54, IV - 55 and IV - 56 show probing tests and plotting of third subsequent yield surface respectively.

Computed yield stress values for all probing tests performed for this third set of subsequent yield surfaces are tabulated in Table 7.

Figure IV - 57 shows the superposition of this three subsequent yield surfaces and the hardening path is shown. It can be seen from figures IV - 50, IV - 53 and IV - 56 that this hardening path introduces anisotropy in the samples.

Figure IV - 58 shows a superposition of all the surfaces obtained.

Kinematic Model (Figures for this section are shown in Appendix D)

From the normality tests we observed that along a

loading path there was no rotation of the yield surface (strain-rate vectors stayed constant in slope). From the experiments for obtaining subsequent yield surfaces we could observe that the end cap does not grow but it displaces in the stress space. From figure IV - 58, we can see that anisotropy is developed upon loading along path 1 or path 3. From these experiments, it can be seen that hardening in the vertical axis does not influence the yield stress values in the z direction. All this happens when there is no large amount of hardening along one direction. If we analyze the experiments performed in section "Introduced Anisotropy", we see that, for small amount of hardening, the statement above is true, but we also see that a large amount of hardening in one direction produces a decrease in the yield stress values along the other direction. This fact leads the author to propose a closing of the end cap to create a yield envelope similar to an ellipsoid, which will behave as a kinematic model.

Figure IV - 59 shows the proposed yield envelope in the σ_1 vs. $\sqrt{2}\sigma_2$ plane.

Different tests were performed in order to obtain the shape of the low hydrostatic stress region of this model.

Figure IV - 60 shows the first of this type of tests. In this test and the following, capital letters will be designated for subsequent yield surfaces and numbers will be designated for each step along the loading paths. The surface A is the initial yield envelope, this surface was dis-

placed to the right by loading $\sigma_{2,3}$ in a conventional compression test at a p_c = 3000 and then unloading it (path 1, 2, 3, 4). A' is the new position of the yield surface ; by lowering the confining pressure to 1000 psi (path 4, 5) a new position B is obtained for the yield envelope.

Stress-strain curve 1 in the probing test (figure IV - 60a) corresponds to a conventional compression test where yield is immediate as it is also seen in the stress space path (figure IV - 60b). The maximum value for $\Delta\sigma_1$ is the distance that surface B displaces (path 5, 6). Our new surface new is C ; stress-strain curves 2, 3, 4 reach values that lay on the same surface (path 7, 8, 9 on figure IV - 60b). In stress-strain curve 5, it can be seen a yield point of 400 psi which corresponds to point ID in the stress space path. The maximum value of test 5 displaces the yield surface to 11. Test 6 shows an hydrostatic yield stress value a little higher than 1000 psi from a confining pressure of 5000 psi (point 12). This value corresponds to point 13 on surface D.

A second test is shown in figures IV - 61, IV - 62 and IV - 63. In figure IV - 62 the initial yield surface is designated by A.

In figures IV - 62 and IV - 61 point is at the confining pressure = 3000, at point 1 yield occurs in compression and surface A displaces to B where 2 is the maximum value of the stress in the conventional compression test ($\Delta\sigma_1$ at 2 = 3000 psi). The sample is unloaded at 3. An extension test is now

performed and at 4 we engage with the surface B and displace it until reaching the value for 5 ($\Delta\sigma_{2,3}$ = 3000) on surface C. The sample is unloaded to p_c = 3000 psi and then loaded on conventional compression, at 6 we engage with the surface C producing yielding ($\Delta\sigma_1$ at 6 = 23000 psi) and displace it to surface D (point 7) ($\Delta\sigma_1$ = 5500 psi) ; the sample is unloaded to confining pressure = 3000 psi again (8) and an extension test is performed, point 9 engages on surface D and displaces it to 10 (surface E) ($\Delta\sigma_{2,3}$ = 6000 psi). The sample is unloaded to p_c = 3000 psi and then reloaded on conventional compression test ; (11) engages surface E almost immediately producing yielding and displacing the yield surface to surface F (12) ($\Delta\sigma_1$ = 8400 psi). The sample is unloaded to p_c = 3000 (13). The loading path for this test is continued in figure IV - 63 where we start at point 13 and surface F. A conventional extension test is performed and at 14 yield occurs where surface F is engaged and displaced to surface G (point 15) ($-\Delta\sigma_1$ = 2000). Then the sample is loaded back to p_c = 3000 and then unloaded hydrostatically to p_c = 1000 psi, at 16 surface G is reached and displaced to surface H to obtain p_c = 1000 (17). At 17 a conventional compression test is performed and at 18 we reach the same surface H. The sample is unloaded to p_c = 1000 and then loaded to p_c = 3000 (19). A conventional compression test is performed and again we hit surface H at 20. The sample is unloaded to p_c = 3000 and loaded to p_c = 4000 (21). Another conventional compression test is performed, at 22

surface H is engaged producing yielding ($\Delta\sigma_1$ = 4200 psi) and it is displaced to surface I (point 23). The sample is unloaded to p_c = 4000 and loaded to p_c = 5000 (point 24). Again a conventional compression test is performed and the surface I is reached at 25 producing yielding ($\Delta\sigma_1$ = 6000 psi).

A third test is shown in figures IV - 64, IV - 65 and IV - 66. In figure IV - 65, the initial yield surface is designated by A_o. At 0 (p_c = 3000 psi) on figures IV - 64 and IV - 65 a conventional compression test is performed, point 1 ($\Delta\sigma_1$ = 2500 psi) engages the initial surface A_o producing yield and displaces the surface A_o to A at point 2 ($\Delta\sigma_1$ = 3000 psi), then the sample is unloaded to p_c = 3000 (point 3). An extension test is now performed and at 4 (surface A) yield occurs until reaching surface B at 5. The sample is unloaded back to p_c = 3000 and a conventional compression test is performed ; surface B is engaged at 6 ($\Delta\sigma_1$ = 2500 psi), producing yield and it is displaced till point 7 ($\Delta\sigma_z$ = 5000) (surface C). The sample is unloaded to p_c = 3000 (8) and an extension test is again performed at point 9 the surface C is engaged and displaced till point 10 ($\Delta\sigma_{2,3}$ = 5000 psi) on surface D. The sample is unloaded to p_c = 3000 and a conventional compression test is performed. The surface D is engaged at 11 ($\Delta\sigma_1$ = 1000 psi) and yield occurs.

In figure IV - 66, the representation of this test in stress space is continued. The surface D is displaced to reach point 12 ($\Delta\sigma_1$ = 2500 psi) (surface E). The sample is

unloaded to p_c = 3000 psi and p_c is daised to p_c = 4000 (13), a conventional compression test is performed and surface E is engaged at 14 ($\Delta\sigma_1$ = 2500 psi) and yield occurs till 15 (surface F) ($\Delta\sigma_1$ = 3500). The sample is then unloaded to p_c = 4000 psi and p_c is now lowered to p_c = 3000 psi to perform another conventional compression test ; at point 16 we reach the same surface F ; the sample is unloaded to p_c = 3000 and this p_c is changed to p_c = 1000 (point 17); a conventional compression test is performed and at 18 the surface F is engaged producing yielding ($\Delta\sigma_1$ = 2800 psi) and displacing this surface till point 19 ($\Delta\sigma_1$ = 5000 psi) on surface G ; the sample was unloaded to p_c = 1000 and a hydrostatic test was performed giving a yield stress σ_1 = σ_2 = σ_3 = 8000 which coincides with point 21 on surface G.

Figure IV - 67 shows the last experiment performed to verify the kinematic model proposed. The loading paths are shown in figures IV - 68 and IV - 69. Before starting the test, the sample was loaded to a very high hydrostatic pressure sliding our yield envelope to the position held by the surface A. At p_c = 1000 psi (point 11) a conventional compression test was performed. Surface A is displaced to point 2 (surface B). The sample was unloaded to p_c = 1000 and this p_c was increased to p_c = 2000 (point 3) ; another conventional compression test was performed and the surface B was engaged (point 4) producing yield at $\Delta\sigma_1$ = 4000 psi, and it was displaced till point 5 ($\Delta\sigma_1$ = 5000 psi) on surface C. The sample was unloaded to p_c = 2000 psi and the

confining pressure was increased to p_c = 3000 psi (point 6) ; another conventional compression test was performed causing yielding when surface C was reached ($\Delta\sigma_1$ = 6000 psi) (point 7) and it was displaced till point 8 on surface D.

The loading path in stress space is continued in figure IV - 69. From 8 the sample is unloaded to p_c = 3000 and this p_c is lowered to p_c = 1000 psi, for which the surface D is engaged at 9 and is displaced to point 10 on surface E ; at 10 a conventional extension test was performed ; point 11 shows immediate yielding and a new surface at $-\Delta\sigma_1$ = 1000 psi (point 12) is reached (surface F). The sample was loaded back to p_c = 1000 psi and this p_c was raised to 2000 psi (point 13) ; another conventional extension test was performed hitting the surface F at point 14, producing yield ($-\Delta\sigma_1$ = 1500 psi) ; the surface reached point 15 on surface G ($-\Delta\sigma_1$ = 2000 psi). The sample was reloaded back to p_c = 2000 psi ; this p_c was raised to p_c = 3000 psi (point 15) ; another conventional extension test was performed, surface G was reached at point 17 ($-\Delta\sigma_1$ = 2100 psi) producing yield. This surface was displaced till $-\Delta\sigma_1$ = 3000 psi which corresponds to point 18 on surface H. The sample was again reloaded back to the hydrostatic axis and p_c was raised now to p_c = 4000 psi (point 19). Another conventional extension test was performed reaching surface H at $-\Delta\sigma_1$ = 3000 psi (point 20) which was displaced till point 21 on surface I ($-\Delta\sigma_1$ = 3200 psi). The sample was loaded back to p_c = 4000 psi and this confining pressure was raised

till p_c = 5000 psi (point 22). A conventional extension test was performed and surface I was reached on point 23.

From the previous four tests described, it can be seen that a kinematic model for the yield envelope of a Cordova limestone is the most appropriate description of its behavior.

V. SUMMARY AND CONCLUSIONS

In order to obtain a good description of the plastic behavior of a general type of material that compacts or shows a volume decrease as it undergoes permanent deformation and exhibit yield strength dependence upon hydrostatic pressure, an experimental study was initiated on Cordova limestone.

Three major investigations were made for this purpose. The first of them was to obtain an initial yield surface and experimentally verify the principle of normality. The experimental data showed normality to be a very good approximation for the actual plastic strains produced by the initial yielding of the material studied.

For different loading paths as hardening took place we could see that the strain-rate vectors stayed constant in slope, which confirms the fact of a non-growing or a non-rotating yield surface.

The second purpose was to study the induced anisotropy due to hardening ; we could see that a small amount of hardening along one axis did not influence the yield stress values along the other axes, but as hardening became larger these yield stress values decreased. This second set of experiments provided data sufficient to close the yield envelope.

The third purpose was to obtain a hardening rule for our yield envelope model that would satisfy the conditions obtai-

ned from the first two investigations ; four different tests were performed in order to verify the shape of the low hydrostatic stress region of this model and it was found that our model could displace in the stress space without changing its shape ; this shows that a kinematic hardening rule would complete the description of the plastic behavior of a limestone.

This study has been an attempt to describe the behavior of materials that compact as they undergo permanent deformation and exhibit yield strength dependence upon hydrostatic pressure, by constructing a yield envelope and proposing a hardening rule that would satisfy the presence of induced anisotropy due to hardening.

The proposed yield envelope and the kinematic hardening rule for it have accomplished this purpose, and their use should advance knowledge about the plastic behavior of these materials.

The author suggests for future work to obtain a complete description of this model and its behavior in a 3 dimensional stress space. For this purpose some modifications of the equipment are suggested in Appendix B.

REFERENCES

1. D.C. Drucker, "A More Fundamental Approach to Plastic Stress-Strain Relations", Proc. 1st U.S. Natl. Congr. Appl. Mech., ASME, pp. 487-491, 1951.

2. G.D.J. De Jong, "Graphical Determination of Slipline Patterns in Soil Mechanics", De Ingenieur, V 29, pp. 61-65, 1957.

3. L. Barden, A.J. Khayatt, "Incremental Strain Rate Ratios and Strength of Sand in the Triaxial Test", Geotechnique, V 16, No.4, pp. 338-357, 1966.

4. A.W. Jenike, R.T. Shield, "On the Plastic Flow of Coulomb Solids Beyond Original Failure", J. Appl. Mech., pp. 599-602, 1959.

5. L.E. Malvern, Introduction to the Mechanics of a Continuous Medium, Prentice-Hall Inc., Englewood Cliffs, New Jersey, 1969.

6. J.L. Sanders, "Plastic Stress-Strain Relations based on Linear Loading Functions", Proc. 2nd U.S. Natl. Congr. Appl. Mech., ASME, pp. 455-460, 1954.

7. D.C. Drucker, "Path Independence and Material Stability for Soils", IUTAM Symp. of Rheology and Soil Mech., Grenoble, pp. 23-43, 1964.

8. F. Stassi D'Alia, "Limiting conditions of Yielding for Anisotropic Materials", Meccanica, pp. 349-363, Dec 1969.

9. Y.G. Fung, Foundations of Solid Mechanics, Prentice-Hall Inc., Englewood Cliffs, New Jersey, 1965.

10. William Prager, "The Theory of Plasticity : A Survey of Recent Achievements", James Clayton Lecture, London, Jan 14th 1955.

11. Hans Ziegler, "A Modification of Prager's Hardening Rule", Quar. Appl. Math. 17, pp. 55-65, 1959.

12. Naghdi, P.M., Essenburg, F., and Koff, W., "An Experimental Study of Initial and Subsequent Yield Surfaces in Plasticity", J. Appl. Mech. V 25, pp. 201-209, 1958.

13. Naghdi, P.M., 1960, "Stress-Strain Relations in Plasticity and Thermoplasticity", in "Plasticity" edited by E,H, Lee and P.S. Symonds, Pergamon Press, N.Y., pp. 121-169.

14. Naghdi P.M., J.A. Trapp, "On the Nature of Normality of Plastic Strain Rate and Convexity of Yield Surfaces in Plasticity", Journal of Appl. Mech., March 1975, pp. 61-66.

15. R.T. Shield, H. Ziegler, "On Prager's Hardening Rule", Z. Ang. Math. and Phys., 1958, pp. 260-276.

16. William Prager, "Models of Plastic Behavior", Proc. U.S. Natl. Congr. Appl. Mech., pp. 435-449, 1966.

17. Avolge, P.G., 1957, "A General Theory of Piecewise Linear Plasticity Based on Shear", J. Mech. Phys. Solids, 5, pp. 242-260.

18. D.C. Drucker, R.E. Gibson, D.J. Henkel, "Soil Mechanics and Workhardening Theories of Plasticity", Trans. ASCE, V. 122, pp. 338-346, 1957.

19. J.B. Cheatham, Jr., "Strain Hardening of a Porous Limestone", Jour. S.P.E. of AIME, Sept. 1967, pp. 229-234.

20. T.W. Miller, "A Consistent Workhardening Theory for Porous Limestone", Unpublished Ph.D. Thesis, M.E. Dept. Rice University, 1970.

21. M.B. Smith, "A Parabolic Yield Condition for Anisotropic Rocks and Soils", Unpublished Ph.D.Thesis, M.E. Dept. Rice University, 1974.

APPENDIX A

TABLE I (sample IV - a - 1)

Computed Strain Values for test in Figure IV - 5

Hydrostatic yield point = 5050 psi

Maximum hydrostatic pressure = 7600 psi = p_c

$-\Delta\sigma_z$ = vertical stress - p_c

	$-\Delta\sigma_z$	$-\epsilon_x$, %	$-\epsilon_y$, %	$-\epsilon_z$, %	$\Sigma\epsilon$, %	$\Delta\Sigma\epsilon$, %
	0	.58	.65	1.98	3.21	0
	.55	.55	.61	2.0	3.16	- .03
	.84	.56	.61	1.98	3.15	- .01
	1.28	.58	.64	1.92	3.14	- .01
	1.7	.57	.64	1.88	3.09	- .05
	2.21	.57	.64	1.82	3.03	- .06
	2.71	.58	.65	1.74	2.97	- .06
	3.15	.58	.67	1.67	2.92	- .05
	3.62	.55	.69	1.62	2.86	- .06
	4.12	.54	.7	1.53	2.77	- .09
A{	4.51	.61	.71	1.43	2.75	- .02
B{	4.82	.66	.73	1.35	2.74	- .01
C{	5.18	.7	.81	1.22	2.73	- .01

TABLE I (continued)

	$-\Delta\sigma_z$	$-\epsilon_x$, %	$-\epsilon_y$, %	$-\epsilon_z$, %	$\Sigma\epsilon$, %	$\Delta\Sigma\epsilon$, %
D {	5.31	.71	.87	1.11	2.69	- .04
	5.4	.79	1.05	.9	2.74	.05
	5.28	1.0	1.29	.51	2.8o	.06
	5.32	1.1	1.49	.25	2.84	.04
	5.28	1.29	1.68	- .05	2.92	.04
	5.28	1.35	1.82	- .2	2.97	.05
	5.31	1.43	1.9	- .38	2.95	.02
	5.31	1.5	1.99	- .5	2.99	.04
	5.31	1.7	2.21	-1.0	2.91	- .08
	5.29	2.12	2.6	-1.7	3.02	.11
	5.3	2.91	3.31	-3.1	3.12	.1
	5.3	3.92	4.07	-4.66	3.33	.21
	5.3	4.61	4.6	-5.68	3.53	.20
	5.3	5.1	5.05	-6.52	3.63	.1
	5.21	5.8	5.6	-7.8	3.6	- .03
	5.2	6.5	6.1	-8.95	3.65	.05
	5.21	7.25	6.35	-10.22	3.38	- .27
	5.21	7.91	6.45	-11.41	2.95	- .43
	5.3	8.6	6.61	-12.82	2.39	- .56
	5.3	9.31	6.7	-14.35	1.66	- .73
E {	5.5	9.9	6.71	-15.88	0.73	- .93
	4.05	11.05	6.85	-19.15	1.25	-1.98
	4.1	11.26	7.05	-19.70	1.39	- .14

TABLE 2 (sample V - d)

Computed Strain Values for Test on Figure IV - 6

Hydrostatic pressure = 2300 psi = p_c

$\sigma_2 = \sigma_3 = 7600$

$-\Delta\sigma_z = (\sigma_z - p_c)$

	$-\Delta\sigma_z$	$-\epsilon_x$, %	$-\epsilon_y$, %	$-\epsilon_z$, %	$\Sigma\epsilon$, %	$\Delta\Sigma\epsilon$, %
	0	.31	.32	.53	1.16	0
	.03	.33	.36	.53	1.22	.06
	.03	.37	.38	.52	1.27	.05
	.01	.40	.41	.53	1.34	.07
A {	.03	.42	.42	.52	1.36	.02
	.04	.42	.49	.52	1.43	.07
	.08	.48	.55	.51	1.54	.11
	.1	.50	.55	.48	1.53	- .01
	.1	.54	.59	.52	1.65	.12
	.09	.6	.61	.51	1.72	.07
	.1	.63	.65	.5	1.78	.06
	.11	.7	.72	.5	1.92	.14
	.16	.76	.82	.42	2.00	.08
	.17	.87	.92	.41	2.20	.20
	.15	.89	.91	.4	2.20	0
	.15	.88	.90	.41	2.19	.19

TABLE 2 (continued)

	$-\Delta\sigma_z$	$-\epsilon_x$, %	$-\epsilon_y$, %	$-\epsilon_z$, %	$\Sigma\epsilon$, %	$\Delta\Sigma\epsilon$, %
	.16	.92	.93	.41	2.26	.07
	.22	1.07	1.04	.36	2.47	.21
	.26	1.06	1.1	.32	2.48	.01
	.16	1.07	1.11	.3	2.48	0
B	.06	1.07	1.11	.22	2.40	- .08
B	0	1.2	1.22	.1	2.52	.12
	.04	1.25	1.31	0	2.56	.04
	.06	1.41	1.49	- .1	2.8	.24
	0	1.56	1.58	- .25	2.89	.09
C	0	1.61	1.72	- .4	2.93	.04
C	.10	1.80	1.88	- .59	3.09	.16
	.06	1.94	1.96	- .72	3.18	.09
	.1	2.1	2.13	- .91	3.32	.14
	.1	2.31	2.35	-1.21	3.45	.13
	.06	2.41	2.42	-1.41	3.42	- .03
	.05	2.55	2.56	-1.6	3.51	.09
	.03	2.7	2.72	-1.79	3.63	.12
D	- .02	3.1	3.12	-2.5	3.72	.09
D	- .05	3.49	3.46	-3.0	3.95	.23
	- .09	4.1	4.06	-4.07	4.69	.14
	- .1	4.39	4.66	-5.18	3.87	- .22
	- .07	4.85	5.26	-6.92	3.19	- .68
	- .09	5.25	5.72	-8.68	2.29	- .90

TABLE 2 (continued)

	$-\Delta\sigma_z$	$-\epsilon_x$, %	$-\epsilon_y$, %	$-\epsilon_z$, %	$\Sigma\epsilon$, %	$\Delta\Sigma\epsilon$, %
E {	- .09	5.25	5.72	- 8.68	2.29	0
	- .16	5.81	6.3	-11.0	1.11	- 1.18
	- .16	6.56	6.6	-13.05	.11	- 1.0
	- .29	7.52	6.65	-15.03	- .86	- .97
F {	- .23	8.16	6.7	-15.6	- .74	.12
	- .20	8.7	6.7	-16.36	- .96	.22
	- .16	9.35	6.71	-16.55	- .49	.47
	- .19	9.55	6.75	-16.57	- .27	.22

TABLE 3

Computed Strain Values for Test in Figure IV - 7

Confining pressure = 2.17 = p_c

$\Delta \sigma_x = \Delta \sigma_y = \sigma_x - p_c$

	$\Delta \sigma_x$	$-\Delta\epsilon_x$, %	$-\Delta\epsilon_y$, %	$-\Delta\epsilon_z$, %	$\Sigma\epsilon$, %	$\Delta\Sigma\epsilon$, %
	.25	.23	.66	.23	1.12	.03
	.98	.36	.8	.22	1.38	.26
	1.79	.39	.97	.2	1.56	.18
	2.36	.43	1.08	.18	1.69	.13
	2.7	.49	1.13	.18	1.80	.11
	3.02	.53	1.2	.16	1.89	.09
	3.78	.63	1.37	.08	2.08	.19
	4.23	.82	1.6	.03	2.45	.37
A {	4.49	1.21	2.04	- .37	2.88	.43
	4.68	1.44	2.27	- .4	3.31	.43
	4.88	1.81	2.6	- .68	3.73	.42
	4.99	2.26	3.05	-1.05	4.26	.53
	4.99	2.82	3.6	-1.53	4.89	.63
	5.19	3.31	4.1	-2.0	5.41	.52
B {	5.29	3.67	4.48	-2.4	5.75	.34
	5.46	3.98	4.81	-2.68	6.11	.36

TABLE 3 (continued)

	$\Delta \sigma_x$	$-\Delta\epsilon_x$, %	$-\Delta\epsilon_y$, %	$-\Delta\epsilon_z$, %	$\Sigma\epsilon$, %	$\Delta\Sigma\epsilon$, %
	5.50	4.32	5.15	- 3.07	6.40	.29
	5.68	4.8	5.64	- 3.57	6.87	.47
	5.79	5.15	6.0	- 4.0	7.15	.28
	5.98	5.4	6.26	- 4.22	7.44	.29
C {	6.19	5.82	6.62	- 4.6	7.84	.40
	6.90	6.38	7.08	- 5.22	8.24	.40
	6.50	6.82	7.43	- 5.77	8.48	.24
	6.56	7.48	8.0	- 6.6	8.88	.40
	6.65	7.98	8.37	- 7.2	9.15	.27
	6.78	8.5	8.8	- 7.82	9.48	.33
	6.98	9.1	9.25	- 8.57	9.78	.30
	7.18	9.72	9.65	- 9.3	10.07	.29
	7.43	10.45	10.03	-10.0	10.48	.41
	7.73	11.22	10.39	-10.73	10.88	.40
	8.01	12.0	10.63	-11.41	11.22	.34

TABLE 4 (sample V - b)

Computed Strain Value for Extension Test on Figure IV - 15

Confining pressure = 2520 psi = p_c

$\Delta \sigma_y = \sigma_y - p_c = \sigma_2 - p_c$; $\sigma_y = \sigma_x$

	$\Delta \sigma_y$	$-\epsilon_x$, %	$-\epsilon_y$, %	$-\epsilon_z$, %	$\Sigma\epsilon$, %	$\Delta\Sigma\epsilon$, %
	0	.31	.46	.21	.98	0
	.3	.3	.48	.21	.99	.01
	.71	.36	.6	.2	1.16	.17
	1.4	.42	.71	.18	1.31	.15
	1.91	.46	.8	.18	1.44	.13
	2.45	.52	.91	.18	1.61	.17
	2.88	.53	1.0	.16	1.69	.08
	3.32	.61	1.08	.11	1.80	.11
	3.1	.65	1.19	.1	1.94	.14
	4.0	.61	1.29	.09	1.99	.05
	4.1	.68	1.31	.09	2.68	.09
	4.47	.77	1.36	.09	2.22	.14
	4.85	.81	1.5	.02	2.33	.11
	5.12	1.0	1.61	- .12	2.49	.16
	5.32	1.18	1.85	- .23	2.80	.31
	5.46	1.56	2.3	- .51	3.35	.55
A_1 {	5.5	2.05	2.82	- .96	3.91	.56

TABLE 4 (continued)

	$\Delta \sigma_y$	$-\epsilon_x$, %	$-\epsilon_y$, %	$-\epsilon_z$, %	$\Sigma\epsilon$, %	$\Delta\Sigma\epsilon$, %
	5.6	2.55	3.31	- 1.42	4.44	.53
A_2	5.71	3.05	3.72	- 1.91	4.86	.42
	5.95	3.76	4.4	- 2.6	5.56	.70
A_3	6.31	4.55	5.17	- 3.48	6.24	.68
B	6.75	5.35	5.91	- 4.39	6.87	.63
C	7.15	5.91	6.95	- 6.0	6.86	- .01
D	7.65	6.72	8.9	- 8.89	6.73	- .13
E	8.35	7.48	10.5	-11.81	6.17	- .56
	8.4	7.9	10.85	-12.6	6.15	- .02

TABLE V (samples XII)

Computed yield stress values from probing tests

for $\Delta \sigma_z$ = 3000, 4000, 5000 psi

Conventional Compression (σ_1/ϵ_1) p_c	$\Delta \sigma_z$ = 3000 yield stress (psi) sample XII-a-1	$\Delta \sigma_z$ = 4000 yield stress (psi) sample XII-b-1	$\Delta \sigma_z$ = 5000 yield stress (psi) sample XII-c-1
1000	3300	3900	4550
2000	3500	4200	4600
3000	3500	4200	5100
4000	3000	3700	5100
5000	2600	3700	4000
6000	2300	2600	3600
7000		2700	3100
8000	hydr. from 6000 psi = 1700	1200	2200
9000			2100
10000			1500

p_c	sample XII-a-2	sample XII-b-2	sample XII-c-2
7000	hydr. from 5000 psi = 500	hydr. from 5000 psi = 1600	1400
6000			3650
5500		3100	
5000	1300	3000	5450
4000	2700	3900	6800
3000	3750	5400	7700
2000	4300	6400	7900
1000	4200	5650	5900

Extension

$\sigma_{2,3}/\epsilon_{2,3}$

p_c	yield stress (psi) sample XII-a-3	yield stress (psi) sample XII-b-3	yield stress (psi) sample XII-c-3
1000	1850	1800	1700
2000	1750	1800	1800
3000	1450	1500	1500
4000	1100	1100	1200
5000	600	600	1000
	hydr. from 5000 psi = 950	hydr. from 5000 psi = 800	hydr. from 5000 psi = 950

p_c	sample XII-a-4	sample XII-b-4	sample XII-c-4
5000	750	600	750
4000	1500	1400	1300
3000	2450	2350	2250
2000	3200	3250	2950
1000	3900	3950	3600
	hydr. from 5000 psi = 600	hydr. from 5000 psi = 400	hydr. from 5000 psi = 550

TABLE VI (samples X)

Computed yield stress values from probing tests

for $\sigma_1 = \sigma_2 = \sigma_3$ = 6000, 7000, 8000 psi

Conventional Compression (σ_1/ϵ_1)	a = 6000	b = 7000	c = 8000
p_c	yield stress (psi)	yield stress (psi)	yield stress (psi)
	sample X - 9	sample X - 13	sample X - 17
1000	2800	3200	3600
2000	3200	3650	3900
3000	2950	3600	4100
4000	2850	3150	4300
5000	2200	2950	4200
6000	2150	2550	4000
7000	1900	2350	3500
8000	1700	1700	3500
9000	1500	1500	3000
10000	1200	1200	3100
11000		1600	2400
12000		2000	2000

p_c	sample X - 10	sample X - 14	sample X - 18
8000			500
7500			800
7000		650	1200
6500		1350	1800
6000	400	2000	2300
5500	900		
5000	1600	2900	3150
4500	2200		
4000	2700	3850	3700
3500			
3000	3650	4700	4400
2000	4050	4800	4500
1000	4000	4600	4500

Extension

$\sigma_{2,3}/\epsilon_{2,3}$

pc	a = 6000	b = 7000	c = 8000
	yield stress (psi)	yield stress (psi)	yield stress (psi)
	sample X - 11	sample X - 15	sample X - 19
2000	3000	3900	4600
2500	3300		
3000	3200	4200	4700
4000	3100	4100	4400
5000	3000	3700	4100
6000	2500	3400	3600
7000	2350	3500	3600
8000	2300	3500	3300
9000	2300	3650	3200
10000		2750	2900
11000		3100	2600
12000		2000	1900

p_c	sample X - 12	sample X - 16	sample X - 20
8000			200
7500			800
7000		300	1500
6500		900	2100
6000	100	1300	2800
5500	800	2000	
5000	1400	2700	3750
4500	2350		
4000	3200	3700	4700
3000	4100	4700	5800
2000	4650	5300	6900
1000	5100	5400	6700

TABLE VII (samples XI)

Computed yield stress values from probing tests

for $\Delta \sigma_{x,y}$ = 3000, 4000, 5000 psi

Conventional Compression (σ_1/ϵ_1)	$\Delta \sigma_{2,3}$ = 3000	$\Delta \sigma_{2,3}$ = 4000	$\Delta \sigma_{2,3}$ = 5000
	yield stress (psi)	yield stress (psi)	yield stress (psi)
	sample XI-a-1	sample XI-b-1	sample XI-c-1
1000	2200	1900	1600
2000	2300	2250	2200
3000	1950	1900	2000
4000	1200	1700	1600
5000	600	1100	1100
6000	400	700	
	hydr. from 6000 psi = 500	hydr. from 5000 psi = 1100	hydr. from 5000 psi = 1300
p_c	sample XI-a-2	sample XI-b-2	sample XI-c-2
5000	450	500	450
4000	1300	1300	1300
3000	2100	2250	2000
2000	2800	2950	2750
1000	3300	3200	3100
	hydr. from 5000 psi = 300	hydr. from 5000 psi = 300	hydr. from 5000 psi = 350

Extension

$\sigma_{2,3}/\epsilon_{2,3}$

p_c	yield stress (psi)	yield stress (psi)	yield stress (psi)
	sample XI-a-3	sample XI-b-3	sample XI-c-3
1000	4450	4800	5300
2000	4250	4800	5900
3000	3500	4550	5800
4000	3200	4200	4900
5000	2500	3800	4700
6000	2100	3000	4300
7000	1400	1700	4000
8000	650	1100	2600
	hydr. from 8000 psi = 900	hydr. from 9000 psi = 2100	hydr. from 8000 psi = 4000
p_c	sample XI-a-4	sample XI-b-4	sample XI-c-4
6000			2700
5000	1300	2600	4000
4000	2800	4050	5600
3000	4000	5150	6900
2000	4700	5600	7100
1000	5350	6000	7600
	hydr. from 5000 psi = 900	hydr. from 5000 psi = 800	hydr. from 5000 psi = 2900

APPENDIX B

In order to be able to construct a tri-dimensional yield envelope for transversely isotropic material, stress-strain curves for the vertical axis and for one horizontal axis are needed.

Load Cell

For the purpose above described, the substitution of one horizontal hydraulic ram by a load cell is suggested.

Figure B - 1 shows the details and dimension of the possible load cell to be installed.

Figure B - 2 shows the electrical setting for the current load cell.

For obtaining stress-strain curves for the horizontal axis the Wheatstone bridge output for the new load cell and displacement transducer should be connected to an X-Y recorder. The calibration procedure used for the X-Y recorder connected to the vertical axis is next described.

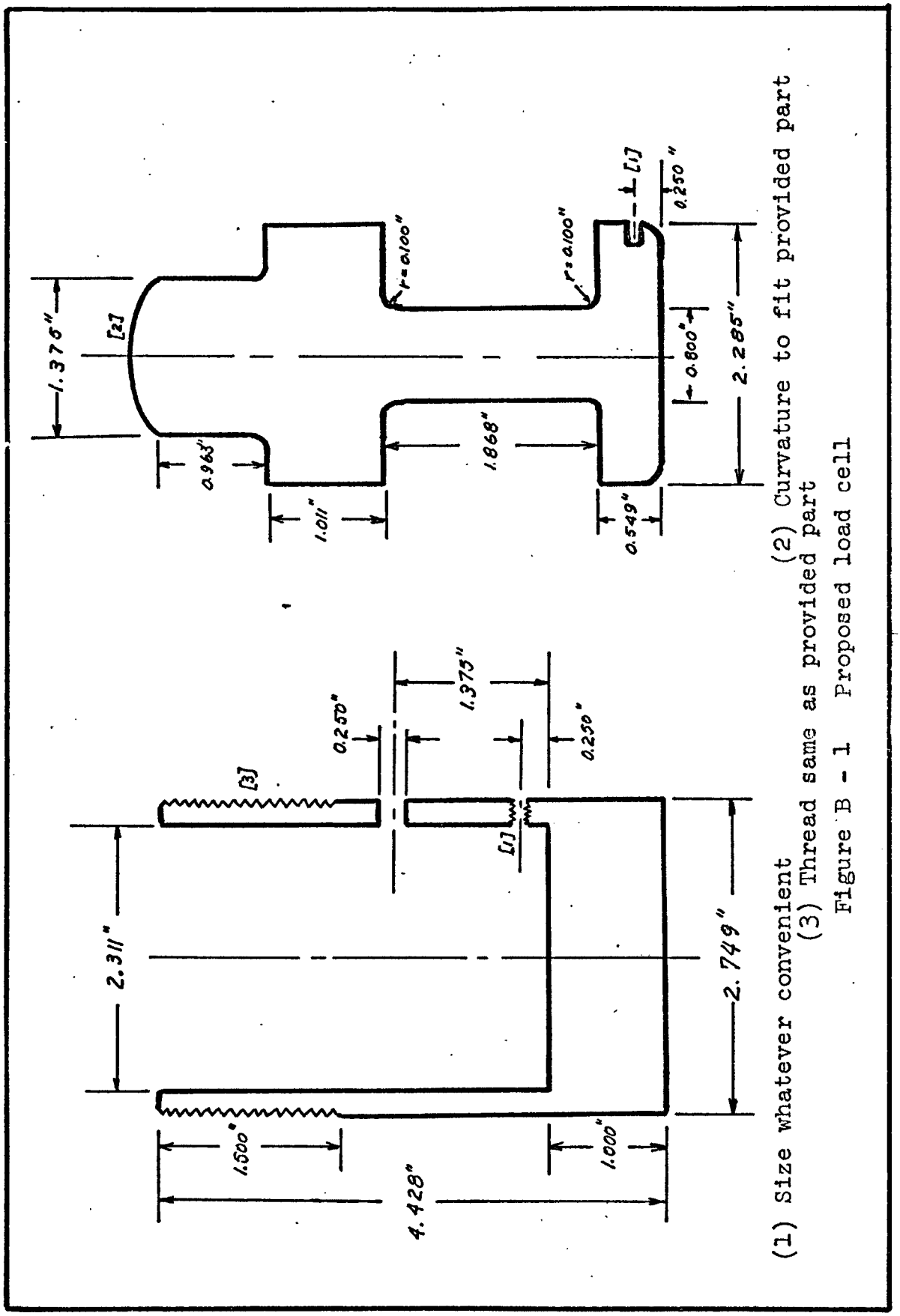

(1) Size whatever convenient
(2) Curvature to fit provided part
(3) Thread same as provided part

Figure B - 1 Proposed load cell

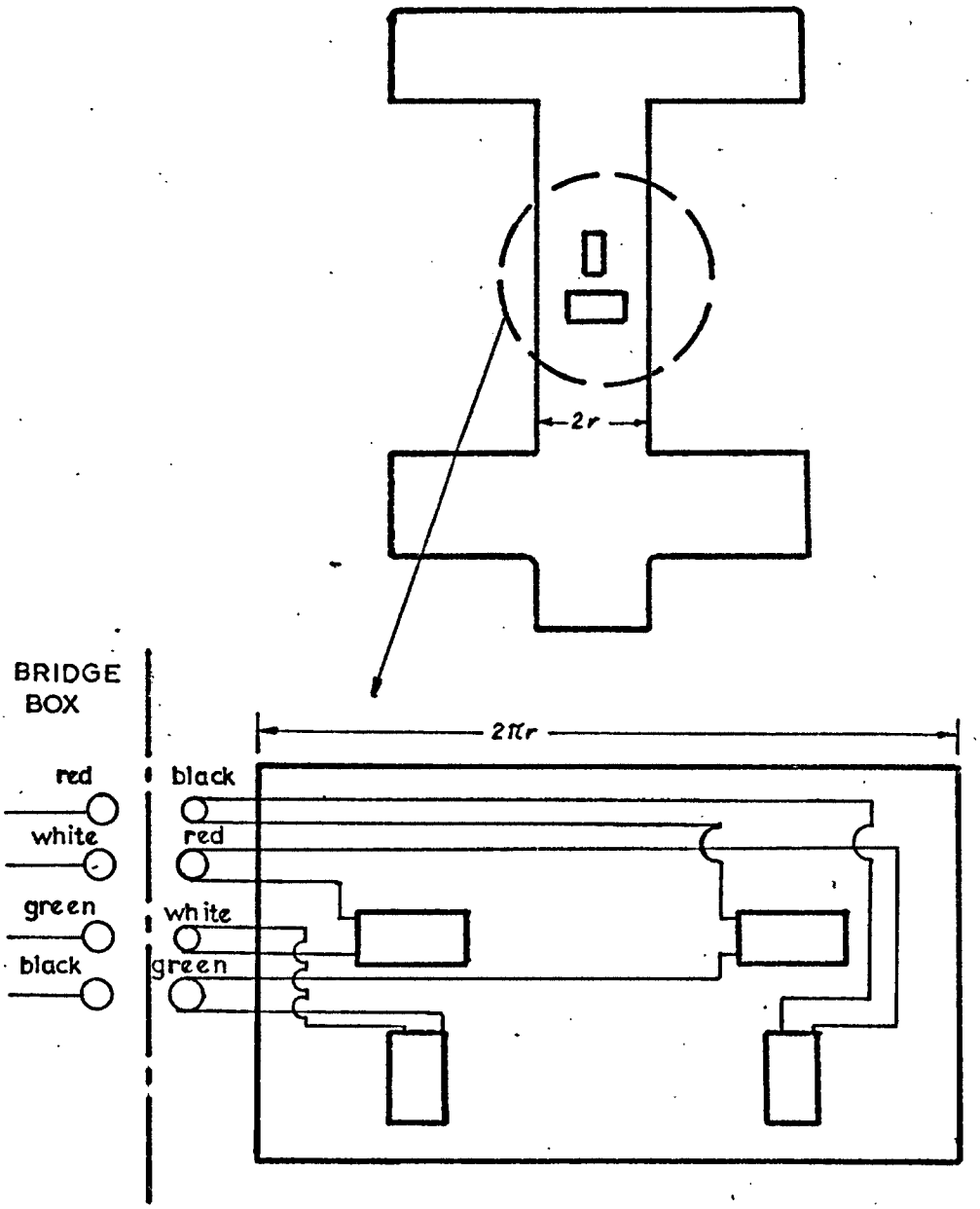

Figure B - 2 Strain gages in load cell

Calibration of X-Y Recorder

A steel sample was loaded up to 12500 psi ; every 1000 psi measurements of the voltage output from the load cell output were made obtaining the following table :

Stress psi	
1500	2.18 mv
2500	2.30 mv
3500	2.43 mv
4500	2.55 mv
5500	2.67 mv
6500	2.78 mv
7500	2.92 mv
8500	3.04 mv
9500	3.17 mv
10500	3.28 mv
11500	3.39 mv
12500	3.52 mv

From this table a scale factor for the stress-measurement was obtained (2000 psi = 1 inch on X-Y recorder)

$$\text{scale factor} = \frac{1.34}{11500}\ \frac{\text{mv}}{\text{psi}} = \frac{1.34}{5.75 \times (2000)}\ \frac{\text{mv}}{\text{psi}} =$$

$$= \frac{1.34\ \text{mv}}{5.75\ \text{inch}} = 0.23\ \frac{\text{mv}}{\text{inch}}$$

The same steel sample was loaded again and readings of strain measurements with a dial indicator and readings of the

voltage output from the displacement transducers were made obtaining the following scale :

% strain	
0.0	1.90 mv
0.1	1.88 mv
0.2	1.86 mv
0.3	1.85 mv
0.4	1.83 mv
0.5	1.81 mv
0.6	1.80 mv
0.7	1.78 mv
0.8	1.7 mv

From this table a scale factor for the strain measurements was obtained (2 % strain = 1 inch on X-Y recorder)

$$\text{scale factor} = \frac{0.12}{0.7}\ \frac{\text{mv}}{\%\ \text{strain}} = .17\ \frac{\text{mv}}{\%} = .34\ \frac{\text{mv}}{\text{in.}}$$

Calibration before starting tests :

(1) Warm up X-Y recorder and voltmeter ;

(2) Hook up voltage source to both x and y axes (it could be a battery with a potentiometer). Attach voltmeter to measure voltage. (Remember input is the same for x and y axes) ;

(3) Draw some lines and adjust gain on x and y axes using 5 and 1 milivolts ;

a) almost horizontal lines for gain in x axis ;

b) 45^{o} lines ;

c) almost vertical for gain in y axis.

(4) Calibrate x and y axes to appropriate values.

Example :

In figure B - 3a, we see a starting position ; using 1.8 mv inch for both axes we get a diagonal line from 0 to 16.2 mv (reading on voltmeter) and we should get the final position shown in figure B - 3b.

This calibration corresponds to :

$2000 \frac{psi}{in.}$ in y axis

2 % strain in x axis

if sweep went too far, turn knob to left slightly (this applies for both axes) until you get the appropriate reading.

Comments :

Turn servo switch off before turning calibration knob.

(5) Hook up displacement and force leads.

In order to get smooth stress-strain curves, it is convenient to use a Ruska pump connected with the ram where the load cell will be installed, this will allow to control a constant stress rate.

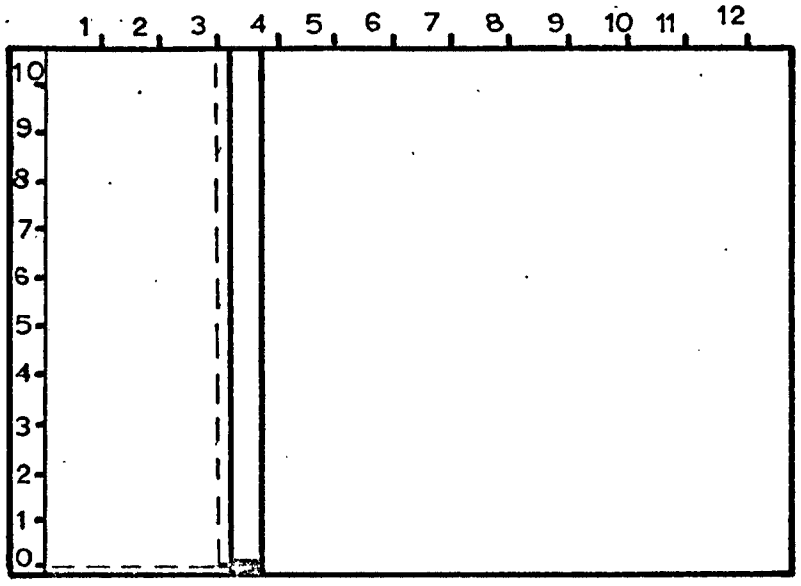

(a) Starting position

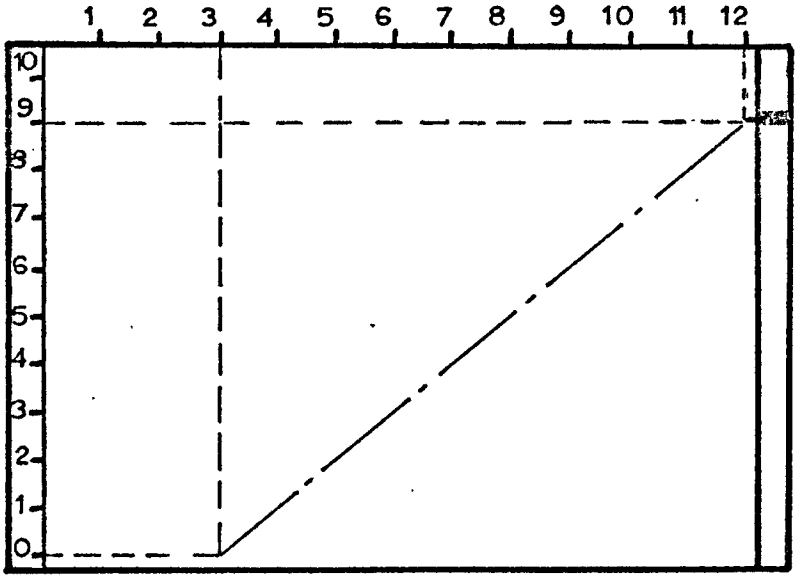

(b) Final position

Figure B - 4 X-Y Recorder calibration

APPENDIX C

Strength Values for Different Cordova Limestones

It was found that Cordova limestone had different strength values depending on where it proceeded from. A chart was developed from the values obtained by different tests on samples cut from 3 blocks of different strength properties. The purpose of these tests was to find a procedure for choosing the limestone of the desired strength at the same quarters. The samples were tested on compression in a Tinius Olsen Machine until fracture occurred ; they also were tested on compression in the true-triaxial equipment. Density was computed for each block by measuring it on ten samples and taking the average value.

A scleroscope was used for testing hardness on each set of samples, also the average hardness of ten samples from each block was tested. A pneumatic impact hammer (Schmidt hammer) was utilized for obtaining another set of values.

It can be seen in the chart shown below that all these values obtained for each set of rocks have similar proportional values between each other.

When the blocks tested with the Schmidt hammer had a cross sectional area of 2 x 3 inches, the readings of strength were very close to the real values.

From this chart we could see that we were enable to use the Schmidt hammer for choosing blocks with the same strength characteristics.

The Schmidt hammer gave an approximate reading of 16 for the obtained blocks.

	Tinius Olsen Compression (psi)	Triaxial equipment Compression (psi)	Impact hammer Reading	Impact hammer values (psi)	Density Average	Scleroscope readings	Scleroscope values $\frac{ton}{in^2}$
1st set of samples	1000	1000	# 15	1000	29.324291	5	6
2nd set of samples	3850	3950	# 31	3900	33.804845	11	13
3rd set of samples	3100	3000	26.2	2800	33.278169	9	9

APPENDIX D

Figures IV - 28 to IV - 69

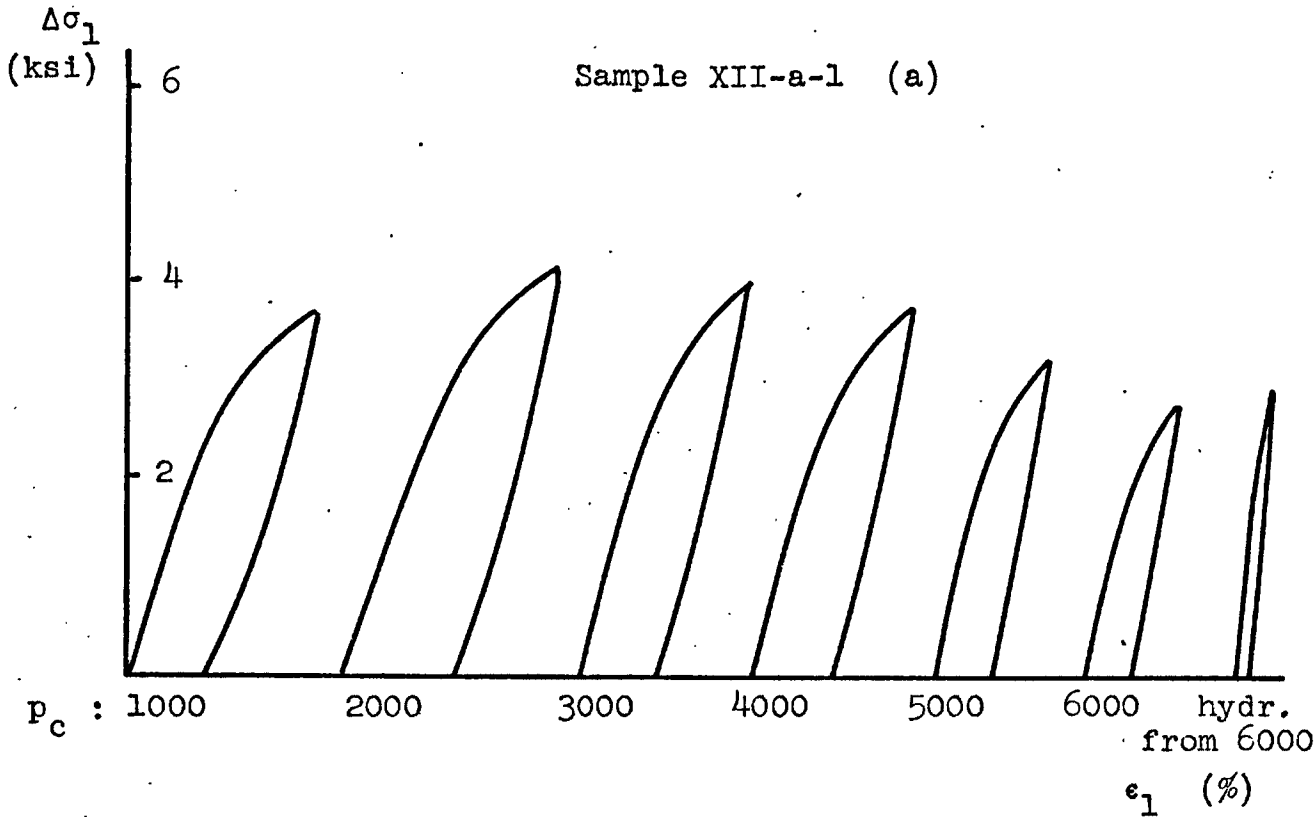

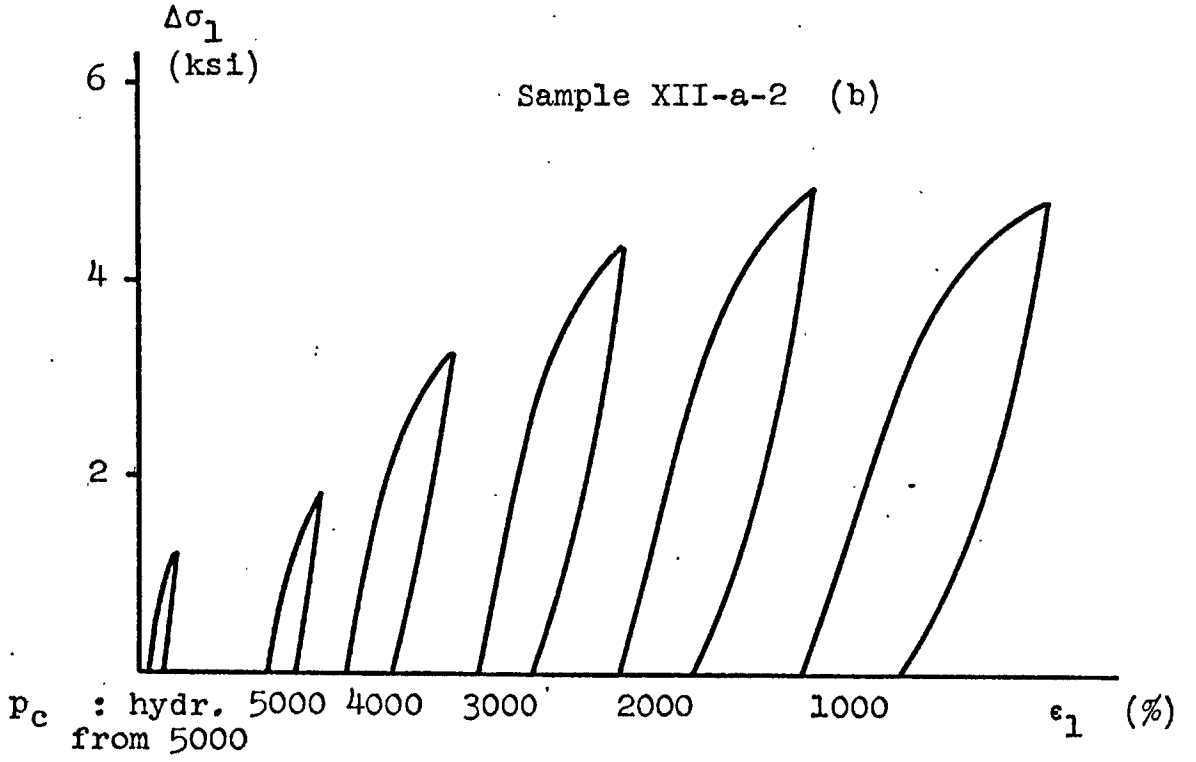

Fig. IV-28 Probing tests ($\Delta\sigma_z$ = 3000)

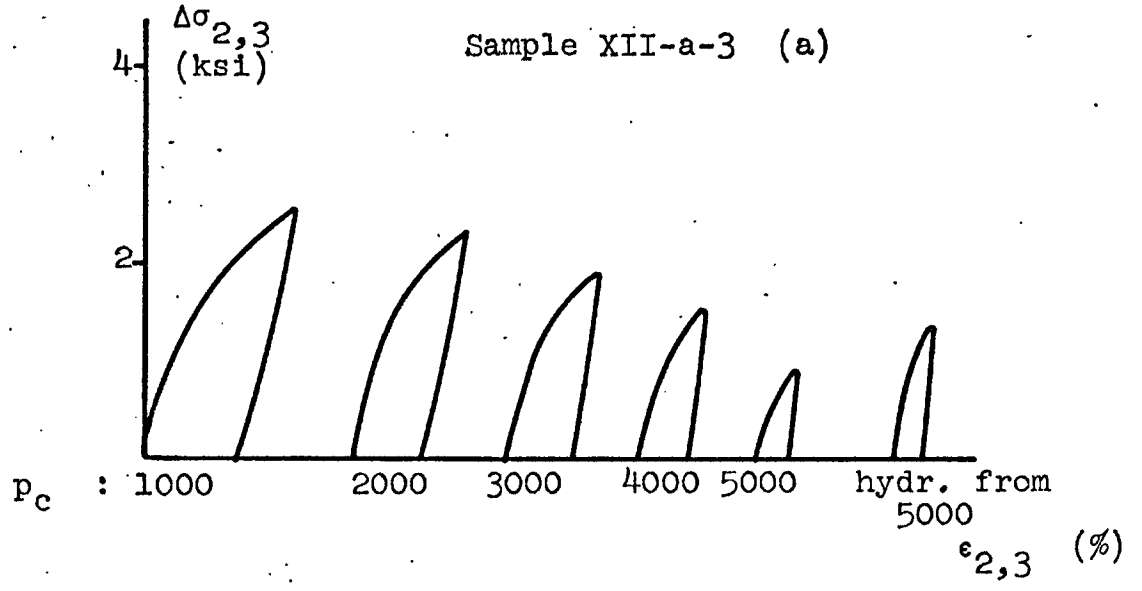

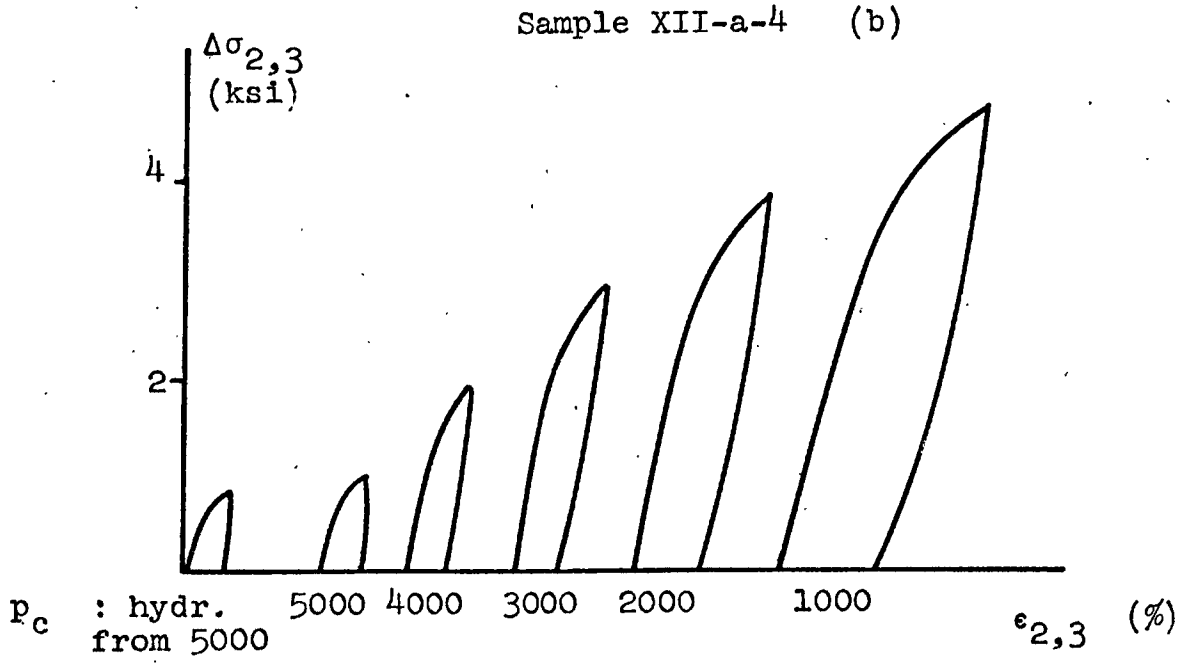

Fig. IV-29 Probing tests ($\Delta\sigma_z$ = 3000)

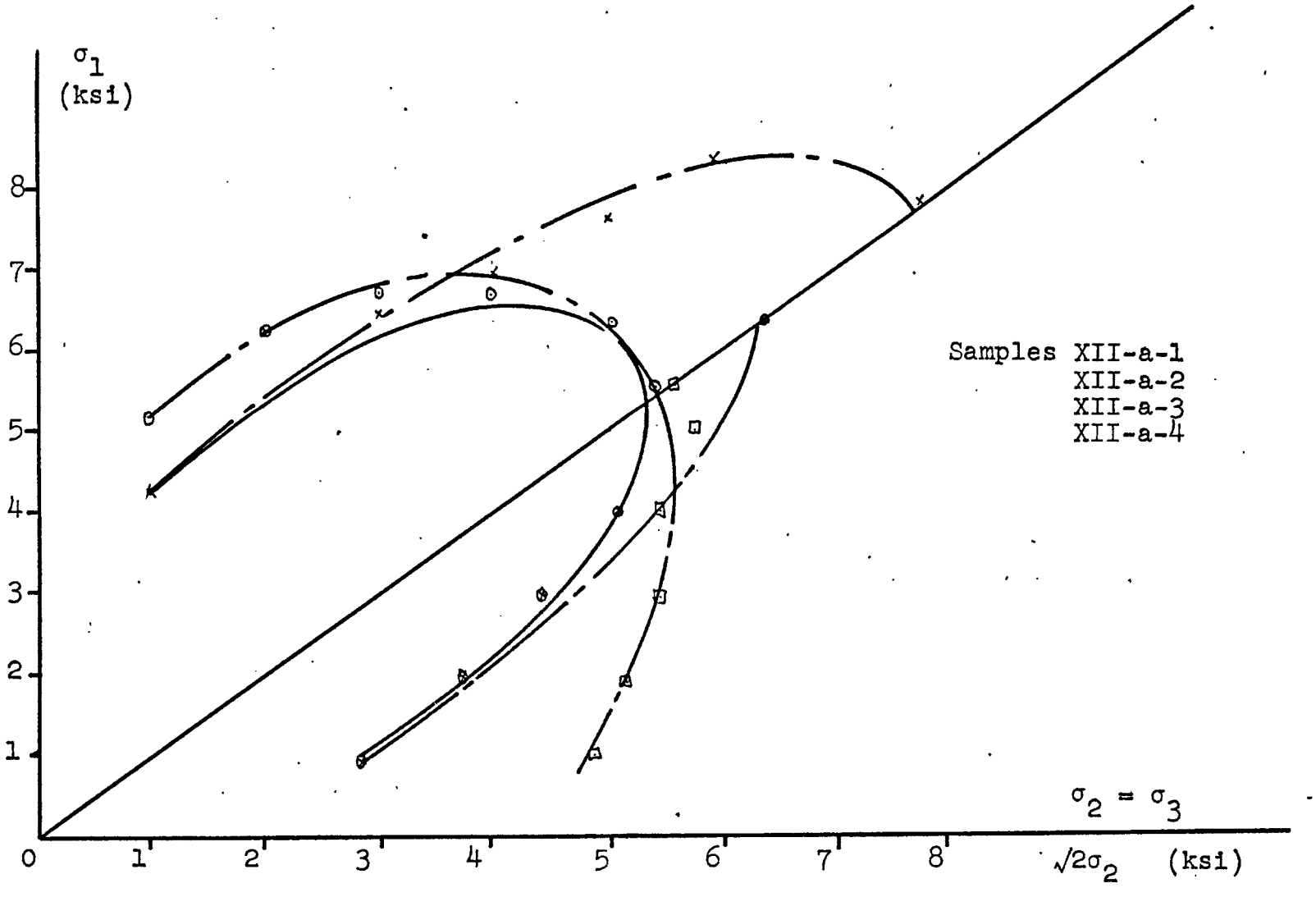

Fig. IV-30 First subsequent yield surface ($\Delta\sigma_z$ = 3000)

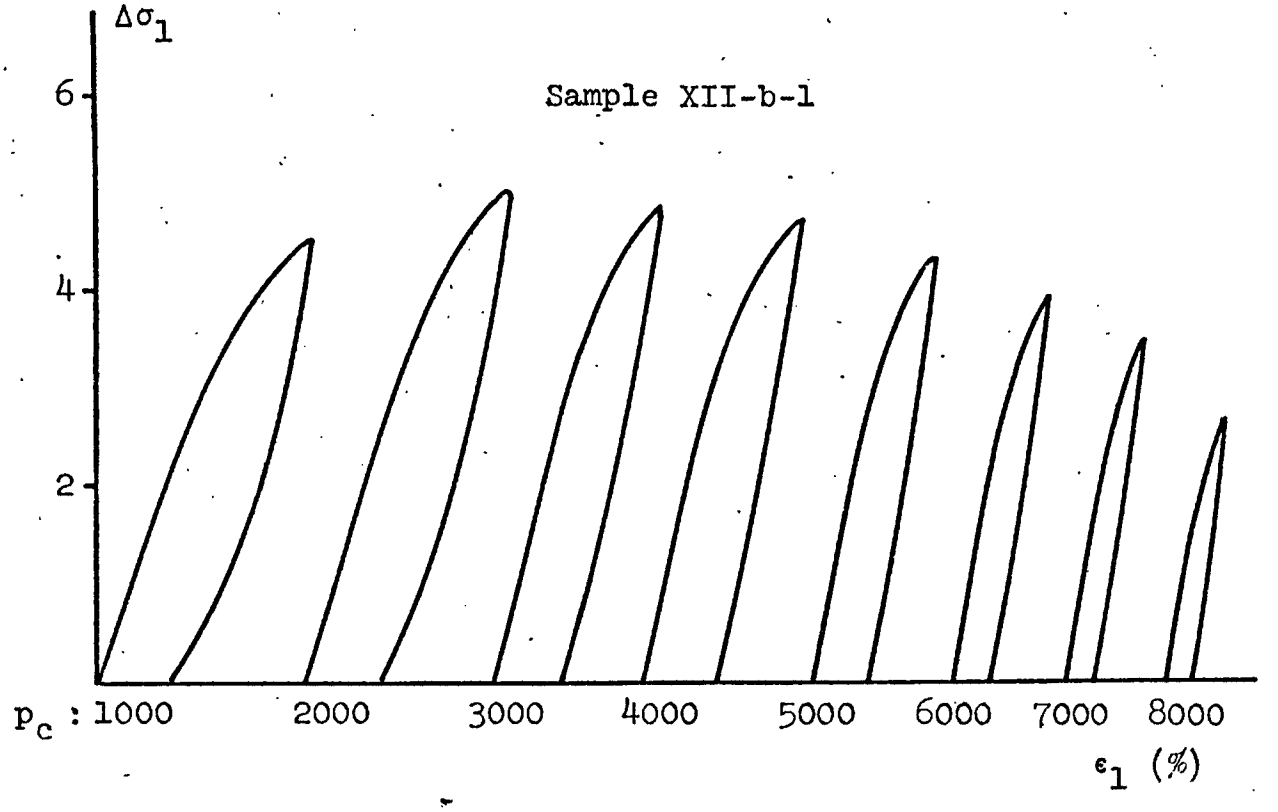

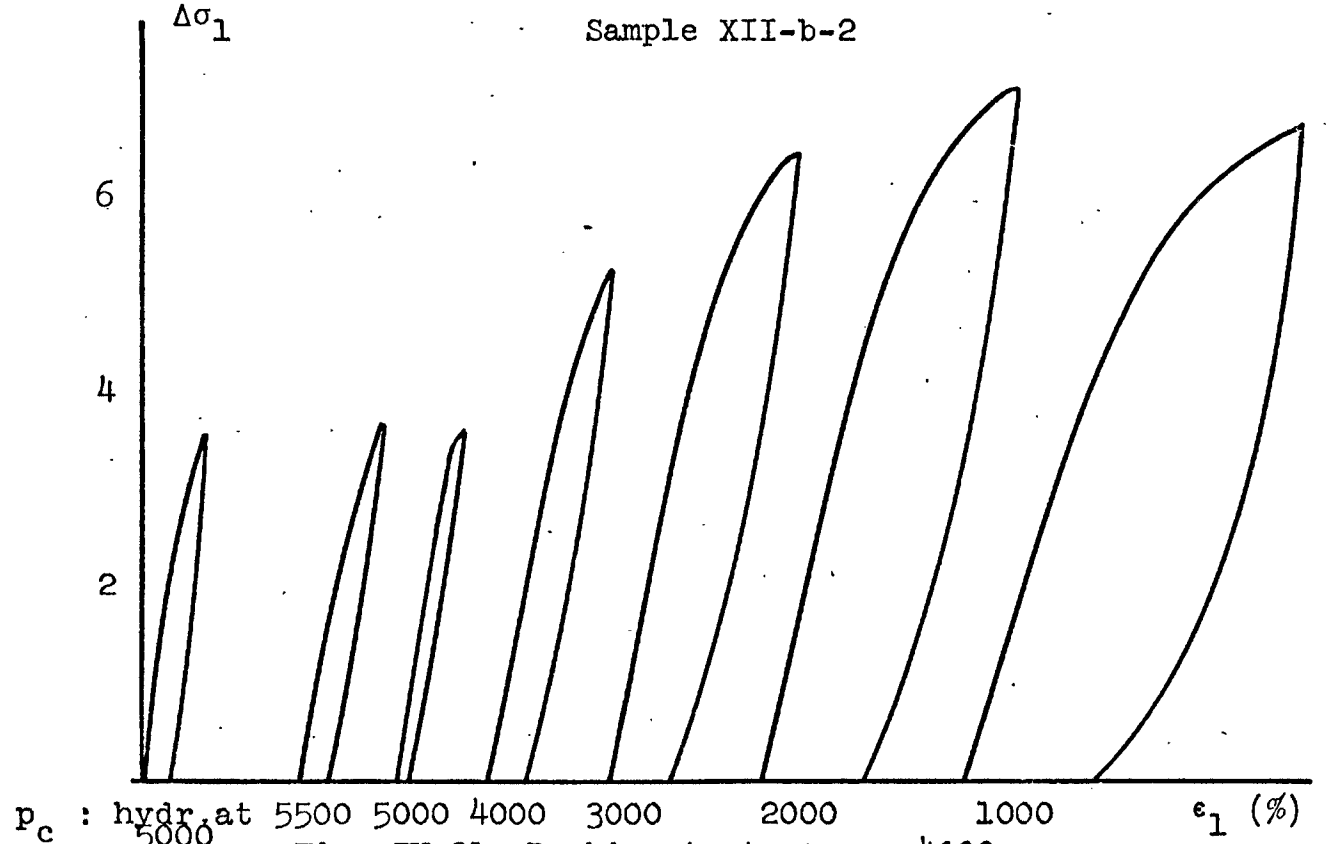

Fig. IV-31 Probing tests $\Delta\sigma_z = 4000$

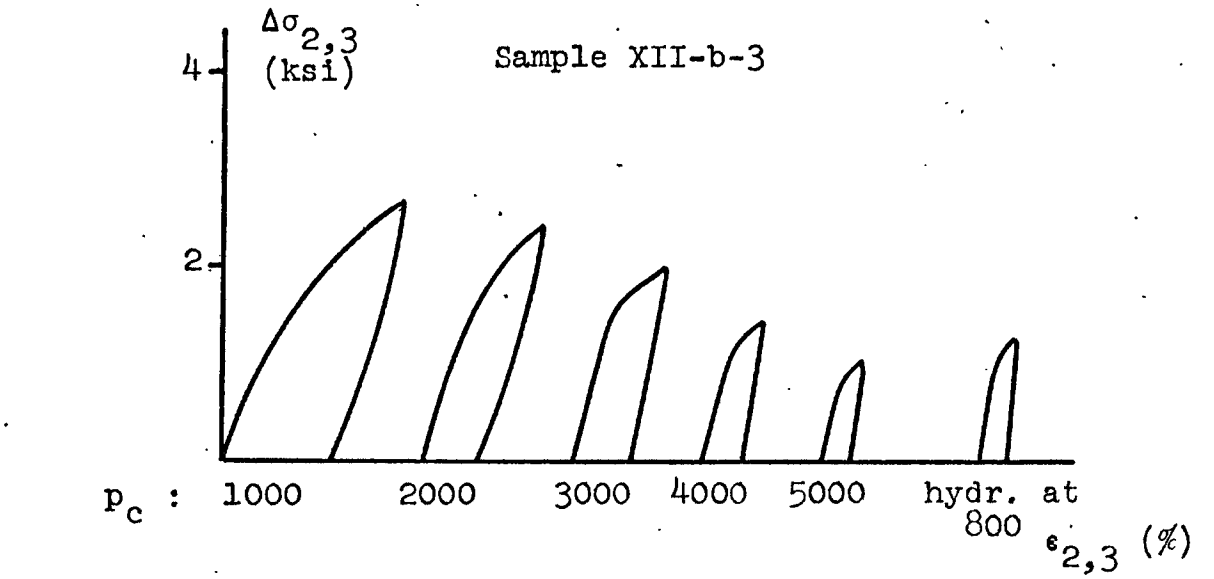

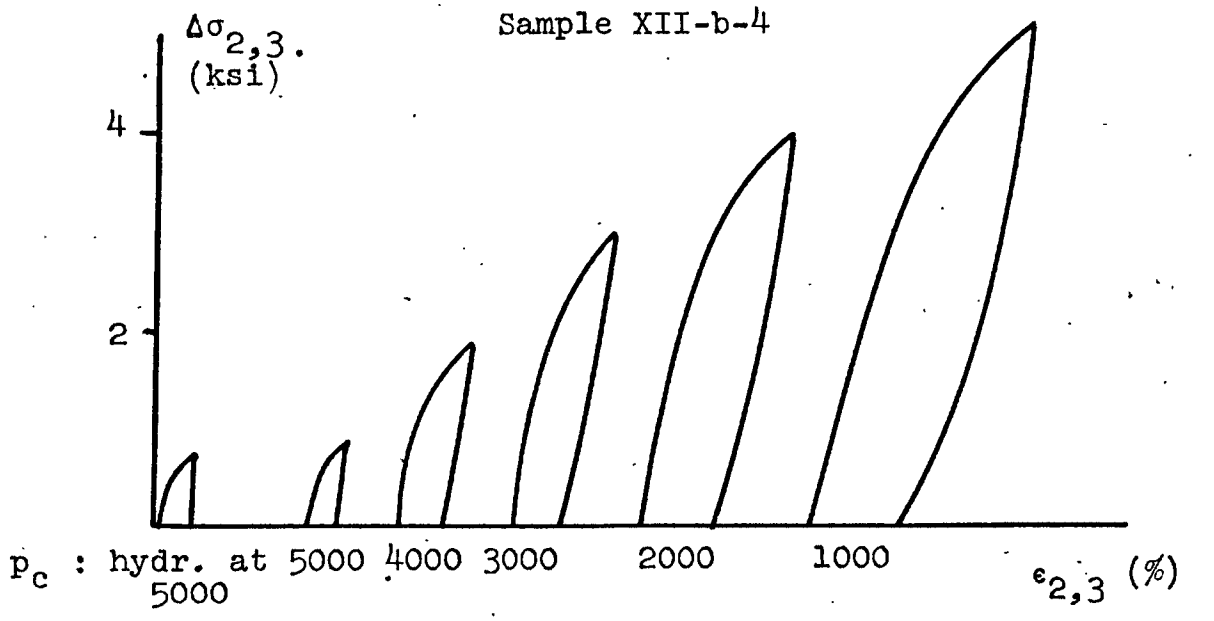

Figure IV-32 Probing tests $\Delta\sigma_z = 4000$

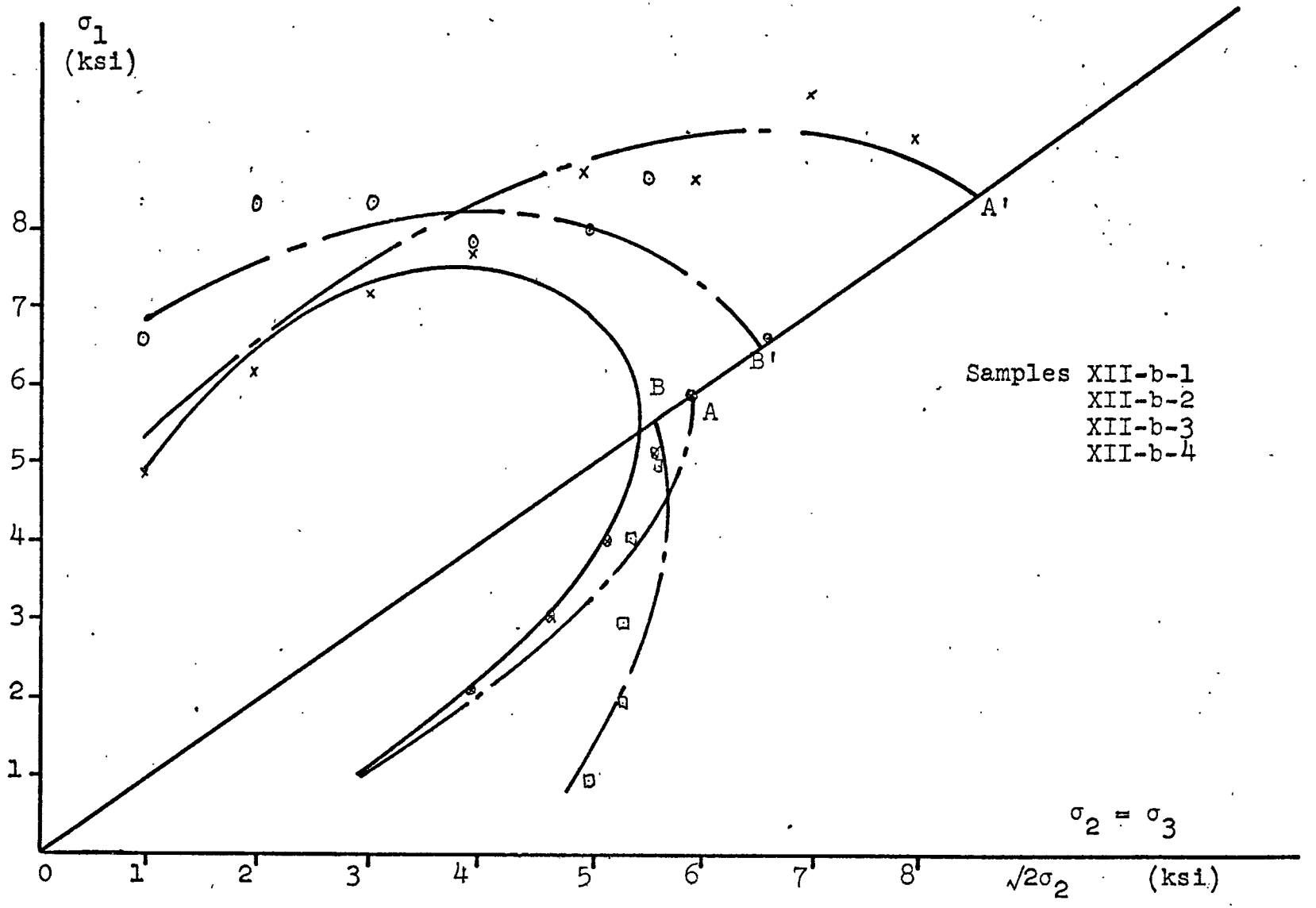

Fig. IV-33 Second subsequent yield surface ($\Delta\sigma_z$ = 4000)

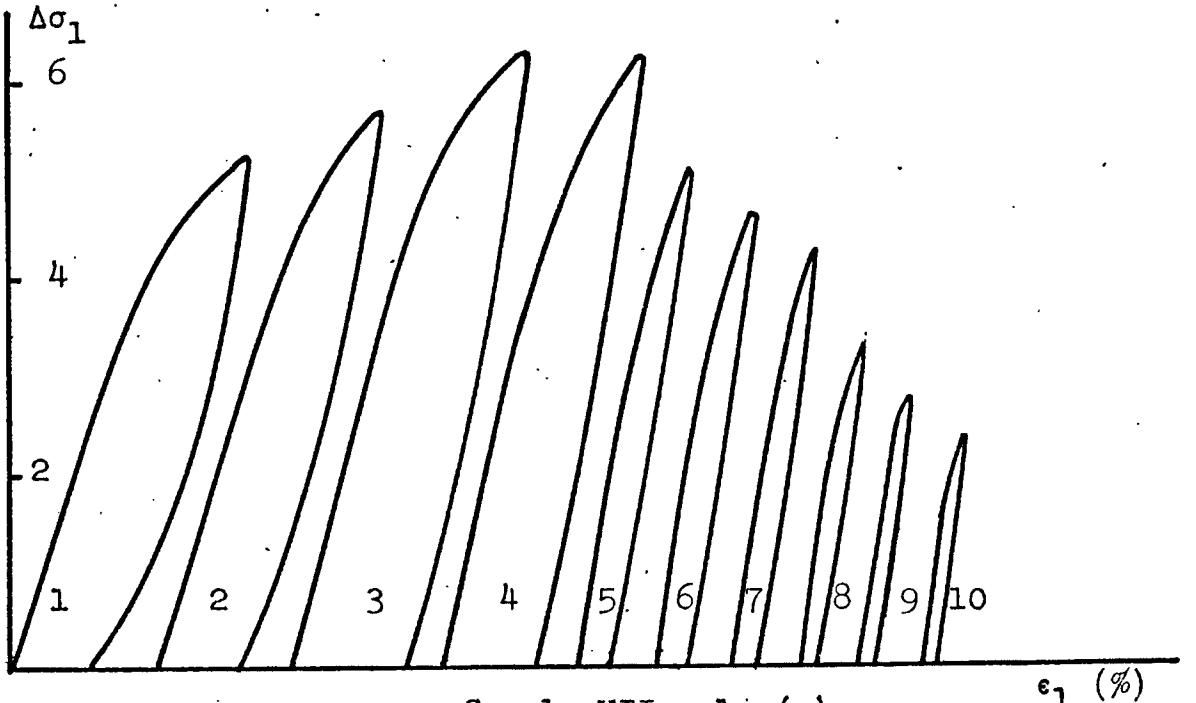

Sample XII-c-1 (a)

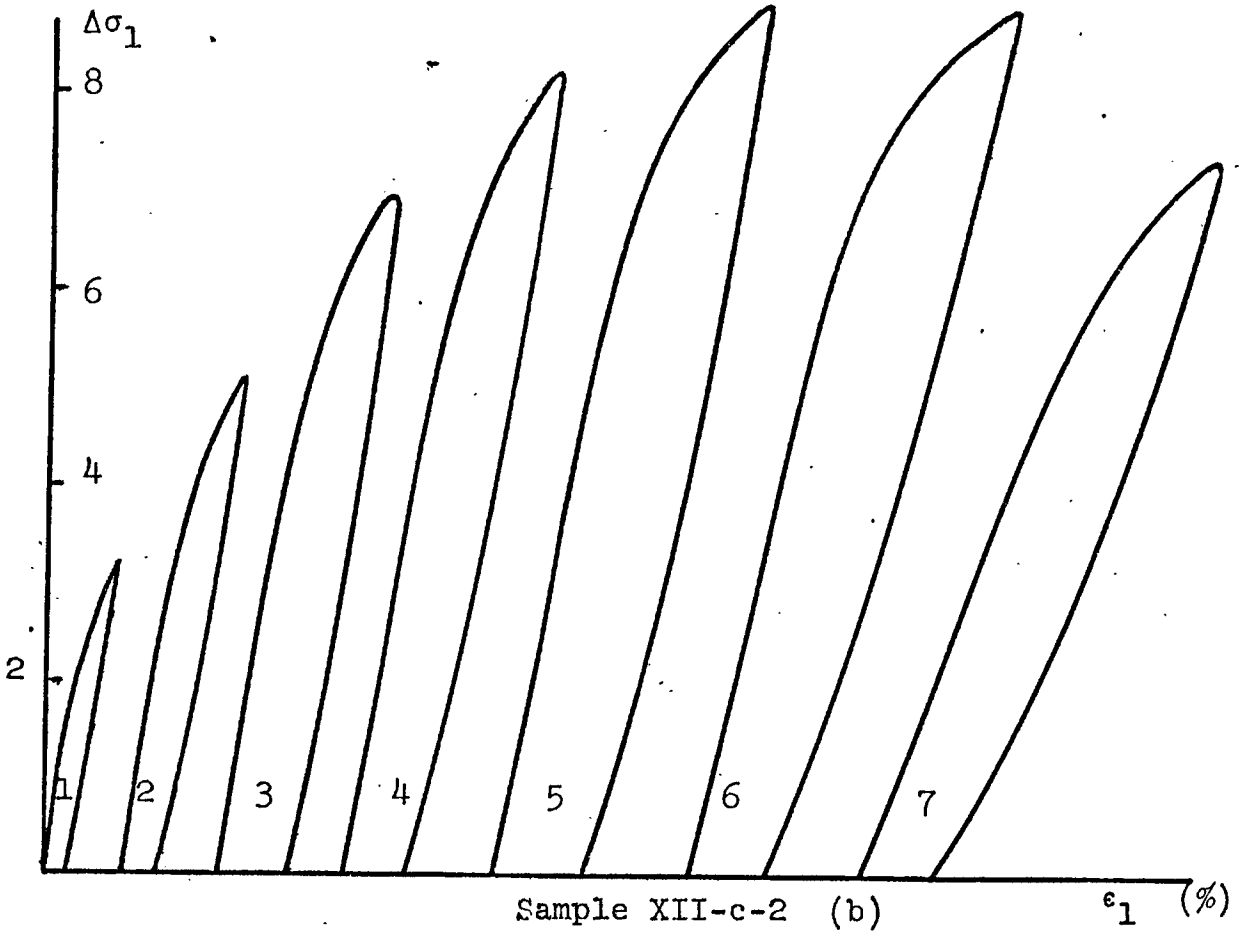

Sample XII-c-2 (b)

Fig. IV-34 Probing tests for third subsequent yield surface ($\Delta\sigma_z$ = 5000)

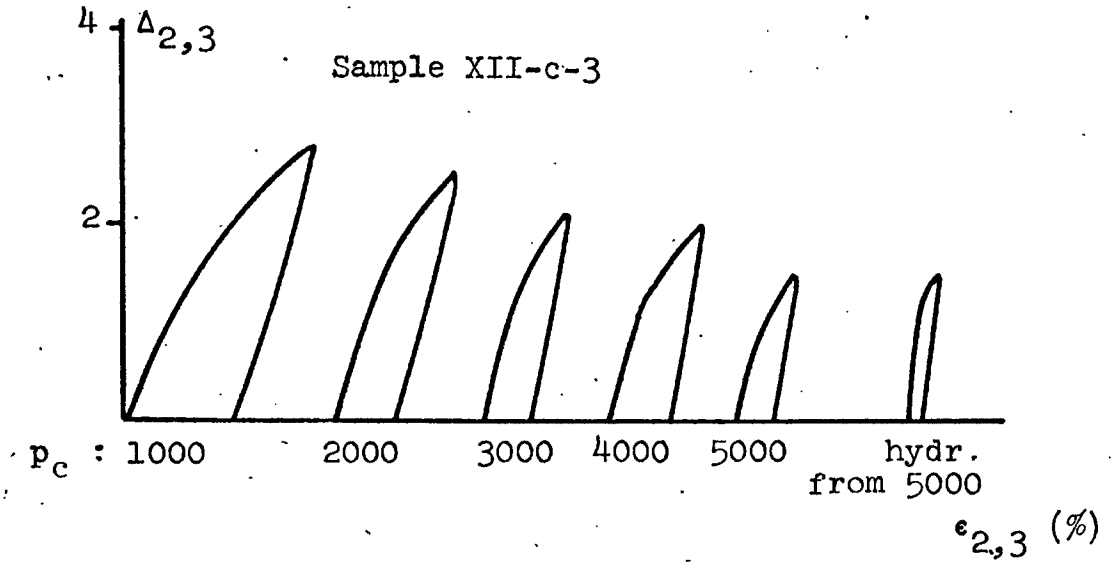

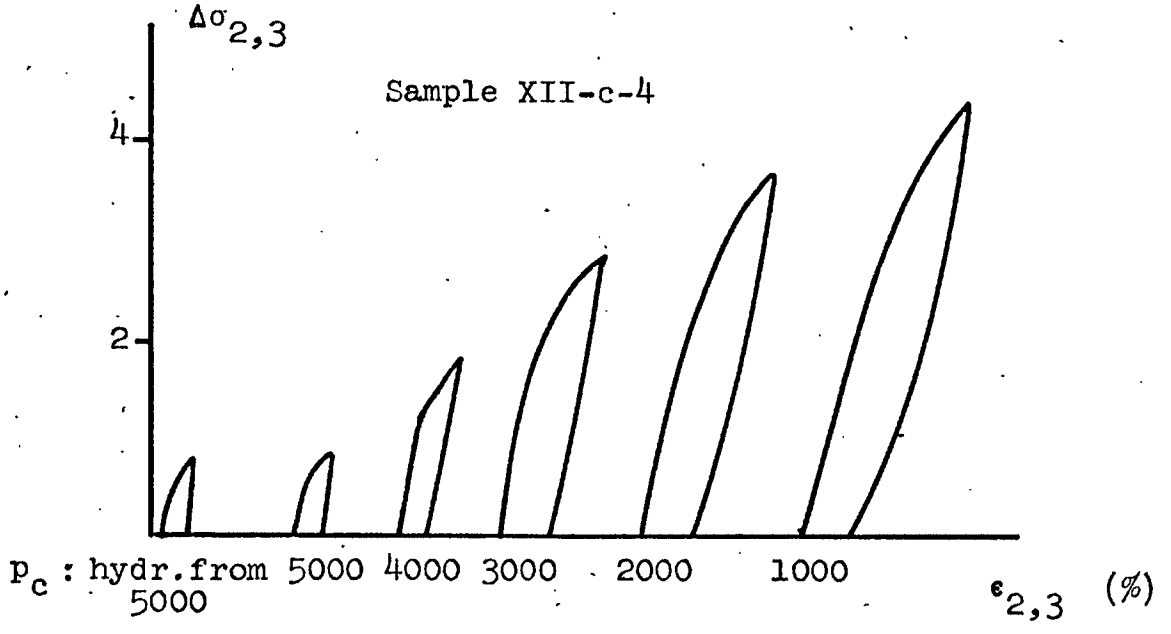

Figure IV-35 Probing tests for third subsequent yield surface ($\Delta\sigma_z$ = 5000)

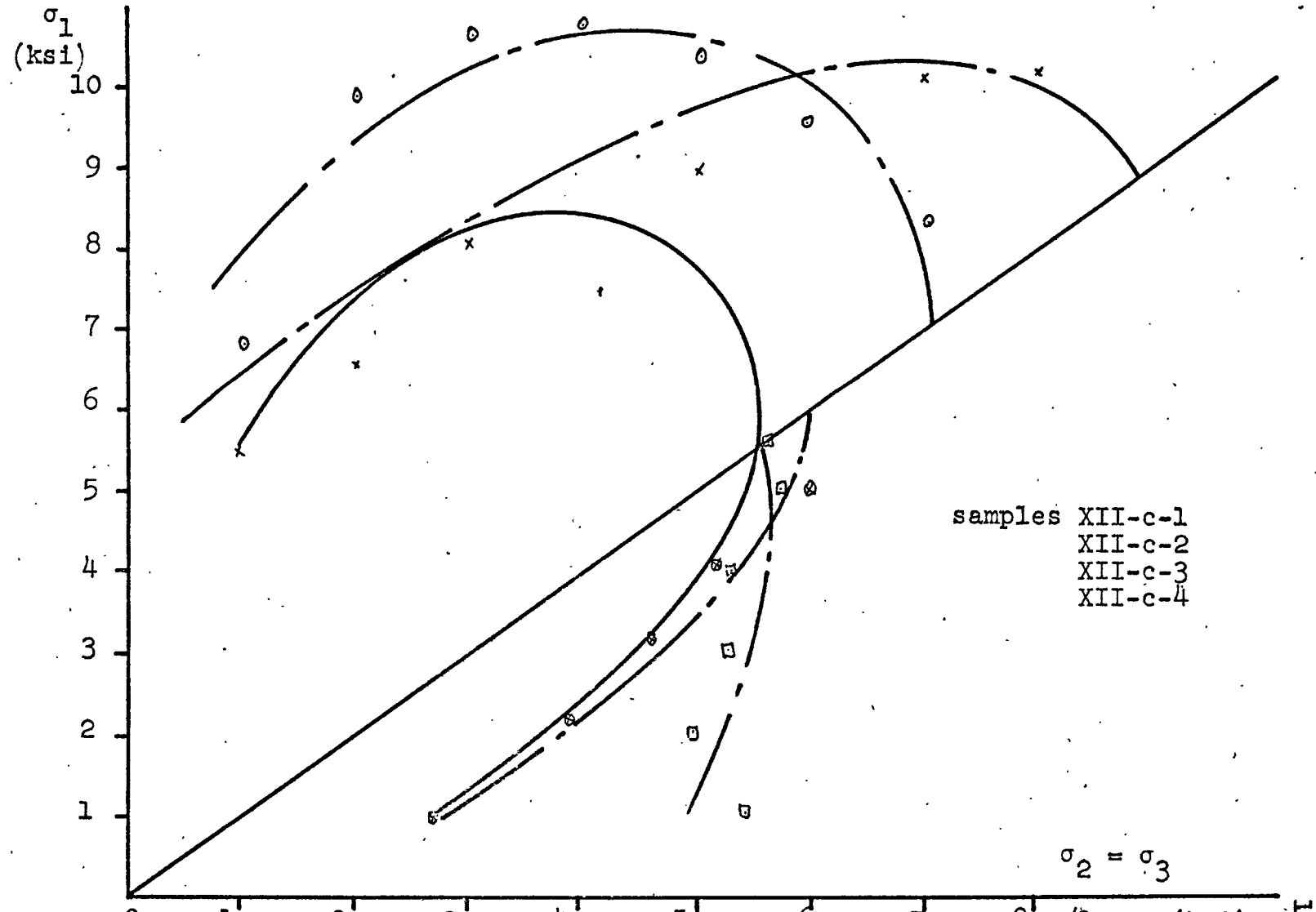

Figure IV-36 Third subsequent yield surface ($\Delta\sigma_z$ = 5000)

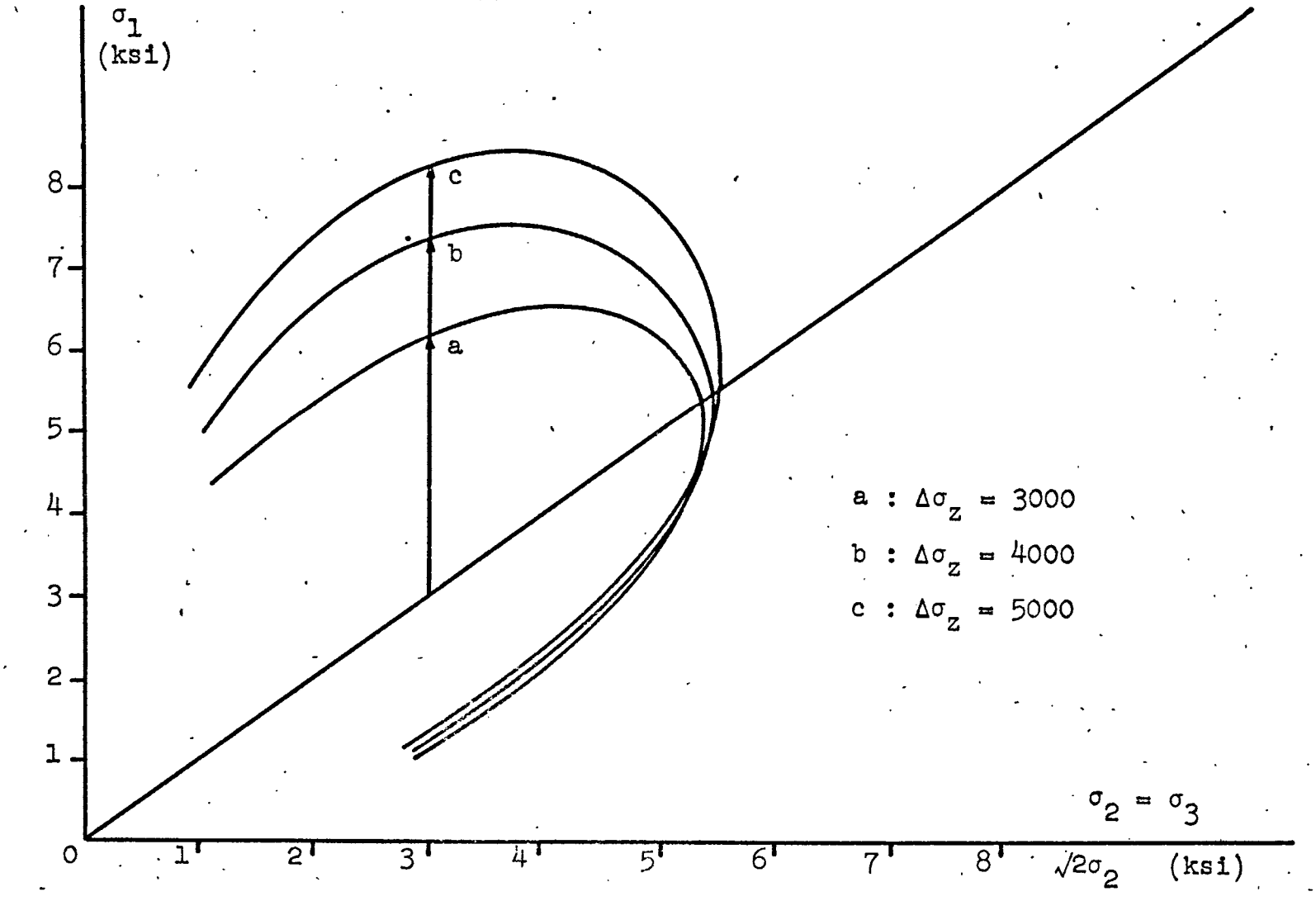

Figure IV - 37 First set of subsequent yield surfaces

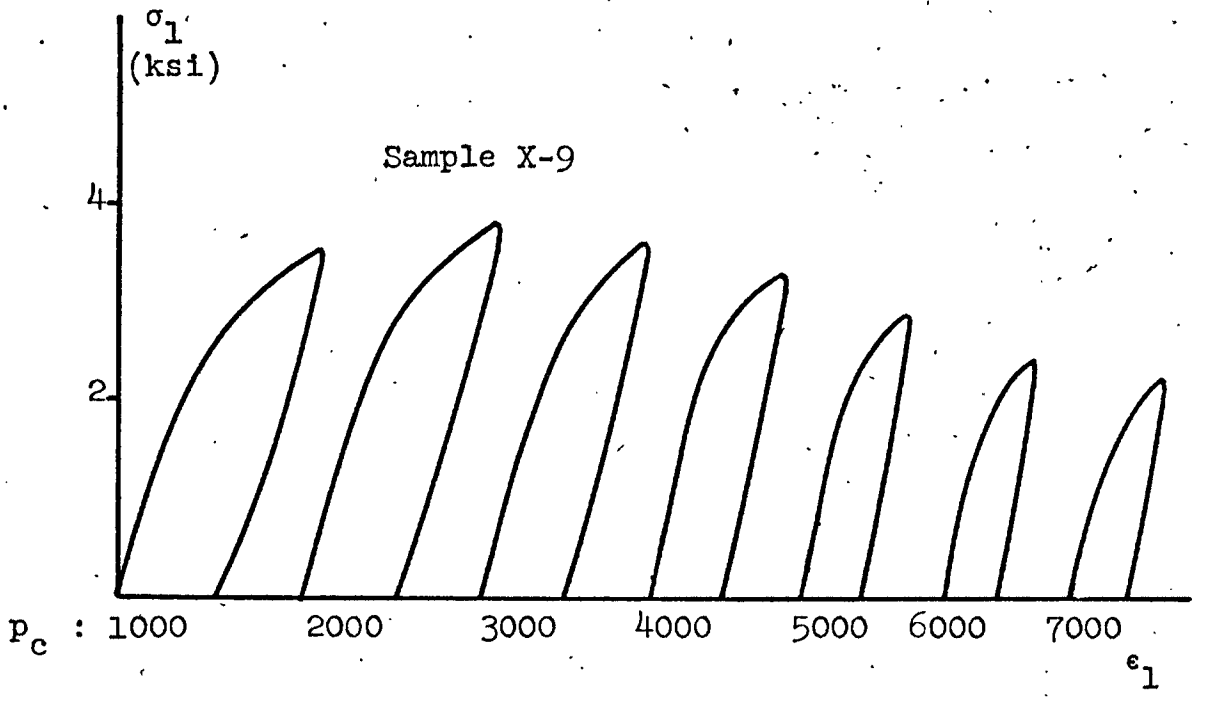

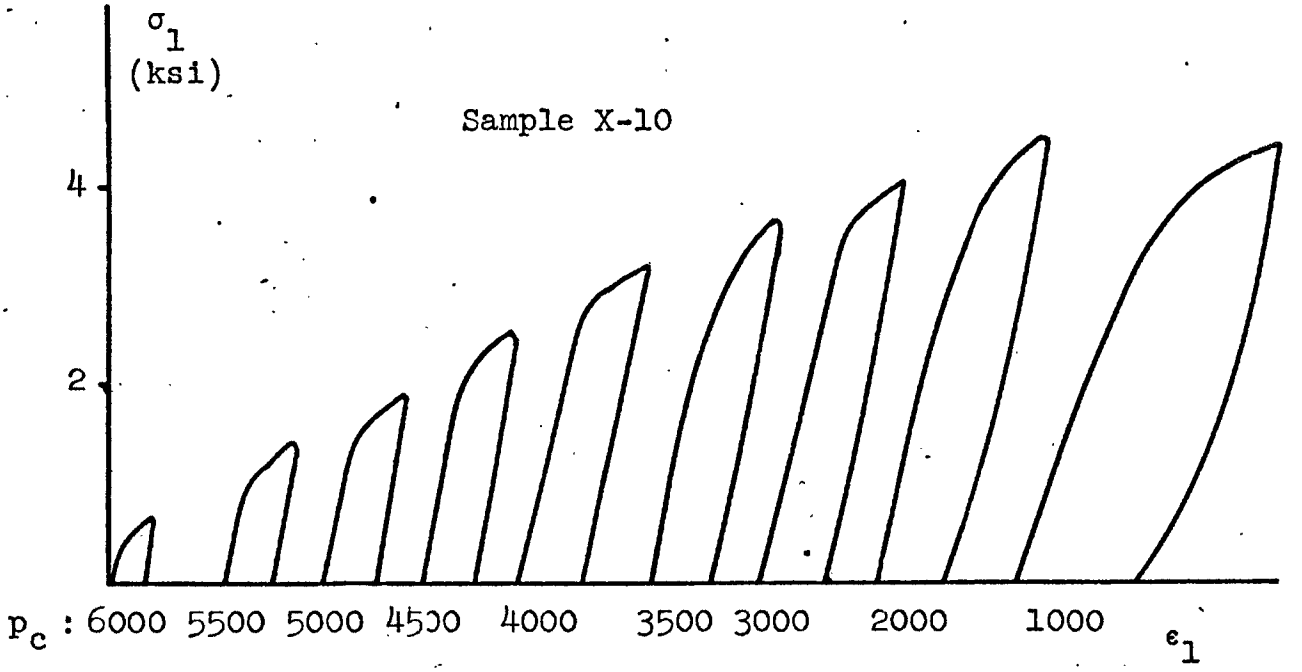

Figure IV-38 Probing tests for yield envelope at $\sigma_1=\sigma_2=\sigma_3 = 6000$

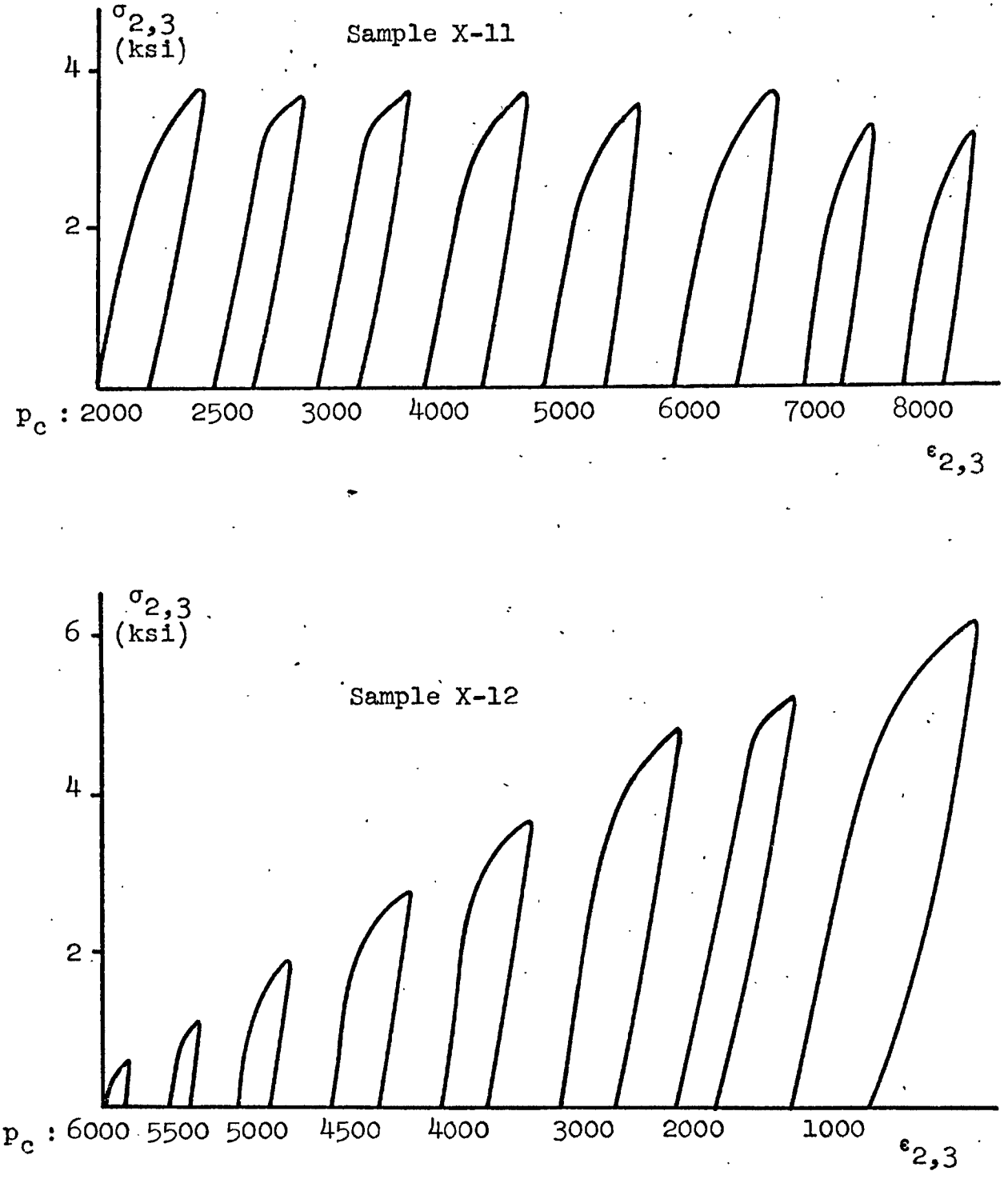

Figure IV-39 Probing tests for yield envelope at $\sigma_1=\sigma_2=\sigma_3 = 6000$

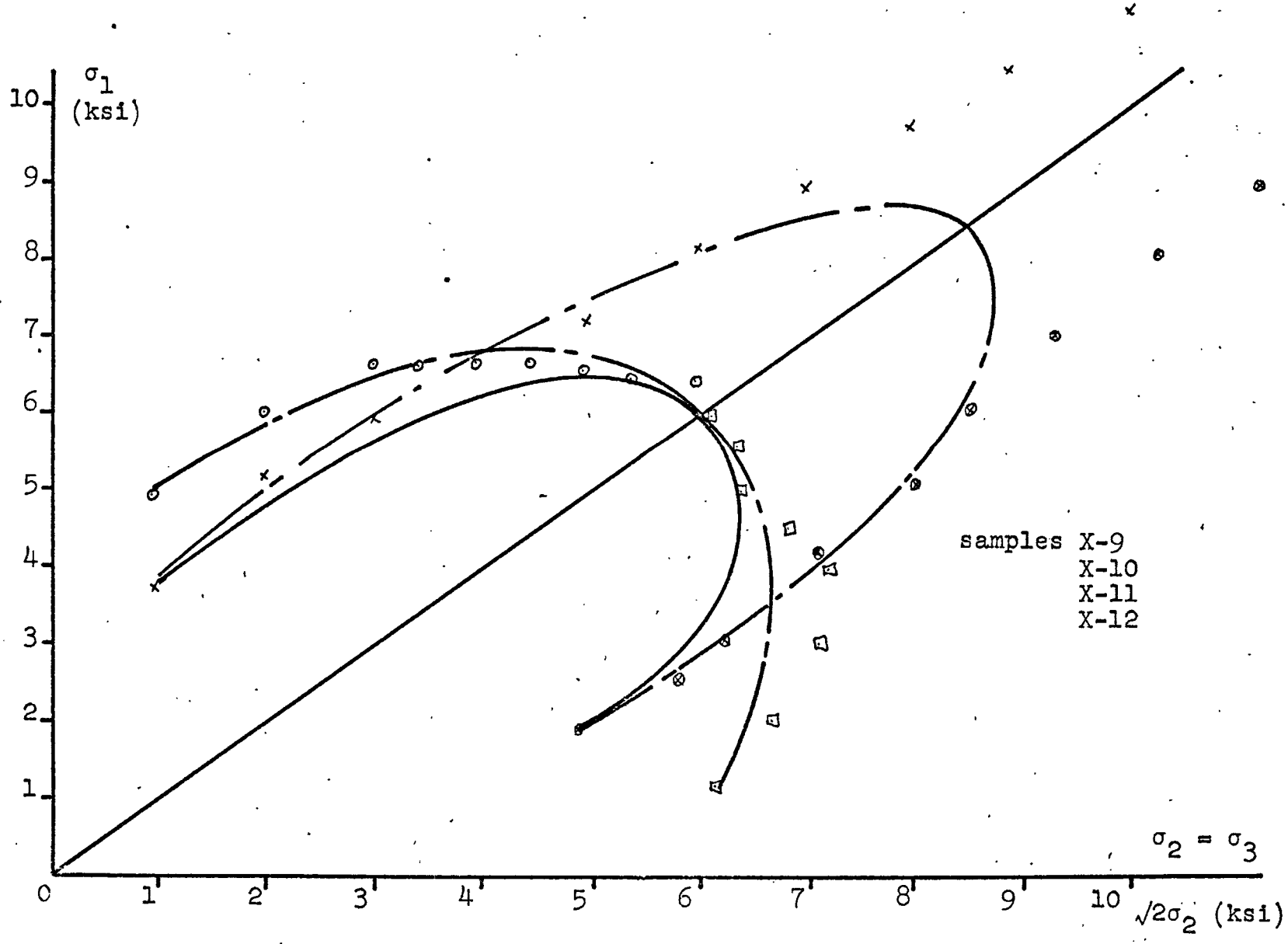

Figure IV-40 First subsequent yield surface ($\sigma_1=\sigma_2=\sigma_3$ = 6000)

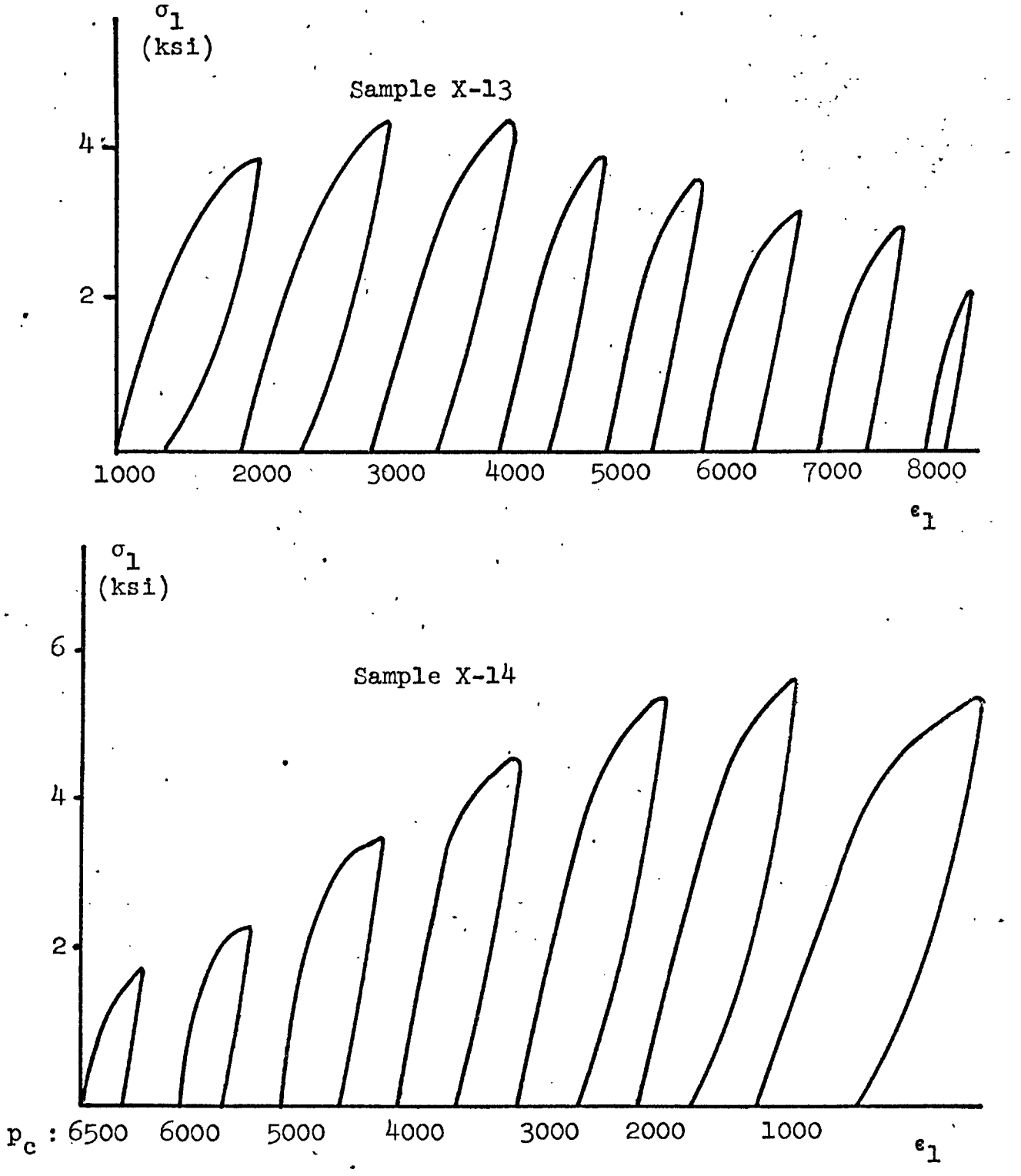

Figure IV-41 Probing tests for yield envelope at 7000 psi ($\sigma_1=\sigma_2=\sigma_3$ = 7000)

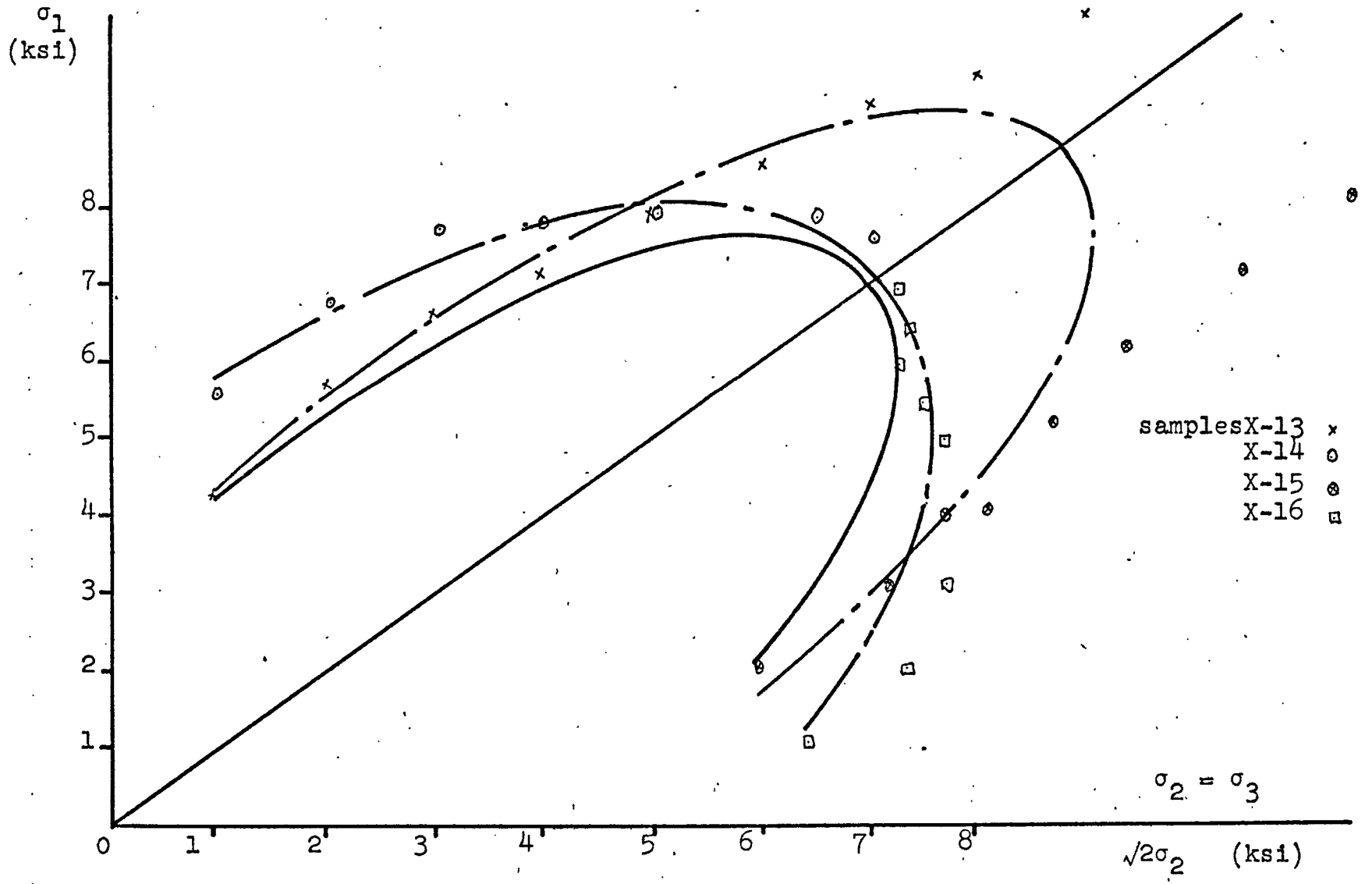

Fig. IV-43 Second subsequent yield surface ($\sigma_1=\sigma_2=\sigma_3$ = 7000)

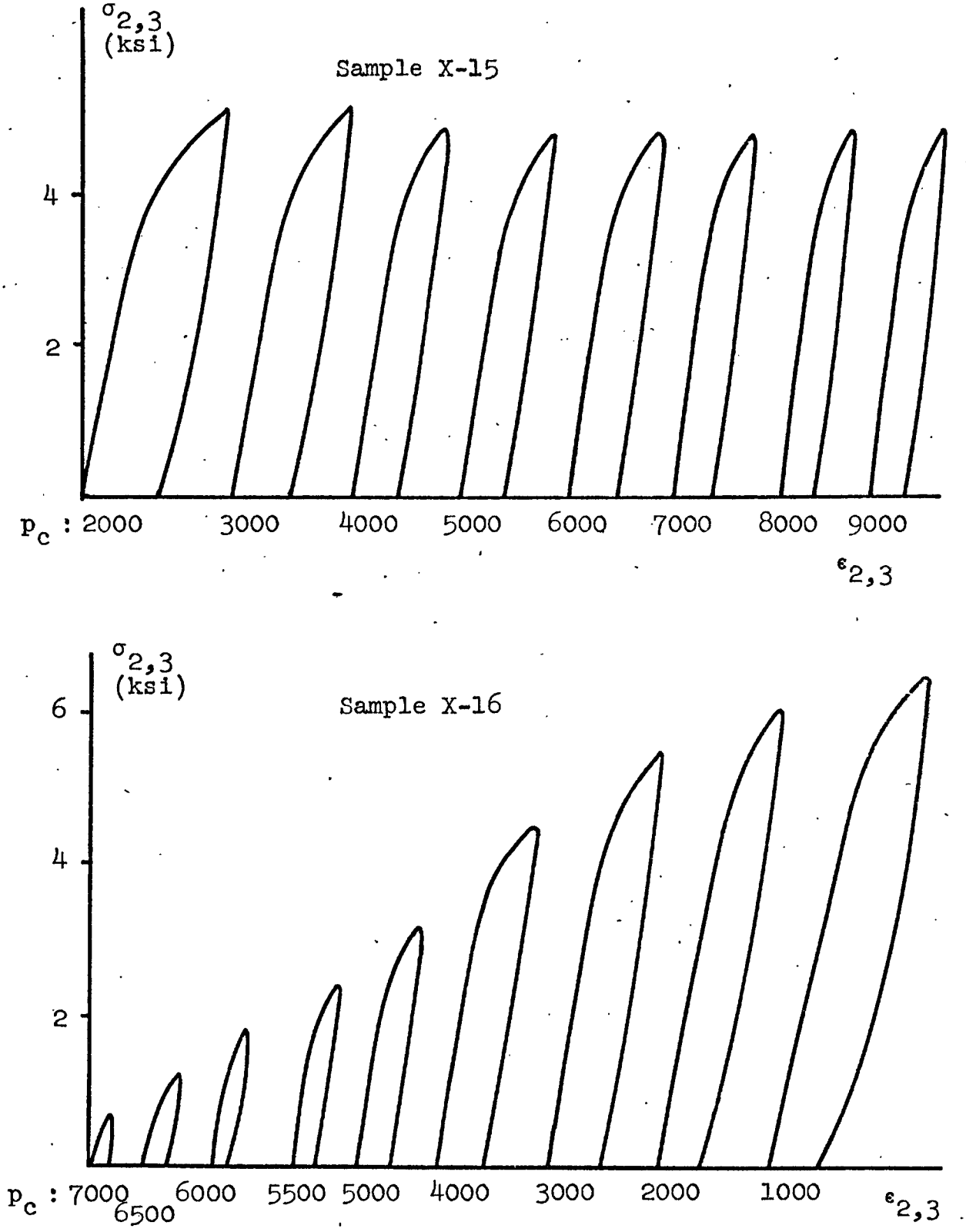

Figure IV-42 Probing tests for yield envelope at 7000 psi ($\sigma_1=\sigma_2=\sigma_3$ = 7000)

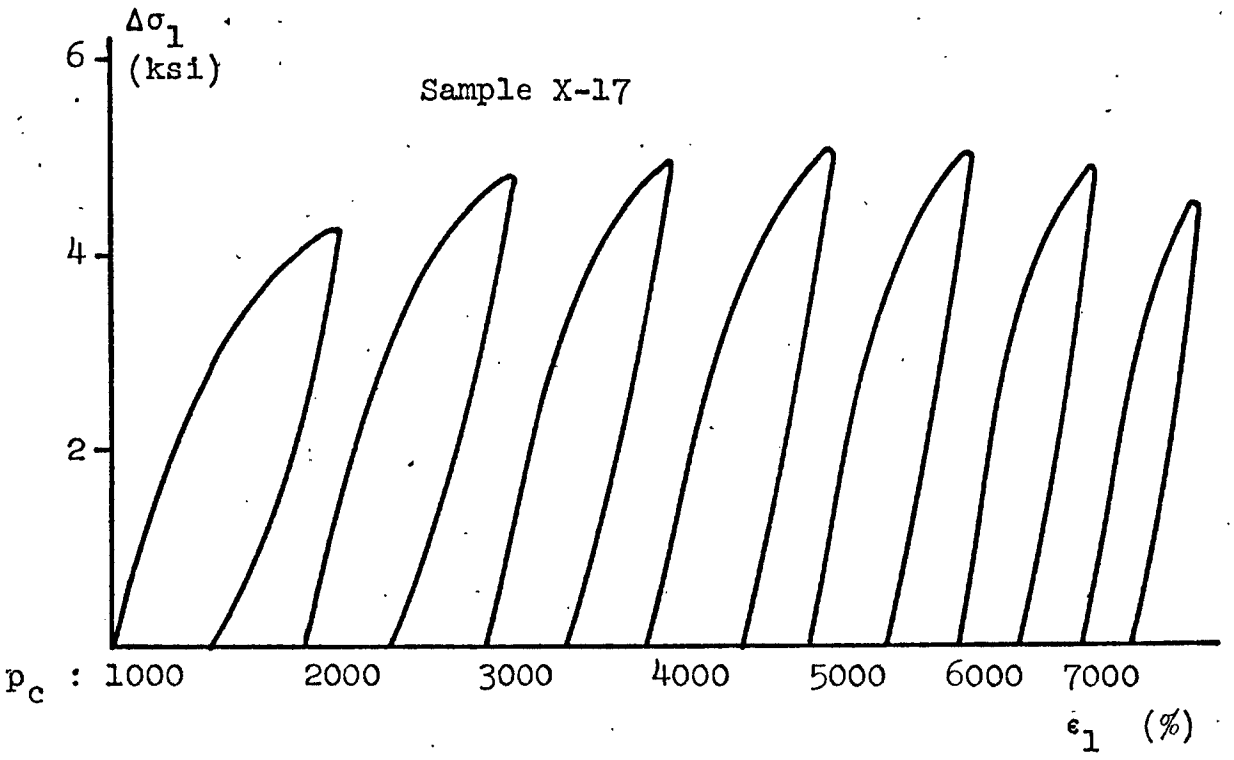

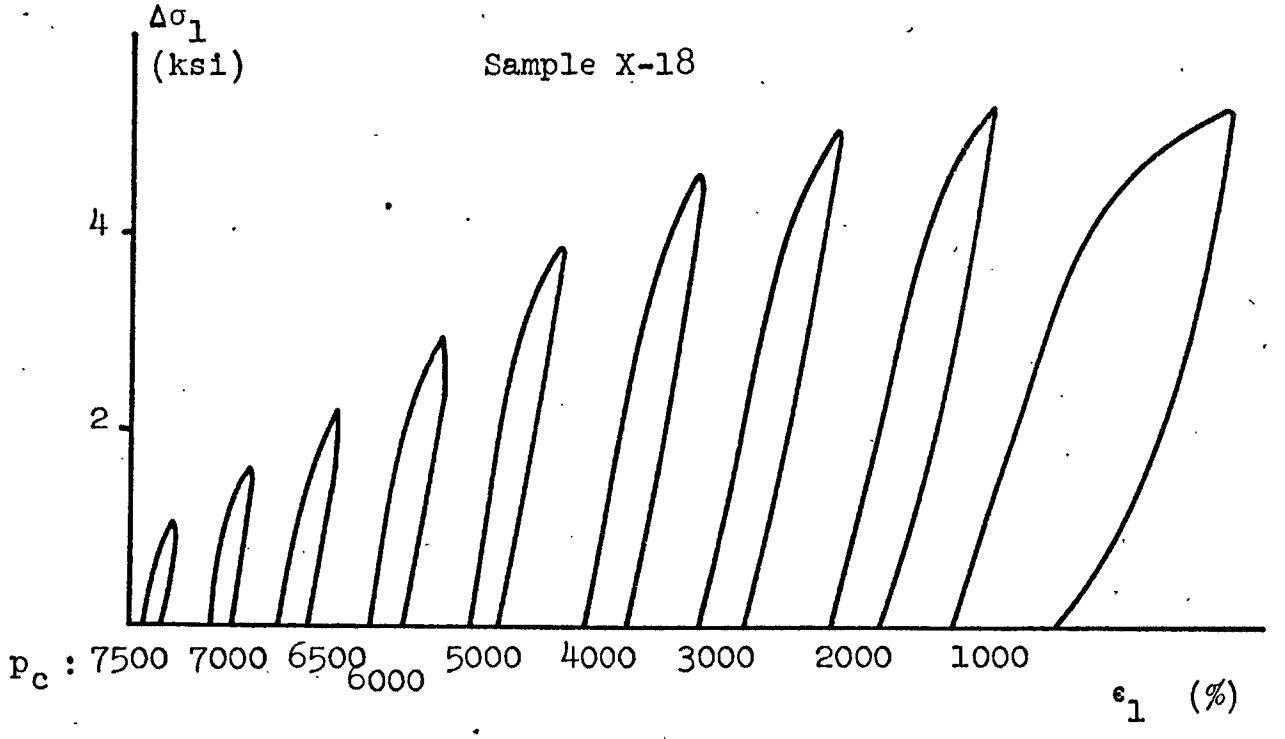

Figure IV - 44 Probing tests for third subsequent yield surface ($\sigma_1=\sigma_2=\sigma_3$ = 8000)

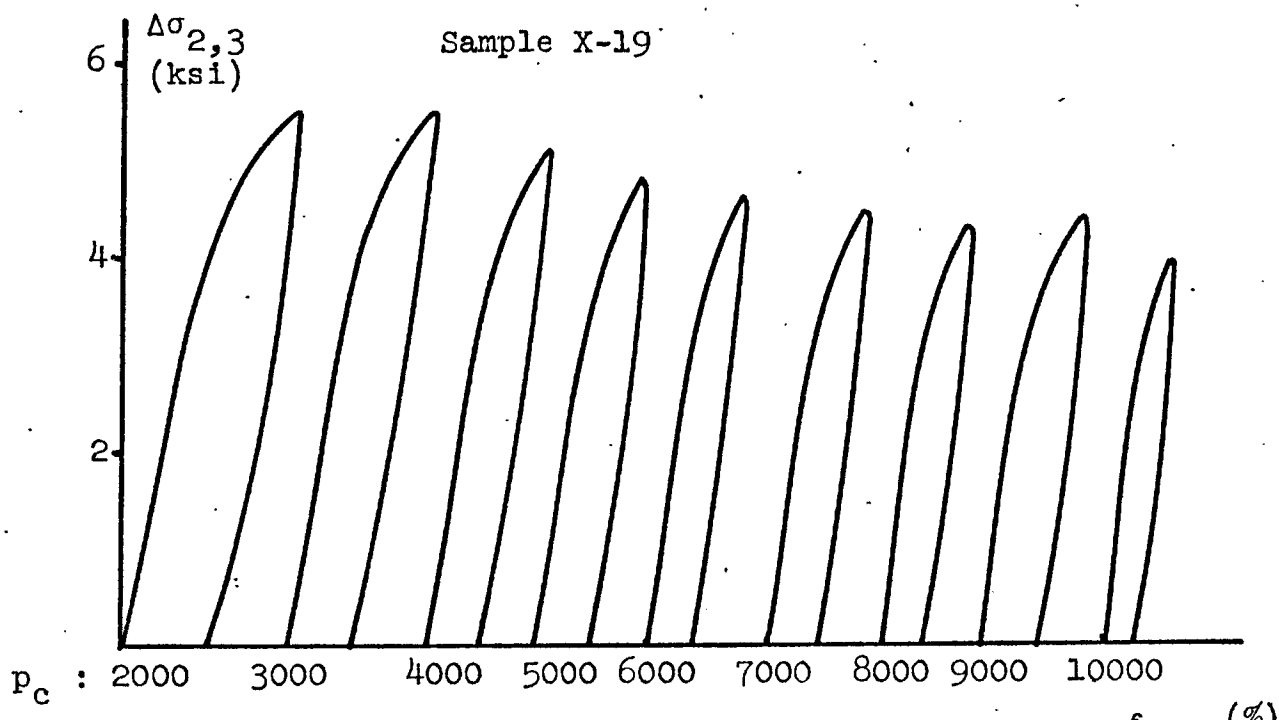

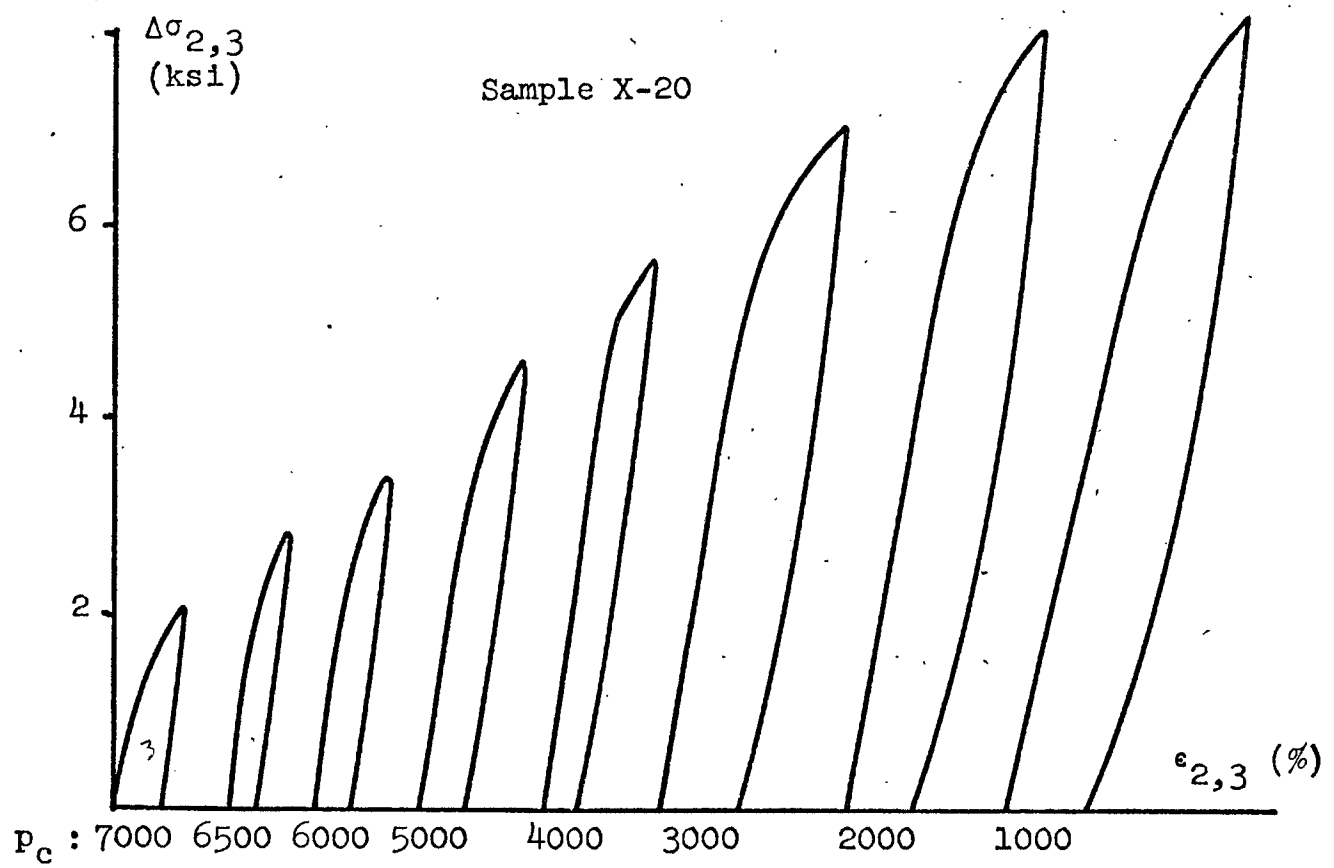

Fig. IV-45 Probing tests for third subsequent yield surface $\sigma_1=\sigma_2=\sigma_3 = 8000$

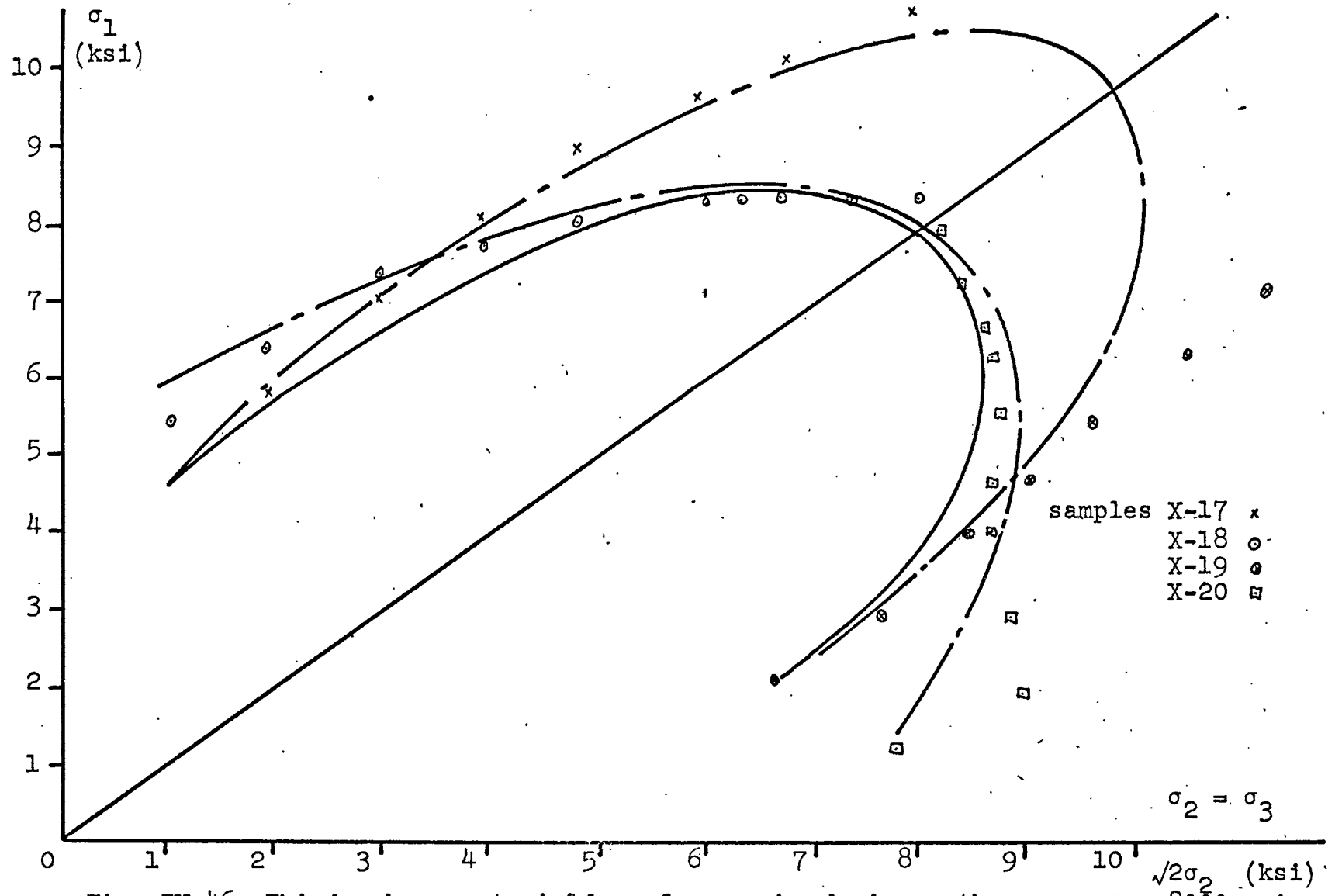

Fig. IV-46 Third subsequent yield surface on hardening path $\sigma_1=\sigma_2=\sigma_3$ = 8000 psi

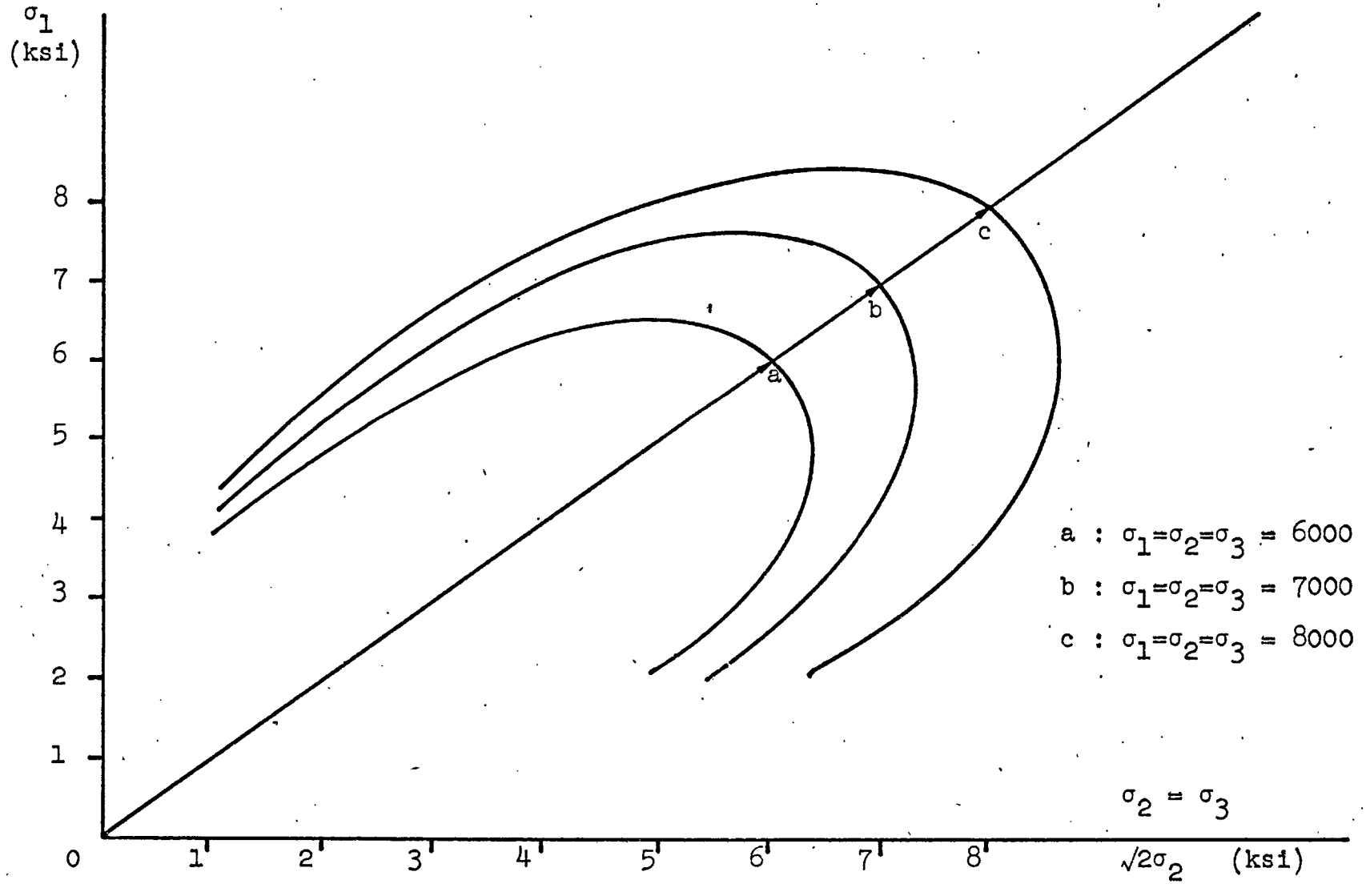

Figure IV - 47 Second set of subsequent yield surfaces and hardening path

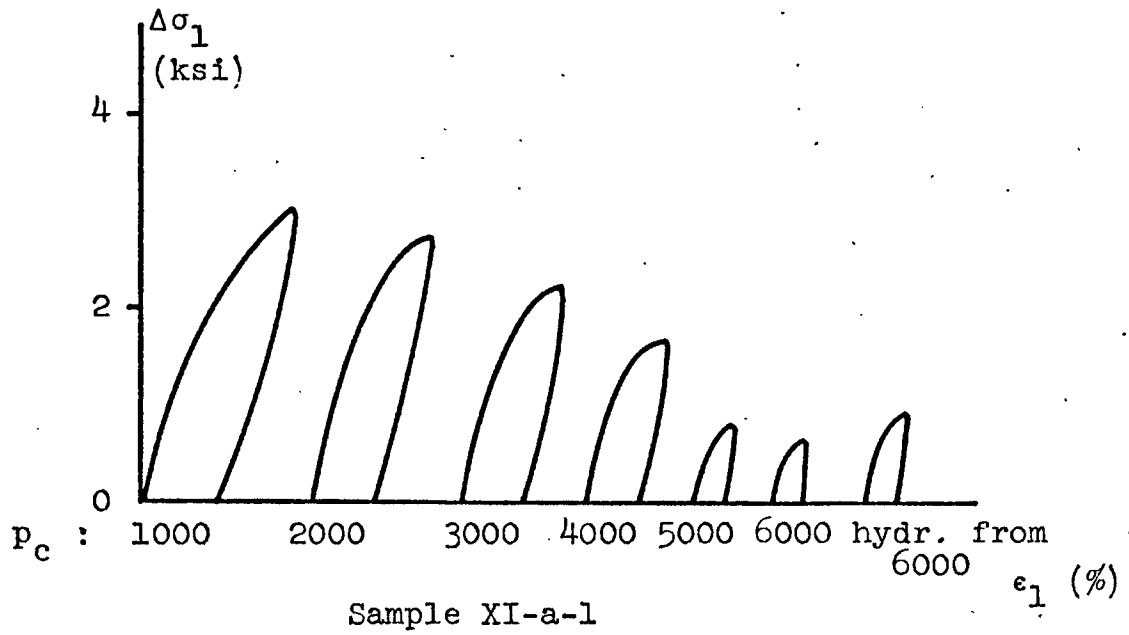

Sample XI-a-1

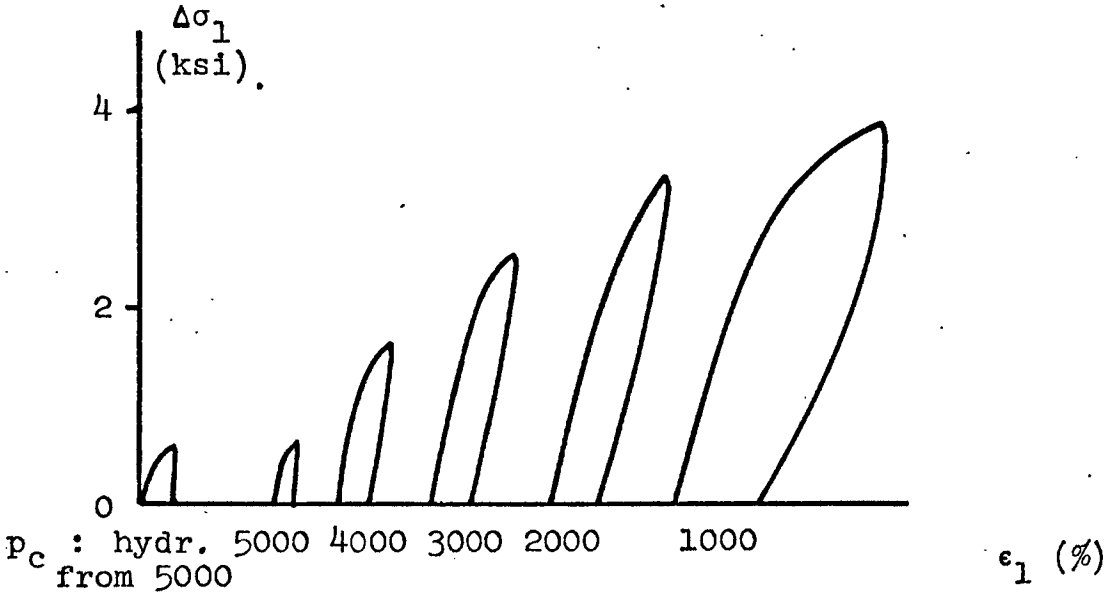

Sample XI-a-2

Figure IV - 48 Probing tests for yield envelope at $\Delta\sigma_{2,3} = 3000$

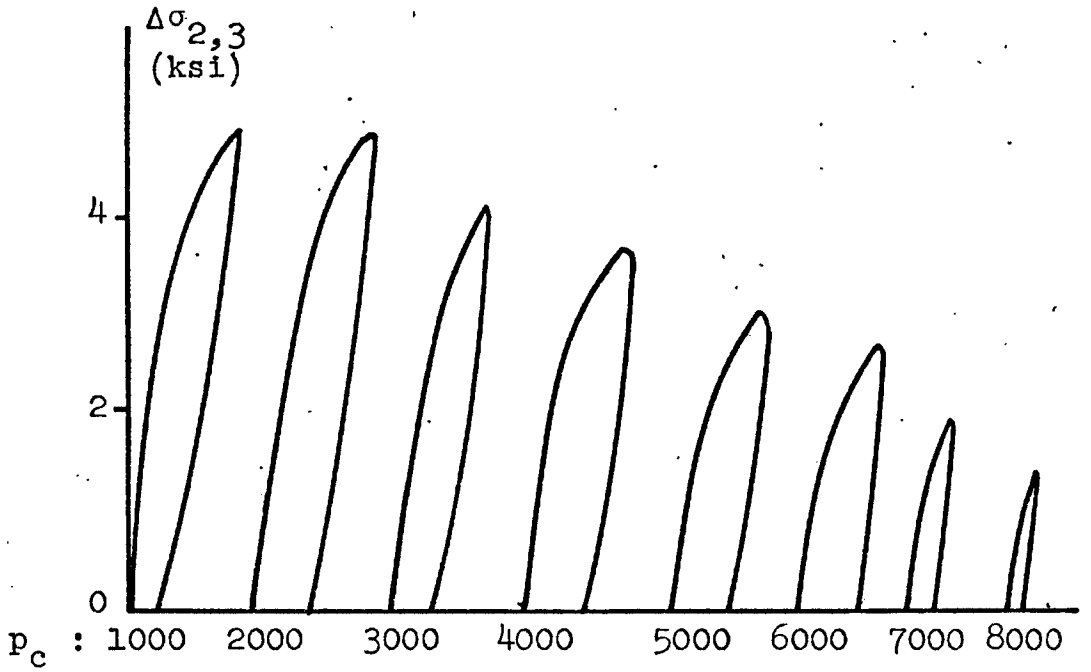

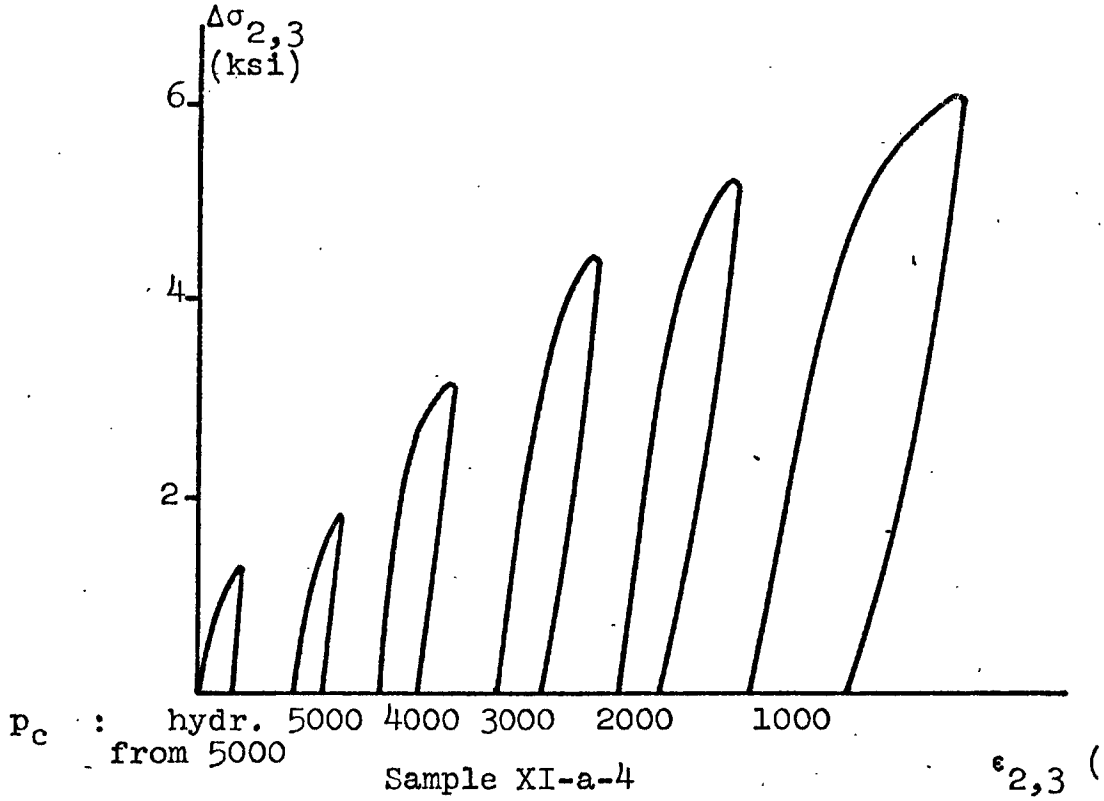

Figure IV-49 Probing tests for yield envelope at $\Delta\sigma_{2,3}$ = 3000

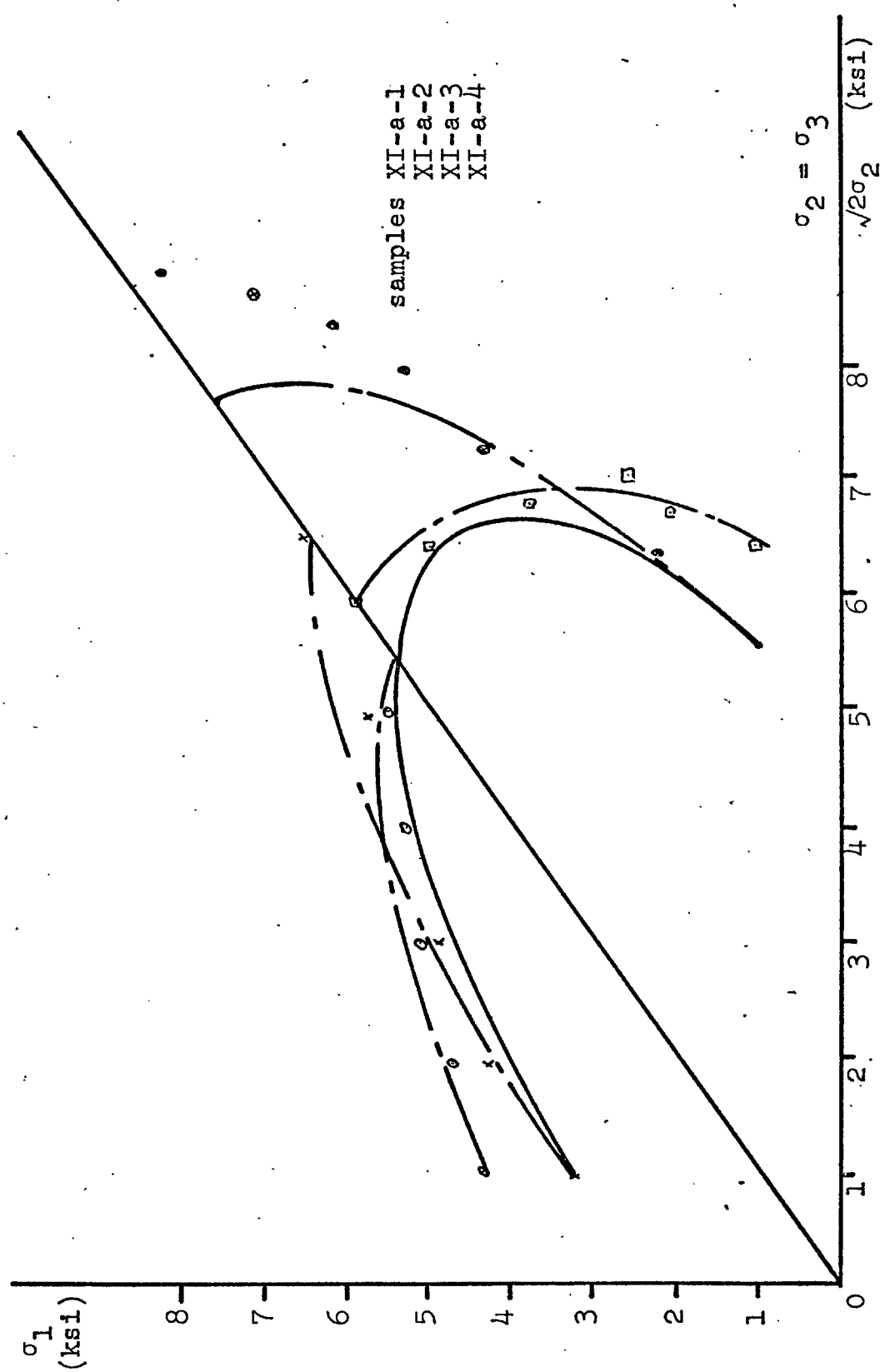

Figure IV - 50 Yield envelope for $\Delta\sigma_{2,3} = 3000$

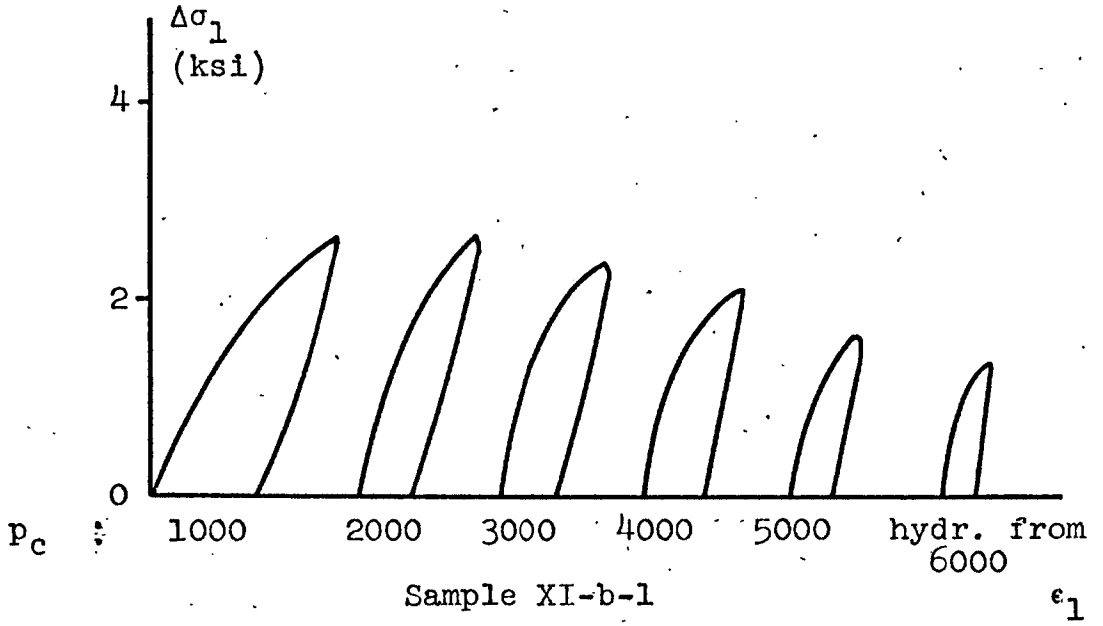

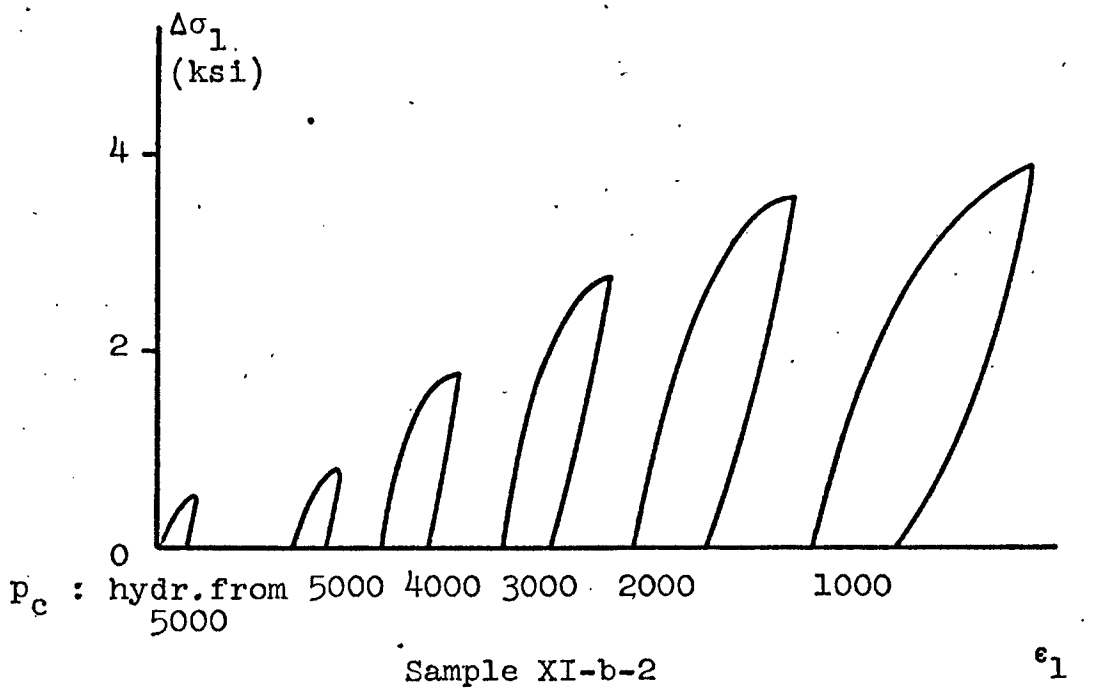

Figure IV - 51 Probing tests for yield envelope at $\Delta\sigma_{2,3} = 4000$

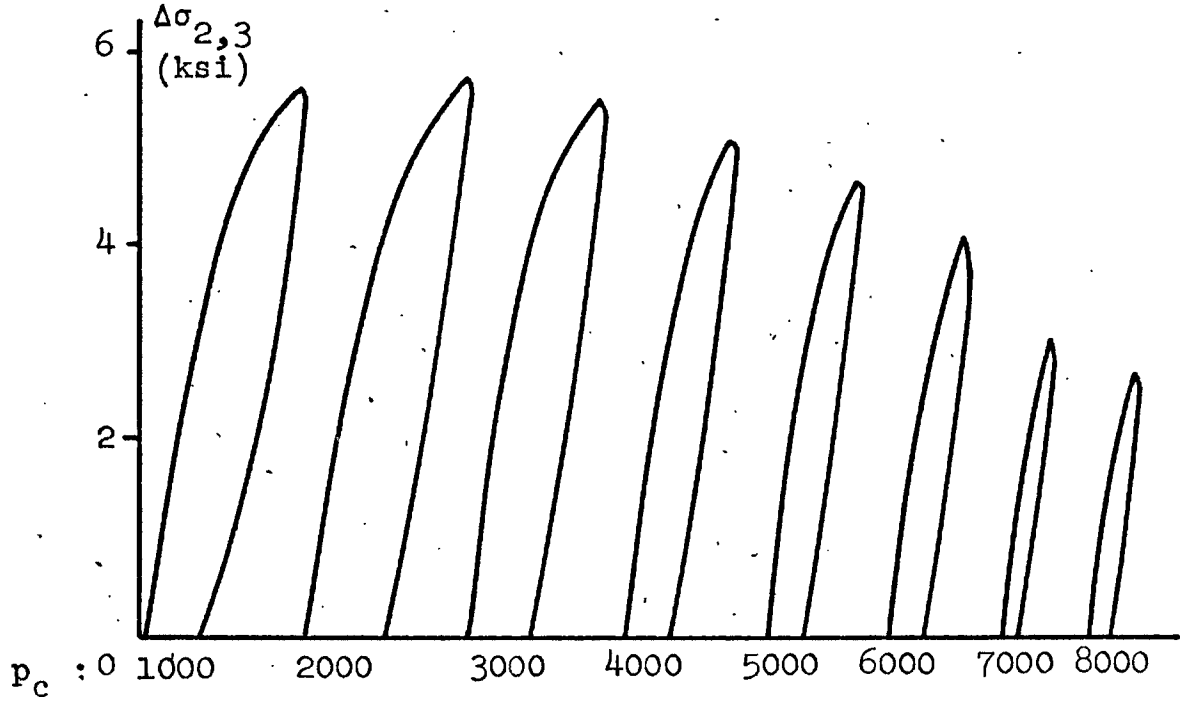

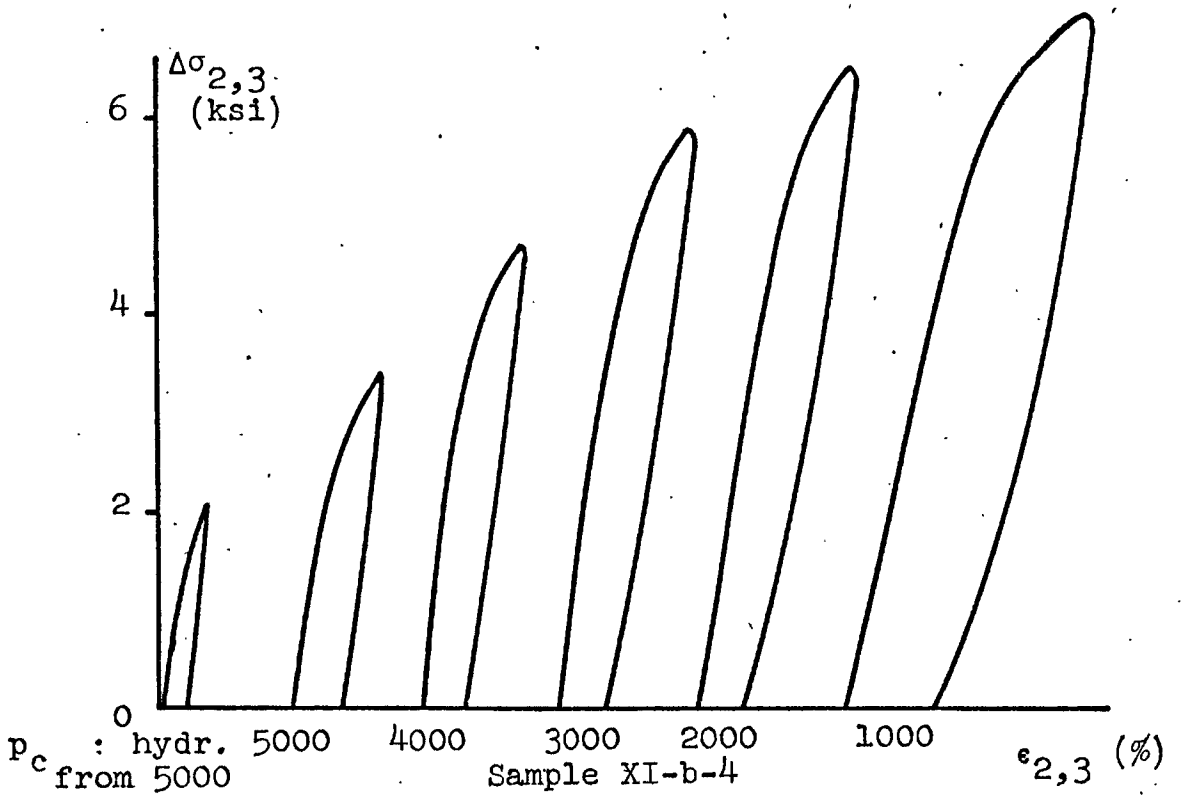

Figure IV - 52 Probing tests for yield envelope at $\Delta\sigma_{2,3}$ = 5000

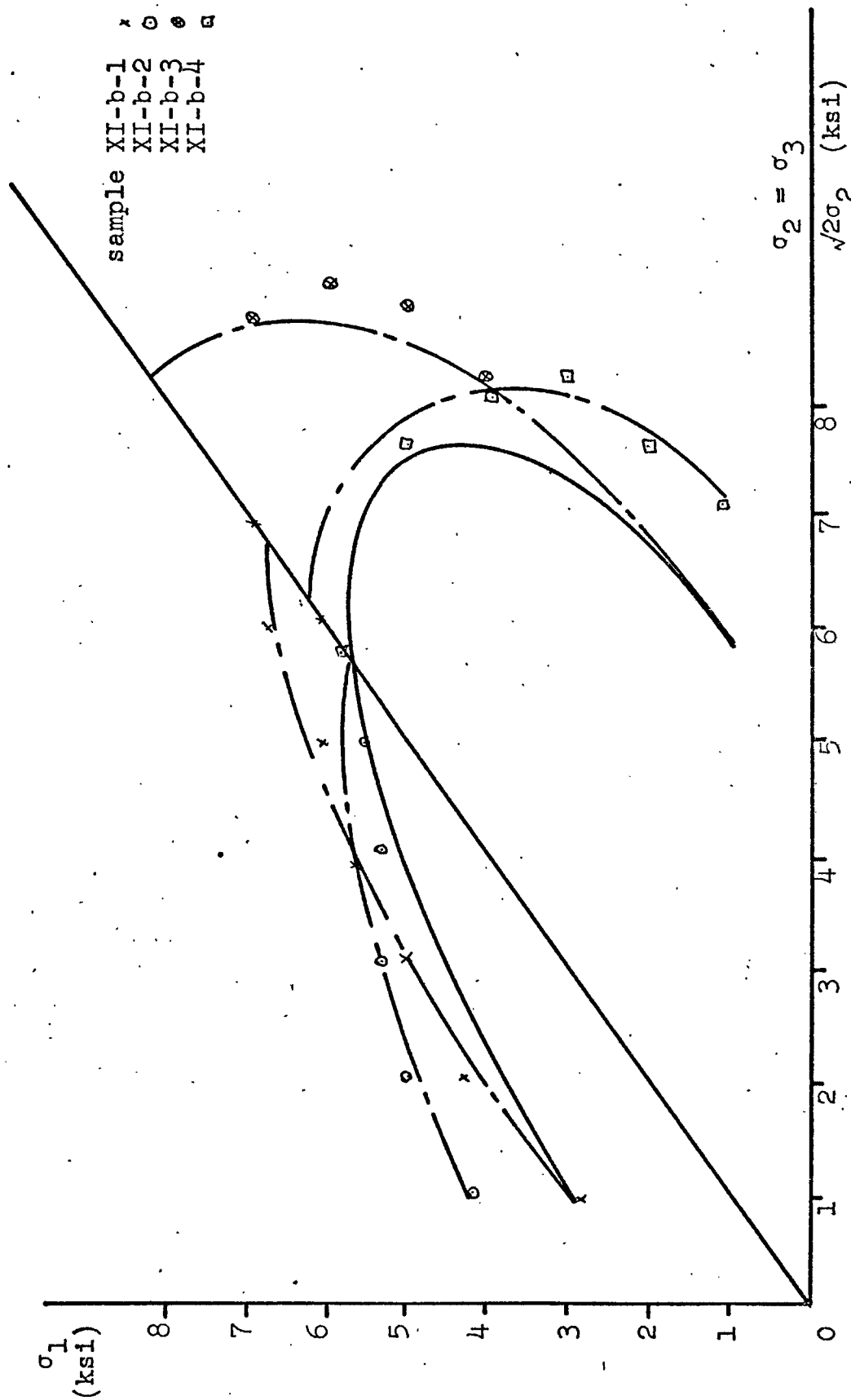

Figure IV - 53 Yield envelope for $\Delta\sigma_{2,3} = 4000$

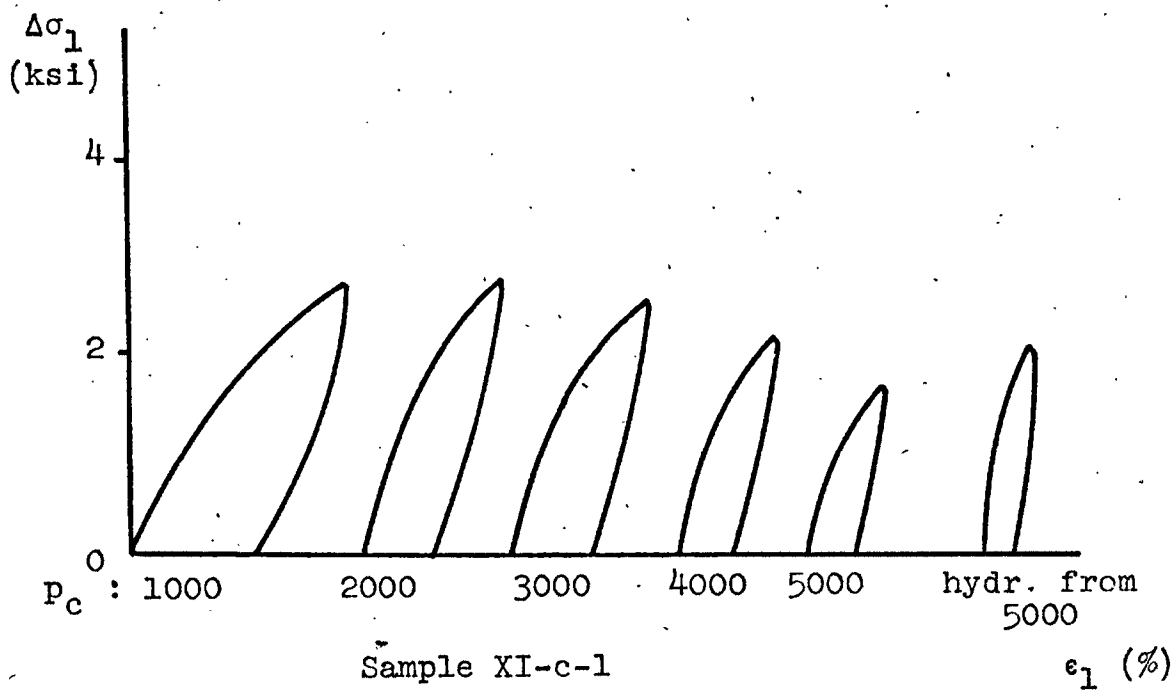

Sample XI-c-1

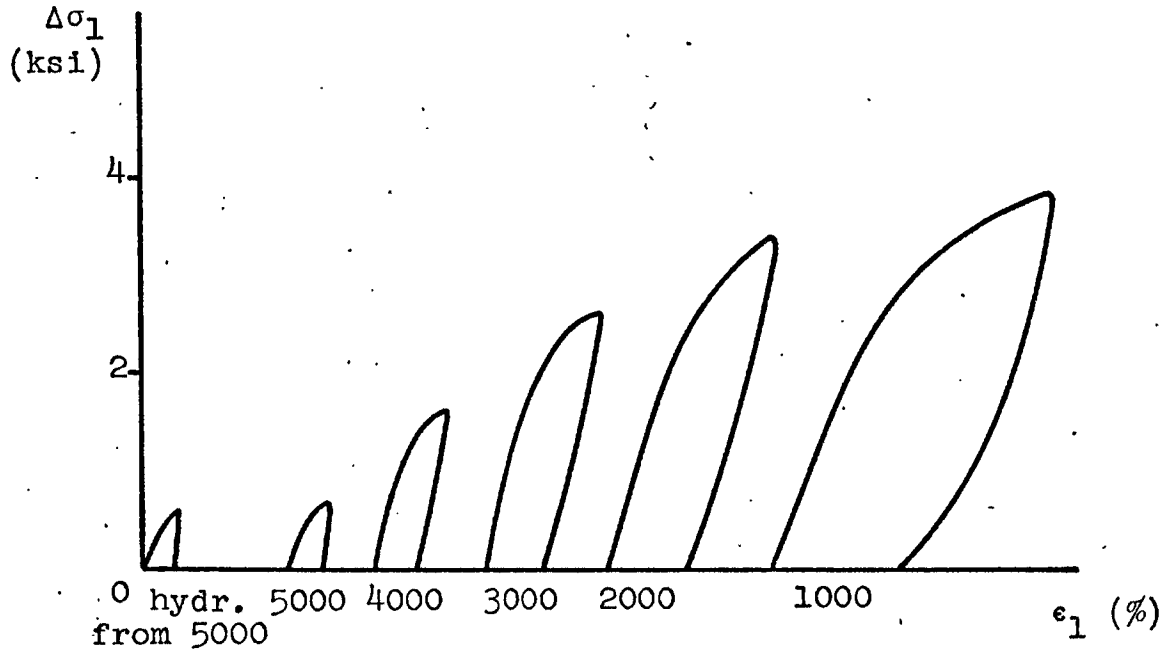

Sample XI-c-2

Figure IV - 54 Probing tests for yield envelope at $\Delta\sigma_{2,3} = 5000$

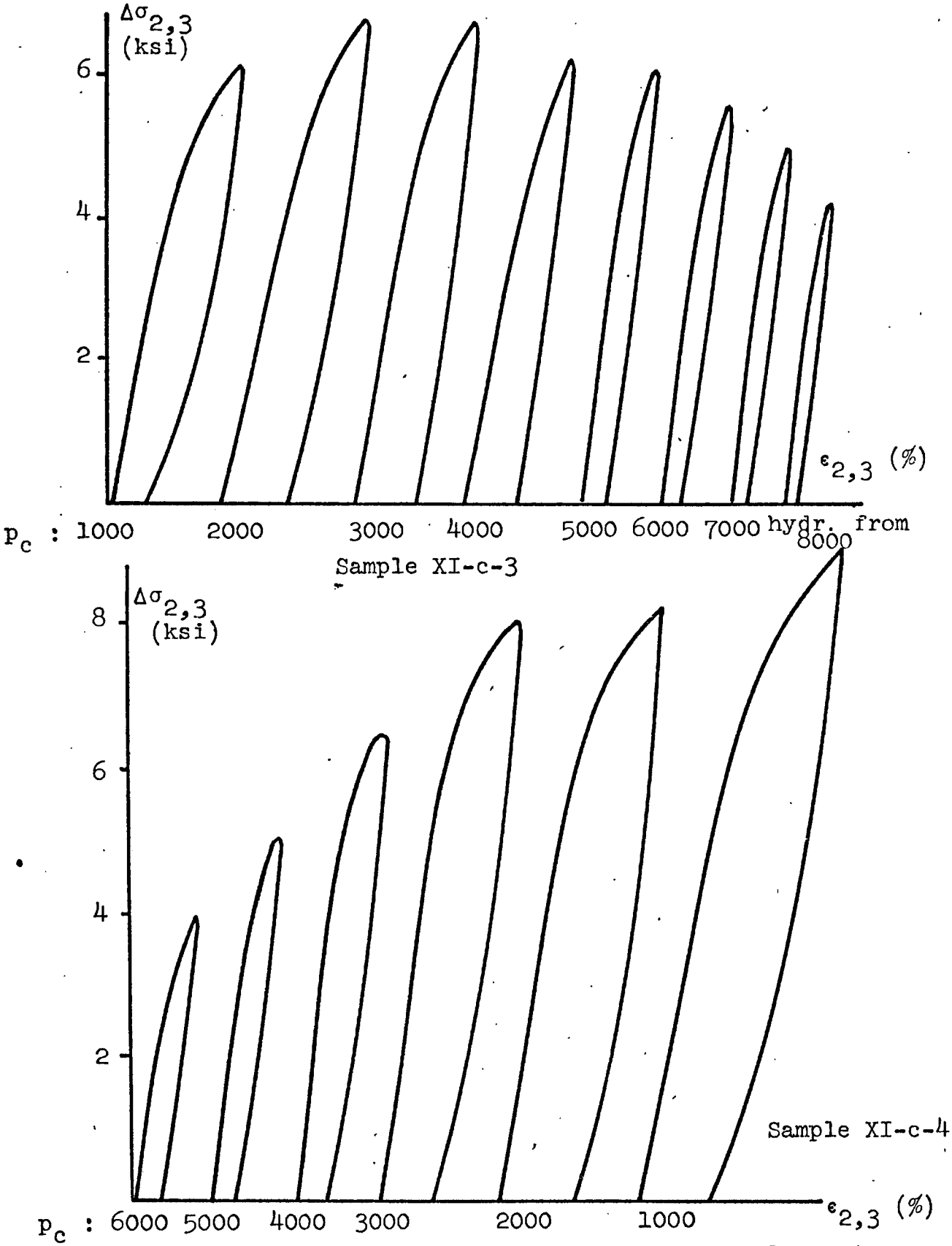

Figure IV-55 Probing tests for yield envelope at $\Delta\sigma_{2,3} = 5000$

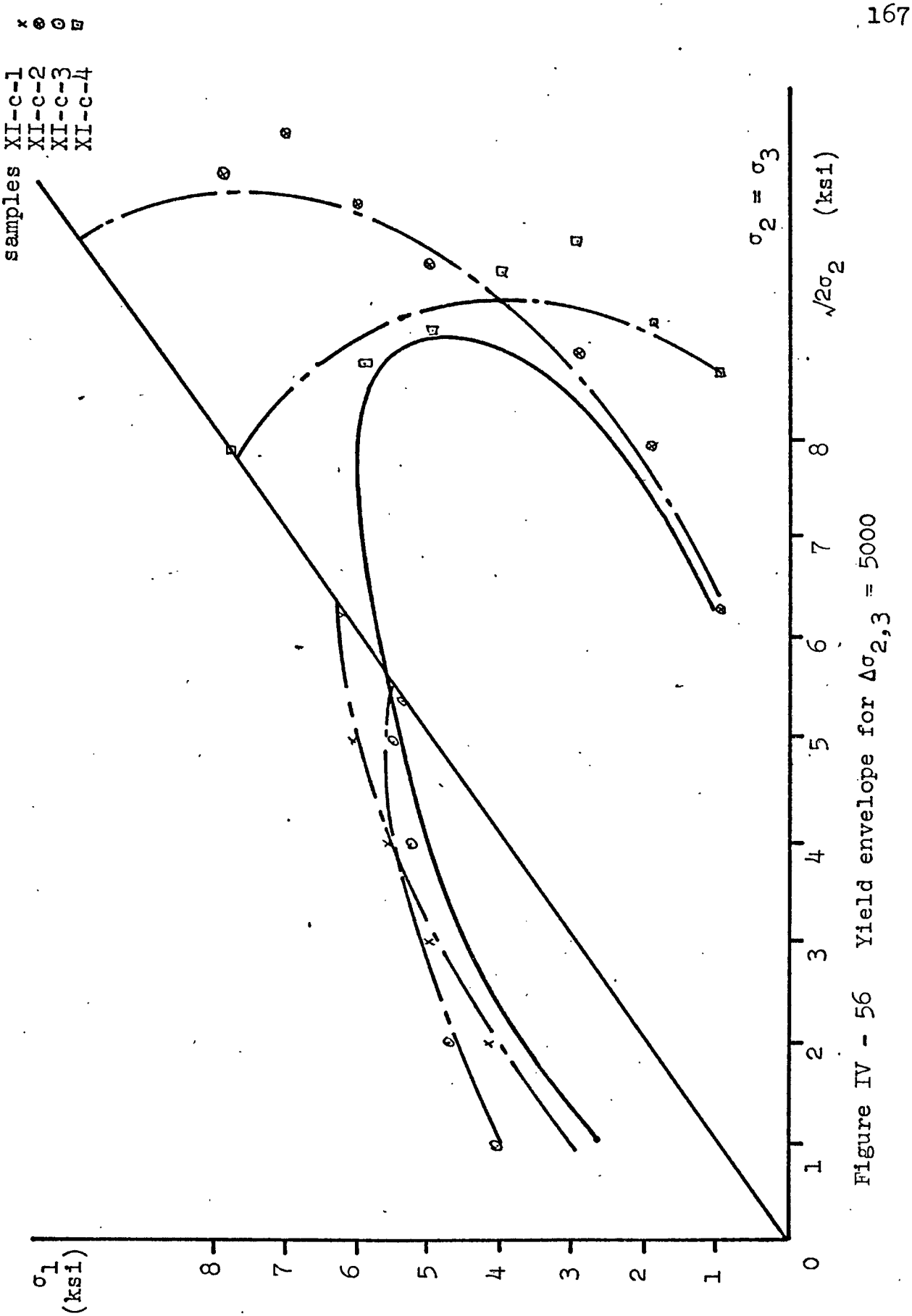

Figure IV - 56 Yield envelope for $\Delta\sigma_{2,3} = 5000$

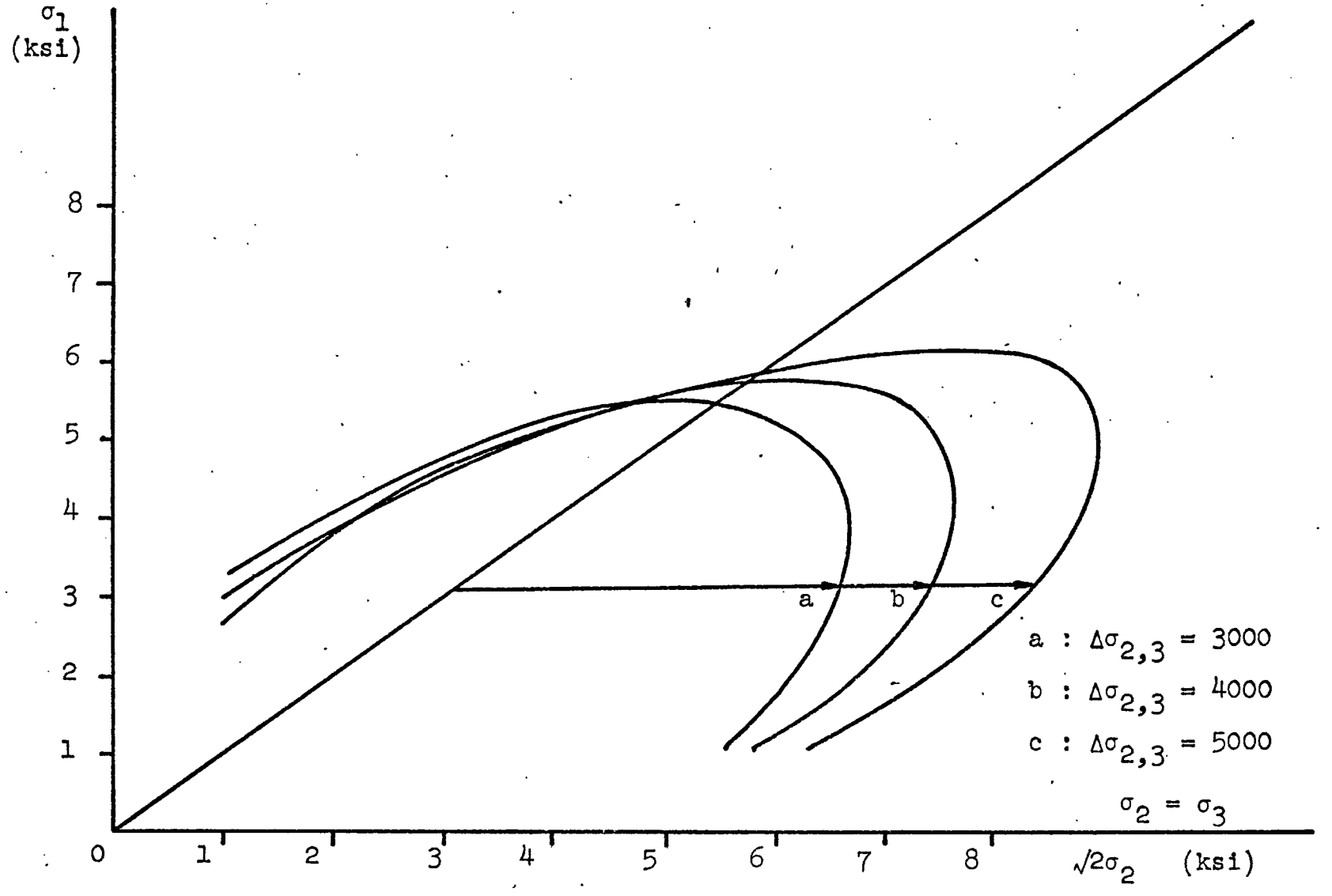

Figure IV - 57 Superposition of third set of subsequent yield envelopes ($\Delta\sigma_{2,3}$)

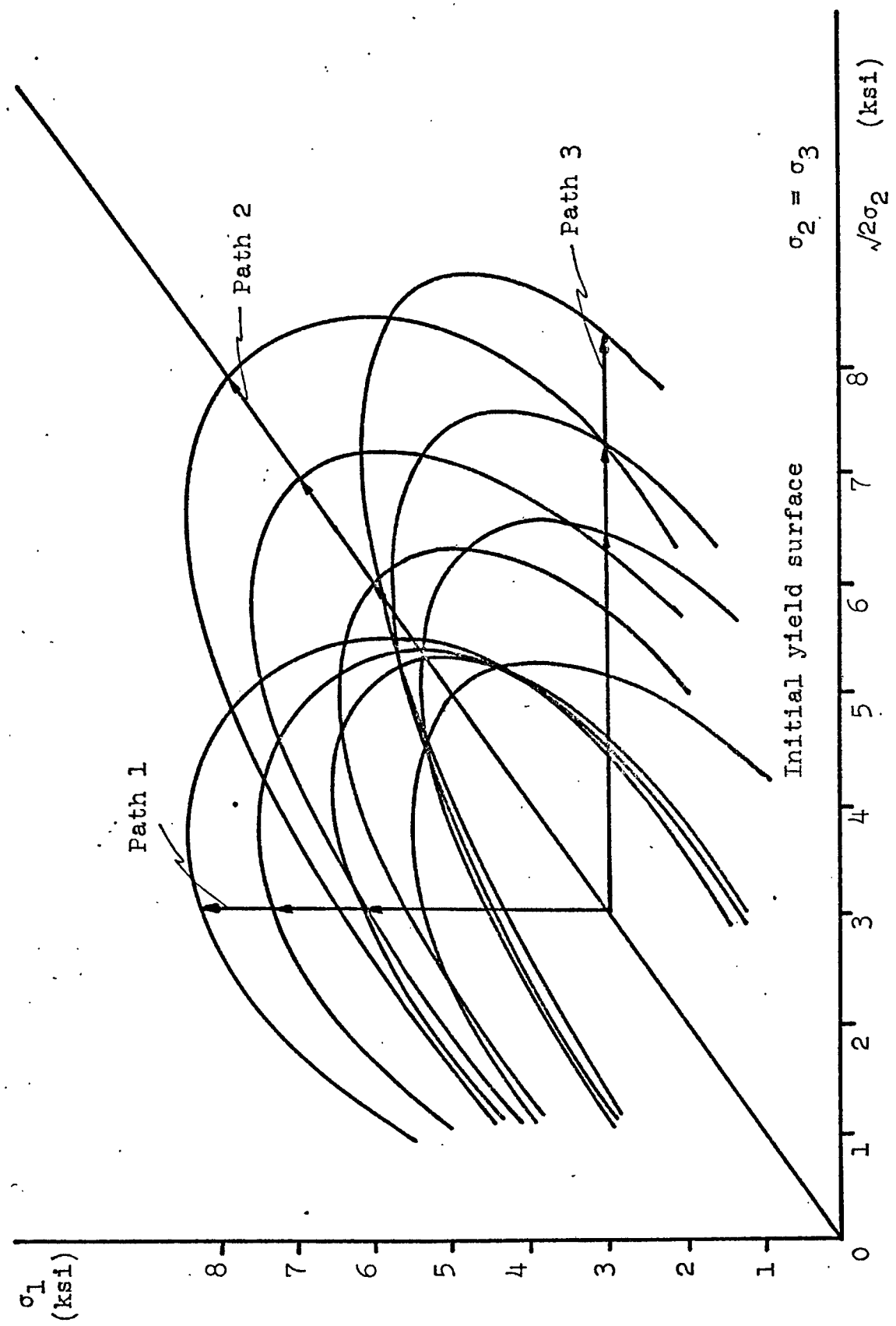

Figure IV - 58 Initial and subsequent yield surfaces

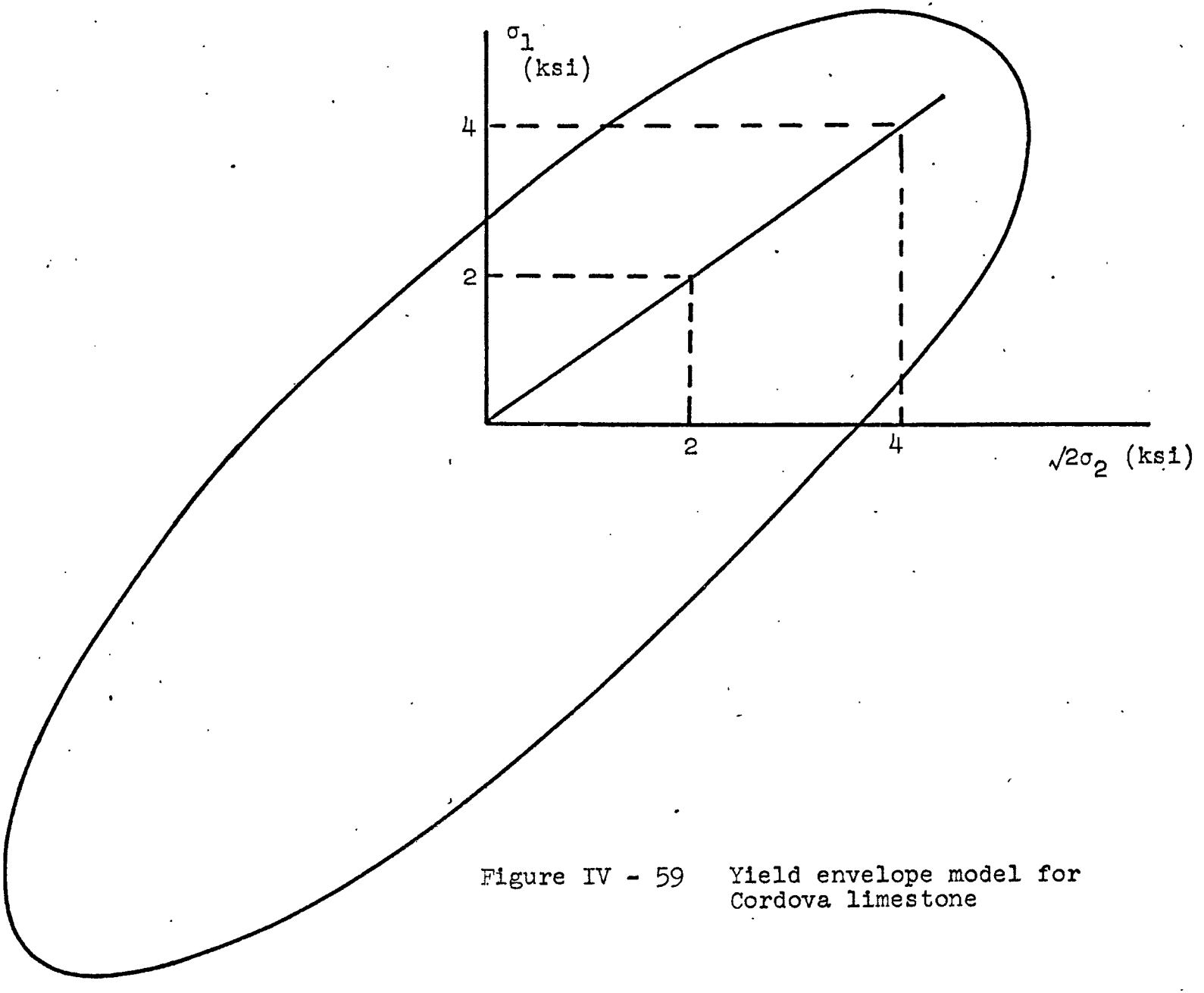

Figure IV - 59 Yield envelope model for Cordova limestone

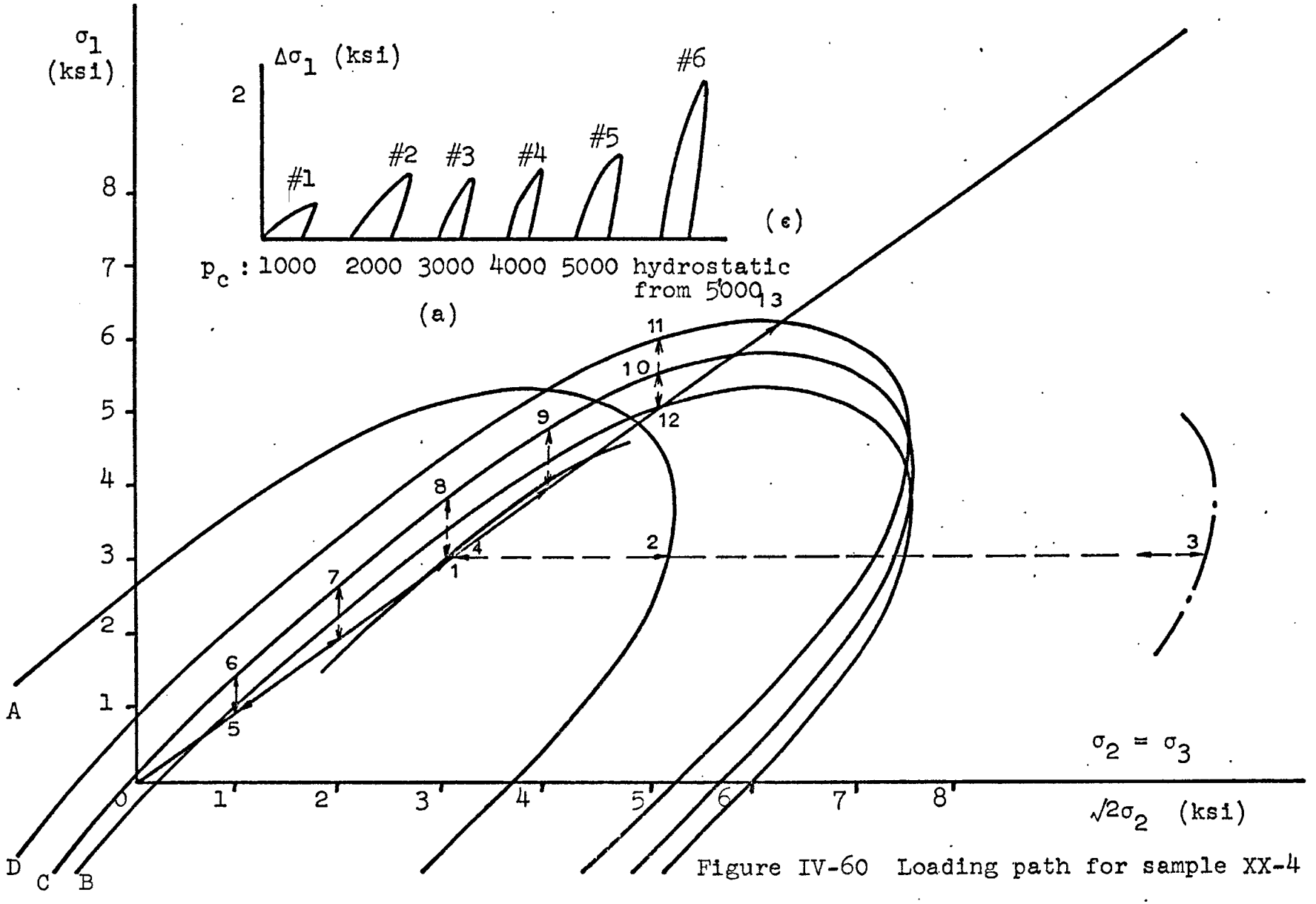

Figure IV-60 Loading path for sample XX-4

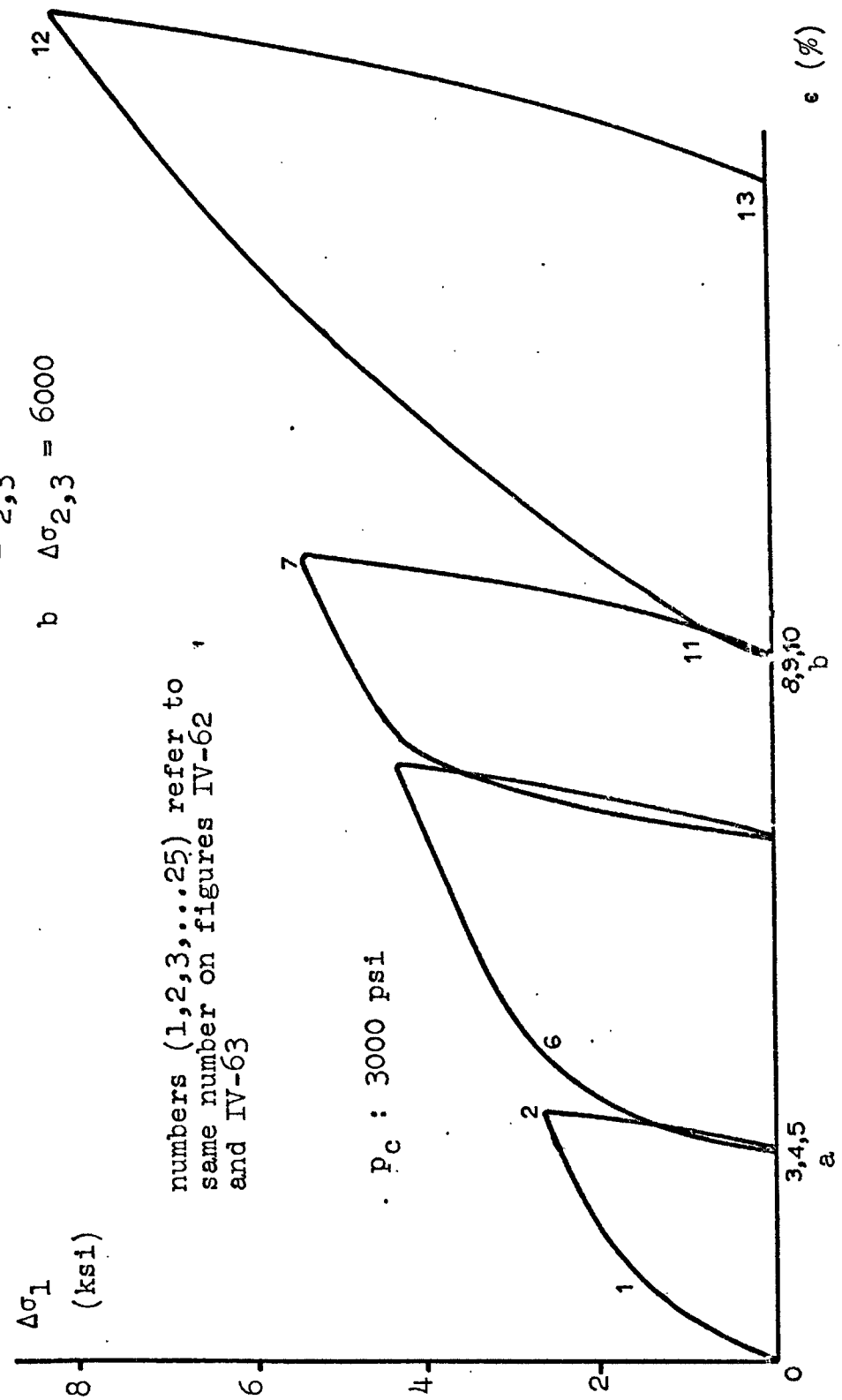

Figure IV - 61 Testing of yield envelope behavior for sample XX - 2

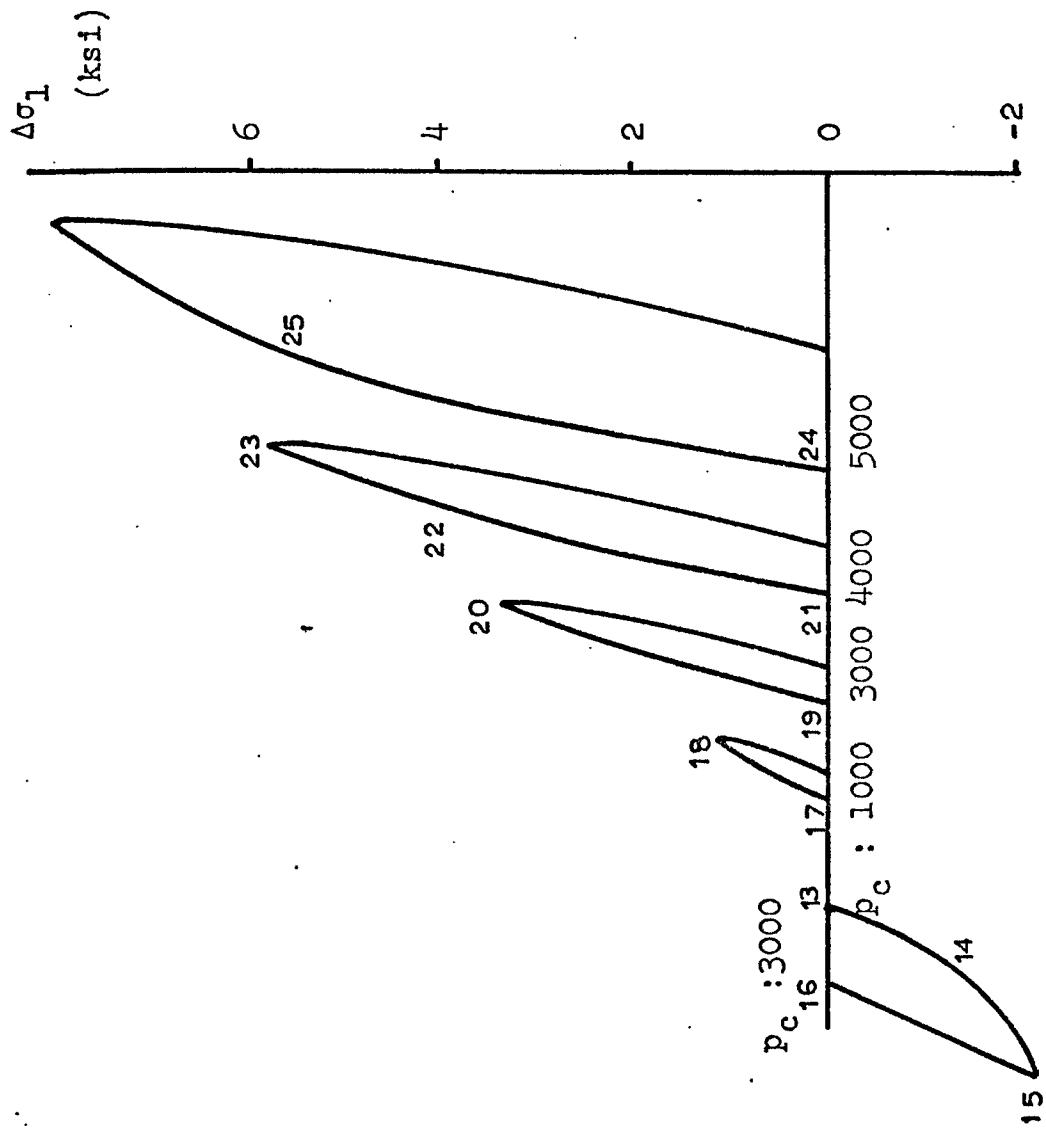

Figure IV - 61 (continued) Testing of yield envelope behavior for sample XX-2

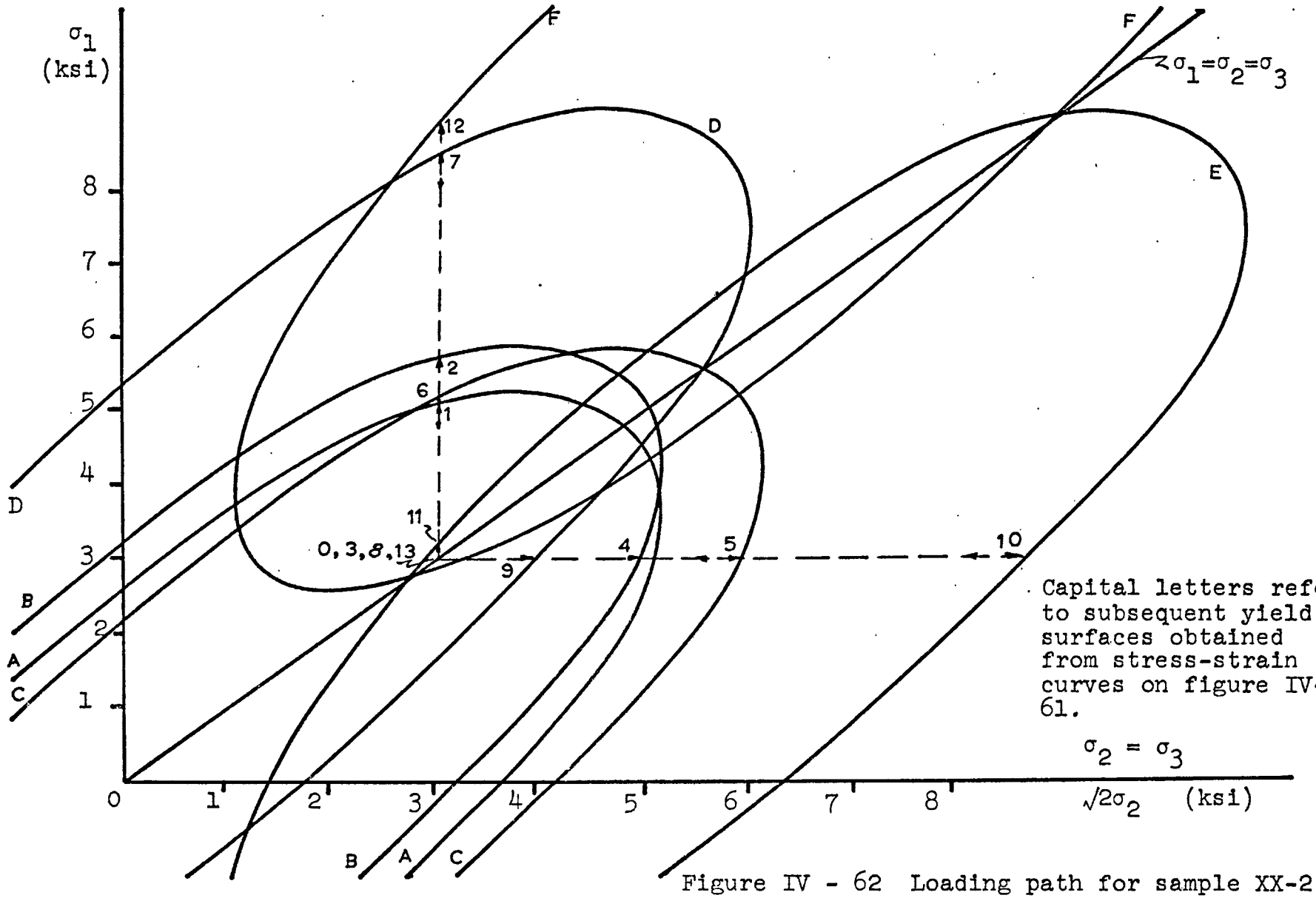

Figure IV - 62 Loading path for sample XX-2

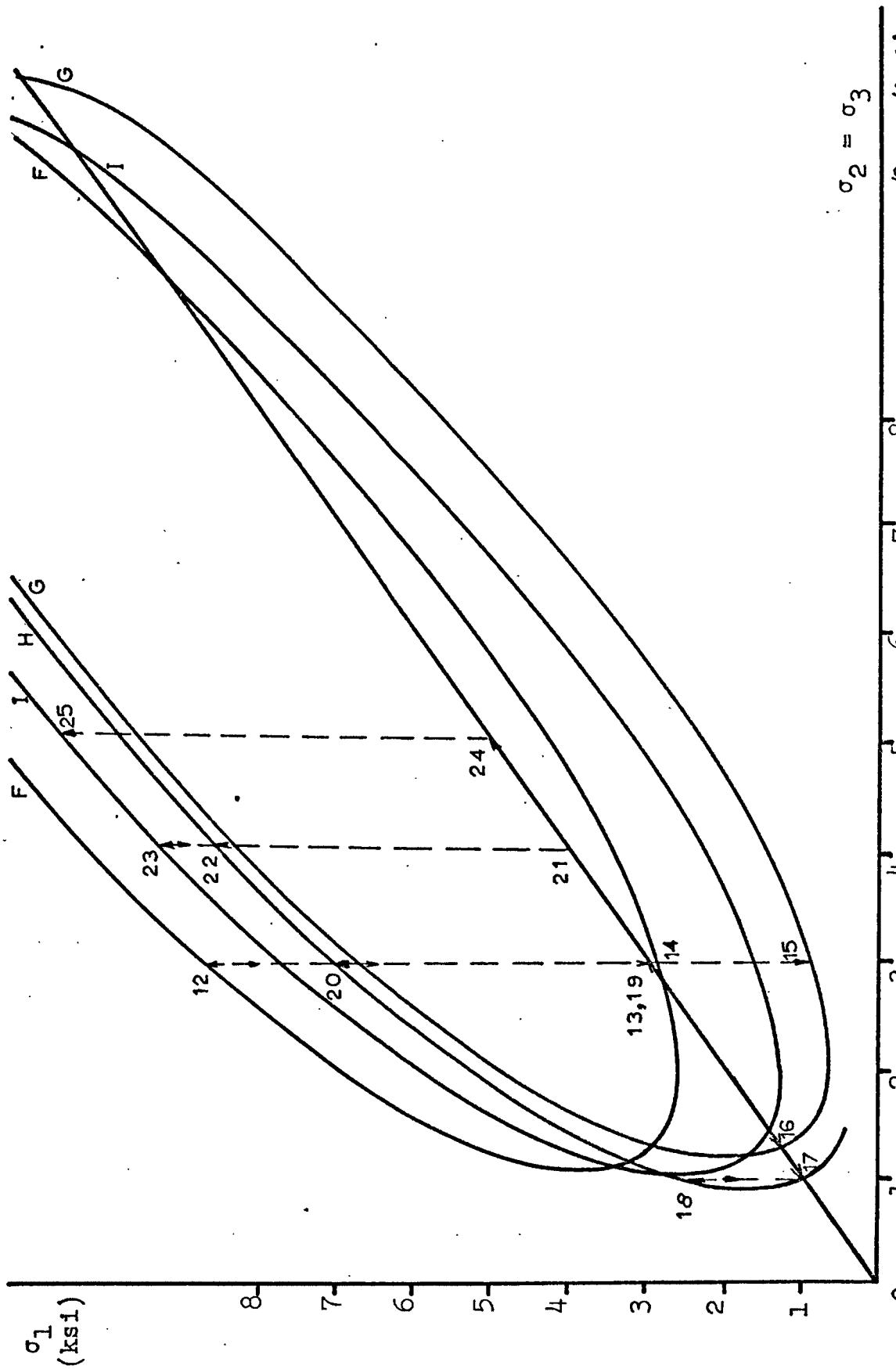

Figure IV - 63 Loading path for sample XX - 2

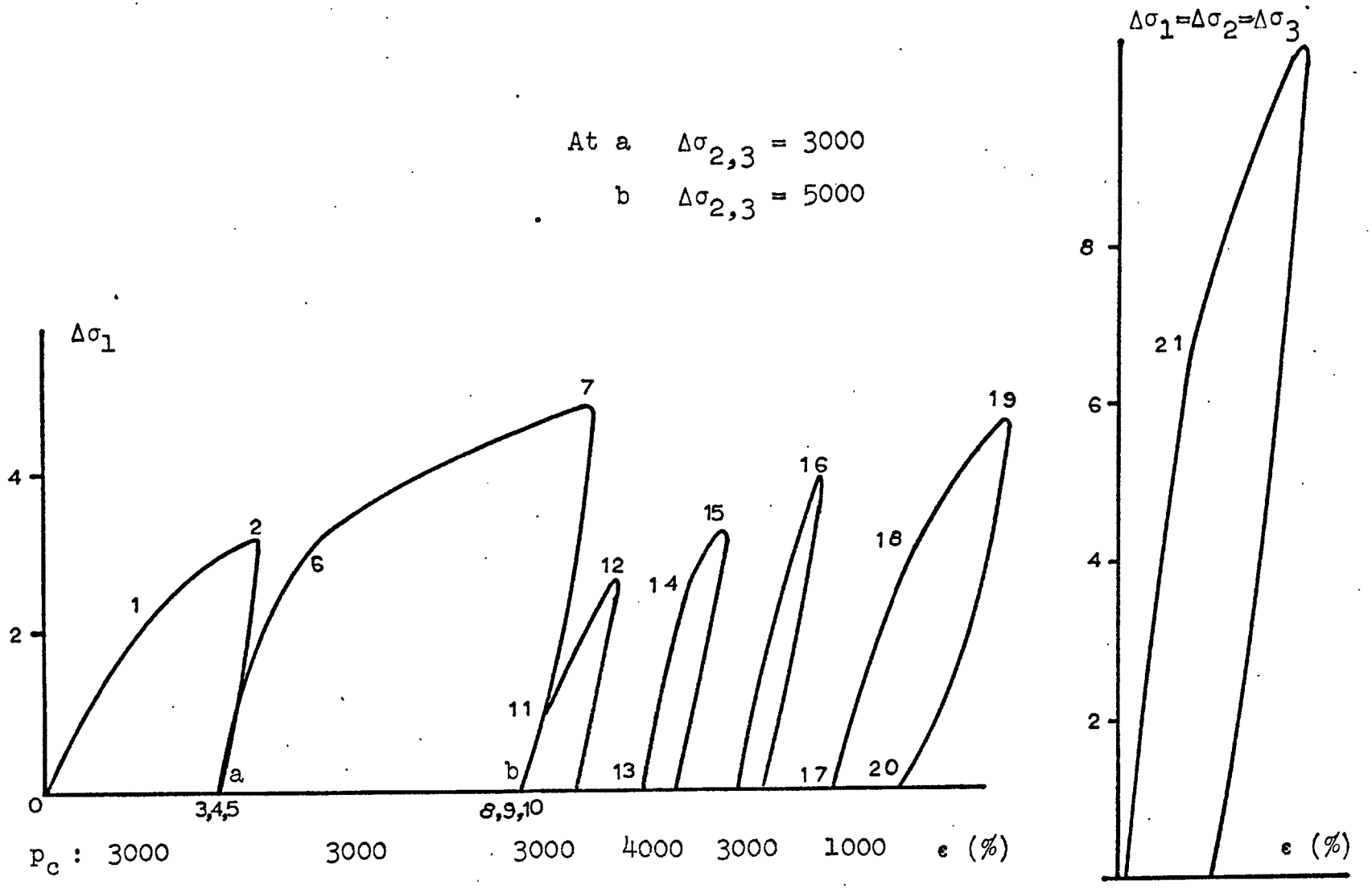

Figure IV - 64 Testing of yield envelope behavior for sample XX - 3

Hydrostatic stress test

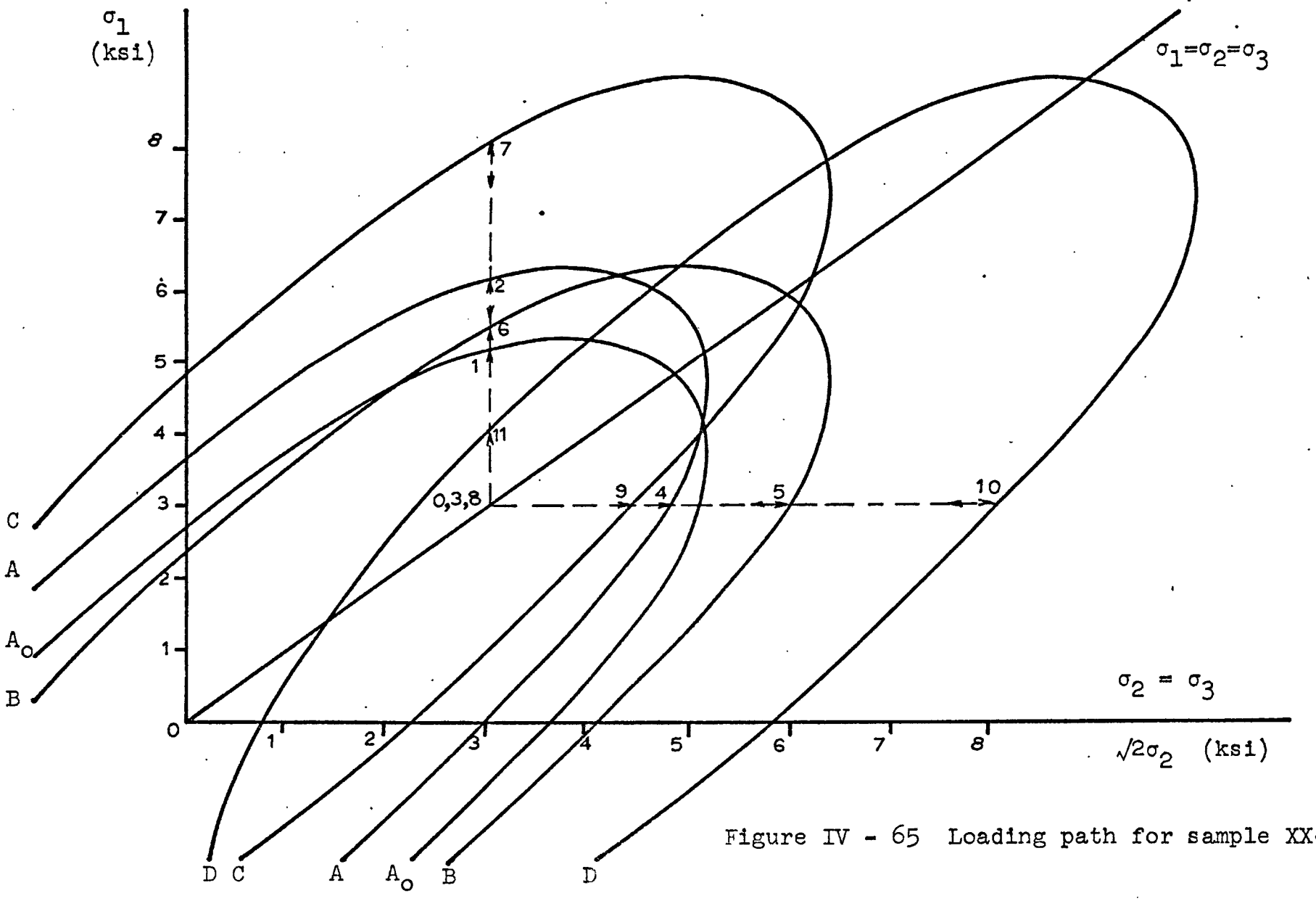

Figure IV - 65 Loading path for sample XX-3

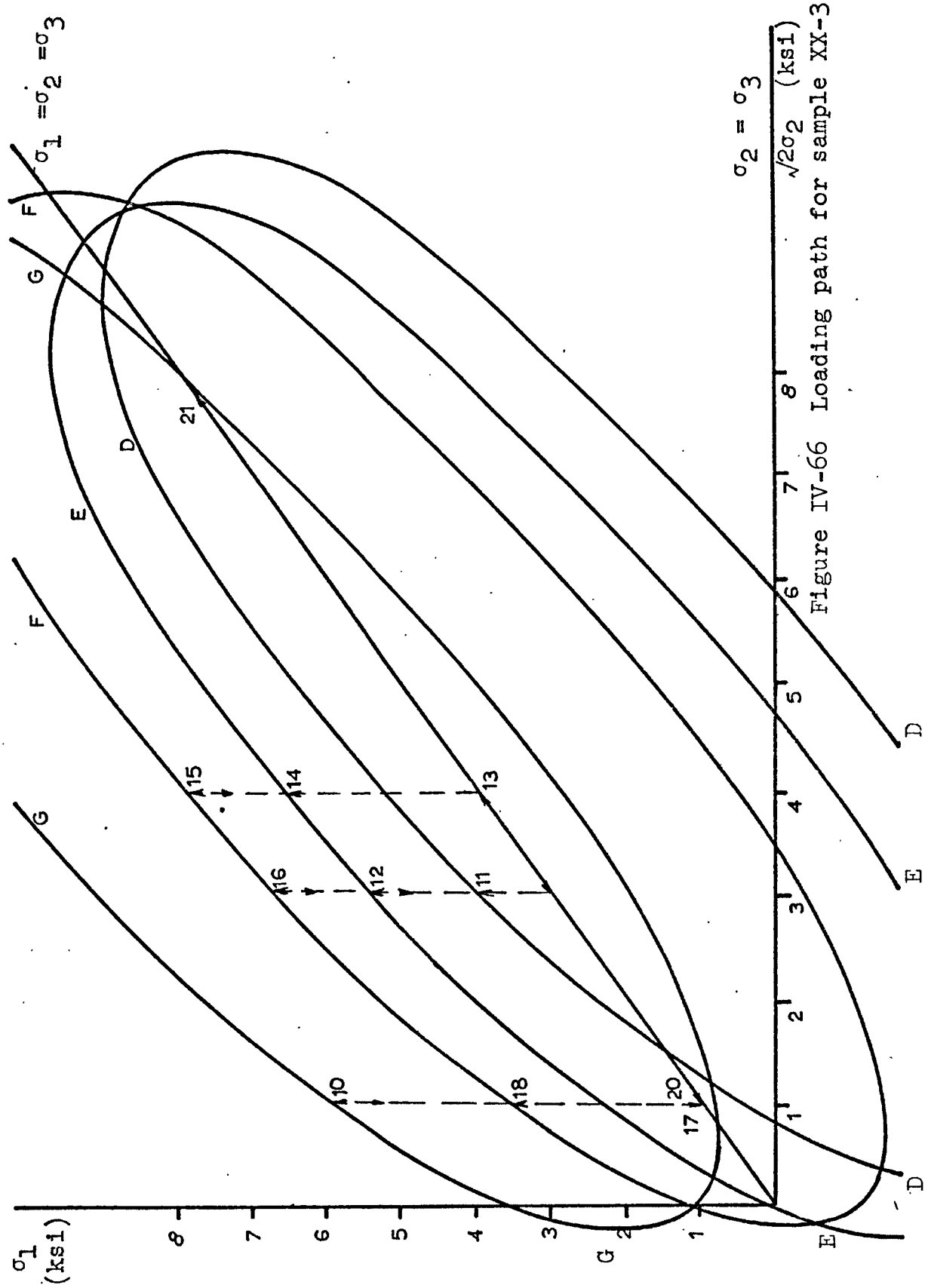

Figure IV-66 Loading path for sample XX-3

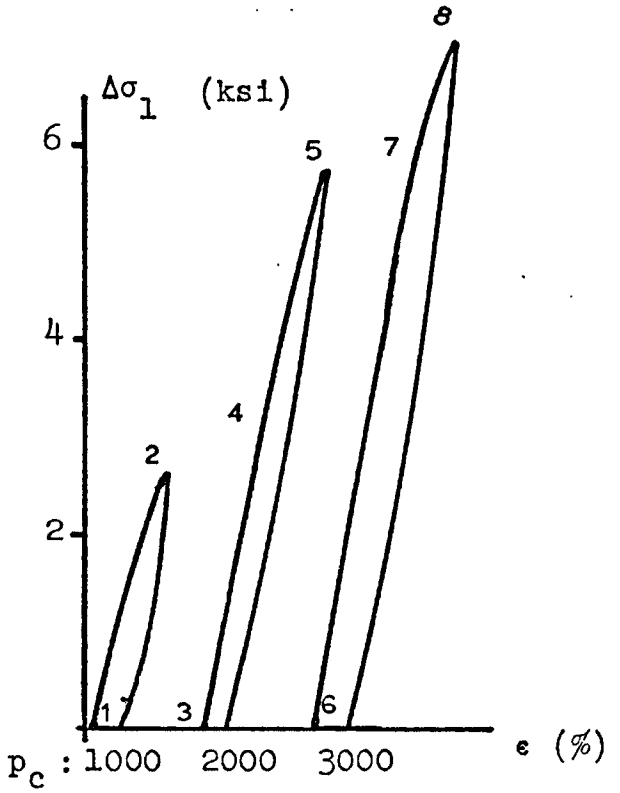

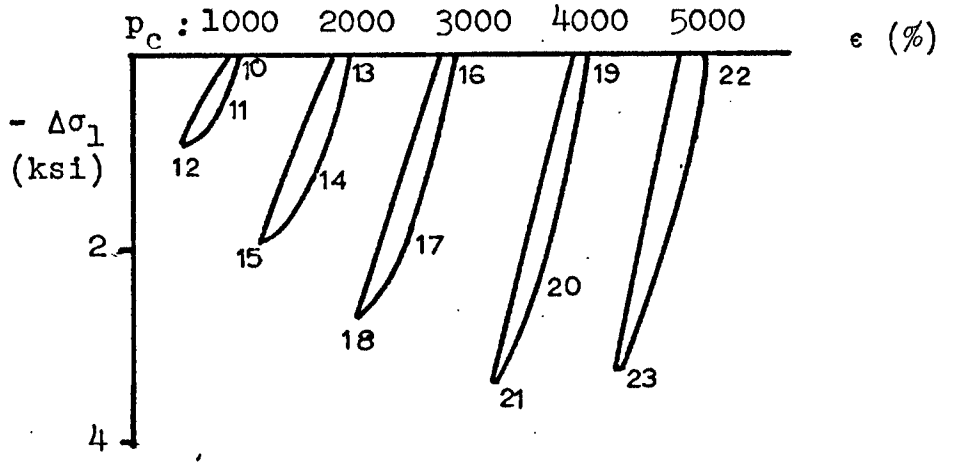

Figure IV - 67 Testing of yield envelope behavior for sample XX - 5

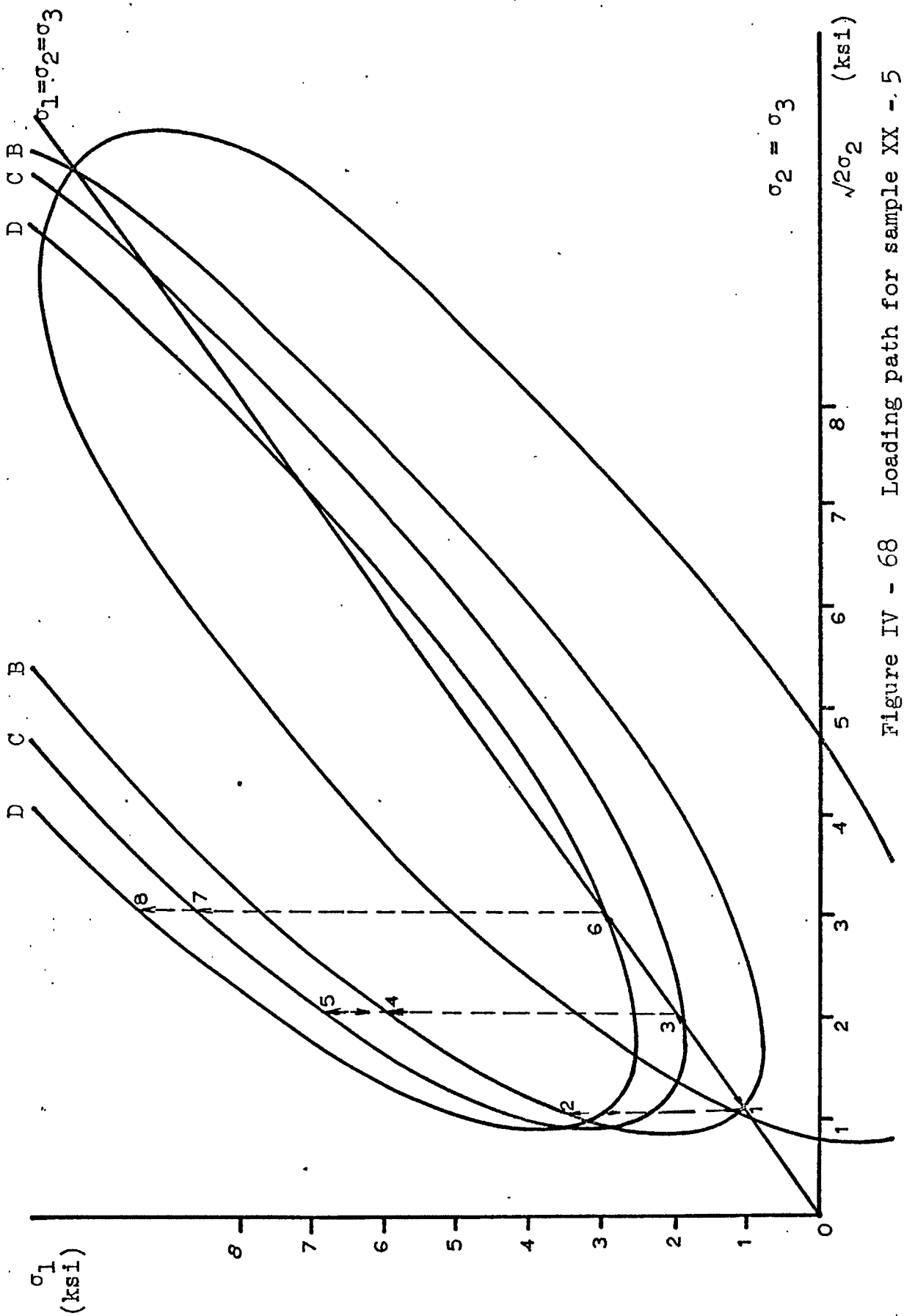

Figure IV - 68 Loading path for sample XX - 5

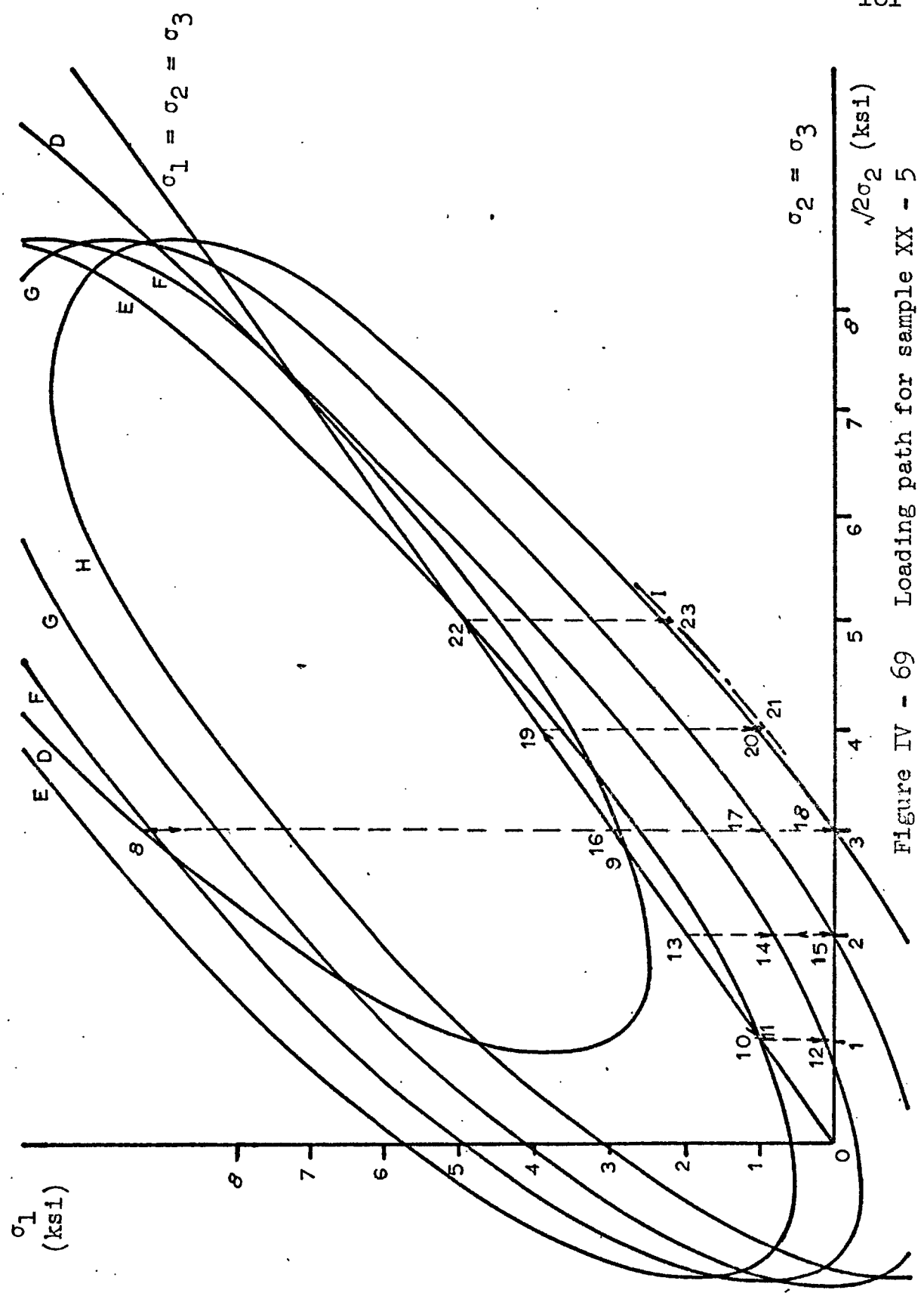

Figure IV - 69 Loading path for sample XX - 5